POLITECNICO DI MILANO

Corso di Laurea Magistrale in Ingegneria Civile – Strutture

Master of Science in Civil Engineering – Structures

POLITECNICO MILANO 1863

NUMERICAL AND EXPERIMENTAL SEISMIC VULNERABILITY ASSESSMENT OF THE SORDO VIADUCT

Supervisor: *Prof. Federico Perotti*

Co-Supervisor: Ing. Ivan Roselli
                 Ing. Fernando Saitta

Master's Degree Thesis of:

Chiara Mariani

Matr. 916089

October 2021

SOMMARIO

L'analisi di vulnerabilità sismica dei ponti esistenti è attualmente argomento di grande importanza, alla luce dei recenti terremoti che hanno colpito il Paese. Le infrastrutture viarie, caratterizzate da schemi strutturali con uno scarso grado di iperstaticità e progettate per la maggior parte attraverso norme tecniche prive di prescrizioni antisismiche, possono subire notevoli danneggiamenti, e nel peggiore dei casi raggiungere anche il collasso a seguito di forti livelli di intensità sismica. Nel campo delle analisi numeriche, la crescita del potere computazionale legato all'elaborazione informatica ha reso possibile un percorso per il raggiungimento di metodi di analisi che siano caratterizzati allo stesso tempo da accuratezza e complessità. Si è dunque gradualmente passati dalla semplicità delle analisi statiche lineari alla complessità e accuratezza di quelle dinamiche non-lineari, rappresentative dell'influenza della natura variabile dell'azione sismica sulla risposta strutturale in termini di spostamenti, deformazioni e azioni interne. A livello sperimentale, per quanto concerne le prove dinamiche non-lineari su ponti e viadotti, le informazioni sono invece tutt'ora piuttosto esigue, in quanto su di essi è stato effettuato un numero limitato di test di questo tipo. La corrente tesi ha come obiettivo quello di approfondire l'ambito numerico e sperimentale dell'analisi di vulnerabilità sismica dei ponti, attraverso l'analisi di un particolare viadotto situato lungo la tangenziale di Catania, il Viadotto Sordo.

ABSTRACT

The seismic vulnerability analysis of existing bridges is currently a topic of great importance, following the recent earthquakes occurred in Italy. The road infrastructures, characterized by structural schemes with a low degree of redundancy and mostly designed through technical standards without anti-seismic prescriptions, can experience considerable damage and, in the worst case, even reach collapse following high levels of seismic intensity. In the field of numerical analysis, the growth of computational power linked to computer processing has allowed to achieve analysis methods that are characterized at the same time by accuracy and complexity. We have therefore gradually moved from the simplicity of linear static analysis to the complexity and accuracy of non-linear dynamic ones, representative of the influence of the variable nature of the seismic action on the structural response in terms of displacements, deformations and internal forces. At an experimental level, as regards the non-linear dynamic tests on bridges and viaducts, the information is still rather limited, as a limited number of tests of this type have been carried out on them. The current thesis aims to deepen the numerical and experimental field of the seismic vulnerability analysis of bridges, through the analysis of a particular viaduct located along the Catania roadway, the Viadotto Sordo.

TABLE OF CONTENTS

List of Figures

List of tables

1

THE SEISMIC ASSESSMENT OF EXISTING BRIDGES

1.1 Introduction

Seismic vulnerability expresses the non-linear correlation existing between the intensity of a seismic event and the expected damage. Therefore, within the context of transport infrastructures, it mainly refers to the possibility of different damage levels experienced by bridges and viaducts under different earthquake intensities.

In our country, the lack of attention of the competent authorities towards bridge seismic vulnerability have only recently become object of attention. This is probably due to the consequences of little relevance arising from the bridge damage following the two major earthquakes that occurred in Italy in the last years: Friuli 1976 and Irpinia 1980. As regards the former, the limited effects were mainly attributable to the fact that, in the area under examination, the road infrastructure construction was in its initial phase. In the case of the Irpinia earthquake there were consequences, albeit limited, mainly due to the constraints unsuitability, which were replaced with more innovative seismic isolation devices.

However, although the Italian earthquakes of the last years have not produced significant damage to the viaducts, the vulnerability analysis recently conducted on this type of works have provided results that and are a sign of the necessity of the seismic risk assessment.

Considering the Italian regulatory framework about the subject, the Circ. Min. LL.PP. No 6736 "Control of the stability conditions of the highway works" of 07/19/1967 represents the first Italian standard in the sector [1]. Although it consists of a few pages, and of qualitative nature, it provides some operational indications, among which the

frequency and type of inspections, identification of skills and responsibilities, qualification of inspectors and obligation to produce documentation on inspections. It is still a current reference standard for many of the maintenance and inspection manuals of road operators in Italy.

The topic of the assessment of existing bridges have been resumed in 1980 with the Circ. Min. LL.PP. No 220977, "General criteria and technical prescriptions for the design, construction and testing of road bridges", up to the Circ. Min. LL.PP. No 34233, "Instructions related to the Technical Regulations for road bridges" of 25/02/1991.

In 2003, with the orientation of the Italian regulatory framework in the direction of European legislation, the monitoring topic has been limited to the analysis of existing buildings. In general, it was decided to pay larger attention, both for bridges and buildings, to the design of new structures.

Afterwards, with the D.M. of 14/01/2008 the "Technical Standards for Construction" (NTC) have been issued, updated by the Ministerial Decree of 17/01/2018 and the Explanatory Circular No. 35 of 11/02/2019, which constitutes the current regulatory reference for operators in the field.

Finally, the regulatory update of the sector is represented by the decree issued by the Ministry of Infrastructure and Transport in 2020, with the consequent drafting of the guidelines on risk classification and management, safety assessment and monitoring of existing bridges drawn up and approved by the Superior Council of Public Works. In parallel a research project was undertaken, financed by the Civil Protection Department and the University Laboratories in Seismic Engineering (Reluis). In its first phase, carried out between 2005 and 2008, a specific line was developed on the "Assessment and reduction of the seismic risk of existing bridges" [2].

Also ENEA is particularly active in assessing the safety of bridges and viaducts. The National Agency for New Technologies, Energy and Sustainable Economic Development has indeed developed over thirty years of expertise in static and seismic monitoring of bridges, as in the case of the analysis carried out on the Ponte all'Indiano

in Florence, on the viaduct for access to Civita di Bagnoregio (VT) and on the footbridge in Forchheim (Bavaria).

The institution is currently engaged in several projects in the area of infrastructure risk management. Among these is mentioned RAFAEL, developed by a vast national partnership led by ENEA. It aims at analyzing the risk of catastrophic events, developing events scenarios that could occur in the short-medium term. Therefore, it identifies the possible risks for infrastructures, with particular interest in the southern regions of the Country, providing an estimate of the possible impacts on services and the consequences on the population.

The current thesis explores a part of the aforementioned project, and has, as main purpose, the numerical modeling and vulnerability analysis of the "Sordo Viaduct" of the Catania freeway. The work tries to identify the assessment need in the examined infrastructure, through the results coming from dynamic analysis. Indeed, the necessity of accurately assessing the state of existing bridges and of detecting the necessity of interventions is clear, and linked to the similar inadequacies observed in highway bridges and viaducts: insufficient strength or ductility of the piers, unacceptable bearings deformations and inability to transmit the inertia forces to the piers.
In this light, the thesis develops as follows:

- The first chapter deals with the issue of safety and damage under seismic attack expected in existing bridges, with particular attention to the definition of the seismic action starting from the seismic hazard of the site where the structure is located;

- The second chapter aims to provide a detailed description of the numerical model of the viaduct under consideration. Starting from the representation of a simplified model of the pier in which the deck was modeled through a mass at the top of the pier itself, a more complex model of the complete viaduct was set, also including a simplified model of the dynamic soil-structure interaction phenomenon. The basic objective is to provide a numerical formulation of the bridge behavior which could capture the physical and mechanical interactions

of earthquake input and structural response. The model is aimed at describing, albeit with reasonable approximation, the geometry, as well as the boundary conditions, the connections between structural elements and the loading distribution, in order to reach a satisfactory correspondence with the real behavior of the structure;

- The third chapter aims to illustrate the results of the dynamic analysis carried out on the models shown in the previous chapter. The correlation between an intensity parameter that describes the seismic action and a damage parameter intended to represent the response of the structure will be specifically discussed, through the curves deriving from an incremental dynamic analysis;

- The fourth chapter analyze the realization of a 1:5 scale physical model of a span of the Sordo Viaduct, aimed at carrying out static and dynamic tests in the non-linear field on shaking table. Particular attention will be paid to the preliminary design of two possible types of seismic isolators that can provide an alternative to the neoprene supports currently present in the viaduct;

- The fifth and final chapter finally illustrates the conclusions drawn from the analysis of the current thesis with possible future developments.

1.2 Bridge damage under seismic attack

Seismic events have the peculiarity of detecting structural weaknesses, with a subsequent concentration of damage in these identified areas. Although their structural simplicity, in some instances bridges have revealed a poor response to recent earthquakes, primarily due to the design philosophy by which they were designed.

The effects of this poor experienced performance in bridges can be particularly relevant, as failure in a structural component can result in a global collapse with disastrous consequences. Indeed they are characterized by a little or absent redundancy in their structural system unlike buildings, which are typically statically indeterminate structures. Therefore, although it guarantees a larger ease in predicting the response under seismic excitation, simplicity leads to an increase in sensitivity to design errors.

Following the aforementioned considerations, the need to pay particular attention to the seismic design and to the assessment of existing bridges is particularly evident. In recent years, design philosophies have thus been introduced to counteract the uncertainties related to the nature of the seismic excitation. The "capacity design" approach, well established for building and included in a series of bridge design specifications, aims indeed to guarantee that, for a structural system, ductile failure mechanisms occur before brittle failure ones, by ensuring that the strength of the elements selected as fragile is larger than those for which a ductile behavior, and so the potential inelastic deformation location, is assumed. As a result, the structure will be characterized by a considerable ability to dissipate the energy transmitted by a seismic event, avoiding undesirable plastic hinge locations and unwanted collapse mechanisms.

Although the design of new infrastructures is of considerable importance, the highway system is already almost fully developed, with the number of new constructions turning out to be very small if compared to the quantity of pre-existing bridges and viaducts. The latter were built before the seismic action was thoroughly analyzed and understood. This has caused and is likely to lead, following future earthquakes, to potential bridge failures in highly seismic areas. These considerations make the

assessment and retrofitting, as well as the design of new works, a matter of great importance.

However, the fact that an older bridge was designed to lower seismic standards than would be required today, does not necessarily mean that it must be expected to collapse or be severely damaged in earthquakes of the intensity provided by current standards. Consequently, methods for retrofit of existing bridges are often treated and considered separately from design for new bridges, with a less conservative approach allowed in the field of assessment of the expected bridge seismic performance.

In order to have a clear comprehension of the possible problems treated in the field of the assessing measures, it can be useful to examine the main failure and damage typologies that arose in bridges due to recent earthquakes. The latter can be considered consequence of the elastic design philosophy characteristic of the large majority of the bridges made up to 70s, in which the design seismic forces were computed as a small percentage of the actual forces that could be developed in an elastically responding structure of unlimited strength [3]. As a consequence of the elastic approach, seismic deflections coming from the specified lateral force levels were severely underestimated. Moreover, the usage of low seismic force altered the ratio between gravity and seismic loads, thus leading to wrong shapes and to the mislocation of the contraflexure points in the moment diagrams. In many cases, in sections in which the moments coming from the vertical and lateral loads were opposite in sign, the resulting design moment could even be incorrect in sign, because of the wrong proportions in the load combinations.

An application of these problems is provided by the example of Priestley et al. in [3], with the representation of a two column bridge under dead load D and transverse seismic load E. The solid curve in the figure below represents the moment resulting from the combined forces D and E corresponding to the level of transverse seismic force according to the elastic design assumption.

(a) Gravity Loading **(b) Seismic Loading** **(c) Combined Gravity and Seismic Loads**
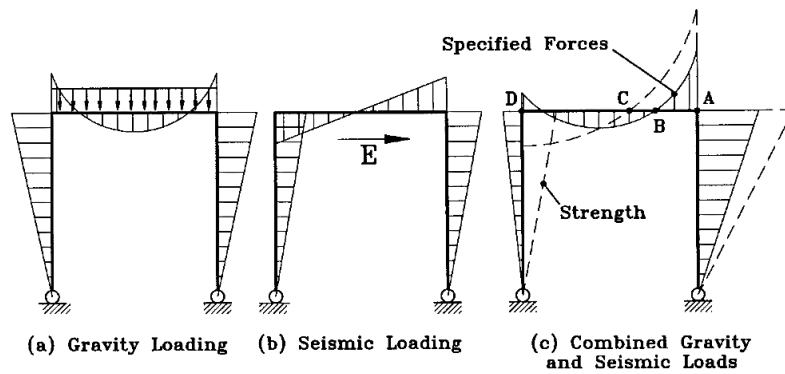
Figure 1 : Elastic moment distribution under dead and seismic loads

However, according to this design philosophy, since material stress levels are below yield or strength values, higher values of lateral forces could be sustained before the achievement of member strengths. It can therefore be assumed to increase the lateral forces until the critical flexural strength in section *A* is reached, with an evident translation of the point of contraflexure *B* predicted by the "elastic" force combination to *C* in the new moment distribution represented in dashed line. Therefore cap beam negative reinforcements, terminated in accordance with the elastic moment distribution, could lead to premature failure in a section at a certain distance from *A*.

Furthermore, according to the elastic distribution in solid line, the opposite joint *D* of the cap beam is stressed by a small negative residual moment, and the joint area will be consequently characterized only by nominal positive moment reinforcements. However, sufficiently high levels of seismic forces could develop the moment capacity in section *A* and a positive moment in *D* of remarkable magnitude for which the reinforcement adopted would cause premature failure.

Finally, another deficiency associated with the elastic design approach is that of neglecting the concept of ductility and capacity design linked to the inelastic structural behavior. In this way member were not designed to avoid the possibility of brittle shear failure, since brittle shear strength was not higher than flexural resistance. The main damage typologies can be mainly attributed to the aforementioned deficiencies.

Looking at the decks, which generally don't have a primary function of seismic resistance, the damage typologies are essentially a direct consequence of the seismic displacements underestimation coming from low lateral force levels and include

7

hammering between adjacent spans and the loss of support. The latter is primarily linked to the inadequacy of the seating lengths under earthquakes and to the lack of resistance of any retaining seismic devices provided at joints. There have been many events of bridge failure caused by relative deck movement in the longitudinal direction exceeding adequate widths, especially for multi-span bridges with tall columns.

The effects of this damage category, which highlights the need for support oversizing, are shown by way of example in the following figure, representing the loss of support found in the Nishinomiya-ko bridge, in Japan following the 1995 Kobe earthquake, where the collapse was mainly attributable to the inadequacy of the seismic restraints.

Figure 2 : Nishinomiya-ko bridge following Kobe earthquake, 1995

On the other hand, as regards the piers, the damage observed is generally due to defects in flexural ductility or in shear strength. The collapse usually occurs due to the exhaustion of the flexural ductility, in some cases combined with the exceeding of the shear strength. Much more rarely, on thick piers, dominant shear collapses have been observed. Until the 70s, designers were generally unaware of the need to develop ductility capacity into the potential inelastic regions, being the concept of plastic hinges not considered in the elastic design philosophy. Four particular deficiencies regarding flexural strength and ductility failure can be identified:

- *Inappropriate and undependable column flexural strength*: The stresses were evaluated starting from low levels of seismic forces; for example in California it was customary to design with lateral forces equal to 6% of gravitational loads. Moreover, piers longitudinal reinforcements were often lap sliced immediately above the foundation with a splice length, up to 70s, generally

equal to 20 bars diameters, insufficient to enable the column flexural strength. However, even larger overlap lengths realized according to the current code requirements, could fail because of the low column ductility levels. The figure below shows the damages of a column base, attributable to lap-splice bond failure following Loma Prieta earthquake in 1989.

Figure 3 : Lap-splice bond column failure, Loma Prieta bridge 1989

- *Inadequate flexural ductility*: Although the high flexural strength of existing bridge reinforced concrete columns, it is still usually lower than that required for elastic response to counteract expected seismic intensities, with the consequent need to possess the ability to deform with several cycles of displacements beyond the yield limit without significant strength degradation. With inadequate levels of ductility, in the plastic hinge regions the concrete compression strains reach the unconfined compression strain capacity, with the occurring of cover concrete spalling. Without suitable confinement given by close-spaced transverse hoops or spirals, crushing rapidly extends into the core, thus leading to the buckling of longitudinal reinforcements. The rapid strength degradation occurred can be farther be accelerated, by the common practice in older bridges of lap splicing the reinforcement in the cover concrete. Figure 4 depicts a flexural plastic hinge failure due to San Fernando earthquake in 1971, where the small amount of transverse reinforcement in the plastic region can be noted.

Figure 4 : Bull Creek Canyon Channel Bridge damage in 1994 Northridge earthquake

- *Premature termination of column reinforcement :* A number of bridge columns developed flexure-shear failures at column mid-height, due to premature termination of the column longitudinal reinforcements, which were based on the design moment envelope, without taking into account the diagonal shear cracking resulting in the tension shift effect. This deficiency was worsen by the short lap splicing length provided at this location. Indeed, in order to economize, to reduce possible congestion of bars, and to accommodate splices, the flexural reinforcement along a member may be curtailed whenever it is allowed by the moment demand reduction and when it is practicable. However the section in which the bars need to be cut must be identified on the basis of the bending moment diagram and taking into account the effects of tension shift due to shear. The latter can be briefly explained starting from the equilibrium of a column segment shown in Figure 5, on the basis of the Ritter-Morsch truss model consisting of concrete compressive struts, tensile longitudinal reinforcements and shear stirrups.
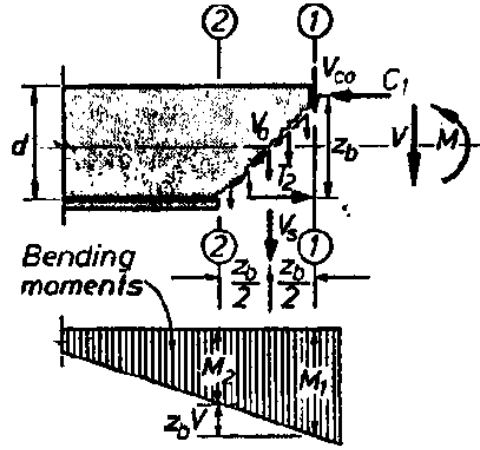
Figure 5 : *Internal forces in a cracked reinforced concrete member for a 45° crack inclination*

As depicted in the figure above, the balance is guaranteed by the following internal forces transmitting a total moment and shear M and V: the mutual forces that arise at the interface of the crack, known as aggregate interlock V_a, as well as the flexural concrete compression C and longitudinal reinforcement tensile force T_2, the vertical tension generated in stirrups V_s, and finally the shear transmitted across the flexural compression non cracked zone V_{co}.

The cracks formation, inclined by θ with respect to the axis, involves an increase in effort of the longitudinal tensile reinforcement. Initially, for a general concrete strut inclination θ, and assuming that the shear reinforcement consists of vertical brackets, the bending moment in section 1 can be expressed as:

$$M_1 = z_b T_2 + 0.5 z_b V_s \cot\theta \qquad (1.1)$$

where z_b is the internal lever arm. Since the moment M_1 is computed, like displayed in the bending moment diagram, as $M_2 + z_b V$, we find that the flexural tension force T_2 at section 2 is not proportional to the moment M_2:

$$T_2 = \frac{1}{z_b}[M_2 + z_b \cot\theta\,(V - 0.5V_s)] = \frac{M_2}{z_b} + (1 - 0.5\eta)V \cot\theta \quad (1.2)$$

Where $\eta = V_s/V$ is the ratio between the shear resisted by stirrups and the total shear. Thus the flexural tension force at section 2 will be proportional to a

11

moment $[M_2 + (1 - 0.5\eta)\, z_b \cot\theta\, V]$ [4]. This relation shows how, due to the diagonal cracks, the bending reinforcement in the abscissa section 2 must be designed for the bending moment that occurs in the section distant, from the section itself, by a quantity e termed *tension shift:*

$$e = (1 - 0.5\eta)\, z_b \cot\theta \qquad (1.3)$$

This is equivalent to "translate" the moment diagram by this quantity. to obtain the values to be used for the dimensioning of the reinforcements. Therefore the inclined flexure-shear cracking in columns results in tension shift, where tensile reinforcement stress is larger than the case in which the section moment comes from the plane-section hypotesis. The amount of shifting is closely linked, as deducible from equation (1.3), to the angle θ of the inclined crack with respect to the column axis and by the quantity of shear reinforcement. When it is assumed that the entire shear V is resisted by web reinforcement, the distance e is taken as the half of the lever arm z_b, approximated to the distance d, multiplied by the cotangent of the cracking angle. Moreover, although for columns the angle of flexure-shear cracking to the element axis can be taken as 30°, with a consequent tension shift :

$$0.5d \cot\theta = 0.87\, d$$

this value can be conservatively rounded up to d, since in routine design the tension shift is not often accurately evaluated. An example of the lack of attention to the moment diagram translation which leads to a premature termination of reinforcements is given by the flexure-shear failure at column mid-height during the Kobe 1995, as depicted in Figure 6.

Figure 6 *: Flexural-shear failure at pier mid-height of Route 43/2 overpass, 1995 Kobe earthquake*

Considering shear failure, its brittle nature is strictly linked to the strength degradation following the rapid increase of the flexure-shear crack widths after the reinforcement yielding. Short columns, due to the high shear-moment ratio, are particularly susceptible to this typology of failure.

Another factor that makes them very prone to shear failure is the conservatism in the flexural strength with which older columns were designed. In older bridges, the design philosophy provided indeed shear strength equations for columns generally less conservative than flexural ones, since shear design was not considered essential. The majority of existing bridges was designed without taking into account the philosophy of capacity design, consequently neglecting the importance of avoiding brittle failure mechanisms and thus overlooking the need to ensure that the actual shear strength exceeds the flexural one.

As an example, analysis on a bridge seriously damaged by Willier earthquake in 1987 have revealed that, in columns in which shear failure had occurred, shear strength was only about 30% of the flexural one. In such columns the shear crack width exceeded 25 mm and many tie were fractured. Furthermore, the observation of failure modes of columns damaged by the 1971 San Fernando earthquake, allows to analyze the impact of bending ductility on shear strength. Indeed, under the action of flexural ductility, the width of the flexure-shear cracks increases, with a reduction in aggregate interlock shear transfer. Consequently, higher shear strength can be observed in nonhanging regions than in the plastic hinge locations, and design equations should thus recognize the influence of flexural ductility demand on shear strength [3].

Two typical brittle shear failure mechanisms in bridges during San Fernando earthquake are shown in the following figures, which compare a pier where there is no indication of the plastic hinging development at member ends and a column with no apparent damage in the mid region. In the latter, the presence of a plastic hinge developed at the member top can be observed, with a consequent shear failure within the hinge region.
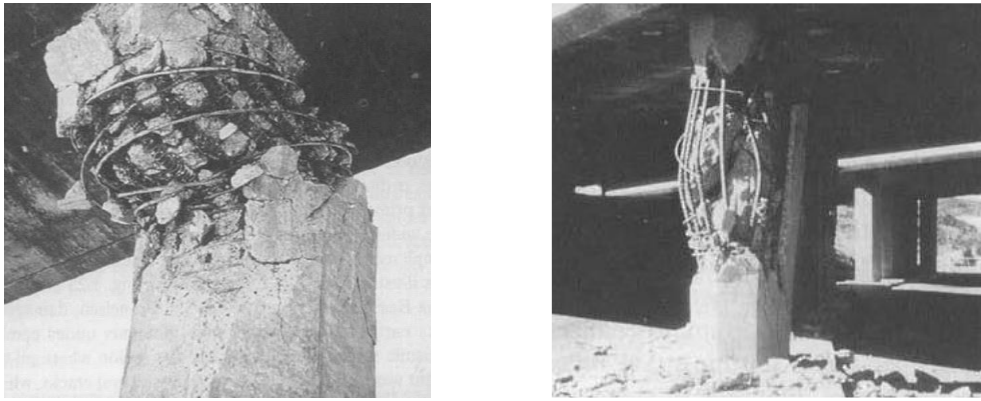
Figure 7 : Shear failure within (left) and outside (right) the plastic hinge region, 1971 San Fernando earthquake

1.3 Bridge retrofit techniques

The current paragraph aims to present the most common technical solutions for seismic retrofitting of the bridges structural components, which involves columns, bearings, foundations and abutments retrofitting; among the components mentioned above, the first two will be treated in particular, as they will be of particular interest for the modeling carried out in the current thesis. In the majority of cases, they must be carried out taking into consideration constraints linked to traffic, with a consequent need for construction in short time of realization, in order to limit the traffic obstructions.

The need to carry out a seismic retrofitting must be assessed starting from the evaluation of the risk of damage or failure, combined with a rating of the available economic resources. In case you opt for the retrofitting, the alternatives regarding the level of intervention must be considered, with a choice of the proper operation in terms of materials and techniques applied, dependent on several factors, such as the typology of structural system considered, as well as the characteristics of structural components, the type of loads acting on the bridge, with particular attention both to aspects related to durability and compatibility of materials and non structural factors like functional requirements, the aesthetics of the solution, the sustainability of interventions and cost balance.

1.3.1 Column retrofit techniques

The main deficiencies of concrete columns designed according to non-seismic criteria, as previously mentioned, are associated to their low flexural ductility, lack of attention in their design to the shear failure mechanisms and in the problems influencing the flexural strength related to inadequate lap lengths and to premature cut of longitudinal reinforcements.
The consolidated retrofitting techniques aimed at solving these problems include steel or concrete jacketing or with precast concrete elements, as well as bandage with fiber-reinforced materials and finally the change of the static pier scheme by interposing shear walls or adding additional columns.

- *Concrete jacketing:* Retrofitting by reinforced concrete jacketing is one of the most used solutions; it is chosen among the alternatives mainly for its competitiveness from an economic point of view and for its more favorable behavior in water. This methodology consists in a thick layer of reinforced concrete around the pier, as shown in Figure 8. With regard to the jacket thickness, although the NTC don't provide precise values, the explanatory circular [5] prescribes that "it must be such as to allow the positioning of longitudinal and transverse reinforcement and an adequate thickness of the cover concrete".

Moreover, it states that reinforced concrete jackets can be applied to columns or walls in order to achieve all or some of the following objectives:

- increase vertical bearing capacity;
- increase in bending and/or shear strength;
- increase in deformation capacity;
- improvement of the efficiency of the overlap joints.

For the purpose of evaluating the strength and deformability of jacketed elements, it is acceptable to consider some simplifying assumptions. Indeed it can be assumed that the jacketed element behaves monolithically, with full adherence between the old and the new components.

Moreover, the axial load is considered applied only to the pre-existing portion of the element for permanent loads, whereas it is enforced to the whole jacketed section for variable loads and seismic actions.

Finally the mechanical properties of the new concrete can be extended to the whole section if the differences between the two materials are not excessive. The jacket can be detached from the base, on average 100-150 mm, providing an increase in ductility and shear strength or alternatively connected to the foundation with anchored longitudinal bars, giving in this case also a contribution to flexural strength. The latter is less common than the former. Indeed, by carrying on the longitudinal reinforcement into the footing with sufficient anchorage length to develop the reinforcement strength, the column

flexural resistance could hence be enhanced, even if it is often necessary to operate contemporaneously on footing flexural and shear strength. The relevant increase in column flexural strength given by the 200-300 mm thickness of the jacket could hence make the foundation inadequate for the new forces transmitted by the pier.

This type of intervention is very effective for piers with a circular section. In the case of columns with a rectangular or other section shapes, on the other hand, it has a reduction in efficiency: longitudinal bars in the central part of each face will be sensible to buckling and only the concrete located near the corners will be effectively confined. Furthermore, the insertion and positioning of bars passing through the section connecting the two faces of the jacket, turns out to be extremely delicate, due to the high risk of truncating the existing reinforcements. The bend of the hook is indeed made in place after threading trough the hole. The problem can be partially solved by the recent development of innovative materials, as plastics reinforced and techniques that involve the use of smaller diameter bars.
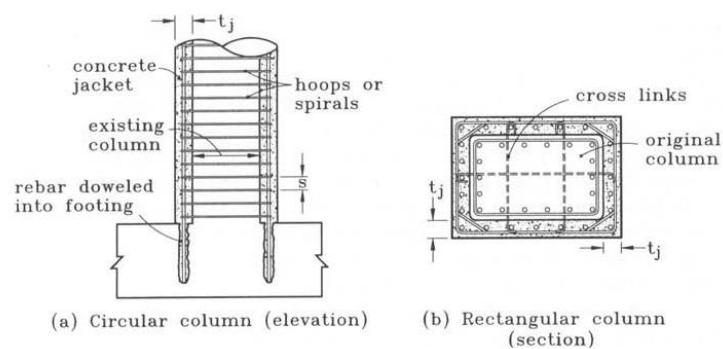
Figure 8 : Concrete jacketing of circular and rectangular columns

- *Steel jacketing*: In the form of circular or, for rectangular sections, elliptical jackets, this technique was one of the first used for piers retrofitting. It has proved to be very effective in many cases, such as during the 1994 Northridge earthquake, in which over fifty bridges reinforced with this technique overcame high peak accelerations at the base without damage to the piers, as well as some Japanese bridges after the 1995 Kobe earthquake, where piers

reinforced with steel jackets and subjected to peak accelerations larger than 0.8g were not damaged. The jacket, welded on site or alternatively fixed with mechanical joints, is usually characterized by a thickness of around $6 \div 12$ mm. The zone that separates the steel jacket from the original pier is filled by injecting cement mortar or resins. The procedure was initially introduced for circular column since, as for the reinforced concrete jacketing technique, the most efficient field of application is that of piers with circular section. This technique is not very competitive from an economic point of view, due to the large amount of steel needed, especially when compared to that already present in the pier; however it should be noted that it gives a relevant increase in the shear and flexural strength. In order to achieve the latter, it is necessary to connect it to the foundation, by welding profiles at the base of the jacket which are then anchored with anchor bolts.
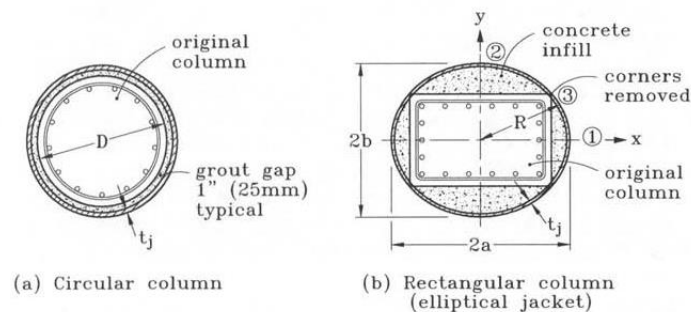
Figure 9 : Steel jacketing for circular and rectangular piers

- *Composite-Materials Jackets:* In the retrofitting of bridge piers, it is possible to choose to use many variants of fiber-reinforced polymers or plastics, depending on the stiffness, strength and failure strain of the type of material selected, such as for example carbon fibers, fiberglass or kevlar. The use of these materials generally involves high costs, although it is still competitive in the moment in which it allows the reduction of the working time, with a consequent decrease in inconveniences related to the interruption of traffic. Furthermore, they are an excellent alternative to reinforced concrete or steel jacketing, since they are normally lightweight and easily manageable and

hence suitable for the situations in which the operating space is limited or uncomfortable.

The materials with the highest elastic modulus and characterized by a linear elastic behaviour up to failure are carbon fibers, which are therefore the most suitable for the purpose of increasing the concrete confinement. In fact, the lateral expansion of concrete is elastically counteracted even at very high levels of deformation. Because of the larger strength of the carbon fiber, smaller thicknesses are needed than for the weaker albeit cheaper fiber glass. The high resistance of the carbon fibers, of the order of ten times with respect to that of the steel of ordinary reinforcements, make the confinement more effective than that resulting from the transverse reinforcement. These materials are supplied in sheets. They are normally used transversely to the axis of the element to increase confinement and shear strength, and have also been experimented vertically, anchored by metal plates in the foundation, to increase the flexural strength. For the rectangular sections, a solution similar to that of the steel jacketing was also used to increase the effectiveness of confinement.

Both in case of carbon fiber and fiberglass, the technique is suitable for circular columns, since, in order to obtain full confinement for other shapes of columns, it is necessary to modify the section shape to enable the jacket to be placed over a continuously curved surface. However, these techniques have allowed to achieve a reasonable increase of rectangular columns ductility.

Figure 10 : Example of carbon fiber jacketing to increase shear and flexural strength

1.3.2 Bearings retrofit

From a seismic point of view, the most common shortcomings in older bridges concern the inadequacy of the supports, which can easily lead to the loss of support and the consequent collapse of entire spans in simply supported decks. Indeed the vast majority of pre-stressed reinforced concrete viaducts of the national road network built between the late 1960s and early 1990s are characterized by neoprene bearings, which have proved to be an economical and effective solution for works located in low and medium seismic intensity. Today this structural solution is less used, due to the infrequent use of pre-tensioned beams in favor of mixed-structure solutions for which are generally adopted other kinds of support. Considered the impressive quantity of works carried out with neoprene supports that requires today extraordinary maintenance interventions, it is evident the need for adequate understanding of the seismic behavior of this bridge component, in order to identify the most effective interventions for the improvement of their performance. Very often in professional practice the presence of neoprene supports is neglected, underestimating the effects that, on the other hand, can be determinants. Such elements are characterized, in fact, by an horizontal stiffness which is significantly smaller than that of the substructures, even in the case of supports of modest thickness. As in presence of stiffnesses working in series the smallest one results as dominating, it is natural that the overall behavior of the structure is strictly linked and influenced by the presence of such flexible elements [6]. Indeed, a few decades after construction, in conjunction with the seismic rehabilitation and adaptation of these works, it is often necessary to replace them. The interventions to adapt the support system are very varied and depend on the type of deck and the quality of the intervention to be carried out. An economical and effective intervention consists in the replacement of the existing supports with new ones of the same type and the creation on the top of the pier of a restraint system that prevents the decks from falling and limits the relative movements. Although in some cases there have been subsequent problems caused by the fragile failure of these devices, the aim of the use of seismic "shear keys" is to ensure that the forces of inertia are transmitted to the pier through the supports, giving the bridge a suitable resistance to seismic actions that act in transverse and/or longitudinal direction.

1.4 Italian seismic classification and expected performance

In order to carry out a correct structural analysis, whether linear or non-linear, it is required the availability of the values of all the geometric and mechanical quantities. The fact that the deck is not significantly involved in the seismic response of the structure leads to a directing of the cognitive investigations mainly to the substructures, consisting of piers and abutments and to the foundations, as well as to the constraint and interconnection systems between the structural elements, such as the supports and joints. In particular the investigations are based on the following characteristics:

- *Geometry* of the work in its current state. It can be deduced from the original construction drawings or from the accounting drawings. This naturally also extends to any changes introduced following structural interventions subsequent to construction;

- *Construction details*, that is arrangement and quantity of the reinforcements. It can be deduced from the original construction drawings or, as for the geometry, from the accounting drawings;

- *Mechanical properties of materials*: conglomerate and steel. The information must be deduced, in addition to the initial design indications, from the results of experimental tests carried out at the time of the structural testing or after it. In the absence of the above documentation, it is necessary to subject the conglomerate to laboratory tests. As regards steel, in the absence of adequate experimental data, it is allowed to refer to the characteristics of the material prescribed in the design, albeit after random checks of the effective use of the latter. The above requirements are valid for the substructure, whereas for the decks, it is sufficient to check their good state of conservation without experimental tests;

- *Geotechnical characterization,* aimed at assigning the site to a soil category.

Furthermore, the current guidelines for risk classification, safety assessment and monitoring of existing bridges [7] illustrate how the classes of attention referred to the bridges in question are involved in a multilevel approach that, from the census of the works to be analyzed, leads to the determination of a class of attention on the basis of which the safety check will be carried out.

The use of this multilevel approach is justified by the high number of infrastructures present on the Italian territory. It allows to evaluate, albeit in an approximate and qualitative way, the urgency and the actual need for intervention on the work in question, through a homogeneous and uniform method. The approach is developed on 6 different levels, characterized by an increasing degree of depth and complexity:

- *Level 0* provides the census of all the works and their main characteristics by collecting the information and available documentation;

- *Level 1 (LC1)*, starting from the works registered in level 0, provides the execution of direct visual inspections and the investigation of the geo-morphological and hydraulic characteristics of the site, with the aim of identifying the state of damage and the main structural and geometric characteristics of the work under examination;

- *Level 2 (LC2)* allows to reach the attention class of each bridge, based on the parameters of risk, vulnerability and exposure, starting from the data deriving from the analysis of the previous levels. According to the classification obtained, it is therefore possible to proceed to the following levels;

- *Level 3 (LC3)* involves carrying out preliminary assessments, aimed at understanding whether it is necessary to carry out further investigations by carrying out accurate level 4 checks;

- *Level 4 (LC4)* provides the execution of accurate analysis according to the provisions of the current technical standards for construction;

- *Level 5 (LC5)* is finally applied to bridges considered of significant importance within the network. For the latter it is appropriate to carry out more sophisticated analysis, aimed at evaluating the interaction between the structure and the road network, with the consequences of a possible

interruption of the traffic on the socio-economic context in which it is inserted.

For most bridges, it must generally acquire an accurate level of knowledge LC3, except for exceptional cases for which an adequate level of knowledge LC2 is admitted.

As previously mentioned, a large part of the existing bridges has shown its inadequacy in performing safely. This unsuitableness is attributable to the fact that they were mostly built in the 1960s and 1970s, following design regulations based entirely on resistance rather than ductility criteria, with static horizontal forces computed as a small ratio of the permanent weights. Furthermore, considerations regarding compatible displacements between decks, admissible bearings displacements were totally neglected, thus leading to non-compliance with current design requirements and standards. In most cases, the pier reinforcements were designed following minimum percentage requirements, without taking into consideration seismic forces.

In fact, only with the regulation of 20 March 2003, n. 3274, unlike the previous legislation prescriptions, the whole national territory has been classified as seismic, divided into 4 zones with different levels of seismic hazard. Although the seismic zones identification in Italy has already occurred with the issue of the royal decree at the beginning of the 1900s following the earthquakes of Reggio Calabria and Messina of 1908, the Italian seismic map classified as seismic only the territories that had been afflicted by destructive earthquakes since 1908; this category therefore included only the municipalities of Sicily and Calabria damaged by the earthquake that occurred on that date, with the possibility of adding the zones that would had been hit later by any future earthquake. Therefore, almost all of the Italian areas, although they were characterized by a certain degree of seismicity, were categorized as non-seismic.

Only in 1974, through the law n. 64, a new national seismic legislation was approved which established the reference framework for the seismic classification methods of the national territory. Following the seismic events of 1976 in Friuli Venezia Giulia, of the Gulf of Patti in 1978 and of Irpinia in 1980, a greater need began to be recognized to rationalize the seismic zoning of the territory.

In fact, the CNR presented a proposal for a seismic classification to the Government, followed by decrees of the Ministry of Public Works that led to the aforementioned ordinance of 2003. This proposal consisted in the subdivision of the Italian territory into three seismic categories, on the basis of parameters deriving from surveys of probabilistic sort, differently from previous Italian classifications.

The latest seismic reclassification proposal prior to that of 2003 is represented by the 1998 study proposed by the National Seismic Service, approved by the Major Risks Commission and sent to the Ministry of LL.PP.. Finally, the aforementioned ordinance n. 3274 was issued in 2003, in the light of which, unlike the previous regulatory provisions, the whole italian territory was classified as seismic, divided into 4 zones, with decreasing seismic hazard; in particular, in the fourth zone, the regions have the faculty to prescribe the obligation of anti-seismic design. This subdivision was based on the analysis of the probability that the area of interest was affected in 50 years by an event exceeding a certain threshold.
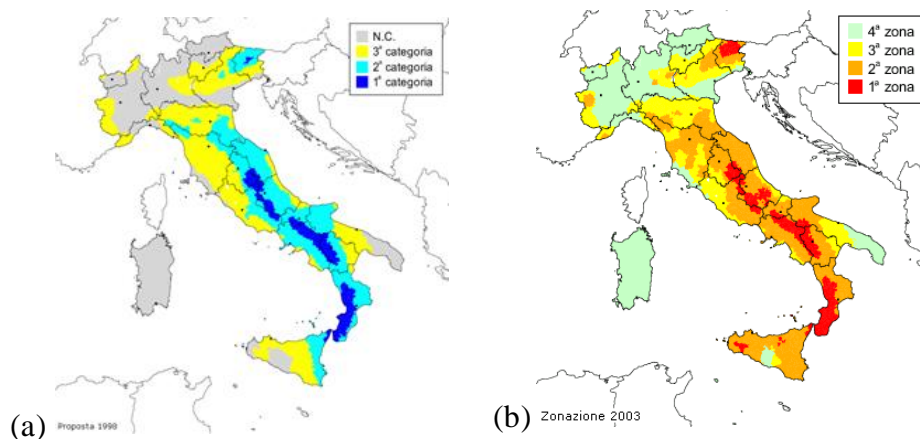
Figure 11 : *1998 Proposal for the seismic reclassification (a) and Seismic zones of the Italian territory according to to Ordinance no. 3274 (b)*

An update of the national reference hazard study was adopted with Ordinance no. 3519 of 28 April 2006. The new hazard study has provided the Regions with an updated mean for the territory classification, by attributing to the four seismic zones intervals for the peak acceleration on rigid ground a_g with a probability of exceeding 10% in 50 years.
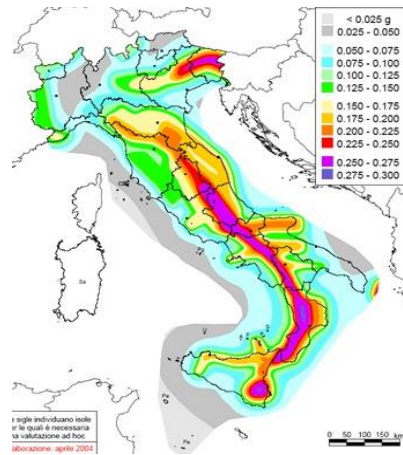
Figure 12 : Seismic zones of the Italian territory (2006) according to Ordinance no. 3519

Seismic zone	a_g intervals
1	$a_g > 0.25$
2	$0.15 < a_g \leq 0.25$
3	$0.05 < a_g \leq 0.15$
4	$a_g \leq 0.05$

Table 1 : Intervals for the peak acceleration in the seismic zones

Moreover, national and international standards provide that the works must be characterized by a level of anti-seismic protection depending on their importance. This level of protection is determined by the interaction of an expected performance, represented by the limit state considered, and a level of seismic intensity.

The latter is defined starting from a particular probability of exceeding P_{V_R} in an assigned period of time, that is the reference life of the work under examination. It is obtained, in accordance with paragraph §2.4.3 of the Technical Construction Standards, by multiplying the nominal life of the work V_n, function of the type of construction, by a coefficient C_u which depends on the four classes of use:

$$V_R = C_U V_N \tag{1.4}$$

Starting from the values of V_R and P_{V_R}, the value of the average return period can be obtained, defined in general as the average time between the occurrence of two successive events of an entity equal to or larger than the assigned intensity value:

$$T_R = -V_R / \ln(1 - P_{V_R}) \tag{1.5}$$

Limit state	P_{V_R}
SLO	81%
SLD	63%
SLV	10%
SLC	5%

Table 2 *: P_{VR} values depending on the limit state*

As can be seen from Table 2, the probability of exceeding is a function of the limit state considered. As regards existing structures, it is generally allowed to verify only the ultimate limit states SLV and SLC, defined in paragraph §3.2.1 of the NTC 2018:

- **Life-saving limit state *SLV***: following the earthquake, the building undergoes failures and collapses of the non-structural components and significant damage of the structural components, associated to a significant loss of stiffness with respect to horizontal actions; the construction instead preserves a part of the strength and stiffness for vertical actions and a safety margin against collapse due to horizontal seismic actions;

- **Collapse prevention limit state *SLC:*** following the earthquake, the building undergoes serious failures and collapses of the non-structural components and very serious damage of the structural components; the construction still reserves a safety margin for vertical actions and a small safety margin against collapse for horizontal actions.

With regard to strategic works, i.e. bridges of use class III and IV, it is also necessary to verify that, following an intense seismic event, complete transitability is allowed. The maintenance of the latter is associated with the limit state of damage, to which a 63% probability of exceeding is associated in the technical regulations. It is defined as follows:

- **Damage limit state *SLD***: following the earthquake, the construction as a whole, including the structural elements, the non-structural elements and the equipment relevant to its function, suffers damage that doesn't jeopardize the users and doesn't significantly compromise the capacity of resistance and stiffness towards vertical and horizontal actions.

1.5 Seismic action representation

In accordance with the technical standards, the seismic action is defined through its three components, X and Y in the horizontal plane and Z in the vertical direction. Although in some particular circumstances the use of a distribution of equivalent forces and the calculation of the response with a static analysis can be possible, these components can be represented alternatively through:

- The elastic design response spectrum in terms of acceleration
- Time history of seismic motion

The seismic action is defined on the basis of the seismic hazard of the site, which, intended in a probabilistic sense, is the expected motion of the soil in a given site with a certain probability of exceeding in a given time interval. In particular, the spectral shapes are defined, for each of the probabilities of exceeding in the reference period, starting from the following values of the local site parameters (referred to free field conditions on rigid soil with horizontal topographic surface), defined starting from a grid of points covering the national territory, given in the annexes of the technical standards:

- a_g, the site maximum base acceleration;
- F_0, maximum value of the amplification factor of the acceleration spectrum ;
- T_c^*, starting period of the constant velocity segment in the acceleration spectrum.

In the annex, the parameter values are provided according to the average return period T_R computed according to equation (1.5). In case the supplied value is not among those in the table, it can be interpolated according to the formula:

$$\log(p) = \log (p_{1)} + \log (p_2/p_1) \log (T_R/T_{R1}) \log (T_{R2}/T_{R1})^{-1} \qquad (1.6)$$

Where p is the value of the parameter of interest and $T_{R1,R2}$ are the nearest values of the return period for which the values of p are given.

The current standards provides an elastic design spectrum, based on statistical analysis of the response spectra for the ensemble of ground motions. The design spectrum should indeed satisfy certain requirements, since it is intended for the design of new structures, and for the seismic safety evaluation of existing structures, in order to resist future earthquakes.

These objectives are not compatible to a response spectrum constructed from a single ground motion recorded during a past earthquake, since the jaggedness in the response spectrum is characteristic of that one excitation. Moreover the response spectrum for another ground motion recorded at the same site during different earthquakes would be characterized by peaks and valleys not necessarily at the same periods, as shown in Figure 13. Hence the necessity to construct a design spectrum which should consist of a set of smooth curves with one curve for each level of damping [8].

However, it should still be representative of ground motions recorded at the site during past earthquakes and, if none have been recorded at the site, it should be based on ground motions recorded at other sites using similar conditions.
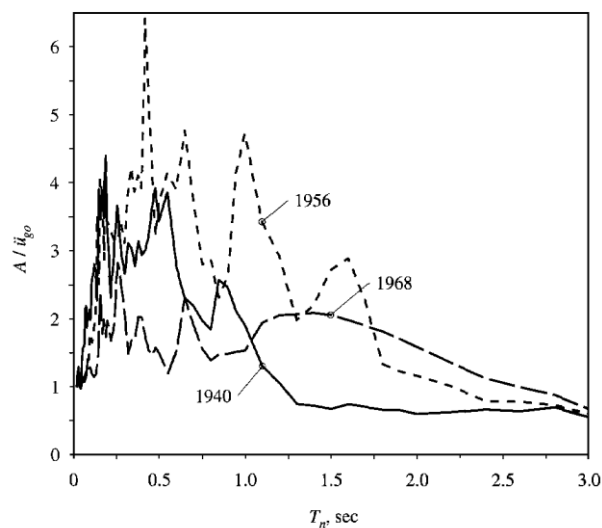
Figure 13 : *Response spectra of ground motions recorded at El Centro, California during earthquakes of 1940, 1956,1968, ξ=2%*

Therefore it may still be useful, in order to understand the concept of response spectrum, to analyze how it can be developed for a given ground motion component $\ddot{u}_g(t)$. Once the ground acceleration is numerically defined, the natural vibration

28

period T_n and damping ratio ξ of a SDF system are selected. The peak value of the deformation response $u(t)$ due to the ground motion is then computed through numerical methods, from which the spectral ordinates of velocity and acceleration are obtained. These steps are repeated for a range of natural periods and damping ratio covering all possible systems of engineering interest.

Alternatively to the response spectrum, if the assessment of seismic safety is carried out through step-by-step dynamic analysis, the seismic action should be represented by means of artificial or natural time histories of the ground motion, generally in terms of acceleration. Each time history describes a component, horizontal or vertical, of the seismic action and the set of the three components normally used in the case of spatial analysis constitutes a group of time histories of the ground motion.

In particular, three typologies of accelerograms can be used:

- artificial recordings;
- real accelerogram recordings;
- synthetic records deriving from seismological models.

The technical construction standards establish the criteria to regulate the use of the various typologies of accelerograms. In general, they foresee that the time histories of the ground motion, whether artificial, simulated or natural, must be coherent with the elastic acceleration response spectrum relative to the site under examination.

With reference to the use of artificial time histories, the NTC 2018 standards establish that their duration must be determined on the basis of the physical parameters linked to the local seismic intensity. In case no specific studies will be carried out, they indicate that the duration of the pseudo-stationary part of the accelerogram must be equal to 10 s, preceded and followed by an increasing and decreasing amplitude to 0, with an overall duration of the time history of not less than 25 s. Compliance with the elastic spectrum results in a verification of the average of the spectral ordinates obtained from the different accelerograms for a viscous damping coefficient ξ of 5%. As regards the component examined in the elastic spectrum, the average spectral ordinate must not have a lower difference of more than 10%, in the points of the larger between the intervals $0.15\,s \div 2.0\,s$ and $0.15\,s \div 2T$ for the checks at the ultimate

limit states, with T period of the structure in the elastic range, and $0.15\ s \div 1.5T$ as regards the verifications at the serviceability limit states.

Furthermore, the number of artificial accelerograms or groups of artificial accelerograms for the spatial analysis must be at least equal to five, except in the case in which it is chosen to consider the spatial variability of the motion [2].

In fact, the seismic motion is generally different in the points of contact of the bridge with the ground, due to the asynchronous nature of the propagation phenomenon and the inhomogeneities and discontinuities that may be present, as well as to the different local response of the ground. In the current thesis, the effects of the spatial variability of motion will not be evaluated, as in general, they should be considered when the properties of the soil along the bridge vary in such a way as not to allow univocally to identify a category of foundation soil in the points of contact of the various piers. In the event that it is chosen to consider it, an approximate alternative to specific models that take into account the correlation of the motions to the supports, consists in carrying out the dynamic analysis on the structure with distinct accelerograms under each pier, each compatible with the relative spectrum response.

It is evident that, in order to carry out a coherent seismic analysis, it is necessary to provide for the examination of a large number of seismic events, in order to give statistical significance to the results. The response of the step-by-step dynamic analysis, in the current thesis, will be evaluated using seven different groups of time histories, in such a way as to be able to represent, in accordance with paragraph §7.3.5 of the technical standards, the effects on the structure through the average of the most unfavorable values.

The artificial signals most commonly used in practice are those produced by the SIMQKE code, which generates one or more signals directly from a reference spectrum, without seismological parameters (i.e. Magnitude, Distance, Site). The code allows to artificially generate a predetermined number of statistically independent accelerograms referring to a specified response spectrum.

The approach employed in SIMQKE is to generate a power spectral density function from the smoothed response spectrum, and then to derive sinusoidal signals having

random phase angles and amplitudes. The sinusoidal motions are then summed and an iterative procedure can be executed to improve the match with the target response spectrum, by calculating the ratio between the target and actual response ordinates at selected frequencies; the power spectral density function is hence adjusted by the square of this ratio, and a new motion generated [9].

In particular, SIMQKE, unlike many artificial recording generation programs, doesn't generate the accelerogram to then create the compatibility spectrum, but operates a priori on the fundamental parameter which is the power spectral density function [10].

What makes this type of accelerogram particularly common for dynamic analysis is the fact that it allows to easily obtain acceleration time series that are almost completely compatible with the elastic design spectrum, which in some cases will be the only information available regarding the nature of the ground motions to be considered.

However, although they are commonly used to determine the structural dynamic response, these accelerograms don't exhibit the same physical characteristics of real recordings, since they actually corresponds to a pure mathematical description of the acceleration time series compatible with the response spectrum and they are represented as a limited duration of a stationary random function segment.

Moreover they can simulate the content in frequencies of a real earthquake only during the "strong motion" phase. In fact the basic problem with spectrum compatible artificial records is that they generally have an excessive number of cycles of strong motion, with a consequent unreasonably high energy content.

The accelerograms generated by SIMQKE are obtained on the basis of a trapezoidal envelope, with fixed values of the duration of the increasing and decreasing sections, which can be defined by the user.
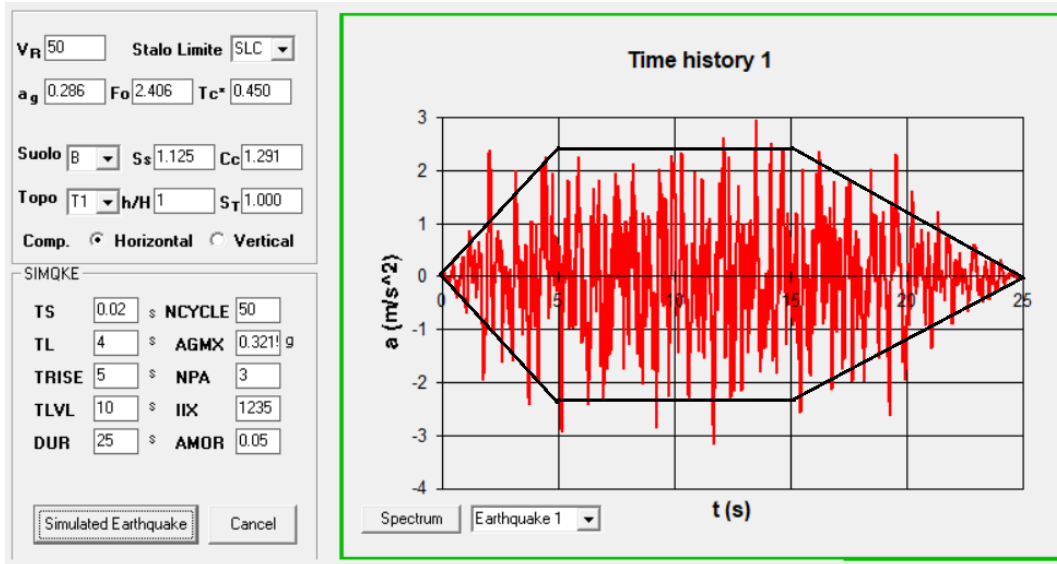
Figure 14 : *Generic accelerogram generated by SIMQKE*

In particular, the input parameters necessary for the generation of an accelerogram are the following:

- TS: Smallest period of desired response spectrum
- TL: Largest period of desired response spectrum
- TRISE: Starting time of the stationary part of the accelerogram
- TLVL: Duration of the stationary part (≥10s)
- DUR: Total duration of the accelerogram
- NCYCLE: Number of iteration to smoothen the response spectrum
- AGMX: Peak ground acceleration (g)
- NPA: Number of artificial earthquakes to be generated
- IIIX: Arbitrary old integer to start the casual generation of accelerogram
- AMOR: Damping ratio

The elastic response spectrum associated with each generated accelerogram is determined starting from the resolution of the equation of motion that regulates the motion of the SDF system:

$$\ddot{v}(t) + 2\xi\omega_1\dot{v}(t) + \omega_1^2 v(t) = -\ddot{u}(t) \qquad (1.7)$$

32

In which the coordinate $v(t)$ takes on the meaning of displacement relative to the reference system, animated by the motion $u(t)$. The parameters ξ e ω_1 represent respectively the damping ratio and the circular frequency of the SDOF system. The figure below shows the software interface, with the three curves representing the design elastic spectrum (blue), the spectrum obtained from the artificial accelerogram (red) and the lower bound according to the technical standard of 10% compared to the reference spectrum (pink).
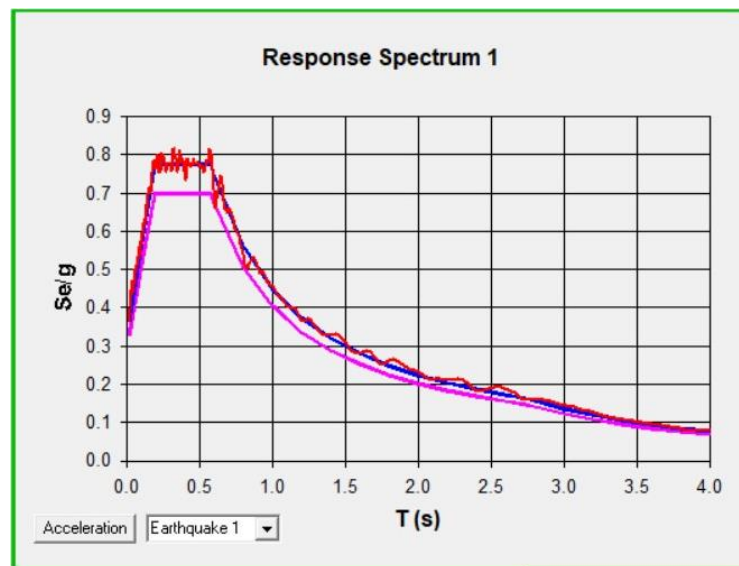
Figure 15 : Response spectrum associated to the accelerogram of Figure 14

When the seismic action is instead represented by natural accelerograms, the NTC 2018 foresees the need for the selection of the signals to be consistent to the seismic hazard expected at the site, in particular with the magnitude and epicentral distance representative of one or more scenario events.

The use of natural recorded time histories is therefore permitted provided that the choice is representative of the site seismicity and justified on the basis of the seismogenic characteristics of the source and the maximum horizontal acceleration expected at the site.

The NTC 2018 also provide that, as for artificial time histories, it is necessary to satisfy the conditions of coherence with the reference spectrum: the recorded time histories must be selected and eventually scaled in such a way that the relative response spectra

approximate the elastic design response spectra in the field of proper periods of interest for the problem under examination. In fact they provide that the average spectral ordinate, in such periods of interest for the work in question, must not have tolerance extending more than 10 % below and an excess difference larger than 30% with respect to the reference elastic spectrum. Natural records of seismic motion can be found for example in one of the following databases:

- *European Strong Motion Data Base* (ESD), at Imperial College, London
- *Strong Motion Catalogne*, at Pacific Earthquake Engineering Research Center

As previously mentioned, the standard requires real records to be selected representative of the seismicity of the site and adequately justified, but it does not univocally explain how to perform the selection. In fact, it is difficult to guarantee, in the chosen records, the representation of all the characteristics of the earthquake and of the site. Therefore, the non-linear dynamic design is often complicated by the scarcity of real records characterizing the seismic hazard at the site in question: there is no clear identification of the earthquakes to be elected, which leads to an evident difficulty in identifying an earthquake scenario that best suits to represent the effects of the site. In order to overcome this problem, in addition to the use of artificial and simulated recordings, the designer can use the following techniques, to resize or modify the real recordings:

- Use real records linearly scaled with respect to a reference spectrum
- Change the frequency and phase content of real records to match to the standard spectrum (adjustment by adding *wavelets*)

Particularly useful, in the first direction shown, is Rexel, software developed in order to allow to search for accelerograms from the European Strong motion Database, compatible to reference spectra being either user defined or automatically generated according to Eurocode 8 and the recently released new Italian seismic code.

In particular, the software has been developed to search for combinations of seven accelerograms with an average compatible with the reference spectra according to code criteria discussed above. It makes also possible to reflect the characteristics of

the source, if available, and site, in terms of magnitude M, epicentral distance R, and soil site classification.

The procedure implemented for record selection, as explained by Iervolino et al. in [11], evolves in four basic steps:

1. The first step consists of the definition of the design reference horizontal and/or vertical spectra which has to be matched by the average of the set of records; it can be built according to EC8, NTC, or user-defined;

2. In the second step the records contained in the ESD and embedded in REXEL, which fall into the magnitude and distance specified by the user for a specific site class, are listed and plotted; the user can therefore choose to search for combinations coming from specific M and R ranges in which the records to be searched must fall, respectively $[M_{min}, M_{max}]$ and $[R_{min}, R_{max}]$.

    This may prove useful if the data about the events of interest are available, for example from disaggregation of seismic hazard, and it is consistent to code criteria which require to select records taking care of the seismogenetic features of the source of the design earthquake.

    After these bounds are defined, the software returns the number of records, and the corresponding number of originating events, available in the intervals. This list constitutes the inventory of records, in which will be searched the seven accelerograms associated to response spectrum in average compatible with the code spectra generated in step 1.

3. In the third step, the period range where the average spectrum of the set has to be compatible with the reference spectrum is assigned, with the associated specification of tolerances in compatibility.

    The non dimensional option corresponds to choose to search for scaled record sets. In fact, REXEL allows to obtain combinations of accelerograms both being not manipulated and linearly scaled in amplitude. By choosing the second option, the spectra of the list previously defined are preliminarily normalized by dividing the spectral ordinates by their PGA and then comparing

the combination of these spectra to the non-dimensional reference spectrum. Furthermore, it is possible to specify the maximum mean scale factor (SF) allowed, discarding consequently the combinations with an average SF larger than what desired by the user.

4. The final step consists of running the search for combinations of seven records including one, two of all three components of motion.

An important feature of REXEL is that the list of records out of step 2, which is an input for this last phase, are ordered in ascending order of the parameter δ, which represents the measure of the deviation of the spectrum of each record from the reference one, shown in the following expression [11]:

$$\delta_j = \sqrt{\frac{1}{N} \sum_{i=1}^{N} \left(\frac{Sa_j(T_i) - Sa_{ref}(T_i)}{Sa_{ref}(T_i)} \right)^2} \tag{1.8}$$

where $Sa_j(T_i)$ is the pseudo-acceleration ordinate of the real j-th spectrum associated to the period T_i, $Sa_{ref}(T_i)$ is the value of the spectral ordinate of the reference spectrum at the same period, and N is the number of spectral ordinates within the considered range of periods. This preliminary operation enables to consider at first the records which have a similar spectral shape with respect to the reference one; consequently the first combinations turn out to be characterized by the smallest scattering with respect to the reference spectrum. This feature proves to be very useful when the *"I'm feeling lucky"* option is selected, which allows to stop the analysis as soon as the first compatible combination is found.

The third category of ground motion records available is that of synthetic accelerograms generated from seismological source models and accounting for site effects. Although the evolution of this typology has been remarkable, they will be briefly treated in the current thesis, since their complex application, in terms of defining the many parameters required to characterize the earthquake source, generally requires the engagement the services of specialist consultant in engineering

seismology. The NTC 2018 foresees that the use of this type of time histories is allowed provided that the hypotheses relating to the seismogenic characteristics of the source are justified and that, in the same intervals of periods indicated for the artificial accelerograms, the average spectral ordinate does not present a difference below 20% with respect to the reference spectrum.

The simulated accelerograms are generated through modeling, with both deterministic and stochastic methods, able to simulate the effects of processes connected with ground motion, such as earthquake genesis, wave propagation and surface response to the site.

2
MODELING OF THE VIADUCT

This chapter aims at describing the adopted dynamic models for the viaduct under examination. The introduction of the work will be followed by an analysis of the representation of the components of this viaduct, preparatory to carrying out the dynamic analysis.

The structural elements will be modeled with the aid of Finite Element Software Midas GEN. In the model, different categories of members will be used to describe the behavior of elements between nodal points defined in the discretization. In particular, beam and plate element will be introduced. When the element to be represented is such as to suggest adequate hypotheses on its state of stress or its way to deform, it is in fact possible to develop approximate structural theories, such as the theory of beams or plates.

As regards the beam theory, particularly useful are the kinematic theories of Euler-Bernoulli and Timoshenko beam theory.

The former is based on the hypothesis that, after deformation, a section initially orthogonal to the beam axis is transformed into a flat section, orthogonal to the deformed axis, keeping its shape. In this way, the deformation regime of the beam is mainly connected to bending, as it is completely characterized by the knowledge of the variation in the length of the axis line and the rotations of the sections, which by hypothesis remain normal to the geometric axis even in the deformed condition.

In the case of beams that are not particularly slender, shear deformations must be taken into account, as they are quite significant, through more refined theories, such as Timoshenko theory.

In Midas GEN the beam element is formulated on the basis of the latter, according to which a plane section initially normal to the neutral axis of the beam remains plane

but not necessarily normal to the neutral axis in the deformed state, thus reflecting shear deformations.

A beam element in Midas GEN has 6 DOFs per node, reflecting axial, shear, bending and torsional stiffness. The following figure shows a general beam element with its element coordinate system (ECS). In particular its convention for beam element forces is highlighted, where the arrows represents the positive directions.
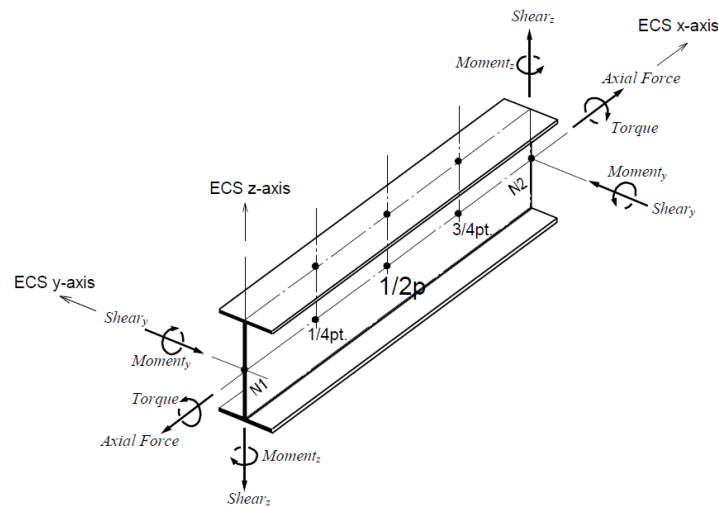
Figure 16 : ECS of a beam element in Midas GEN

Three or four nodes placed in the same plane define a plate element. This typology of element is able to account for in-plane tension/compression, in-plane/out-of-plane shear and out-of-plane bending behaviors. As regards the out of plane stiffness, in Midas GEN two types of element are included: The Discrete Kirchhoff element, developed on the basis of a thin plate theory, and the Discrete Kirchhoff Mindlin one, based on the thick plate theory of Mindlin-Reissner [12].

In the study of plates, it is usual to divide the thickness into two halves through a plane parallel to the faces, which is therefore called the middle plane. The ratio between the thickness h, measured in the direction normal to the medium plane, and the smallest in plane dimension l of the plate allows the element to be categorized as a thin or alternatively thick plate; in the case of the current thesis, 4-node elements following the Mindlin-Reissner theory will be used, as the ratio h/l in all the discretizations of

the plate elements used will be larger than 1/20, as the limit between the two plate theories.

Differently from beam finite element, in the plate elements only five nodal DOFs are typically present. The element's translational DOFs exists in the ECS x, y and z directions defined in the following figure, and the rotational ones exists in the ECS x and y-axes.
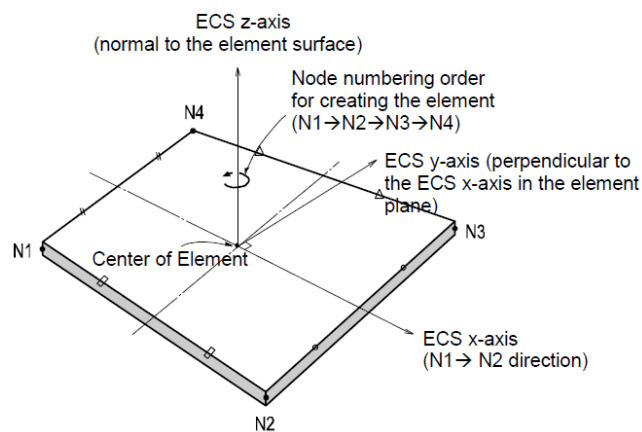
Figure 17 : ECS for a quadrilateral plate element in Midas GEN

In the case of a quadrilateral element with 4 nodes, the thumb direction signifies the ECS z-axis. The rotational direction is determined passing through the nodes N1→N2→N3→N4 and following the right hand rule. The ECS z-axis originates in the center of the element surface and is perpendicular to the surface itself. Furthermore the line connecting the mid point of N1 and N4 to the mid point of N2 and N3 defines the direction of ECS x-axis, while the perpendicular direction to the x-axis in the element plane identifies the ECS y-axis by the right hand rule. While the four corner node formulation is simple, a large number of elements and a fine discretization with a large number of DOFs is generally necessary to overcome the limited flexibility in these four node elements. Although not feasible in Midas GEN, which includes triangular and quadrangular plate elements, the alternative suggested by Priestley et al. in [3] provides the addition of mid side and center nodes in order to add flexibility, in order to model the most common deformation and strain states.

2.1 Description of the Sordo Viaduct

A detailed description of the work was provided by the executive technical report carried out by Anas S.p.A., from which it has been possible to take the data necessary for the modeling, such as location, structural elements, static scheme, geometry and construction details. The Sordo Viaduct is located along the Catania freeway at km 11+750 in the municipality of Misterbianco (CT).

Figure 18 : Location of the viaduct

It consists of two decks with independent piers and with common abutments, similar and parallel, on each of which a carriageway is arranged in each direction of travel. The carriageway towards Messina will conventionally be called the "right carriageway", while that towards Syracuse will be indicated in the following as the "left carriageway". The viaduct develops approximately in a straight line along 11 spans, with a maximum span of 21.8 m and a minimum of 20.5 m, for a total length of about 237 m. The deck, characterized by a total width of 12.20 m, is made with prestressed concrete beams and a collaborating concrete slab.

On the basis of archival research and information collected in the ANAS compartments and archives in Catania, it was possible to reconstruct the technical-administrative history of the work: the viaduct was built in the late 1970s - early 1980s; in particular, in July 1984 the load test was carried out on the viaduct. As regards the original project loads, the work was designed in accordance with the current legislation of the time for

the bridges (Circular of the Superior Council of Public Works n. 384 of 02/14/62). Furthermore, on the basis of the research carried out and the information collected, there is no evidence that the work was subject to significant events and that it was subjected to interventions subsequent to construction. To facilitate the description of the structural elements, from this section onwards reference will be made to the dimensions of the bridge through a global reference system in which the longitudinal direction of the bridge development is identified by the X axis, the vertical direction by the Z axis, and the transversal one by the Y axis.

As far as the deck is concerned, it consists of 5 post-tensioned prestressed concrete T-beams 1.20 m tall, placed at a distance between centers of 2.40 m and approximately 21 m long, with a collaborating concrete slab characterized by a thickness of 22 cm. The slab has two lateral overhangs with a length of approximately 95 cm. At the ends of the beams there are two reinforced concrete transversal girders with rectangular section and a further cross girder is located at each midspan.

As regards the piers, they are made of reinforced concrete and characterized by a single shaft. It should be emphasized that for modeling purposes only one of the two carriageways will be represented and analyzed, in particular the right carriageway, as they are similar to each other. The shafts are solid and have an octagonal section inscribed within a rectangle measuring 3.30 m x 1.80 m. The heights of the piers, referring to the sum of the height of the shaft and that of the cap beam, for both carriageways, are shown in the following table:

LEFT CARRIAGEWAY - Pier height (m)									
P1	**P2**	**P3**	**P4**	**P5**	**P6**	**P7**	**P8**	**P9**	**P10**
6.1	8.5	9.9	13.35	16.4	18	17.7	15.2	11.5	6.7
RIGHT CARRIAGEWAY – Pier height (m)									
P1	**P2**	**P3**	**P4**	**P5**	**P6**	**P7**	**P8**	**P9**	**P10**
8.4	9.7	11.3	15.4	18.1	18.5	17.5	14.1	11.9	6.9

Table 3: Pier heights (m)

The cap beam is made in reinforced concrete and has a trapezoidal shape with larger base of 11.02 m, smaller base 3.60 m, height 1.60 m and width 2.80 m. Finally, the foundations, both of the abutments and of the piers, are of the direct type. The plinths of the piers have dimensions 10.50x7.50 m. The static scheme of the deck can be

considered isostatic for all life and loading phases of the work, as it consists of beams simply supported on piers and abutments, with any slab interrupted at each pier and abutment.

The following figure shows the longitudinal and transversal view of the tallest pier, identified in Table 3 with the number 6, including the cap beam, the deck and the foundation.
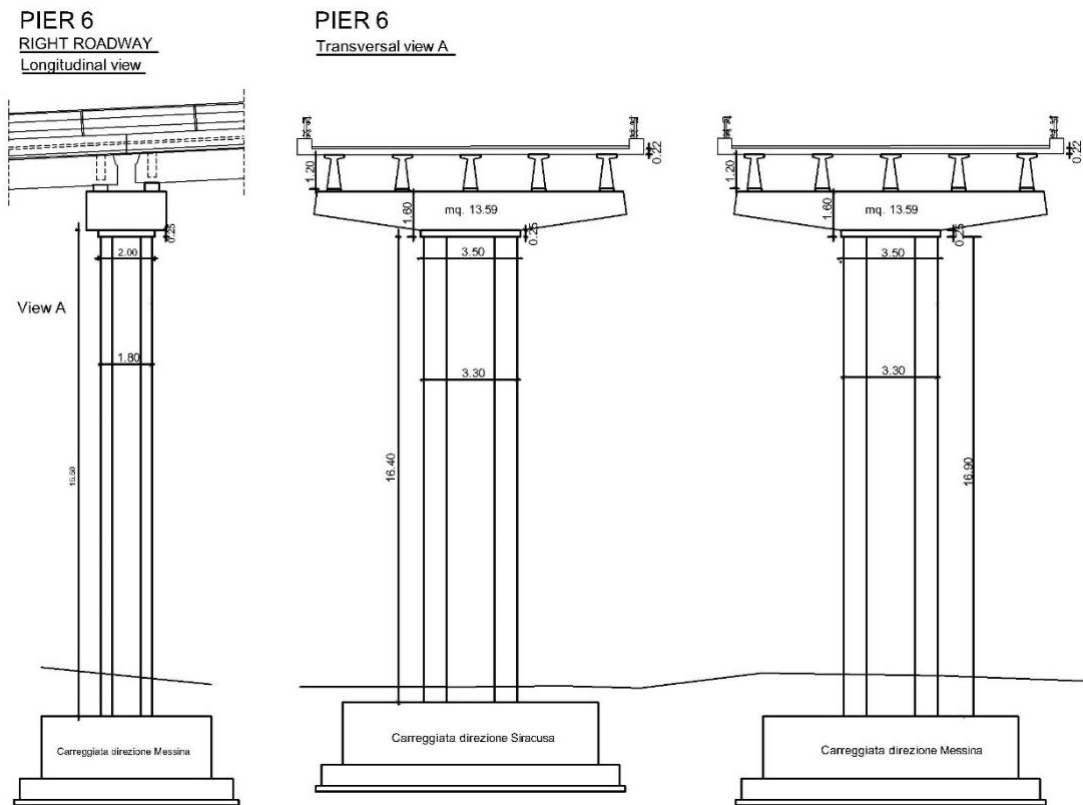
Figure 19 : Longitudinal and transversal view of Pier 6

Finally, as far as the support devices are concerned, they consist of non-reinforced neoprene bearings; moreover, it was not possible, during the inspection phase, to fully assess the presence, or the arrangement and geometry of seismic restraints.

For this reason, the current thesis will first analyze the option regarding the complete absence of seismic restraints both in the transverse and longitudinal direction of the bridge; then the response of the bridge to the common type of intervention that provides for the arrangement of transverse seismic restraints will be studied.

As for the materials used for the construction of the viaduct, they were collected from the project documentation. The beams were made of concrete with cubic strength of the conglomerate at 28 days of curing R_{bk} 500 kg/cm^2, corresponding to the characteristics of the current class of concrete C40/50, with a reinforcement pattern consisting of A38 steel and prestressing cables in harmonic steel in wires made with a diameter of 6mm, characterized by an ultimate stress R_{ak} equal to 18 t/cm^2.

The pier and cap beam were instead made with lower concrete class R_{bk} 300 kg/cm^2, corresponding to a class C25/30 and with corrugated reinforcement bars made of A38 steel, which, subsequently replaced in the regulatory framework by the FeB38k class, has the following characteristics:

Tensile ultimate load (kg/mm^2)	Yielding limit (kg/mm^2)
≥ 46	≥ 38

Table 4 : Steel A38 mechanical characteristics

Nevertheless, the information received regarding the piers doesn't include the design of their reinforcement. In order to carry out non-linear dynamic analysis, however, it is necessary to know the arrangement and pattern of the reinforcements.

For this purpose the work carried out in [13] has been examined, concerning a research program aimed at defining seismic damage scenarios for buildings and bridges of the city of Catania in Sicily. The aforementioned paper is intended to introduce fast and simple assessment methods in order to allow to analyze seismic damage scenarios, where bridges can be considered both as single structures and the vulnerable component of a road system. The work involves a preliminary description of all bridges, preparatory to comparing a measure of the bridge capacity to a corresponding demand, with respect to different performance levels. The bridge capacity is thus represented by a set of fragility curves, representing the probability of exceedance in function of the peak ground acceleration. The bridge demand is finally defined by the introduction of a target fragility curve, referred to the same bridge designed according to modern seismic codes.

Of particular interest for the current thesis is the initial part of this work, which concerns the description of the bridges belonging to the highway system of the city of Catania, that is the urban network which will be analyzed in the paper for the fragility curves development. Among the four typologies of bridges identified as needy of accurate assessment at the end of the preliminary screening, the category "Bridge 4" of the Buttaceto area in the paper turns out to be very similar to the Sordo Viaduct, as they are all part of the road network of the city of Catania. Furthermore, as can be seen from Figure 20, as well as the Sordo Viaduct, the bridges of the Bridge 4 category are girder bridges made up of single-shaft octagonal piers inscribed in a 3.3m x 1.8m rectangle. They are also similar in the size of about 12 m of the deck width, which is made up of 5 T-beams in both cases. Finally, as in Sordo Viaduct, transversal and longitudinal "shear keys" are absent.

Assuming that these bridges were designed in the 1970s with the same design strategy, according hence to the nominal seismic design regulations of that time, with horizontal forces computed as a small ratio of the permanent weights and no attention paid to ensuring ductile behavior, the same reinforcement pattern of the Bridge 4 category bridges in the aforementioned paper will initially be assumed for the Sordo Viaduct. The section is thus reinforced with 54 bars ϕ24, with non closed transverse reinforcements characterized by a diameter of 16 mm and by a spacing of 25 cm. Finally a strain-hardening ratio for steel of 5 ‰ will be assumed.

Despite this, after an initial adoption of this reinforcement configuration, a check of the same is necessary, as there is no perfect correspondence between the dimensions of the bridges analyzed in the paper and those of the Sordo Viaduct; such discrepancies can be noted for example in the size of the spans of the bridges of category Bridge 4, which are 17 m and therefore less than the 21.8 m of the Sordo Viaduct.

In order to carry out the preliminary check of the pier reinforcement, the forces acting at the base of the highest pier were computed, through the simplified model of a simple oscillator, a one degree of freedom system with the mass of the pier itself, concentrated at the top, including cap beam and deck, by attributing the latter by influence areas.
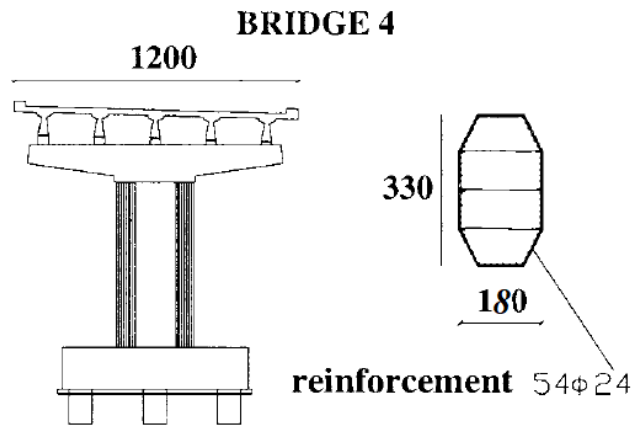
Figure 20 : Bridge 4 geometry from [13]

This type of analysis consists in the application of forces equivalent to the forces of inertia induced by the seismic action. The magnitude of these forces is obtained from the ordinate of the design spectrum corresponding to the fundamental period of the bridge in the two directions considered.

The Reluis guidelines for the evaluation of seismic safety and the rehabilitation of existing bridges introduce a model with an effective mass of the pier concentrated at the top, for constant section piers, equal to the sum of the mass of the deck, the mass of the cap beam and finally 30% of the mass of the pier. The total mass for the generic pier will therefore be equal to:

$$m_{tot} = 0.3m_{pier} + m_{capbeam} + m_{deck} \qquad (2.1)$$

For the purposes of the resistance and ductility checks for the ultimate limit state, the standards provide that the actions to be considered in addition to the seismic one are only those due to permanent loads. In relation to the Sordo Viaduct, the loads were evaluated starting from the following dimensions, in which the quantities are expressed in reference to three orthogonal directions, in which the X axis identifies the longitudinal axis of the bridge, the Y axis the transverse direction and the Z axis the vertical one.

Pier			T beams		
A_{xy}	5.3	m^2	A_{yz}	0.47	m^2
H_{shaft}	16.9	m	H	1.20	m

	Cap beam			Transversal Girder	
A_{yz}	13.6	m^2	H	1	m
L_x	2.8	m	L_x	0.3	m
H	1.6	m	L_y	9.6	m
	Slab			Deck flooring and curbs	
H	0.22	m	$H_{flooring}$	0.08	m
L_y	12.2	m	$A_{yzcurbs}$	0.175	m^2

Table 5 : Geometrical dimensions of Sordo Viaduct

The simple oscillator model will be characterized by different heights in the transverse and longitudinal direction. In fact, the height of this mass from the base for the analysis in the transverse direction is given by the expression:

$$H_{trans} = \frac{(0.3m_{pier} + m_{capbeam})H_{cb} + m_{deck}H_{deck}}{m_{tot}} = 19.09m \qquad (2.2)$$

Where H_{cb} e H_{deck} are the coordinates, with respect to the foundation extrados, respectively of the cap beam center of gravity and of the deck. As regards the analysis in the longitudinal direction, the effective height is expected to be equal to the distance from the plane of the support devices to the base of the pier, equal in the case at study to $H_{long} = 18.5 \ m$.
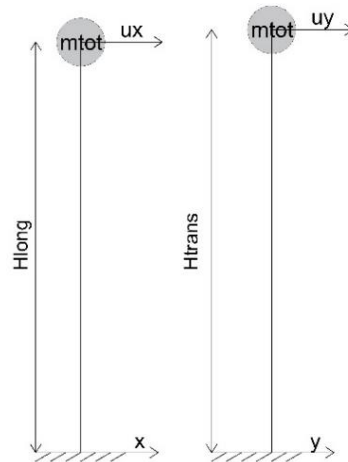
Figure 21 : Longitudinal and transversal SDOF models

Starting from the data shown in Table 5, the loads attributable to the deck and to the pier were evaluated, subsequently transformed into masses for the calculation of m_{tot}.

		Structural elements	Weight (kN)
DECK	***Permanent structural loads***	Deck beams	1292.5
		Slab	1462.8
		Transversal girders	216.0
	Permanent non structural loads	Deck flooring	531.9
		Curbs	190.8
		Metallic road safety barriers	49.7
		DECK TOTAL LOAD	3743.6
PIER	***Permanent structural loads***	***Pier Shaft***	2239.3
		Cap beam	952

Table 6 : Permanent loads

The permanent non structural loads were computed starting from a road pavement represented by a surface action of 250 kg/m^2, while as regards the barriers, a metal barrier of type H3 was adopted, characterized by a weight per meter of 0.57 kN/m. The total mass lumped at the top is therefore equal to $m_{tot} = 547.4\ ton$.

Once known the mass m_{tot}, it is now possible to compute the natural period of the two SDOF systems through the following relationship:

$$T = \sqrt{\frac{m_{tot}}{K}} \tag{2.3}$$

Where the bending stiffness of the system fixed at its base is expressed as:

$$k_i = \frac{3EI_i}{H_i^3} \tag{2.4}$$

The expressions (2.3) and (2.4), for the longitudinal and transversal directions, lead to the stiffness values reported in Table 7:

Longitudinal direction			*Transversal direction*		
H	18.5	m	H	19.09	m
I_y	1.22	m^4	I_x	4.14	m^4
k_x	18222.5	kN/m	k_y	56189.7	kN/m
T_x	1.09	s	T_y	0.62	s

Table 7 : Natural periods of the SDOF systems

As can be noticed from the following figure, the inertia with respect to the longitudinal axis X of the bridge, and therefore the inertia which comes into play in the bending resistance linked to the application of a force in the transverse direction Y, is larger than the inertia with respect to the transverse axis I_y. Consequently, although the SDOF system with a single degree of freedom u_y is characterized by a larger height H that gives a reduction in the bending stiffness, it has a bending stiffness k_y larger than the SDOF system with degree of freedom u_x in the longitudinal direction.
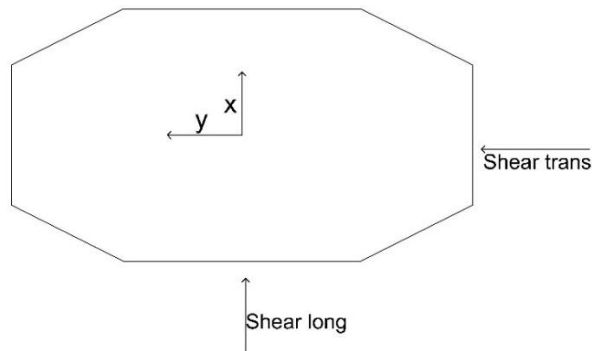
Figure 22 : Pier cross section representation

Consequently, the model in the transverse direction will be characterized by a shorter natural period than in the longitudinal direction.

Once known the mass and the period of the two systems, it is finally possible to evaluate the seismic force acting at the head of the pier model, starting from the acceleration spectral ordinate, associated to the two natural periods, through the following relationship:

$$F_i = m_{tot} S_{des}(T_i) \qquad (2.5)$$

To determine the intensity of the seismic action, a useful life of the work of 50 years and a class of use II, associated to works of ordinary importance, will be assumed, with a consequent C_U coefficient equal to 1. This choice was dictated first of all by the indications of the executive technical report of the viaduct provided by Anas S.p.A.. The latter refers to the fact that the safety checks of existing bridges, in general, will be carried out by classifying them as works of ordinary importance and therefore belonging to a class of use II. Secondly, it was intended to make the modeling and the

results of the analysis as general as possible; the same operative strategy will be followed for the characterization of the scale specimen of a span of the viaduct itself.

The reference useful life V_r, calculated in accordance with equation (1.4), is therefore equal to 50 years. The current resistance checks will be performed for the ultimate life safety limit state SLV. Therefore, the probability of exceeding P_{Vr} associated with this limit state is assumed, as indicated in Table 2, to be 10%. Consequently, the corresponding average return period, evaluated with the well known expression set out in equation (1.5), is equal to 475 years.

The reference acceleration expected on site was calculated, in accordance with Ministerial Decree 14/01/08, according to the geographical coordinates of the work. Starting from the grid of points covering the national territory provided by the INGV, the following parameters characterizing the spectrum were obtained, previously defined in paragraph §1.4 of the current thesis:

LON	LAT	a_g/g	F_0	T_C^* (s)
15.02	37.49	0.2062	2.45	0.36

Table 8 : Site spectrum parameters at SLV

Given these parameters, the elastic acceleration spectrum of the horizontal components of the seismic motion is almost defined. Finally, it is necessary to evaluate the parameter S, which takes into account the category of soil and the topographical conditions, and the periods T_B, T_C e T_D. The latter are defined respectively as the period corresponding to the beginning of the constant acceleration, velocity and displacement part of the spectrum and are calculated through the relations:

$$T_c = C_c T_c^* \quad (2.6) \qquad T_B = T_c/3 \quad (2.7) \qquad T_D = (4a_g/g) + 1.6 \quad (2.8)$$

The parameter C_c is a function of the category of soil and a function of T_c^*; in the case of the viaduct in question, which is associated with a soil category B for its entire development, it assumes a value of 1.35. As regards the coefficient S, it was also calculated for a soil category B and considering a topographic category of type T1.
The pseudo-acceleration elastic spectrum characteristic of the site under examination, once the above parameters are known, is therefore represented in the following graph:
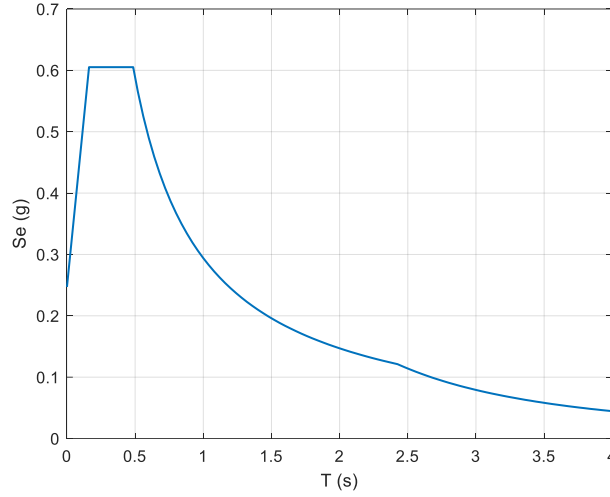
Figure 23 : *SLV pseudo-acceleration elastic spectrum for Sordo Viaduct site*

The current NTC 2018 technical standards provide that, in the case of linear analysis, the seismic demand for both dissipative and non-dissipative structures can be reduced by using an appropriate behavior factor q. The values of the latter vary according to the structural behavior and the limit states considered, as they are linked to the extent of the plasticization typical of each limit state. In the case at study, assuming a dissipative behavior for which plasticization occurs at the base of the pier, the structure behavior factor at the SLV has a lower limit of 1.5. The upper limit q of the behavior factor relating to the SLV limit state is computed using the following expression:

$$q = q_0 K_r \tag{2.9}$$

Where q_0 is the basic value of the behavior factor at SLV and K_r is a parameter that depends on the characteristics of regularity in height. In accordance with §7.9.2.1 of the technical standards, q_0 has been calculated, considering a high ductility class, equal to 3.5 λ, with λ function of the parameter $\alpha = L/H$, where L is the distance of the plastic hinge section from the zero moment section and H is the dimension of the section in the plane of deflection of the plastic hinge.

In the case of the analyzed pier, L is equal to the height of the entire pier, since the plastic hinge section is assumed to be at the base of the pier itself. For both cases of bending around the longitudinal and transverse axis, the value of $\alpha \geq 3$; therefore the value of λ is equal to 1. Known the value of the factor $q_0 = 3.5$, it is necessary, in order to assume this value as definitive, to check the value of the normalized

51

compressive stress ν_k, equal in the case at study to 0.04 and obtained by dividing the normal stress N_{Ed} by the simple compressive strength $A_c f_{ck}$. The value of q_0 obtained is valid, as the requirement on the value of ν_k to be smaller than 0.3 is verified.

As regards the factor K_r, the standards provide that it is preliminarily set equal to 1, and subsequently that checks are carried out on the ratio r_i between the acting moment and the resistant moment at the base of the pier, thus concerning the regularity of the geometry of the bridge. In the current model, regarding the single pier, K_r will be evaluated equal to 1; therefore the value of q is equal to 3.5. The pseudo-acceleration design spectrum obtained for the Sordo Viaduct site is shown in the following figure:
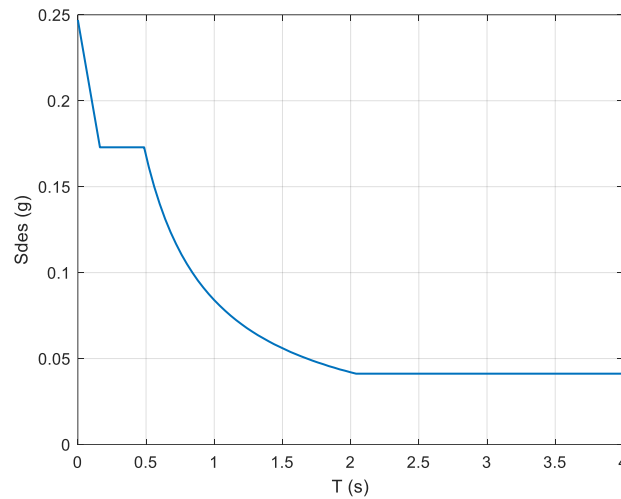
Figure 24 : SLV pseudo-acceleration design spectrum for Sordo Viaduct site

It is now possible to compute the forces acting at the top of the pier for the two directions, according to expression (2.5), and the bending moments at the pier base.

Longitudinal direction			Transversal direction		
S_{Des}	0.76	m/s^2	S_{Des}	1.33	m/s^2
$Shear_{long}$	414.01	kN	$Shear_{trans}$	727.23	kN
M_{long}	7660.82	$kN\,m$	M_{trans}	13886	$kN\,m$
N	5367.40	kN	N	5367.40	kN

Table 9 : Shear and bending moments for the SDOF systems

With these values of the acting bending moments and axial forces, it is now possible to carry out the combined compression-bending checks. The check will be carried out assuming that the failure occurs due to bending and not to shear; moreover, it will be

considered as uniaxial, so as to be in line with the approximate setting of the two models in the two directions as separate systems with one degree of freedom. As can be seen from the following graphs, the acting stresses are within the M-N domain for both directions.
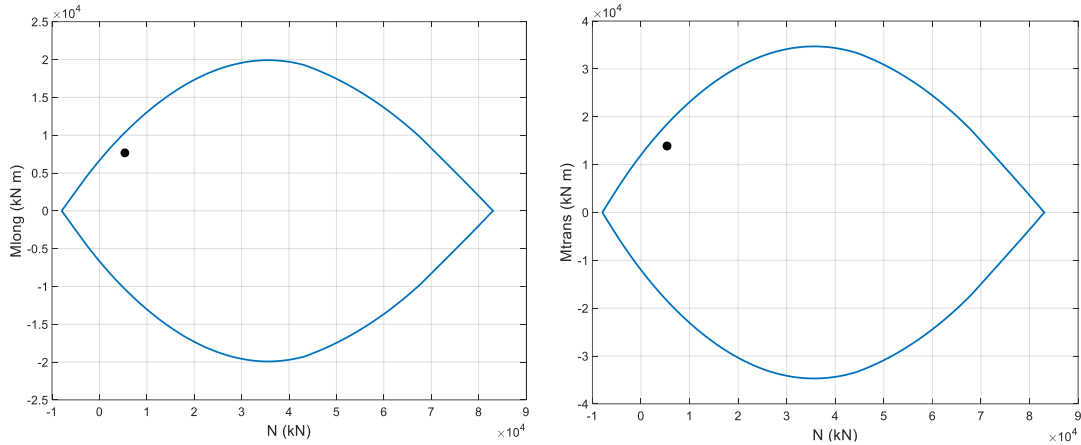
Figure 25 : M-N interaction domain for the SDOF systems

The constitutive laws used for the construction of the M-N domain in this preliminary phase are respectively a parabola-rectangular law for concrete and an elastic-perfectly plastic behavior for steel, considering the following characteristic parameters of the materials:

	Concrete			*Steel*	
f_{cd}	14.17	N/mm^2	f_{yd}	326	N/mm^2
ε_{c2}	2	‰	ε_{yd}	1.63	‰
ε_{cu}	3.5	‰			

Table 10 : Materials characteristics

where f_{cd} and f_{yd} represent the design resistances of the respective materials, ε_{c2} the deformation value associated with the maximum ordinate of the parabola, ε_{cu} the ultimate deformation of the concrete and finally ε_{yd} represents the deformation in which the design value f_{yd} of the steel yield strength is reached.

2.2 Material non-linearity

2.2.1 Fiber model

The use of a numerical model in the context of a finite element program, in order to carry out non-linear analysis, must aim to represent the best compromise between predictions accuracy and computational costs. A primary aspect to be evaluated to ensure a correct choice of the analytical tool concerns the methodology of modeling the non-linearity of the material. In fact, it is possible to opt for different alternatives, with lumped plasticity on one hand, and models with distributed plasticity on the other.

As regards the first option, the plasticity is lumped in point plastic hinges placed in the section where the formation of the plastic hinge is assumed to take place. Therefore, according to this modeling methodology, the non-linearity is concentrated only in these sections, while the rest of the element remains characterized by a linear elastic behavior. This type of approach has the advantage of being computationally less expensive than the fiber approach described below, despite having a lower accuracy in predicting the non-linear response of the structure.

A valid alternative to lumped plasticity models is therefore to represent the entire structural element by dividing it into further sub-elements characterized by a non-linear constitutive law, called fibers. This will be the approach used in the current thesis, as it presents a good balance between accuracy and computational cost, although the latter is, as previously mentioned, much larger than that which would be experienced with a concentrated plasticity modeling. The advantage of this type of modeling is to allow a different non-linear constitutive behavior to be attributed to each fiber, and therefore the confined concrete for the core, the unconfined for the concrete cover, and a different constitutive law for steel.

Working at the section level with simple uniaxial constitutive models, the section behavior due to axial and bending forces is obtained through the integration of the stresses relating to the single fiber over the entire cross section. Therefore the stress-deformation state of the elements is obtained through the integration of the non-linear, uniaxial response of the individual fibers in which the section has been discretized. If

the number of fibers is sufficiently high, the distribution of mechanical non-linearities due to the materials on the surface of the section is accurately modeled, even in a highly inelastic field, unlike a model with concentrated plasticity.

Reinforced concrete section   *Non confined concrete fibers*   *Confined concrete fibers*   *Steel fibers*
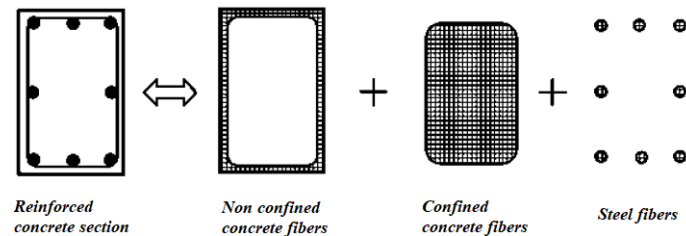
Figure 26 : Fiber section discretization

There are two possible alternative versions for a fiber finite element modeling, based on a stiffness or flexibility formulation. In the former, which represents the most commonly used methodology called displacement-based design, the field of deformations on the element is obtained from the displacements of the nodes through appropriate interpolating functions.

The fundamental limitation of such approach is linked to the lack of precision in describing highly non-linear behaviors, due to the inadequacy in the representation of the curvatures trend along the element.

For example, if the displacements were approximated with cubic type functions, and therefore through third degree Hermite polynomials, the trend of the curvature could be at most linear. Consequently, in order to consider the modeling of the non-linear response sufficiently accurate and complete, the elements used must have a limited length, binding the user to the usage of multiple finite elements for each element [14]. Instead, in the flexibility formulation, the interpolation functions are used for the internal forces. This type of formulation of the finite element, called force-based element, ensures, although its disadvantage of an increase in the computational cost, even in the case of highly inelastic behavior, accurate predictions using a not too high number of finite elements. In particular, since in this formulation the shape functions are used to describe the trend of the stresses on the element based on the nodal forces,

the non-linear analysis becomes independent of the approximation of the displacement field.

In the software Midas GEN the fiber formulation is implemented, thus allowing to obtain the moment curvature relationship of the section, based on the definition of the stress-strain relationship of the fiber material and the distribution pattern of sectional deformation.
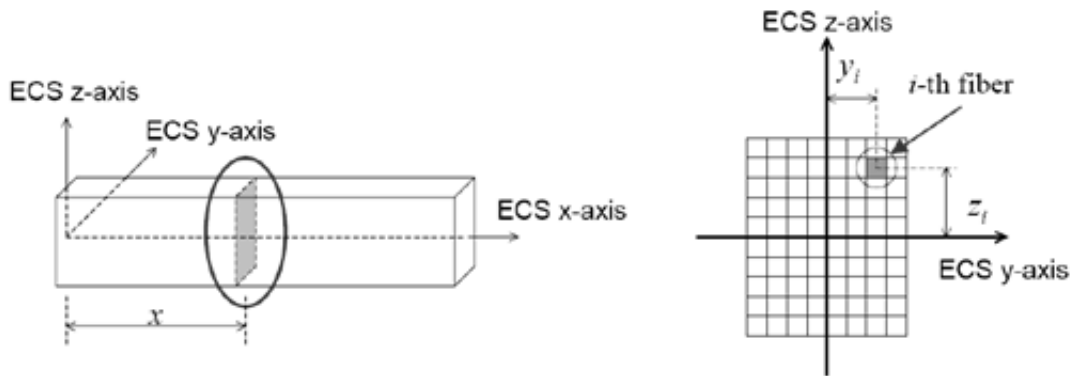
Figure 27 : Section discretization in the fiber model in Midas GEN

The fiber model in Midas is based on the assumption that the sections are perpendicular to the element axis and that they remain plane after the deformation process. Furthermore, the centroidal axis of the section is assumed to be a straight line throughout the entire length of the beam element. Following the assumptions mentioned above, the relationship between the fiber deformations and that one of the section is expressed as :

$$\varepsilon_i = [-z_i \ -y_i \ 1]\begin{bmatrix} \chi_y(x) \\ \chi_z(x) \\ \varepsilon_x(x) \end{bmatrix} \tag{2.10}$$

where

- x is the location of the section along the element axis;
- y_i and z_i represent the coordinate of the i-th fiber in the section;
- ε_i is the deformation of the i-th fiber;
- $\varepsilon_x(x)$ is the deformation of the section in the axial direction;

- $\chi_y(x)$ and $\chi_z(x)$ are the section curvature about respectively y and z axis according to the Element Coordinate System.

The description of the element follows the flexibility formulation described by Spacone et al (1996). The nodal forces are the two moments M_1 and M_2 and the axial force N, while the corresponding deformations are represented by the two nodal rotations θ_1 and θ_2 and the axial displacement u. The vectors P and U are represented below, collecting respectively the forces and the nodal displacements:

$$P = \begin{Bmatrix} M_1 \\ M_2 \\ N \end{Bmatrix} \qquad (2.11) \qquad\qquad U = \begin{Bmatrix} \theta_1 \\ \theta_2 \\ u \end{Bmatrix} \qquad (2.12)$$

The forces acting on the section at a generic x coordinate on the element axis are instead the axial load $N(x)$, the shear $T(x)$ and the bending moment $M(x)$, whereas the corresponding deformations of the section are the axial deformation $\varepsilon_o(x)$, the curvature $\chi(x)$ and the shear deformation $\gamma(x)$.

The following vectors $s(x)$ and $\varepsilon(x)$ collect respectively the internal forces and the deformations in the section placed at a generic position on the axis of the element:

$$S(x) = \begin{Bmatrix} N(x) \\ T(x) \\ M(x) \end{Bmatrix} \qquad (2.13) \qquad\qquad \varepsilon(x) = \begin{Bmatrix} \varepsilon_0(x) \\ \gamma(x) \\ \chi(x) \end{Bmatrix} \qquad (2.14)$$

As previously explained, the Midas software operates through a flexibility formulation for the fiber model. Therefore, shape functions are defined to determine the stress field, and allow to express the internal forces acting on the generic section as a function of the components of the nodal force vector through the relationship:

$$S(x) = \mathbf{N}(x)P \qquad (2.15)$$

The matrix $\mathbf{N}(x)$ of the shape functions has been built by imposing, according to Spacone et al., a linear force interpolation function for the bending moments and a constant force interpolation function for the axial force. It is expressed as:

$$\mathbf{N}(x) = \begin{bmatrix} 0 & 0 & 1 \\ -\dfrac{1}{L} & -\dfrac{1}{L} & 0 \\ \dfrac{x}{L} - 1 & \dfrac{x}{L} & 0 \end{bmatrix} \tag{2.16}$$

Following the definition of the forces and displacements vectors described above, the Principle of Virtual Works is applied:

$$\delta \boldsymbol{P}^T \boldsymbol{U} = \int_0^L \delta \boldsymbol{S}^T(x)\boldsymbol{\varepsilon}(x)dx \tag{2.17}$$

Introducing in the expression (2.17) the constitutive law of the material that links stresses and deformations through the flexibility matrix $\boldsymbol{f}(x)$:

$$\boldsymbol{\varepsilon}(x) = \boldsymbol{f}(x)\boldsymbol{S}(x) \tag{2.18}$$

and replacing the relation expressed in (2.15) in equation (2.17) we obtain:

$$\delta \boldsymbol{P}^T \boldsymbol{U} = \int_0^L \delta \boldsymbol{P}^T \, \mathbf{N}(x)^T \boldsymbol{f}(x)\boldsymbol{S}(x)dx = \int_0^L \delta \boldsymbol{P}^T \, \mathbf{N}(x)^T \boldsymbol{f}(x)\mathbf{N}(x) \, \boldsymbol{P}dx \tag{2.19}$$

Simplifying the arbitrary variation $\delta \boldsymbol{P}^T$, independent of the coordinate x, the following equation is obtained:

$$\boldsymbol{U} = \boldsymbol{F}\boldsymbol{P} \tag{2.20}$$

Where the flexibility matrix $\boldsymbol{F}$ of the element is expressed as:

$$\boldsymbol{F} = \int_0^L \mathbf{N}(x)^T \boldsymbol{f}(x)\mathbf{N}(x) \, dx \tag{2.21}$$

It should be noted as this formulation, contrary to that of the Euler-Bernoulli beam element, is "force-based" rather than "displacement-based". As previously explained, the interpolation functions don't link the nodal displacements to the internal ones, since they act on the stresses.

Furthermore, in this case the constitutive law has been taken over the formulation by introducing a link between the deformations and stresses through flexibility, and not through stiffness as occurs for an Euler-Bernoulli element.

2.2.2 Constitutive laws for the fiber model

As previously explained, a generic section of reinforced concrete divided into fibers allows the use of uniaxial constitutive laws associated with different regions of the cross section considered, which can be categorized into three characteristic areas:

- Unconfined concrete;
- Confined concrete;
- Reinforcements steel.

2.2.2.1 Kent and Park model

As regards concrete, it is a non homogeneous material composed of cement paste and aggregates, which is characterized by a non-linear behavior even for states of pure compressive stress. This non-linearity is caused by the internal microcracking that is generated as a result of a concentration of stresses at the interface between the cement paste and the aggregate.

The adoption of a constitutive model that takes into account exclusively the contribution of concrete, neglecting the effects of the interaction with the steel reinforcements present in the section, leads to acceptable results only for very low deformation states.

Therefore, with the aim of evaluating the structural response to larger cyclical actions, models are adopted, as in the case of the current thesis, which are able to consider the degree of confinement of the section, where the reinforcements produce it, as the latter significantly influences the ultimate deformation and the deformation path. A very widespread model for the representation of the non-linear link between stresses and deformations in concrete is the one provided by Kent and Park (1973) modified by Scott and Park (1982) in [15].

This model was chosen among the various ones available in the literature, since it is widely used for fiber modeling of reinforced concrete sections, as for example in the case of [16], in which a non-linear time history analysis is carried out on prestressed bridge piers.

In general, the curve that represents in the stress-strain plane the behavior of a concrete element subjected to a monoaxial compression test, has an increasing branch up to the resistance value f_c, to which is associated the strain ε_{c0}, and a decreasing branch up to the ultimate strain indicated by ε_{cu}.

The law, which can be considered non-linear for stress states close to 30% of the peak tension, is influenced both by the concrete composition, such as water-cement ratio, diameter of the aggregates, but above all by the presence of containment reinforcement, which, if properly made, is able to increase strength and ductility, in terms of ultimate deformation, with respect to the case of an unconfined element [17].

As previously mentioned, the model provided by Kent and Park modified by Scott et al. is perfectly capable of grasping these characteristics; the stress-strain law described is illustrated in the following graph:
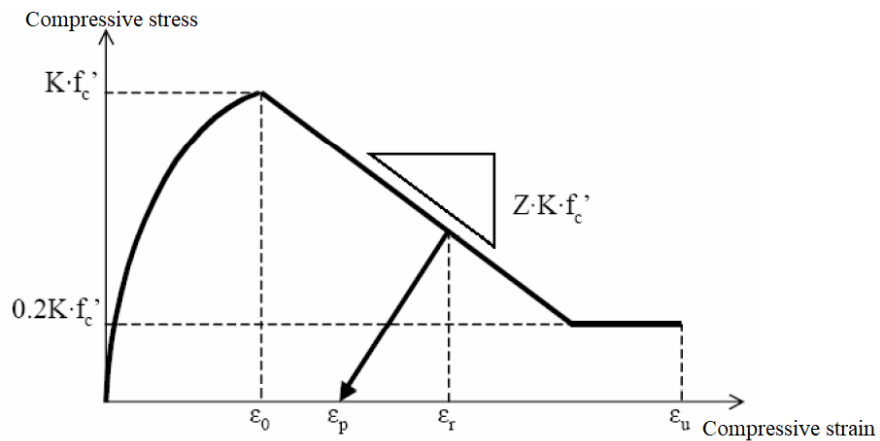
Figure 28 : Kent and Park stress-strain concrete model

- f_c' is the concrete cylindrical strength;
- K is a factor that indicates the change in resistance due to confinement, determined through the following expression:

$$K = 1 + \rho_s f_{yh}/f_c' \qquad (2.22)$$

- ρ_s is the ratio between the volume of the stirrups and the volume of the concrete core;
- f_{yh} is the yielding limit for the steel stirrups;

- Z represents the slope of the softening curve, which is the decreasing linear stroke, calculated as:

$$Z = \frac{0.5}{\dfrac{3 + 0.29 f_c'}{145 f_c' - 1000} + 0.75 \rho_s \sqrt{\dfrac{h'}{s_h}} - 0.002K} \qquad (2.23)$$

- h' is the dimension of the longest side of the concrete core;
- s_h is the step of the stirrups;
- ε_0 is the deformation at the stress peak, equal to $0.002K$;
- ε_{cu} is the ultimate strain.

Scott et al. in [15] provide as an approximate bound for ε_{cu}, by suggesting that the maximum concrete compressive strain could be taken as:

$$\varepsilon_{cu} = 0.004 + 0.9 \rho_s \frac{f_{yh}}{300} \geq \varepsilon_{c0} + \frac{0.8}{Z} \qquad (2.24)$$

In this expression, it is thus assumed that the maximum compressive strain for unconfined concrete is 0.004, that is the lower bound value for the strain at crushing of the cover concrete found in the tests conducted by Scott and al. in [15]. Furthermore the enhancement in strain capacity due to the presence of a strain gradient, such as in eccentric loading, is neglected.

At the analytic level, the constitutive law can be represented by the following expressions:

for $\varepsilon_c \leq \varepsilon_0$
$$\sigma_c = K f_c' \left[2 \left(\frac{\varepsilon_c}{\varepsilon_0} \right) - \left(\frac{\varepsilon_c}{\varepsilon_0} \right)^2 \right] \qquad (2.25)$$

for $\varepsilon_0 \leq \varepsilon_c \leq \varepsilon_u$ $\qquad \sigma_c = K f_c' [1 - Z - (\varepsilon_c - \varepsilon_0)] \geq 0.2 K f_c' \qquad (2.26)$

The increasing branch is represented by a parabola limited to the deformation ε_0, followed by a descending linear section significantly influenced by the pattern of the transverse reinforcement, since its inclination is a function of the parameter ρ_s.

The strain corresponding to the end of this branch is read on the diagram at a certain percentage of the maximum stress, and increases as the slope of the descending section decreases; in the case of the presence of an high percentage of stirrups, the second branch tends to be placed in a horizontal position.

During the unloading phase, straight branches are followed from the point which represents the beginning of the unloading (ε_r, f_r), belonging to the curve, to the point $(\varepsilon_p, 0)$, and subsequently the origin is reached again, following the abscissa axis, as the constitutive model assumes that there is no contribution to the tensile strength of the concrete. The unloading path is analytically described by the following expressions:

$$\text{for} \quad \frac{\varepsilon_r}{\varepsilon_0} < 2 \qquad\qquad \frac{\varepsilon_p}{\varepsilon_0} = 0.145 \left(\frac{\varepsilon_r}{\varepsilon_0}\right)^2 + 0.13 \left(\frac{\varepsilon_r}{\varepsilon_0}\right) \qquad\qquad (2.27)$$

$$\text{for} \quad \frac{\varepsilon_r}{\varepsilon_0} \geq 2 \qquad\qquad \frac{\varepsilon_p}{\varepsilon_0} = 0.707 \left(\frac{\varepsilon_r}{\varepsilon_0} - 2\right) + 0.834 \qquad\qquad (2.28)$$

Although the nature of the behavior is clearly non-linear, it may be interesting to find the expression of the elastic modulus of the material in the origin, in order to have an estimate of the most appropriate value for the representation of the elastic properties of the material.

This can be performed starting from the expression of the stresses in the initial section, in accordance with (2.25), and by deriving this expression with respect to ε_c. The limit of this derivative for which ε_c tends to zero represents the Young's modulus around the origin, and is represented by the following expression:

$$E_0 = K f_c' \left(\frac{2}{\varepsilon_0}\right) \qquad\qquad (2.29)$$

For the case at study, by considering the materials and the reinforcement pattern shown in paragraph §2.1, the values of the parameters of the Kent and Park model shown in the table below were obtained, respectively for confined and unconfined concrete:

	Confined concrete			Unconfined concrete		
f_c'	25	MPa	f_c'	25	MPa
f_{yh}	372	MPa	ρ_s	−	−
ρ_s	0.0014	−	K	1	−
K	1.02	−	Z	262.5	−
Z	94.46	−	ε_0	0.002	−
h'	250	cm	ε_{cu}	0.005	−
s_h	25	cm			
ε_0	0.002	−			
ε_{cu}	0.011	−			

Table 11 : Kent and Park model parameters for a Sordo Viaduct pier

As can be seen from the table above, for unconfined concrete there is no beneficial contribution of the transverse reinforcement to the concrete strength; this results mathematically into a cancellation of the terms in which the term ρ_s appears, making the ultimate deformation of the concrete independent of the parameters regarding the transverse reinforcement.

2.2.2.2 Menegotto and Pinto Model

As regards steel, it was decided to represent the non-linear behavior through the model developed by Menegotto and Pinto (1973), later modified by Filippou et al. (1983), which includes the hardening isotropic strain.

The model originally proposed by Menegotto and Pinto is a uniaxial material model able to simulate the main aspects of the cyclic response of steel. Indeed it is widely used to simulate the dynamic response of steel bars of reinforced concrete structures. It is an improvement of the first formulation of the model, published in 1970 by Giuffrè and Pinto, which considered the possibility of unloading and reloading paths. The model proposed by Giuffrè and Pinto was improved by Menegotto and Pinto to simulate kinematic hardening, in turn followed by Filippou et al. in [18], that refined on the model through the introduction of the isotropic hardening. The latter also noted that, partial unloading and reloading paths taking place at strains lower than the maximum recorded values, led to stresses higher than those expected. However,

Filippou et al. argued that these errors were not particularly relevant in the response of reinforced concrete structures, thus not proposing modification to the analytical formulation of the model.

The relation that provided the normalized stresses in Menegotto and Pinto model is:

$$\sigma^* = b\varepsilon^* + \frac{(1-b)\varepsilon^*}{(1+\varepsilon^{*R})^{\frac{1}{R}}} \qquad (2.30)$$

Where

- b is the strain hardening ratio, that is the ratio of the elasticity modulus of the second asymptote to the initial Young's modulus of steel. In the case under examination it will be taken equal to 5‰.
- R is a parameter which takes into account the Bauschinger effect; in order to describe this effect accurately, it is function of the plastic excursion of the previous loading path ξ, defined as the difference between the maximum deformation value in the direction of loading or unloading and ε_0 (absolute value). A graphic representation of the parameter ξ can be observed in the constitutive model schematization in Figure 29:
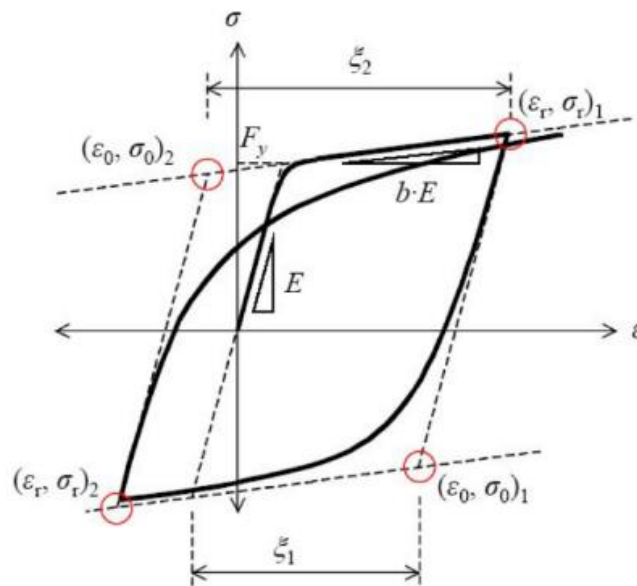
Figure 29 : *Menegotto and Pinto model*

The expression for the computation of the parameter R is given by the following relation [19]:

$$R = R_0 - \frac{a_1 \xi}{a_2 + \xi} \qquad (2.31)$$

where R_0 is the value of the parameter R during first loading, a_1 and a_2 are experimentally determined parameters to be defined together with R_0. The values of R_0, a_1 and a_2 are taken respectively equal to 20, 18.5 and 0.15, according to Filippou et al..

- σ^* and ε^* can be finally evaluated following the expressions:

$$\sigma^* = \frac{(\sigma - \sigma_r)}{(\sigma_0 - \sigma_r)} \qquad (2.32) \qquad \qquad \varepsilon^* = \frac{(\varepsilon - \varepsilon_r)}{(\varepsilon_0 - \varepsilon_r)} \qquad (2.33)$$

where σ_0 and ε_0 are the value of stress and strain at the point in which the two asymptotes of the branch under consideration intersect, whereas σ_r and ε_r are stress and strain at the starting point of unloading.

As an example, the figure 30.a shows the points $P_0(\varepsilon_0, \sigma_0)$ and $P_r(\varepsilon_r, \sigma_r)$ corresponding to the first load reversal of steel. It should be noted that the parameters $\varepsilon_0, \sigma_0, \varepsilon_r, \sigma_r$ and R are updated after each strain reversal, as shown in Figure 30.b, where the change in $P_0(\varepsilon_0, \sigma_0)$ and $P_r(\varepsilon_r, \sigma_r)$ for four load reversal is illustrated.

The formulation of Menegotto and Pinto has been subjected to following studies with the aim of analyzing its positive aspects, as well as its deficiencies. Some research studies, such as that of Stanton and McNiven (1979), have led to the conclusion that the explicit formulation proposed by Menegotto and Pinto is efficient from a numerical point of view and that the results provided by this model match the experimental ones of cyclic tests on reinforcing steel bars [19].

Some researchers have also proposed to improve the accuracy of the model, such as Filippou et al., that included the possibility to consider the isotropic hardening, as noted in laboratory tests on reinforcing steel bars.
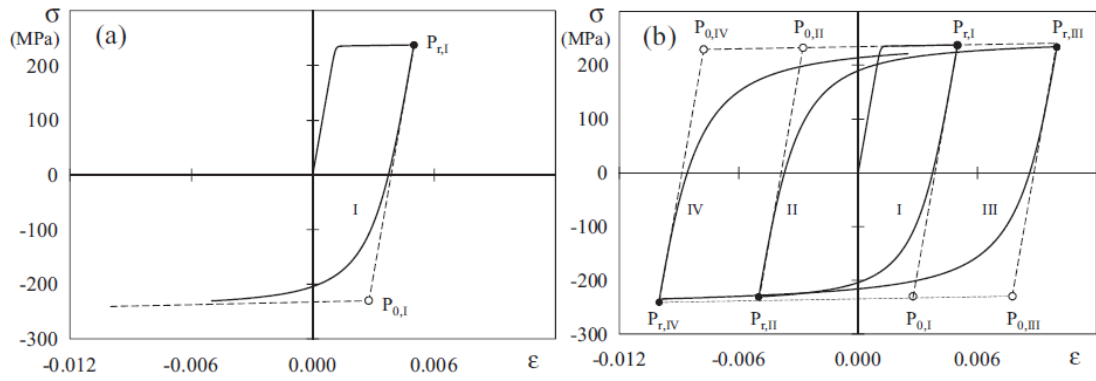
Figure 30 : *Model proposed by Menegotto and Pinto for (a) first cycle on the left and (b) for subsequent cycles on the right*

For the present case, given the material data set out in paragraph §2.1 and the considerations on the constitutive law for steel, the values of the parameters of the Menegotto Pinto model shown in the table below were obtained:

	Steel	
f_y	372	MPa
E	210000	MPa
b	0.005	−
R_0	20	−
a_1	18.5	−
a_2	0.15	−

Table 12 : *Menegotto Pinto model parameters for a Sordo Viaduct pier*

2.3 Numerical evaluation of the dynamic response

To fully understand the modeling criteria of the structural elements, it is necessary to analyze the typologies of dynamic analysis that will be carried out and the way in which they are implemented in the modeling software used. In the current work, the objective in the field of viaduct modeling is to arrive at the execution of an incremental non-linear dynamic analysis, in which to examine the response of the model in terms of steel and concrete deformation as a function of the increase of parameters related to the seismic intensity.

However, prior to carrying out this type of analysis, it is advisable to examine the response of the structure both to time history dynamic analysis with direct integration, and to linear dynamic analysis with response spectrum, which is computationally less expensive than the latter. These comparisons, as will be noted below, are also functional to the investigation of the influence of the introduction in the model of the ground-structure interaction.

2.3.1 Direct integration Time History Analysis

Let's Consider a MDOF system subjected to external dynamic forces $p_j(t)$. Its dynamic response to the excitation is defined by the displacements $u_j(t)$, velocities $\dot{u}_J(t)$, and accelerations $\ddot{u}_J(t)$. The external forces collected in the vector $\boldsymbol{p}(t)$ may be seen as distributed among the three components: the stiffness component $\boldsymbol{f}_S(t)$ associated to the displacement, the damping one $\boldsymbol{f}_D(t)$ related to the velocity, and the mass component $\boldsymbol{f}_I(t)$ linked to the acceleration. The sum of the three components must equal the applied forces $\boldsymbol{p}(t)$, thus resulting in the equation:

$$\boldsymbol{f}_S(t) + \boldsymbol{f}_D(t) + \boldsymbol{f}_I(t) = \boldsymbol{p}(t) \tag{2.34}$$

For an inelastic system, hence the equation of motion to be numerically solved will have the form:

$$\boldsymbol{M}\ddot{\boldsymbol{u}}(t) + \boldsymbol{C}\dot{\boldsymbol{u}}(t) + \boldsymbol{f}_S\big(\boldsymbol{u}(t), \dot{\boldsymbol{u}}(t)\big) = \boldsymbol{p}(t) \tag{2.35}$$

where M and C are respectively the mass and damping matrix characterizing the MDOF system and subjected to the initial conditions regarding the displacements and the velocity vector $u = u(0)$ and $\dot{u} = \dot{u}(0)$.

The numerical solution procedures that have proven to be more efficient and numerically reliable for the integration of the equations of motion, are those of time-stepping. In such methods the integration of the differential equations is applied by discretizing the time axis in precise instants fixed in advance. Thus the time domain is discretized into a finite number of intervals that could also be not equally spaced. Given a time interval $\Delta t_i = t_{i+1} - t_i$, the response is determined at the discrete time instants t_i; the displacements, velocities and accelerations are respectively $u_i, \dot{u}_i$ and $\ddot{u}_i$; these values, supposed to be known, satisfy the equation (2.35) at time i:

$$M\ddot{u}_i + C\dot{u}_i + f_{s,i} = p_i \qquad (2.36)$$

Where $f_{s,i}$ is the resisting force at time i. It has to be noticed that, in the case of a linearly elastic systems, $f_{s,i}$ would have been assumed equal to Ku_i, differently from the formulation for an inelastic system where it cannot be expressed in this way, due to its dependence on the prior displacement and velocity history. The time stepping procedures allow to determine the displacements, velocities and accelerations at the time instant i+1, which satisfy equation (2.35) at the time instant t_{i+1}:

$$M\ddot{u}_{i+} + C\dot{u}_{i+1} + f_{s,i+1} = p_{i+1} \qquad (2.37)$$

When applied for the subsequent time stepping, the procedure can give the response at the time instants of the discretization; it should pointed out that the information necessary to start the numerical procedure are supplied by the known initial conditions.

Both in the linear and non-linear direct integration in Midas GEN, the procedure implemented is that developed by N. M. Newmark. He developed a family of time-stepping methods based on the following equations on the displacements and velocity at the time i+1. For simplicity of notation, the method will be explained for a single degree of freedom system.

$$\dot{u}_{i+1} = \dot{u}_i + [(1 - \gamma)\Delta t]\ddot{u}_i + (\gamma \Delta t)\ddot{u}_{i+1} \qquad (2.38)$$

$$u_{i+1} = u_i + \Delta t\, \dot{u}_i + [(0.5 - \beta)\Delta t^2]\ddot{u}_i + [\beta(\Delta t)^2]\ddot{u}_{i+1} \qquad (2.39)$$

The parameters β and γ define the acceleration variation over the time step and influences significantly the accuracy and stability of the method. The software allows to choose between the more widespread constant acceleration and linear acceleration method, or alternatively to choose a different value of β and γ through an user manual input, although it suggests the use of the constant acceleration method for stability issues, since it is stable for any Δt. For that reason it will be followed in the current work. The latter is identified by the values of the Newmark parameters $\beta = 0.25$ and $\gamma = 0.5$, with a constant acceleration along the time step, as depicted in the graph below:
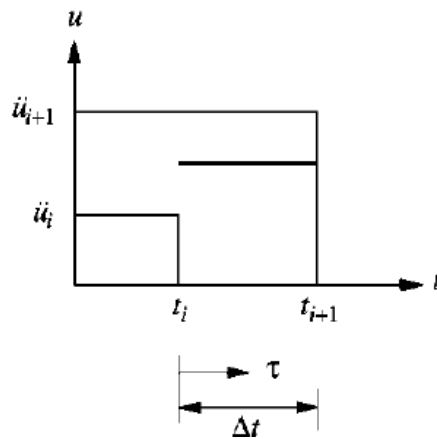
Figure 31 : Constant acceleration Newmark method

Both the equations (2.38) and (2.39), together with the equation (2.37) applied to a single degree of freedom model, allow to compute $u_{i+1}, \dot{u}_{i+1}$ and $\ddot{u}_{i+1}$ at time i+1, starting from the known values of $u_i, \dot{u}_i$ and $\ddot{u}_i$ at time i. It should be pointed out the necessity of an iterative procedure to implement these computations, since the still unknown value of $\ddot{u}_{i+1}$ is also located in the right part of the equations (2.38) and (2.39). However, in the case of linear systems, a modification in the Newmark formulation illustrated above can be made, in order to provide a solution of the equations (2.37), (2.38) and (2.39) even without the usage of iteration.

The proceeding for a linear time history analysis, implemented also by Midas GEN, can be explained in a few simple steps. Following the procedure set out in [8], the

69

equations (2.38) and (2.39) can be firstly written in the different following incremental form:

$$\Delta \dot{u}_i = \Delta t \ddot{u}_i + (\gamma \Delta t) \Delta \ddot{u}_i \tag{2.40}$$

$$\Delta u_i = \Delta t \, \dot{u}_i + 0.5 (\Delta t)^2 \ddot{u}_i + \beta (\Delta t)^2 \Delta \ddot{u}_i \tag{2.41}$$

Then the equation (2.41) can be rearranged and be expressed in function of $\Delta \ddot{u}_i$:

$$\Delta \ddot{u}_i = \frac{1}{\beta (\Delta t)^2} \Delta u_i - \frac{1}{\beta \Delta t} \dot{u}_i - \frac{1}{2\beta} \ddot{u}_i \tag{2.42}$$

Subsequently, by substituting the equation (2.42) into the equation (2.40) we obtain the following expression for the incremental velocity $\Delta \dot{u}_i$:

$$\Delta \ddot{u}_i = \frac{\gamma}{\beta \Delta t} \Delta u_i - \frac{\gamma}{\beta} \dot{u}_i + \Delta t \left(1 - \frac{\gamma}{2\beta}\right) \ddot{u}_i \tag{2.43}$$

The equations (2.42) and (2.43) can be substituted into the incremental equation of motion, where the resisting forces $f_{s,i}$ and $f_{s,i+1}$ at the two subsequent time instants, due to the linearity assumption for the system, have been expressed respectively as ku_i and ku_{i+1}:

$$m\Delta \ddot{u}_i + c\Delta \dot{u}_i + \Delta f_{s,i} = \Delta p_i \quad (2.44.a) \quad \rightarrow \quad m\Delta \ddot{u}_i + c\Delta \dot{u}_i + k\Delta u_i = \Delta p_i \quad (2.44.b)$$

The substitution leads to the following expression, obtained by collecting the terms of the equation related to Δu_i, substantial for the computation of the incremental displacement:

$$\hat{k} \Delta u_i = \Delta \hat{p}_i \tag{2.45}$$

in which:

$$\hat{k} = k + \frac{\gamma}{\beta \Delta t} c + \frac{1}{\beta (\Delta t)^2} m \tag{2.46}$$

$$\Delta \hat{p}_i = \Delta p_i + \left(\frac{1}{\beta \Delta t} m + \frac{\gamma}{\beta} c\right) \dot{u}_i + \left[\frac{1}{2\beta} m + \Delta t \left(\frac{\gamma}{2\beta} - 1\right) c\right] \ddot{u}_i \tag{2.47}$$

It should be noted that the terms $\hat{k}$ and $\Delta \hat{p}_i$ are known, since derived from the properties k, m and c, from the algorithm parameters γ and β, and finally from the values of the velocity and acceleration at the beginning of the time step $\ddot{u}_i$ and $\dot{u}_i$. It

has to be pointed out that the value of the acceleration $\ddot{u}_0$ to start the computations had been computed by the expression:

$$\ddot{u}_0 = \frac{p_0 - c\dot{u}_0 - ku_0}{m} \tag{2.48}$$

From equation (2.45) the incremental displacement Δu_i can hence be derived, consequently allowing to compute the quantities $\Delta \ddot{u}_i$ and $\Delta \dot{u}_i$ from the relationships (2.42) and (2.43). Then the values of $u_{i+1}, \dot{u}_{i+1}$ and $\ddot{u}_{i+1}$ can be derived by the equations; then the procedure is repeated for the next time step, by replacing i by $i+1$:

$$u_{i+1} = \Delta u_i + u_i \quad (2.49) \qquad \dot{u}_{i+1} = \Delta \dot{u}_i + \dot{u}_i \quad (2.50) \qquad \ddot{u}_{i+1} = \Delta \ddot{u}_i + \ddot{u}_i \quad (2.51)$$

In order to extend the Newmark method to the treatment of non-linear systems, it is necessary to make some considerations on the changes to be made to the method. Starting from the expression of the incremental equilibrium represented in the expression (2.44.a), the main difference from the Newmark method for linear systems lies in the expression of the resisting forces $\Delta f_{s,i}$. In fact, since the system is non-linear, they are expressed as the product of the incremental displacement Δu_i and the secant stiffness $k_{i,sec}$, being the latter not determinable, since the displacement u_{i+1} has not been computed yet. In order to understand the nature of the parameter, the graph below illustrates the trend of the resisting forces in function of the displacements, with the secant stiffnesses associated to each time instant of the discretization.
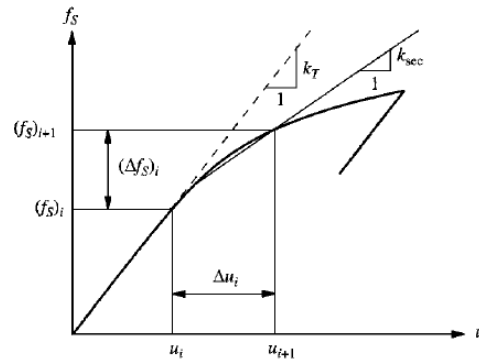
Figure 32 : Secant stiffness for an inelastic system

If the assumption that, in a small time interval Δt, the secant stiffness is replaced by the tangent stiffness called $k_{t,i}$ in the instant of the beginning of the time step is

considered legitimate, the resisting forces $\Delta f_{s,i}$ can be approximated as the product of the incremental displacement Δu_i and of the tangent stiffness $k_{t,i}$. The equilibrium equation can thus be rewritten as

$$m\Delta\ddot{u}_i + c\Delta\dot{u}_i + k_{t,i}\Delta u_i = \Delta p_i \qquad (2.52)$$

From a formal point of view, at this stage the same non-iterative procedure used for linear systems could be applied to the non-linear case, simply by replacing the stiffness of the linear system with the tangent stiffness $k_{t,i}$ evaluated at each time step. However, this procedure with a constant time step could result in inaccurate results. This deficiency is mainly linked to two aspects, that are the delays in noticing the variations in the force-displacement relationship and the approximation of the secant stiffness to the tangent stiffness.
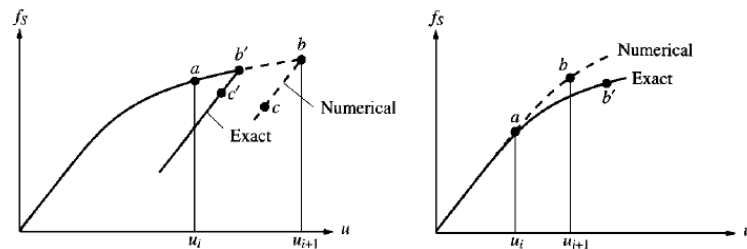
Figure 33 *: Problems in the Newmark's non iterative method for non-linear systems*

In the left graph can be observed the first aspect mentioned: supposing a given displacement in the time instant t_i, that is the lower bound of the considered time step, let's assume a positive velocity $\dot{u}_i$, with an associated increasing displacement. The kinematic state at the instant t_i is identified on the graph by point a. Now suppose that the displacement and velocity at the instant of time t_{i+1} have been found with the Newmark method described above. Point b was therefore obtained on the graph in correspondence of the upper limit of the current time step considered. If the velocity at instant t_{i+1} is negative, there would be a decrease in the displacement. In particular, in a time instant within the time step, associated with point b' on the graph, there have been a change in the sign of the velocity. Following the classic procedure, to start from point b for the next time step would lead to point c; on the other hand, if we were able to determine the time step associated to point b', the proceeding for the next time step started from b' would lead to point c' on the graph. Therefore, not locating b' in any

72

velocity reversal, results to a wrong path in the diagram, which can cause significant errors in the results. This kind of error can be removed by locating b' appropriately, with an iterative process that resumes the integration from the instant t_i, but with a smaller time step. The size is gradually adjusted until the velocity at the end of the adjusted time step is approximately equal to zero.

As far as the second aspect is concerned, as can be seen on the right graph in the Figure 33, the use of the tangent stiffness instead of the secant one leads to a relevant discrepancy between the exact and the numerical solution. The software Midas GEN minimizes the error through an iterative procedure, called the modified Newton-Raphson method. In this procedure the equation used in Newmark method, modified for non-linear systems, is written as below, by neglecting the subscript "i", from this point on, for the sake of simplicity:

$$\hat{k}_t \Delta u = \Delta \hat{p} \qquad (2.53)$$

With

$$\hat{k}_t = k_t + \frac{\gamma}{\beta \Delta t} c + \frac{1}{\beta (\Delta t)^2} m \qquad (2.54)$$

and $\Delta \hat{p}_i$ computed following the equation (2.47). The first iterative step is the application of the (2.53) to determine $\Delta u^{(1)}$, that is the approximation of the first iteration aimed at finding the displacement Δu. The real force $\Delta f^{(1)}$ associated to $\Delta u^{(1)}$ is lower than $\Delta \hat{p}$, consequently leading to a residual force defined as $\Delta R^{(2)} = \Delta \hat{p} - \Delta f^{(1)}$. There will be an additional displacement $\Delta u^{(2)}$ due to the residual force $\Delta R^{(2)}$, which will be determined from the equation:

$$\hat{k}_t^{(2)} \Delta u = \Delta R^{(2)} \qquad (2.55)$$

The procedure will be implemented until convergence, when the incremental displacement after n iterations $\Delta u^{(n)}$ will be small if compared to the current estimate of Δu, that is when $\left(\Delta u^{(n)} \Big/ \sum_{j=1}^{n} \Delta u^{(j)} \right) < \varepsilon$. In this way, the displacement increment in the time step from t_i to t_{i+1} will be $\Delta u_i = \sum_{j=1}^{n} \Delta u^{(j)}$. Actually, the software allows to choose between three types of convergence criterion; in addition to the displacement

one it provides the possibility to select the force and energy criteria, although the displacement criteria will be chosen for the current analysis.

The operating procedure performed on the software aimed at carrying out a linear or non-linear time history dynamic analysis consists of a series of steps. Specifically, the static gravitational loads are initially attributed to the elements, categorized into appropriate "Static Load Cases", subsequently converted into masses through the "Load to masses" command; if the self weight has been automatically attributed to the elements, it is used the function to automatically convert it into masses by the software through the "Convert self weight into masses" command.

Then an accelerogram or a group of accelerograms are imported into the "Time History Functions" window; actually, the NTC 2018 provide that, in order to consider the effects on the structure as the average of the most unfavorable values, at least seven different time histories or groups of time histories must be used for spatial analysis. As explained in Chapter 1, the use of artificial accelerograms has been chosen, created through the SIMQKE software and then imported into Midas GEN.
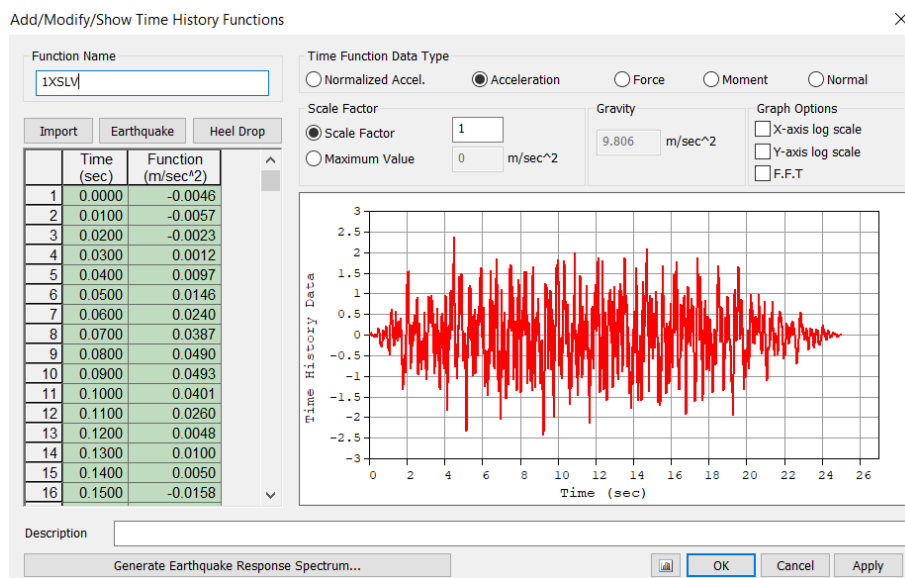
Figure 34 : Graphic interface in Midas GEN to import accelerograms

In the case of linear analysis, the next step consists in creating a "Time History Load case", in which the choice of a linear dynamic analysis for direct integration can be set, and to which the static loads can be added by superposition. On the other hand, unlike elastic time history analysis, inelastic time history analysis cannot be carried

74

out using the principle of superposition. Analysis results from static loads and earthquake loads cannot be simply combined to represent the results of the loads acting simultaneously. Therefore, for an inelastic time history analysis, they are applied as individual time history load cases and the loading sequence must be assigned for analysis. The preliminary creation of a ramp function is therefore necessary to be associated with the static loads through the "Time varying static Loads" function, functional to the setting of a non-linear static analysis, for which the loads are applied through an increment method with load control.
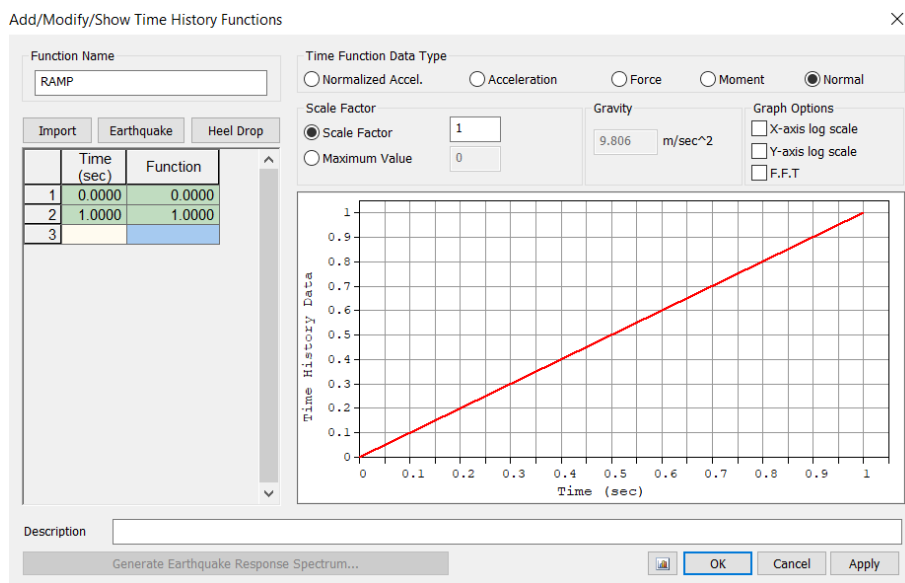
Figure 35 : Graphic interface in Midas GEN for the ramp function creation

If there are several static load cases, their simultaneous action on the structure is defined using the "Subsequent to" command, which allows to select a time history analysis condition previously defined, which precedes the time history analysis condition currently being defined. From the preceding time history load case condition, displacement, velocity, acceleration, member forces, are thus obtained and used as the initial condition for the current analysis. Then, the loading at the final state of the preceding analysis condition is assumed to constantly remain in the current analysis condition by checking on the command "Keep Final Step Constantly".

Finally, the time history load case for non-linear dynamic analysis is associated with a ground motion, so that the accelerogram can be attributed to the chosen direction, with a fixed scale value, and associated with the selected time history load case. In this way

it is possible to obtain spatial analysis or alternatively in one direction only, depending on whether the accelerograms are assigned respectively to one or more directions. In order to the create the time history load case for a non-linear system, given two static load cases such as the self-weight and the permanent non-structural loads, the following scheme is followed:

TH Load case name	TH_1	TH_2	TH_3
Assigned loads	Static load: Self weigth	Static load: Permanent non structural loads	Dynamic load: Accelerogram
Associated function	Ramp function	Ramp function	Accelerogram
Load typology	Time varying static load	Time varying static load	Ground acceleration
"Subsequent to"	None	TH_1	TH_2

Table 13 : Time history load case creation scheme for inelastic systems

It may be useful, to clarify the procedure explained, the visualization of the graphical interface for the creation of the time history load cases, shown in Figure 36, where it is evident the application of the Newmark method with the Newton Raphson iteration to carry out the analysis. As regards the choice of the time step, the constant acceleration method has been used, characterized by the absence of stability problems, regardless of the Δt used. However, the time step should be a good compromise between computational cost and accuracy, as it affects both significantly.

It is reasonable to consider it strictly related to the periods of higher modes and of the period of the applied force. In general, it is taken equal to one tenth of the highest modal period under consideration; however, if it is necessary to consider for the analysis a very high number of modes, the expression $\Delta t = T_p/10$ suggested leads to a very small value of Δt, being the natural frequency linked to the highest mode very small. In these cases it is advisable to choose a time step that is the right balance between the high computational cost and the accuracy of the results, like in the current work, where a time interval Δt equal to 0.005s was selected.

Another aspect that is usually taken into consideration is the attention to the input frequency; in fact, considering the expression:

$$f_{max} = \frac{1}{2\Delta t} \tag{2.56}$$

which represents the maximum frequency considered, it is evident that the choice of inadequately large Δt leads to neglect a wider range of frequencies.
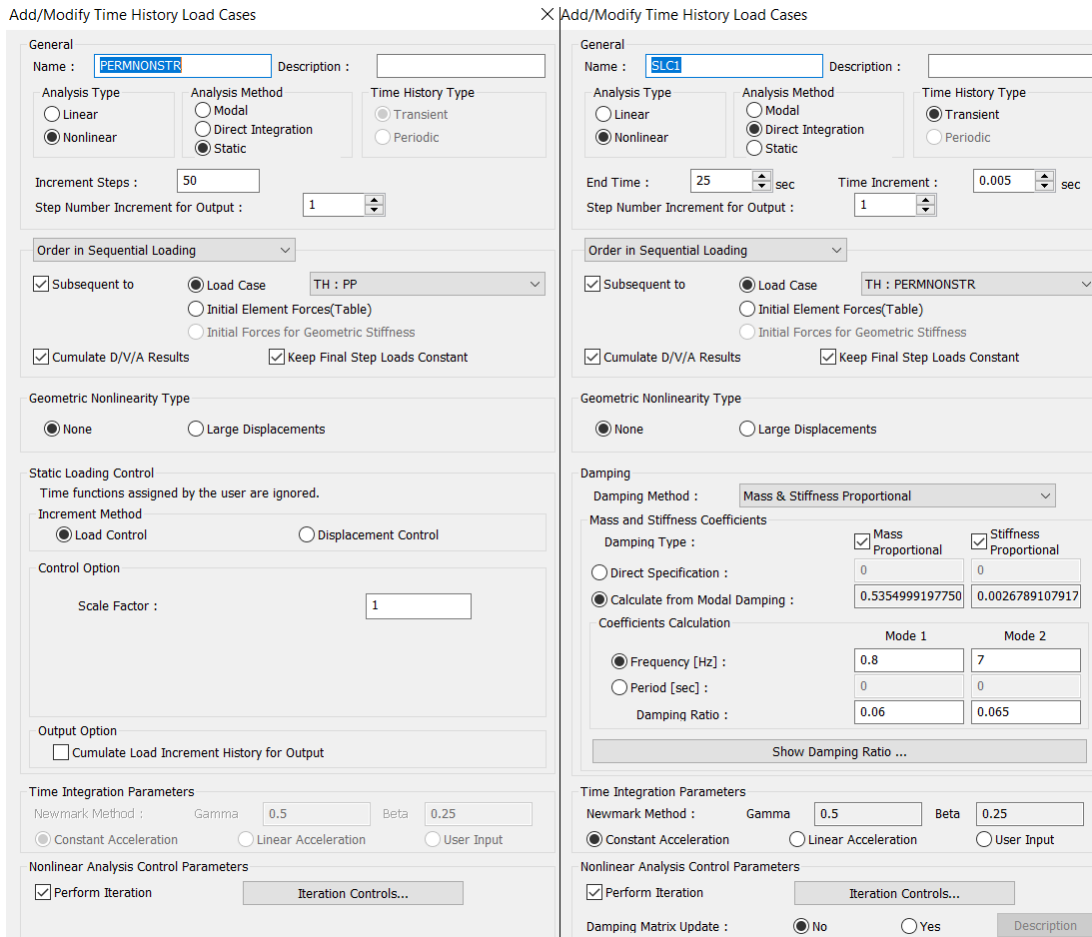
Figure 36 *: Graphic interface in Midas GEN for time history inelastic analysis*

In the graphic interface, the option concerning the damping matrix update can be noted, that was not used by choice. According to this option, when direct integration is used in nonlinear time history analysis, the user can choose whether to continuously update the element damping matrix based on the change in stiffness. If this command is unchecked, the element damping matrix is based on the initial stiffness of the elastic state. Otherwise, the element damping matrix is thus evaluated using the presently modified stiffness. A further step consists in carrying out the non-linear dynamic analysis for increasing input scale factors: the incremental dynamic analysis, also called IDA, which will be deepened and carried out in the next chapter.

77

2.3.2 Response spectrum analysis

The response spectrum analysis consists in a linear analysis typology that represents very often a valid alternative to the non-linear dynamic analysis. Starting from the dynamics equilibrium of a MDOF system subjected to a ground motion, the response spectrum analysis allows to compute its response as a combination of the response of SDOF systems. This is made possible through the eigenvalues analysis, in which the dynamic characteristics including the vibration modes, the natural periods and the modal participation factors of an undamped system under free vibration are obtained from the following equation:

$$K\phi_n = \omega_n^2 M\phi_n \tag{2.57}$$

Where K and M are respectively the mass and the stiffness matrix, ω_n^2 is n-th mode eigenvalue and finally ϕ_n is the n-th mode eigenvector. The first mode shape is associated to the least deformation energy, whereas the subsequent higher modes are defined by shapes formed with increases in energy.

In a given mode, the spectral value which is associated to the period computed through the eigenvalues analysis is evaluated. The maximum response for each mode is thus obtained, and then will be combined with an adequate method.

As an example, starting from the computed peak design spectral acceleration, the inertia force for a n-th mode is expressed as:

$$F_{n,x} = \Gamma_n \phi_{n,x} M_{n,x} S_{an} \tag{2.58}$$

Where:

- Γ_n represents the n-th modal participation factor, which gives an indication of the mode contribution to the total modes;
- $\phi_{n,x}$ is the n-th modal vector at location x;
- $M_{n,x}$ is the mass at location x;
- S_{an} is the spectral ordinate in acceleration associated to n-th modal period.

It should be noted that, at this point, all the modes with significant effective modal mass must be considered; it would be appropriate to consider a number of modes

whose the total effective modal mass is equal to 90%, anyway not neglecting the modes characterized by an effective modal mass larger than 5%.

For the mode combinations, the option provided by the current standards has been chosen, that is the complete quadratic combination CQC, whose use is recently increasing, since it accounts for a probabilistic correlation between modes. The CQC can be expressed as follows:

$$E = \sqrt{\sum_j \sum_i \rho_{ij} \, E_i E_j} \qquad (2.59)$$

Where

- E_j is value of the effect associated to the j-th mode;
- ρ_{ij} is a correlation coefficient between the two modes i and j, computed with the hypothesis of same damping for the two modes, through the equation:

$$\rho_{ij} = \frac{8\xi^2 {\beta_{ij}}^{3/2}}{(1 + \beta_{ij})[(1 + \beta_{i,j})^2 + 4\xi^2 \beta_{ij}]} \qquad (2.60)$$

- ξ is the damping factor of the two modes;
- β_{ij} is the ratio between the reverse of the periods ($\beta_{ij} = T_j/T_i$).

From a practical point of view, the software Midas GEN allows to carry out the response spectrum analysis through the steps which consist firstly in the definition of the response spectrum function. Subsequently, the latter is associated to one ore more response spectrum load cases. In particular, the horizontal spectrum has been exploited for the definition of the load cases linked to X and Y orthogonal direction, whereas the vertical response spectrum has been applied for the load case linked to Z. Among the modal combination methods implementable in the software, such as the abovementioned CQC, or the Square Root of Sum of the Squares (SRSS), the former has been chosen because of its greater accuracy and since it takes into account the coupling of the vibration modes by means of the correlation coefficient.

Furthermore, the program allows to select only the modes that are considered relevant for dynamic analysis. This function proved to be very useful in the carried out analysis,

as it allowed to considerably reduce the computational time, given the high number of modes required to reach the 90% effective modal mass.

The last aspect to be considered is the combination of seismic actions. The standards provide in fact that the structure response shall be obtained by computing the response for the three seismic action components and then applying the expression:

$$1,00 \; E_x + 0.30 \; E_y + 0.30 E_z \qquad (2.61)$$

The heaviest effects are then derived by comparing the three combinations, obtained by permuting the multiplicative coefficients and their sign. The model is therefore subjected to 24 combinations, which consists in the sum of the permanent loads and of seismic actions deriving from the following 24 sums:

1	$+1E_x + 0.3E_y + 0.3E_z$	13	$-0.3E_x + 1E_y + 0.3E_z$
2	$+1E_x - 0.3E_y + 0.3E_z$	14	$-0.3E_x + 1E_y - 0.3E_z$
3	$+1E_x - 0.3E_y - 0.3E_z$	15	$-0.3E_x - 1E_y + 0.3E_z$
4	$+1E_x + 0.3E_y - 0.3E_z$	16	$-0.3E_x - 1E_y - 0.3E_z$
5	$-1E_x + 0.3E_y + 0.3E_z$	17	$+0.3E_x + 0.3E_y + 1E_z$
6	$-1E_x + 0.3E_y - 0.3E_z$	18	$+0.3E_x - 0.3E_y + 1E_z$
7	$-1E_x - 0.3E_y + 0.3E_z$	19	$+0.3E_x - 0.3E_y - 1E_z$
8	$-1E_x - 0.3E_y - 0.3E_z$	20	$+0.3E_x + 0.3E_y - 1E_z$
9	$+0.3E_x + 1E_y + 0.3E_z$	21	$-0.3E_x + 0.3E_y + 1E_z$
10	$+0.3E_x - 1E_y + 0.3E_z$	22	$-0.3E_x + 0.3E_y - 1E_z$
11	$+0.3E_x - 1E_y - 0.3E_z$	23	$-0.3E_x - 0.3E_y + 1E_z$
12	$+0.3E_x + 1E_y - 0.3E_z$	24	$-0.3E_x - 0.3E_y - 1E_z$

Table 14 : Combinations for Response spectrum analysis

The NTC prescribes, for the bridge seismic assessment, an accidental mass eccentricity only for the deck, equal to 3% of its dimension, in absence of a more accurate evaluation. Within the context of this thesis and with reference to the characteristics of the existing bridge deck, perfectly symmetric, the mass eccentricity has been neglected, assuming an accurate determination.

A final consideration regarding the response spectrum analysis concerns the representation of damping. For the models for which the dissipative effects are uniformly distributed in the structure, the value of the characteristic damping factor of the structure itself will be used; on the other hand, in the models in which the soil-structure interaction is considered, as will be seen below, it will be necessary to carry

out the analysis with the so-called "weighted" damping factors, which take into account the non-homogeneity of the dissipative effects provided by the soil. This is done in Midas through the "Strain and energy proportional damping" function; this procedure will be analyzed in detail in the following.

2.3.3 Damping modeling

The modeling of dissipative effects in the computation of the response of damped systems with multiple degrees of freedom is a topic of considerable importance. In fact, in general, unlike the mass and stiffness matrices **M** and **K**, the matrix **C** is not diagonal. Therefore, the effects of damping cannot always be easily treated within the modal analysis, as the equations of motion are not generally decoupled. In order to understand the problems related to damping, the system of equations that describes the motion of a damped MDOF system is introduced:

$$m\ddot{q} + c\dot{q} + kq = Q \tag{2.62}$$

If the transformation is performed in the coordinates of the undamped system $\phi y = q$, then pre-multiplying all the terms of the equation of motion by the transpose of the eigenvector of the undamped system ϕ, the following equation is obtained :

$$M\ddot{y} + \phi^T c\phi\dot{y} + Ky = \phi^T Q \tag{2.63}$$

If the principal modes of the damped system were used, the system of equations of motion described by (2.63) would be decoupled. However, the search for the complex eigenvalues and eigenvectors of the damped system is unfamiliar from the computational point of view, therefore this path is followed only in particular cases. However, it can be verified that the matrix **C**, despite being full, in many cases of practical interest is characterized by rather small extra diagonal terms compared to those located on the main diagonal.

However, given the typical uncertainties of the modeling of dissipative phenomena, in these cases the hypothesis of neglecting the off-diagonal terms is considered legitimate, consequently using a forced decoupling of the equations. If this

approximation is possible, the equation of motion referred to the j-th principal coordinate is:

$$\ddot{y}_j + 2\xi_j\omega_j\dot{y}_j + \omega_j^2 y_j = \frac{\boldsymbol{\phi}_j^T \boldsymbol{Q}}{M_j} \tag{2.64}$$

associated to the expression of the damping factor relative to the j-th mode [20]:

$$\xi_j = \frac{C_j}{2\sqrt{K_j M_j}} \tag{2.65}$$

Usually the damping matrix isn't known in practical cases, differently from the damping factors of the materials that characterize the structure. If the latter is composed of a single material, then in (2.64) the damping factor of that material is simply imposed, which will be the same for all decoupled equations. In non-homogeneous systems, for which different dissipative characteristics are present in the structure, as in the case in which the soil-structure interaction is considered, this approach is not possible, as the problem of defining the different modal damping factors arises. A solution that, although in an approximate way, takes into account the different nature of the energy dissipations in the various components of the system, consists in the definition of equivalent "weighted" modal damping factors ξ_j; this option will be analyzed in a specific way and used in the current thesis when the dampers at the base of the pier that simulate the dissipative effects of the ground will be introduced. However, it is preferable for non-homogeneous systems to directly integrate the equations of motion, without passing through principal coordinates and decoupling the equations. Despite this, it may be interesting to evaluate the differences, in the response of the non-homogeneous system, between an analysis through direct integration and a modal analysis with response spectrum through the use of weighted damping. As regards the analysis with direct integration of the equations of motion in the time domain, it is necessary to define the damping matrix. A decoupled damping matrix that does not introduce a greater need for memory than the one used for the definition of mass and stiffness matrices is the Rayleigh matrix, expressed as:

$$\boldsymbol{c} = \alpha\boldsymbol{m} + \beta\boldsymbol{k} \tag{2.66}$$

where α and β are the Rayleigh coefficients.

If the modal damping matrix $C = \phi^T c\, \phi = \alpha M + \beta K$ is considered and the elements of the principal diagonal are expressed as a function of the modal damping factor ξ_j, you get that $C_j = 2\xi_j \omega_j M_j = \alpha M_j + \beta \omega_j^2 M_j$, from which the modal damping can be derived as a function of the two Rayleigh parameters:

$$\xi_j = \frac{1}{2}\left(\frac{\alpha}{\omega_j} + \beta \omega_j\right) \tag{2.67}$$

The expression of the damping factor therefore consists of a part that increases linearly with the frequency, proportional to the stiffness, and a component proportional to the mass that decreases hyperbolically as the frequency increases. The Midas GEN software allows, by selecting the type of damping method "mass & stiffness proportional", to select two frequencies with associated two damping factors. Chosen these four parameters, through the two unknowns system:

$$\begin{cases} \xi_1 = \dfrac{\alpha}{2(2\pi f_1)} + \dfrac{\beta(2\pi f_1)}{2} \\ \xi_2 = \dfrac{\alpha}{2(2\pi f_2)} + \dfrac{\beta(2\pi f_2)}{2} \end{cases} \tag{2.68}$$

it is possible to find uniquely the parameters α e β. The choice of the two damping factors and of the two frequencies was carried out with the aim of making the damping factor almost constant in the range of frequencies of interest. The parameters chosen in Figure 37, for example, were intended to make ξ approximately equal to 5% for frequencies within the range $(0.97\ Hz;\ 5.4\ Hz)$; the associated curve is represented in the following graph:
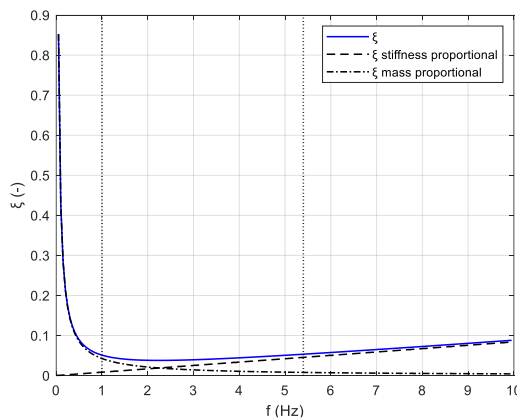
Figure 37 : Rayleigh damping graph

83

2.4 Structural components modeling

As previously mentioned, in order to model the Sordo Viaduct, two types of elements will be used in the Midas GEN software, i.e. beam and plate elements. The current paragraph will show the operating mode of modeling the viaduct, focusing on its different structural components. As regards the choice of the distribution of non-linearities in the various structural elements, some considerations related to the supports functionality and operativity are necessary. In fact, the viaduct in question is characterized by the presence of neoprene bearings, which are associated with a small stiffness to shear deformations, linked to the rubber characteristics of which they are composed. Their behavior and the other components response to their deformations can significantly influence the philosophy with which the viaduct is analyzed.

In fact, their presence leads on the one hand to a mitigation of the seismic effects, with an increase in the structure period and consequently to accelerations decrease which, if of significant magnitude, could significantly reduce the horizontal forces transmitted to the piers. This could therefore allow, as happens with the presence of real isolation devices, an isolation of the deck and the reduction of the actions that the deck itself transmits to the piers and to the abutments. Indeed, the basis of the concept of bridges seismic isolation is the fact that, the presence of isolation devices placed between the substructure, which includes foundation, piers and abutments, and the superstructure, consisting of the deck, means that all the aforementioned elements remain in a substantially elastic range also for ultimate limit state checks actions, as a consequence of the decrease in accelerations due to the increase in the structure period.

Another design philosophy consists in treating the system as a non-isolated system, whereby the dissipations are located at the base of the pier. The main problem related to this strategy is that the hypothesis on the plasticization to occur at the base of the pier may not be compatible with the real bridge behavior. The deficiency is in fact linked to the deformation limit of the supports: when the inertia force is applied to the deck, the support system must be able to transmit it to the pier without reaching shear deformations beyond the limit, which would lead to its consequent failure.

In both design strategies it is therefore important and necessary to check the bearing deformation. In the case at study of the non-reinforced neoprene supports placed between the substructure and the superstructure in the Sordo Viaduct, as previously mentioned, there are no "shear keys" that limit the deformations, both in the transverse and longitudinal direction.

 It is therefore very likely that the problem linked to the deformation of the devices is confirmed and that they are unable to transmit the inertia forces at the base of the pier. Therefore, in the current configuration for which the supports are free to deform in both directions X and Y in the horizontal plane, modeling the non-linearity at the base of the pier would be inappropriate.

In the current thesis, it was therefore chosen to operate according to a modeling strategy whereby, preliminarly, in a model for which the actual configuration of the neoprene supports was reproduced as free to experience shear deformations in the transverse and longitudinal directions, it was assumed that all elements remained in the linear elastic range, including the piers.

In this model, the degree of isolation provided by the neoprene supports was evaluated, through the analysis of the natural frequencies and mode shapes of the bridge, and subsequently, in the same model, the extent of the supports deformations was evaluated. All this was carried out by first considering a fixed pier base, and then the dynamic interaction between the ground and the structure was introduced by means of springs and dampers at the base.

The response of the structure to an intervention that simulates the common practice of introducing transverse seismic "shear keys" was then studied, using a model in which the supports were also blocked in their shear deformations in the transverse direction, assuming in this case the localized non-linearity at the base of the piers, with the aim to study the ductility requirement at the base of the piers themselves; the deck was assumed to remain in the elastic range even in this model.

2.4.1 Pier modeling

The piers were modeled as beam elements, in accordance with Timoshenko's beam theory, starting with the basic practical steps on the Midas GEN software, which concern the definition of the materials that constitute the shaft and cap beam. Starting from the data on the materials exposed to the paragraph §2.1, the definition of the cross section of the shaft and the realization of the cap beam geometry were carried out. It should be noted that, in this phase, the pier is fixed at the base, therefore the effects of the dynamic soil-structure interaction are so far neglected.

As regards the definition of the pier shaft, the Midas GEN software doesn't provide for the creation of octagonal cross sections such as those in the case at study. It was therefore necessary to use the "Sectional property calculator" tool, which allows to import any geometry from the AutoCAD software and export it in turn to Midas GEN.
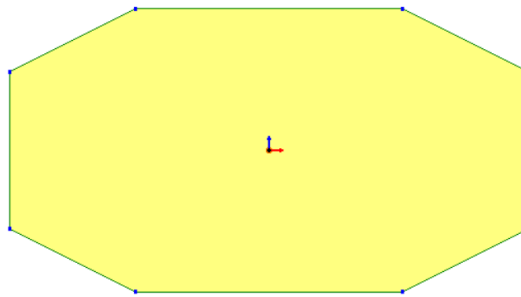
Figure 38 : Pier section in the Sectional property calculator

As regards the cap beam, you can opt for a first modeling option, according to that the cap beam is represented as a tapered beam element, i.e. a beam element with axis parallel to the transverse direction of the bridge, for which a linear section shape variation is required. Following its realization, it is necessary to reproduce the connections with the shaft and with the supports base, with suitable links that allow to reproduce the right kinematic behavior. Anticipating the fact that the supports, whose properties will be discussed in larger depth later, are also modeled as beam elements that connect the upper part of the cap beam to the base of the T-beams, it is possible to observe the representation of the shaft and cap beam with the corresponding connections in the following figure:
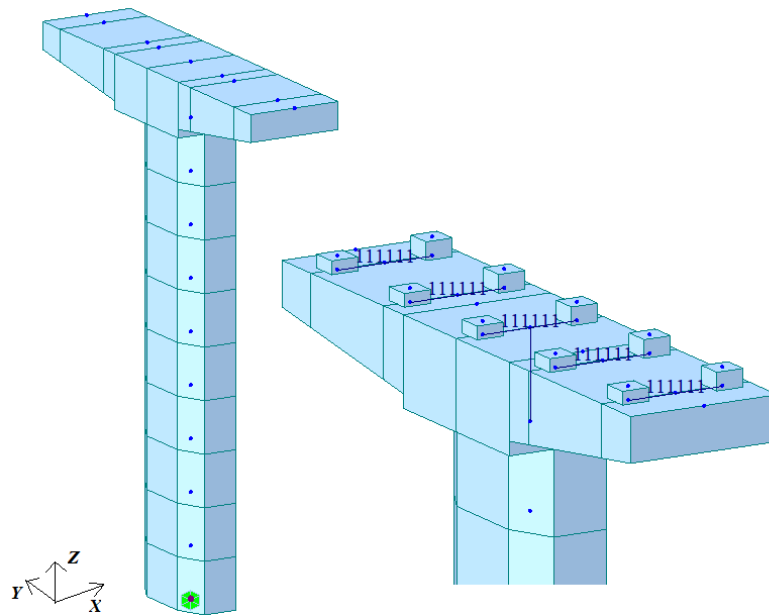
Figure 39 : First option for the cap beam modeling in Midas GEN

As can be seen from the figure above, it was necessary to discretize the element representing the cap beam in such a way that the nodes deriving from its discretization were at the same Y coordinate of the nodes of the base of the supports. As will be seen later, this is functional to the links realization between the cap beam and the supports. The cap beam is in fact connected in a first place to the shaft and to the two central supports with a rigid link that constrains the 6 degrees of freedom. In this way, the nodes at the base of the central supports and the node at the top of the pier shaft will be the slave nodes rigidly linked to the movements of the master node, which is the midspan node of the beam element that models the cap beam. It is also necessary to constrain the rest of the supports to the cap beam, with rigid links between nodes placed at the same Y-coordinate, which connect the slave nodes of the bearings bases to the master nodes constituted by the nodes deriving from the discretization of the cap beam. Even the beam element that reproduces the shaft has been discretized, since in the software, when the self weight is converted into lumped masses, the total mass of the element is directly distributed to the nodal points of an element.

The second option for the cap beam reproduction will be the one used for the analysis on the viaduct, since it is relevant to the real behavior of the cap beam and simplifying for the creation of the links between the shaft and supports. It consists in representing

the cap beam as a rigid body. This is done by concentrating the cap beam mass in its center of gravity and by attributing to the mass its rotational inertias.

The connection with the shaft of the pier and with the bearings bases consists simply of a single rigid link that connects the slave nodes of the supports bases and the node of the top of the pier shaft to the master node located in the center of gravity of the cap beam and therefore in the point in which the mass with rotational inertias was placed. The link is shown in the following figure:
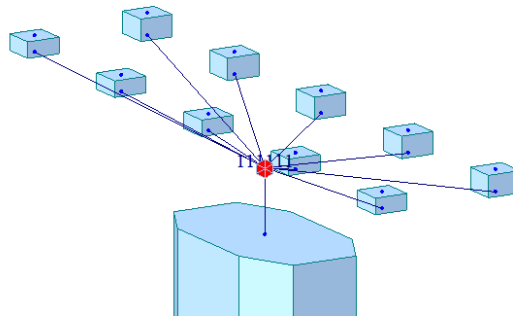
Figure 40 : Second option for the cap beam modeling in Midas GEN

The moments of inertia of the cap beam, considered as a rigid body of volume V, around a generic barycentric axis z, can be expressed through the expression:

$$I_z = \int_V \rho\, r^2 dV \qquad (2.69)$$

obtained by adding the contribution of the material points of volume $\Delta V \rightarrow 0$ of which the rigid body is constituted, located at a distance r from the axis of rotation. If the density of the rigid body ρ is constant as in the case at study, it is possible to calculate the moments of inertia around the three center of gravity axes with the help of the AutoCAD software.
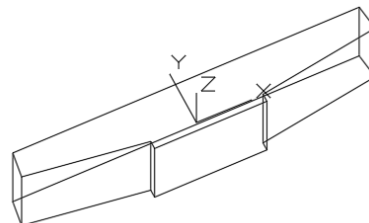
Figure 41 : Cap beam representation with ECS in AutoCAD

In the "solid" space, after having fixed a triad of local axes and having placed the origin of such axes in the center of gravity of the cap beam, it was possible to obtain the moments of inertia with a simple command that reports the properties of the rigid body for a unit density.

Taking into account the cap beam density, the values referred to the global axes of Figure 39 were obtained, shown in the following table:

m	95.2	t
I_x	783.9	$t\,m^2$
I_y	78.1	$t\,m^2$
I_z	830.27	$t\,m^2$

Table 15 : Cap beam mass and moments of inertia

The non-linearities at the base of the pier have been represented, in the models in which their insertion is expected, with the fiber formulation, by means of the indications provided in paragraph §2.2.

At an operational level, the validity of this formulation was investigated using a model which, similarly to that used for the check of the pier reinforcement, is characterized by the concentration of the cap beam and deck mass at the top of the pier itself. This was carried out by attributing directly a nodal mass of $479\ kN/g$ at the pier top, that included the weight of the deck for influence areas and of the cap beam, both subsequently converted into mass. However, in this case the mass of the pier shaft was not concentrated at the top. Rather, its distribution along the height of the shaft was simulated, discretizing the element and automatically attributing, through a software function, the weight to the elements. Subsequently the latter was converted into masses concentrated at the nodes deriving from the discretization. The height considered for this model is therefore equal to the height of the shaft of the highest pier $(H = 16.9\ m)$ in both the transverse and longitudinal directions of the bridge. Also in this model, the pier was considered as fixed at the base. Furthermore, in order to study, in this preliminary phase, the pier response separately in each direction in the horizontal plane, the degree of freedom in the node at the top of the pier, regarding the translation in the direction orthogonal to that of motion, was constrained. This means that, as an

example, in the study of the motion along the Y direction, the node at the top of the pier will not be able to translate in the X direction and vice versa. The eigenvalues analysis leads to an evaluation of the natural frequency for the two models in the X and Y direction of respectively 1.06 Hz and 1.94 Hz. This is consistent to the fact that the pier is more rigid in its flexure in the transverse direction of the viaduct than in the longitudinal one.
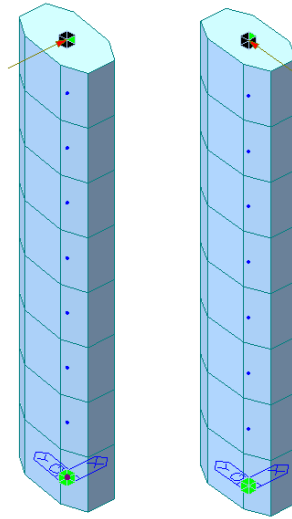
Figure 42 : Pier under sinusoidal loading modeling

Once defined the material, the geometry and the effective mass of the pier model, it was decided to subject the model to a sinusoidal dynamic load to study its response, following a non-linear time history analysis through direct integration, in which the non-linearities were taken into account through a fiber modeling. The sinusoidal force was applied on the base of the definition of the following parameters:

Model with motion along x direction		Model with motion along y direction	
Amplitude	$1000\,kN$	**Amplitude**	$1000\,kN$
Frequency of excitation	$2.12\,Hz$	**Frequency of excitation**	$3.87\,Hz$

Table 16 : Input forcing function parameters

Particular attention was paid to the ratio between the input circular frequency and the natural circular frequency of the pier. The parameter $\beta = {}^{\omega}/_{\omega_1}$ in fact significantly influences the response of the model. In the expression representing the vibrations due

90

to harmonic actions, there is a first term that represents the effect of the initial conditions of motion, which, after a sufficiently long time, tends to become negligible. The so called steady state vibrations described by the second term are hence established in the system. The latter is relevantly linked to the β factor through the amplification factor $N(\beta)$. Subjecting the two models to a sinusoidal action characterized by the same β, chosen equal to 2, rather than by the same input frequency value, seems to be therefore functional to a more immediate comparison between the response of the two models, free from the dependence on the amplification factor.

As regards the definition of the non-linearity, the latter was attributed to the pier base by the definition of the inelastic properties through the fiber model formulation. Firstly the inelastic material properties were defined for confined and unconfined concrete and for steel, as determined in paragraph §2.2.2 of the current thesis. The following step consisted in the fiber distribution definition; the section was discretized by using the three fibers types associated to the constitutive laws of the three sorts of material behavior that compose the section: in particular, assuming a concrete cover of 5 cm, in the figure can be distinguished the unconfined concrete fibers in blue, the confined concrete fibers in yellow, and finally the steel fibers in pink.
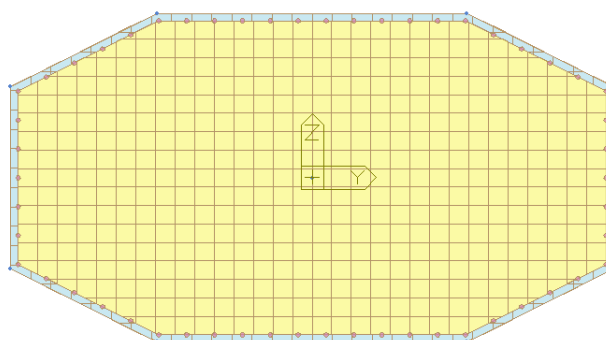
Figure 43 *: Fiber discretization of section*

After having carried out the fiber discretization of the section, the fiber inelastic hinge properties have been assigned to the elements. In this case, being the single pier model not significantly heavy from a computational point of view, they have been attributed to the elements of the whole pier; this will not be done in the model that involves the whole bridge components, as the computational cost would be too high; in this case, as will be seen later, the inelastic properties will be assigned for a certain "plastic

length" from the base of the pier. The trends that represent the evolution of the displacement of the node at the top of the pier for the two models subjected to sinusoidal action are shown below:
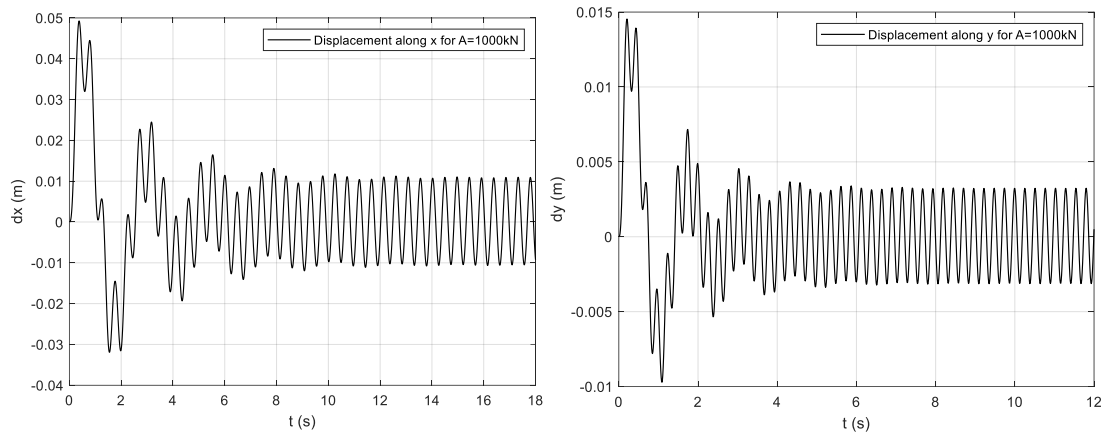
Figure 44 *: Top pier displacement under sinusoidal loading with A=1000kN*

This trend is consistent to what is expected on a theoretical level. After a transition phase, the steady state response is characterized by sinusoidal vibrations, whose amplitude, for the same amplification factor, decreases as stiffness increases. For the stiffer model in the Y direction, the amplitude of the steady state response is smaller than longitudinal one. It may be interesting to investigate what happens to the response as the forcing value increases, that is, when the fibers which compose the section are no longer in the elastic range and the stiffness in no longer constant. Repeating the analysis for a sinusoidal force characterized by $A = 5000\ kN$, the following results were therefore obtained:
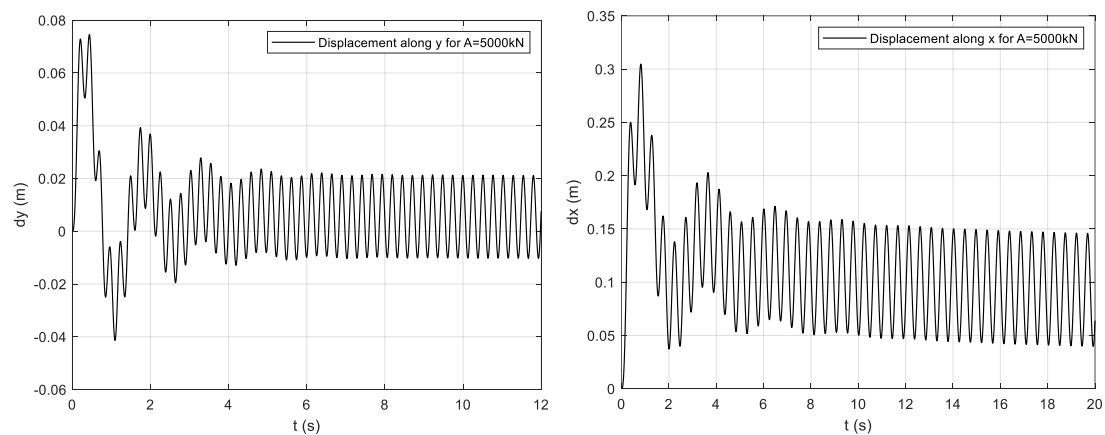
Figure 45 *: Top pier displacement under sinusoidal loading with A=5000kN*

92

It can therefore be observed that the steady state vibrations are no longer oscillations around the abscissa axis, but are characterized by a residual displacement, indicating that the elastic limit has been reached at the sectional level. By analyzing the state of the individual fibers of the section associated to the last time step of the time history analysis, it is in fact evident that, whereas in the previous case all fibers remained in the elastic field both in compression and in tension, with the force of $A = 5000\ kN$ almost all the steel fibers have reached the yielding limit:
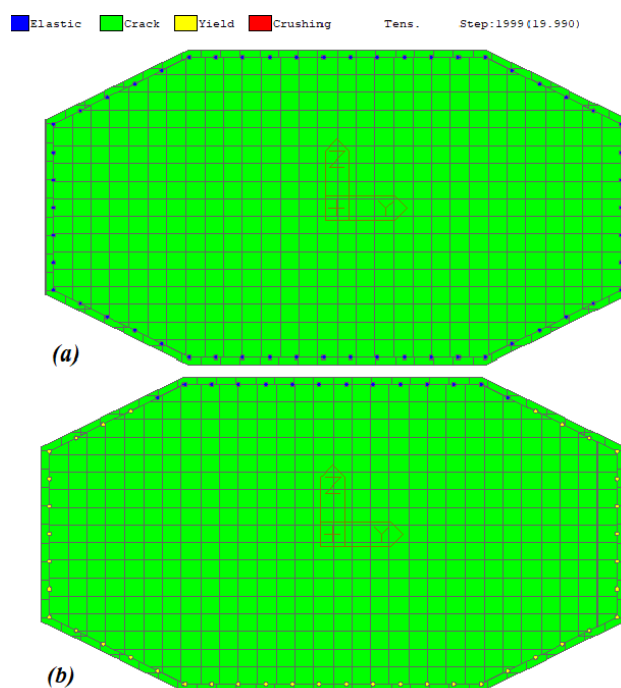
Figure 46 : Tension state of fibers under sinusoidal force with A=1000 kN (a) and A=50000 kN (b)

At this point, once established that fiber modeling gives consistent results and doesn't lead to divergence problems of the iterative procedure, with the aim of taking another step towards predicting the behavior of the pier under seismic action, it was necessary to analyze some important aspects.

A first feature to be taken into consideration is the extent of the section discretization: the shear at the base of the pier was evaluated for discretizations with an increasing degree of refinement, until the percentage error about the variation of the maximum or minimum of the shear history between two successive discretizations was acceptable. In addition, in this case the model was subjected to a dynamic action, represented by

93

group of three artificial accelerogram generated with the SIMQKE software, compatible with the response spectrum defined for the Catania site. Hence a non-linear dynamic analysis was carried out, following the procedure explained in paragraph §2.3.1: after the application of the permanent structural and non structural loads through a time history non-linear static analysis, the dynamic load was applied to the pier model through a non-linear dynamic direct integration time history analysis.

Three accelerograms, being two compatible with the horizontal spectrum and one with the vertical one, were generated at the SLC ultimate limit state, as in accordance with the NTC 2018, it is the limit state associated with the evaluation of the ductility demand, if non-linear models are used. The parameters selected for the accelerograms whose meaning were previously explained in Chapter 1, have been reported in the following table:

a_g/g	0.286
F_0	2.406
T_c^*	0.45 s
TL	4 s
$TRISE$	5 s
$TLVL$	10 s
DUR	25 s
$NCYCLE$	50
$AMOR$	0.05

Table 17 : SLC parameters for the accelerograms in SIMQKE

Another aspect to pay attention to certainly concerns the fact that it cannot be assumed that the stirrups perform the function of confinement, as the piers of the viaduct in question are characterized by non-closed transverse reinforcements. Therefore, at this level of analysis, the section was divided simply into unconfined concrete fibers and steel fibers.

In the model, characterized by a natural period $T = 0.95\ s,$ four discretizations associated with the following numbers of fibers in the longitudinal X and transverse Y direction of the bridge were performed.

Discr	nx	ny	Shear x min	Shear x max	Shear y min	Shear y max	Err% Shearx max	Err% Shearx min	Err% Sheary max	Err% Sheary min
1	13	7	-600.2	632.9	-866.5	1113.1	—	—	—	—
2	18	10	-602.4	639.2	-868.8	1139.9	9.9	3.6	6.1	2.7
3	**23**	**13**	**-603.7**	**640.6**	**-868.9**	**1141.4**	**2.2**	**2.1**	**1.2**	**0.1**
4	27	16	-603.7	640.7	-868.9	1142.3	0.2	0	0.2	0

Table 18 : % Errors in the refinement of the fiber pier distribution

As can be seen from the table above, the step in which a non-negligible percentage error is experienced is that from discretization 1 to discretization 2. In general, however, the errors are not very high, as they reach a maximum of 9.9%. Since increasing the number of fibers considerably increases the computational time, discretization 3 has been chosen for the following models, as it represents a good compromise between percentage error and calculation costs.

The configuration selected is shown below:
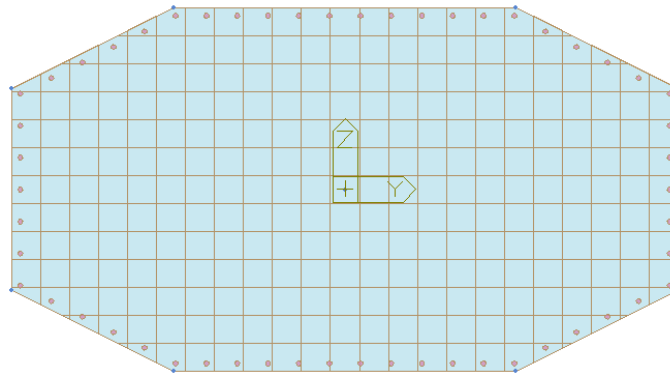
Figure 47 : Fiber discretization selected

2.4.2 Bearings modeling

As mentioned previously, the modeling of the supports significantly influences the bridge response. It was therefore necessary to effectively model their behavior, especially with regard to shear deformations. The viaduct supports are made of neoprene, like most of the bridge bearings which constitutes the national road network built between the end of the 60s and the beginning of the 90s.

They were modeled in the current thesis with beam elements with linear elastic behavior. This means that, in the model, the support can ideally transmit a force of inertia of any intensity to the pier without reaching its failure condition. A check will therefore be required, in order to investigate that the support has not actually reached its limit in terms of deformations. As for the stiffness modeling of the beam element created for each support, it was followed what suggested in [6], where an element with a finite length larger than that of the real support has been used, as in the model it is convenient to disregard the actual vertical dimension of the object.

In particular, in the viaduct under examination, to reproduce the constant slope of the bridge of 3° around the transversal direction, the bearing elements were created with a height of 32 cm and 23 cm. The proportion on the shear stiffness of the i-th finite element that reproduces the support is therefore equal to:

$$(GA)_{FE} = \frac{GA_{base}}{\chi t_{real}} t_{FE} \qquad (2.70)$$

Where:

- G is the shear modulus characterizing the neoprene material;
- A_{base} is the base area of the finite element;
- t_{real} is the real bearing stiffness;
- t_{FE} is the thickness of the finite element;
- χ is the shear factor, assumed equal to 1.2 for rectangular sections.

In the case at study it was therefore chosen to represent a neoprene bearing with a total thickness of $40\ mm$, with a base area of $2.5 x 10^5\ mm^2$ and a shear modulus typical of neoprene equal to $0.9\ MPa$. The horizontal shear stiffness of the actual neoprene support would therefore be equal to:

$$k_{bearing} = \frac{GA_{base}}{\chi t_{real}} = 4687.5 \frac{kN}{m} \qquad (2.71)$$

Proceeding according to this criterion, in order to define the overall horizontal stiffness of the supports exclusively by the equivalent shear behavior, it is necessary to impose a fictitious value to the flexural stiffness of the element, so that it is infinitely flexurally stiff $(EJ \rightarrow \infty)$. As regards the vertical element stiffness, although of secondary

importance for the seismic response of the structure, it was also considered almost infinite ($EA \rightarrow \infty$) as the neoprene bearings are usually not very compressible, since characterized by high axial stiffness. Finally, to simulate the support condition between the beam and the neoprene devices, it was necessary to introduce a beam end release regarding the rotations around the three axes in the upper node of the support.

$(GA)_{FE}$

$(EJ)_{FE} \rightarrow \infty$

$(EA)_{FE} \rightarrow \infty$
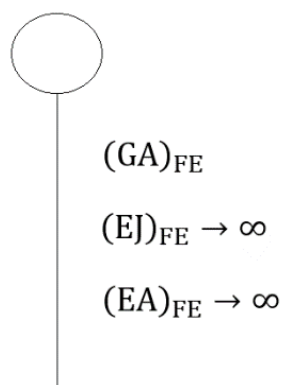
Figure 48 : Bearing FE schematization

At the operational level, the characteristics of the neoprene material were initially attributed to the support elements, namely:

Weight density	$15 \ kN/m^3$
Poisson's ratio v	0.49
Modulus of elasticity E	$2.682 \ x \ 10^3 \ kN/m^2$

Table 19 : Material properties of neoprene

The elastic modulus E was chosen starting from the value of $G = 0.9 \ MPa$, considering the relationship for isotropic material $E = 2G(1 + v)$. Once the material properties were attributed to the elements, scale factors were given to their axial flexural, torsional and shear stiffness. Having in fact realized the elements with a thickness larger than the real one, the shear stiffness requires a majorative scale factor equal to the ratio between the length of the finite element and the real thickness of the support t_{FE}/t_{real}, which is equal to 5,8 and 8 respectively for the supports 23 and 32 cm thick. As for the axial, torsional and flexural stiffness, very large values have been associated to them. The software attributes the scale factors simply through the "section stiffness scale factor" command. Thus the two types of bearings were

97

categorized into your different "section properties", although they have the same cross section; in this way it was possible to attribute different scale factors to them.

Scale Factor		Scale Factor	
Area	1000000000	Area	1000000000
Asy	5.8	Asy	8
Asz	5.8	Asz	8
Ixx	1000000000	Ixx	1000000000
Iyy	1000000000	Iyy	1000000000
Izz	1000000000	Izz	1000000000
Weight	1	Weight	1

Table 20 : Scale factor for the 32 cm bearing (right) and 23 cm bearing (left)

In a subsequent model, in which the presence of transverse seismic restraints will be simulated, the same factor attributed to inertias will also be attributed to the shear area concerning the transverse shear deformations.
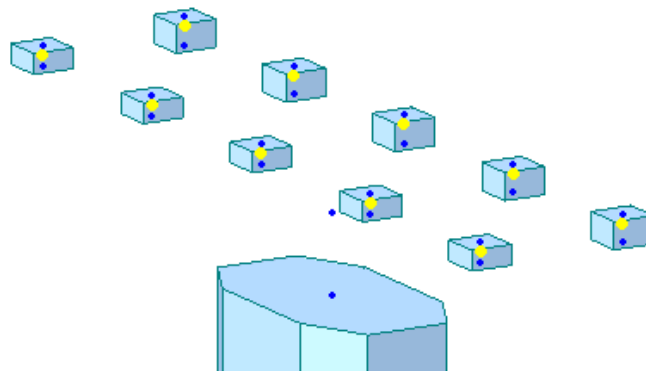
Figure 49 : Beam end releases (in yellow) for the neoprene bearings

In correspondence of the abutments, the bearings have been modeled in a similar way to those placed to support the piers. The only difference is that the lower node of the support has been fixed in this case. The constraint in this node has not been modeled as a support because anyway there is the deformability of the support and the beam end release in its upper node.

As regards the checks on the bearings, in accordance with [6] it was decided to set a limit to the shear strain, considering as limit a unit shear deformation:

$$\varepsilon_{shear} = \frac{F_{shear}}{GA_{base}} \leq 1 \qquad (2.72)$$

This expression can be reordered in terms of tangential stresses; considering that the ratio between the horizontal force F_{shear} and the support footprint represent the tangential stress τ_h, the previous expression takes the form:

$$\tau_h \leq G \qquad (2.73)$$

It is also necessary to check that problems don't actually occur in the contact between the beam and the bearing, in particular with regard to the friction phenomena between the neoprene and the concrete that constitutes the deck beam. Considering the friction coefficients between these two materials evaluated as included in the interval $0.6 \leq \mu \leq 0.8$, the expression (2.73) can be rewritten as:

$$\tau_h \leq \mu\sigma_v \qquad (2.74)$$

In which for the Italian works the compression stress σ_v is between 2 and 3 MPa. Taking the most conservative values for the right-hand term of the inequality and considering a shear modulus G equal to 0.9 MPa, the check to be carried out takes the following form:

$$\tau_h \leq \alpha G \qquad (2.75)$$

With the coefficient α equal to 1.33. As will be seen later, this methodology will provide bearing capacity limits less conservative than those obtained through (2.72). On the other hand, in the event that material degradation conditions subsists, the selected limits must be reviewed with appropriate corrective coefficients. Not having, through the technical report, appropriate information about the current state of the neoprene material that constitutes the bearings, it was chosen as a precaution to opt for a limit deformation of the support equal to 75% instead of 100%.

2.4.3 Deck modeling

Mainly there are two types of deck modeling, the first consists in the use of beam elements for the slab and beams, while in the second option, typical of mixed steel-concrete deck bridges, the slab is made through plate-type elements. The difference between the two element types was previously introduced at the beginning of the current chapter. The first option is considerably less expensive at a computational level, since it leads to a significantly smaller number of degrees of freedom, although it requires more work to reproduce the stiffness of the deck in the horizontal and vertical plane in the best possible form. The second one, on the other hand, requires particular attention in the creation of the mesh; in fact, the degree of refinement of the latter influences the natural frequencies, as well as the stress components in the deck and the internal forces in the structural components of the bridge.

The type of modeling which reproduces the deck through both beams and plate elements provides the following scheme:
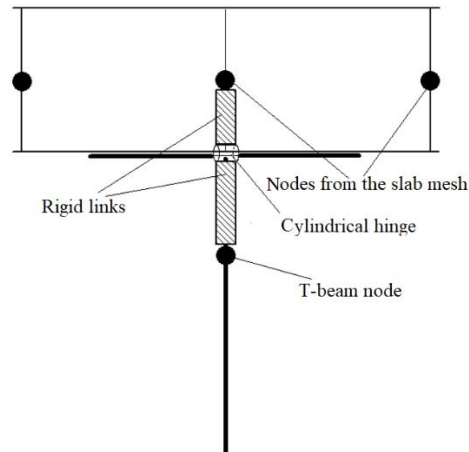
Figure 50 : Scheme for the shell deck modeling

As can be seen from the figure above, in each of the 5 beam elements representing the T-beams, the connection with the slab is made with suitable links. The first connection joins the node placed in the center of gravity of the beam to the upper edge of the beam itself. At the level of the upper edge of the beam, in order to recreate the situation where no moments around the transversal direction are transmitted between the slab and the beam, the rotations around the Y axis have been released. This node was then

connected to the node in the middle plane of the slab by means of a rigid link. Finally, although it has not been represented in the diagram in Figure 50, there is a connection for which the node in the center of gravity of the beam and the upper node of the element representing the bearing have been rigidly connected. Finally, the cross girders, in the end and in midspan of the deck, were modeled using beam elements that connected the nodes of the beam centers of gravity, with an offset attributed to their cross section so that their upper edge coincided with the upper edge of the T-beams.

The scheme described was applied within the code, up to the following representation of the deck, in which the elements of the cross girders were inactivated to ensure a better view of the connections between the elements:
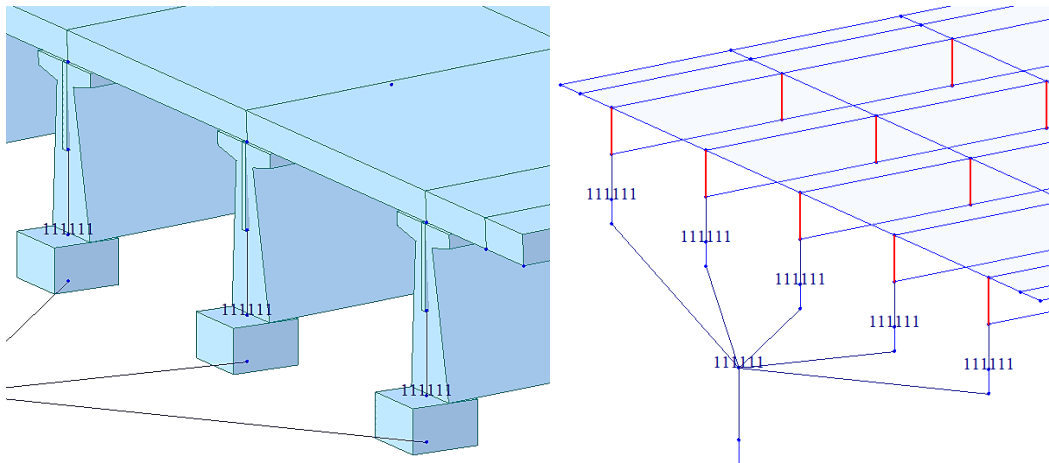
Figure 51 : Connections between deck components

With reference to the single beam, the slave node in the upper edge of the supports was rigidly connected to the master node of the beam center of gravity through the "Rigid link" function; in order to constrain the upper beam edge to the center of gravity of the beam itself, it was necessary to interpose a rigid link by creating an element of zero mass, characterized by a very high elastic modulus defined in the properties of the material. To reproduce the cylindrical hinge, the bending moment around the Y axis of the upper node of this element has been released. Finally, in order to avoid the creation of a new node in the upper edge of the beam to be constrained to the node in the middle plane of the slab, an offset has simply been attributed to the slab thickness;

101

this produces the same effect of a rigid link between the node at the upper end of the rigid element and the middle plane of the slab.

Finally, the beam elements have been discretized in their development along the longitudinal axis of the bridge. In each node deriving from this discretization, the rigid link described above was placed between the center of gravity and the upper edge of the beam, with associated beam end release of the upper node of the element itself. As regards the loads, the self-weight was automatically assigned and converted into lumped masses. The permanent non structural loads were instead attributed to the slab as a surface load of $2.5\ kN/m^2$ and $8.75\ kN/m^2$ in the areas where the sidewalk is also present, later also converted into lumped masses.

At this point, having defined the modeling strategies of the various structural components, it is possible to carry out an eigenvalue analysis in order to derive the natural frequencies and periods of the structure, with the aim of identifying the appropriate degree of refinement of the mesh. Starting from the model fixed at the base with the bearings modeled as indicated in Table 20, the initial discretization, which is not characterized by any node between the center distance of the beams, has been progressively increased.
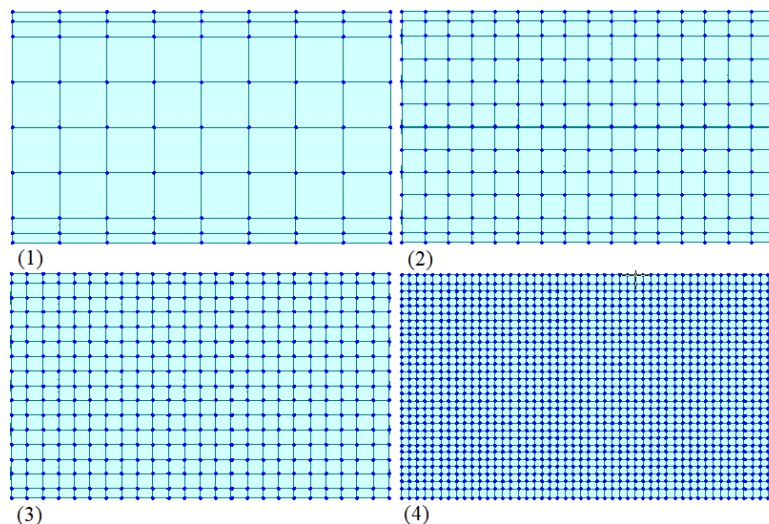
Figure 52 : Slab mesh options

In the errors calculation in terms of frequencies, in the passage from a discretization to the subsequent one, the following results were obtained for the first modes along the X, Y and Z directions:

Discr	Mode X	Mode Y	Mode Z	Err% X	Err% Y	Err% Z
1	1.01 Hz	1.26 Hz	5.25 Hz	—	—	—
2	1.02 Hz	1.22 Hz	5.29 Hz	0.99	3.17	0.76
3	**1.04 Hz**	**1.18 Hz**	**5.31 Hz**	**1.96**	**3.28**	**0.36**
4	1.07 Hz	1.04 Hz	5.32 Hz	2.88	11.86	0.21

Table 21 : Percentage error in the refinement of the slab mesh

As it can be seen from the values in the table, a monotonous decrease is not present in the percentage errors of the mesh. This is attributable to the fact that, in the refining of the mesh, the increase of the slab nodes is associated with a denser discretization of the T-beams in the longitudinal direction, with an increase in the number of rigid links with which the center of gravity of the beams is connected to the slab. This results in a change in the stiffness of the model, which therefore leads to a change in the system natural frequencies. Paying particular attention to the way in which the most significant deformations of the slab occur, which is mode 50, there is in this case the desired effect of gradually decreasing the percentage error with the increasing of the mesh. In particular, it can be observed that this error is small, equal to 0.36%, even in the passage from discretization 2 to discretization 3. Furthermore, the discretization model 4 was very heavy from the computational point of view, as it is characterized by a very high number of degrees of freedom, although it leads to a smaller percentage error for the Z direction, equal to 0.21%. However, the discretization 3 was chosen, as it reconciled a low computational cost and a small percentage error.

Another aspect that was taken into consideration when choosing the mesh, was the analysis of the internal forces in the piers and supports and acceptable errors were found in the transition between discretizations 2 and 3. In fact, the analysis of the error on the natural frequencies, although it is a more intuitive and faster approach, is not sufficient to identify the most appropriate discretization. It was decided to analyze the internal forces in the piers and supports as an alternative to the very long procedure of investigating the stress components in certain critical points of the deck. It may be interesting to analyze the trend of the bending moment around Y for the central beam belonging to the fifth span, for the mesh 3, under the combination of permanent structural and non-structural loads:
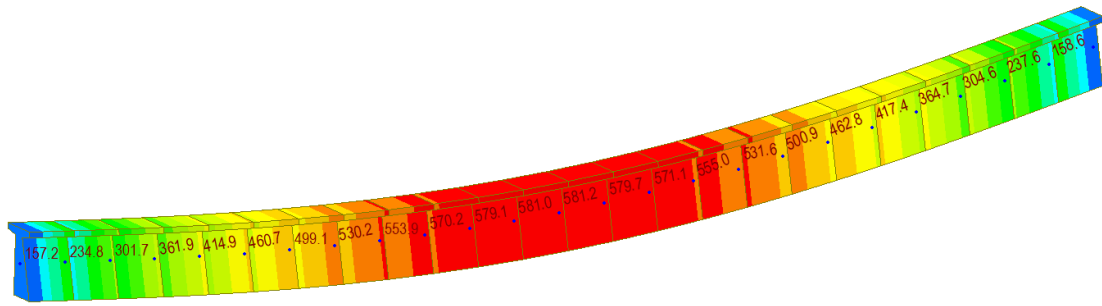
Figure 53 : My in the deck T-beam under gravitational loads for discretization 3

The occurrence of a bending moment also at the end of the beam, although the beam is supported, can be noticed; this state of stress is to be attributed to the presence of the lower extremity of the rigid link in the node of the beam center of gravity. In the analysis of the diagram of the bending moment M_y for the discretizations 1 and 3, it can be highlighted how the increasing of the mesh leads to a smaller jump of the moment between the elements in which the beam is discretized, with a more continuous trend for a higher level of mesh refinement:
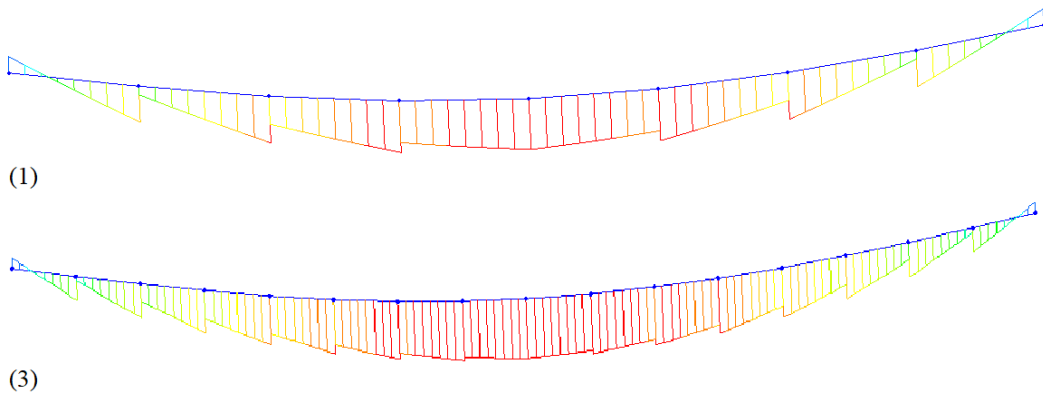
Figure 54 : My diagram for a T-beam in the discretization 1 and 3

Since the structural components have been defined and the discretization of the slab has been determined, the model can be used for dynamic analysis.

It is composed of bearings free to have shear deformation in both the longitudinal and transversal directions; therefore, as previously mentioned at the beginning of §2.4, it is probable that the problem linked to the bearings deformation is confirmed and that they can't transmit the inertia forces at the pier base. Consequently, the choice not to model the non-linearities at the base of the pier and therefore to consider a non dissipative behavior also for the pier, leads to linear dynamic analysis, which are

104

compatible with the choice of considering a shell-beam deck, to which higher computational costs are associated. This model will for now on be called Model 1.
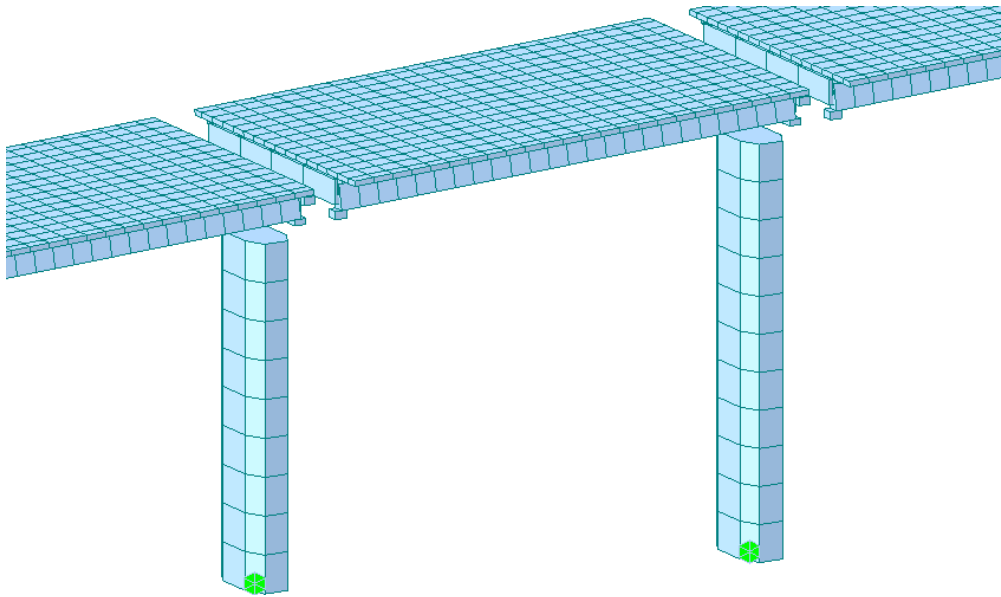
Figure 55 : View of a bridge span of Model 1

For the model, the mode shapes are reported, for the first modes associated to a significant effective mass in the X, Y, Z directions. The modal analysis leads to the following frequencies for the first 12 modes, and for the first mode with significant effective mass in the vertical direction Z:

Mode	Direction	f (Hz)	T (s)
1	X	1.04	0.97
2	Y	1.18	0.85
3	X	1.26	0.80
4	RZ	1.31	0.77
5	X	1.42	0.71
6	Y	1.43	0.70
7	RZ	1.50	0.67
8	X	1.53	0.65
9	Y	1.56	0.64
10	Y	1.60	0.63
11	X	1.62	0.62
12	Y	1.64	0.61
50	Z	5.31	0.19

Table 22 : Natural frequencies for Model 1

The first mode with a significant effective mass is the 50th, with an associated effective mass of 16%. In order to reach the 90% prescribed by the current standards, the 161-th mode must be reached as regards the X and Y directions; 90% of the effective mass along Z is instead reached for the 464-th mode.

Mode 1
f = 1.04 Hz

Mode 2
f = 1.18 Hz

Mode 50
f = 5.31 Hz
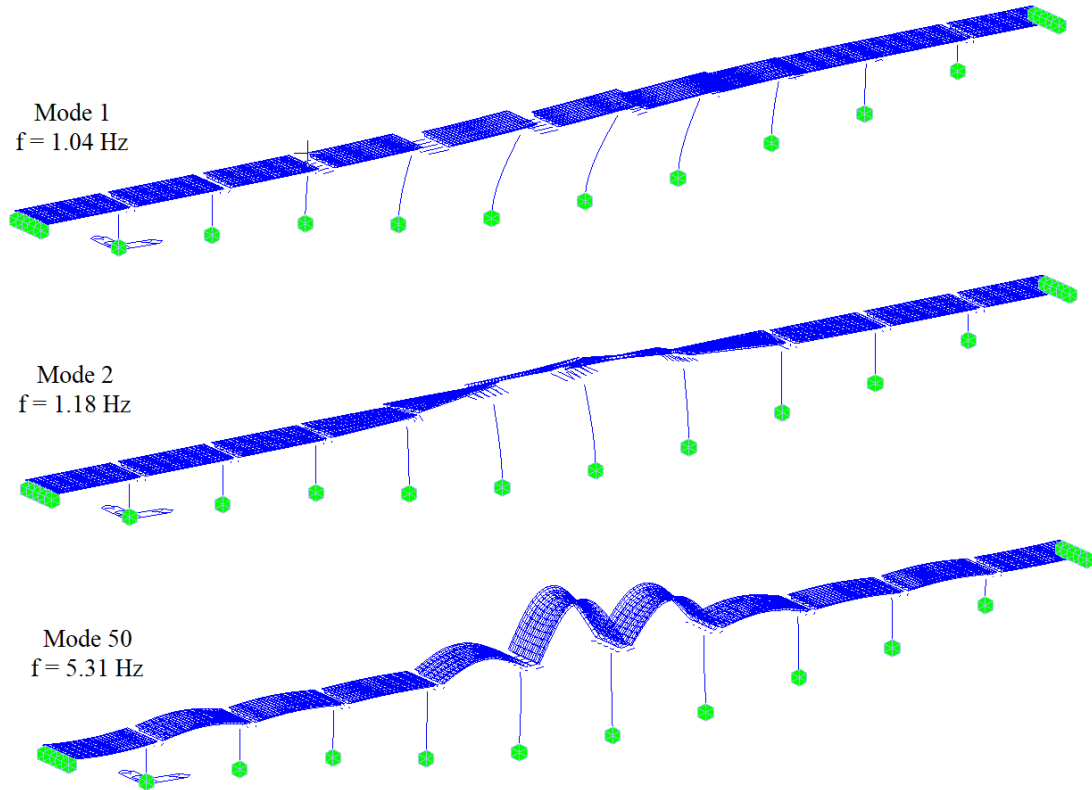
Figure 56 : *Vibration Mode shapes of Model 1*

From the modal shapes it is possible to observe that the bearings doesn't completely perform the function of isolating the superstructure from the substructure. This can be deduced from the fact that in the vibration mode shapes there is an inflection of the piers, although the high shear deformability of the supports has ensured the increase in the natural periods of the structure.

In order to carry out non-linear dynamic analysis, associated with a high computational cost, it is necessary to adopt measures to reduce the degrees of freedom of the model which could consequently allow a decrease in the computation time. This can be done by creating a grillage deck consisting exclusively of beam elements. This type of modeling requires that the stiffness in the horizontal plane is modeled mainly by means

of a single beam, having the properties of the entire slab, while the torsional and vertical stiffness are almost entirely attributed to the T beams elements, connected by the cross girders. A strategy that greatly simplifies the kinematic behavior without significantly changing the structural response, consists in placing the center of gravity of the T-beams and the mean plane of the element representing the slab at the same height. In this way, the coordinates of the center of gravity of the slab and the center lines of the beams are aligned:
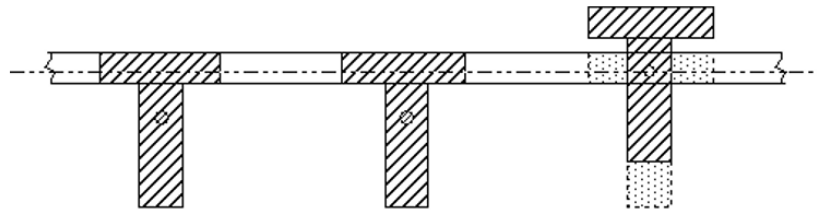
Figure 57 : Scheme for the beam grillage of the deck

The deck is therefore composed of the following components:

- A single beam characterized by a cross section with height equal to the height of the slab and width equal to the width of the entire slab in the Y direction;
- 5 T-beams;
- 3 cross girders for each span, two at the extremities and one at midspan;
- Transversal "slab strips" with axis parallel to Y direction.

The longitudinal element of the slab is then created, discretized following the same discretization of the T-beams in the longitudinal direction; the end nodes of each slab element coincide with the center of gravity node of the central T-beam.
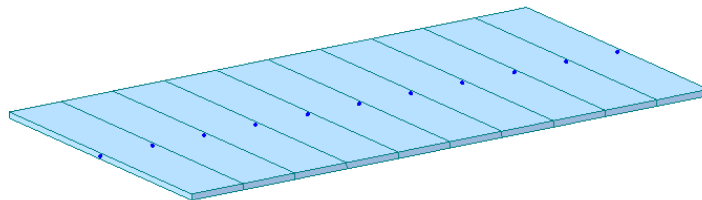
Figure 58 : Longitudinal slab for beam grillage

As for the T-beams, their cross-section was defined by directly comprising the collaborating slab. Since if a width initially equal to 10 times the thickness of the slab is considered a dimension of 2.2 m is given, it was chosen to approximate it in a

107

preliminary way to the entire spacing between the beams of 2.4 m, and 2.5 m for the edge beams. Subsequently, analyzing the natural frequencies of the "vertical" modes of the model, for which the slab deformation is more relevant, and comparing them with those of the model with shell slab, it was concluded that there was no need for a new calibration of its width, as the errors between the two models were very small. Similarly to what was carried out for the octagonal cross section of the pier, the following cross sections were imported into Midas GEN after their definition in the "Sectional property calculator" tool:
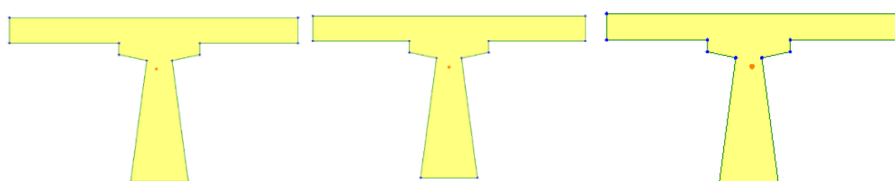
Figure 59 : Cross section of the T beams in the beam grillage

As regards the edge beams, in order not to overlap the widths of the collaborating slab, an offset was attributed to their cross section, as the insertion of the collaborating slab in the cross section of the T-beams led to the displacement of the Y coordinate of the center of gravity of those on board. Furthermore, a zero scale factor has been attributed to the weight of the longitudinal slab element, so as not to calculate it twice, as it is also present in the section of the T-beams; a scale factor was also applied to the T beams area, in order to take into account only the area under the slab for the horizontal stiffness.

The T-beams were then constrained to the slab longitudinal element only for the motion in the plane of the slab. The result at a kinematic level consists of T-beams which are free with respect to the slab element in their vertical displacements and in the two rotations around the horizontal axes, but which are constrained to the slab in the XY plane. In this way the section remains undeformed only in motions in the horizontal plane.

This is carried out with a rigid link that rigidly connects the translations in the X and Y direction and the rotations around the Z axis of the slave nodes consisting of the center of gravity of the beam elements to the master node which is the node of the longitudinal element of the slab. This rigid link is applied at each X coordinate in

which the longitudinal slab elements are discretized. The constraints are shown in the following figure, where the cross girders have been inactivated in order to assure a better visualization:
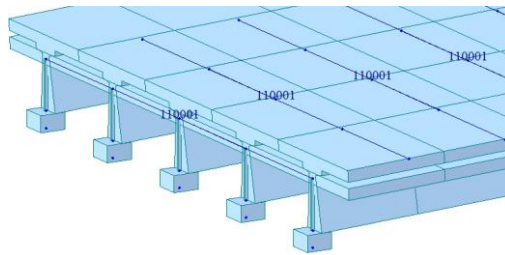
Figure 60 : Link between T-beams and slab in the beam grillage

To ensure that the beams are like hinges in the horizontal plane, and therefore act only in the vertical plane, there is the possibility to alternatively act on the inertia value of or on releasing the bending moment forces in the horizontal plane through the function "beam end release". In this case, the first option was chosen, attributing a zero scale factor to the inertia of the T-beams associated with the bending in the horizontal plane.

In the vertical plane, the stiffness is instead mainly given by the presence of the T beams with their collaborating slab. The slab, on the other hand, contributes to the vertical stiffness in the transverse direction through "slab strips", transverse elements joining the nodes of the T-beams and with a cross section having a height equal to the thickness of the slab and a width equal to the center distance between the nodes from the discretization of the T beams. Even to these elements was given a zero scale factor to the weight, which is counted exclusively through the collaborating slab of the T beams. In the end sections and in the midspan, there is the contribution of the cross girders to the vertical stiffness, therefore these transversal slab elements have not been placed.
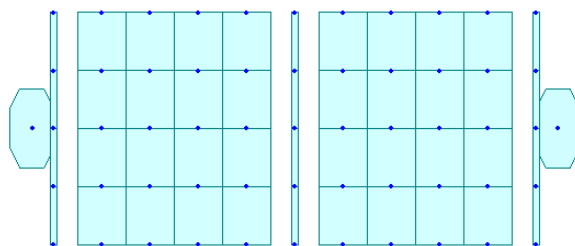
Figure 61 : Top view of the transverse girders and of the transversal slab strips in a span

To ensure that these strips of slab act as connecting rods in the horizontal plane, also in this case was chosen to act on the inertia, annulling that associated with the flexure in the horizontal plane. This choice was also made with regard to the longitudinal element of the slab, for which a null value was instead attributed to the inertia associated with the bending in the vertical plane.

Finally, the center of gravity of the T-beams was constrained to the upper node of the support through a beam element of zero mass and very high elastic modulus. The loads were attributed in the same way as in Model 1 and subsequently converted into masses. The only difference lies in the fact that the permanent non-structural loads were assigned as element loads distributed on the beams, differently from Model 1 in which they were attributed as surface loads on the slab. What is obtained for a generic Model 2 deck is shown in the following figure:
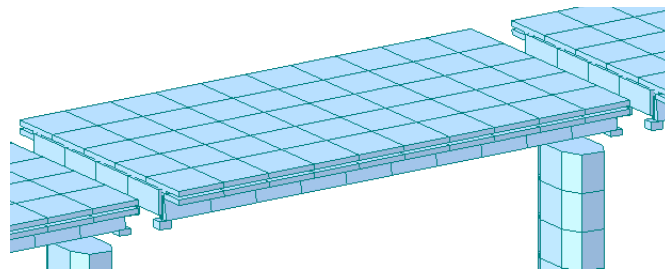
Figure 62 : View of a bridge span modelled with beam grillage

A comparison with the frequencies of the shell model is appropriate, as it allows us to understand if the grillage deck captures the behavior and stiffness in the horizontal and vertical planes. In particular, the comparison will be made between a model with a shell slab and a model with a beam grillage deck, both considering the bearings as free to undergo shear deformations exclusively in the longitudinal direction. This is because the beam deck will be used when non-linear dynamic analysis will be carried out, in a model characterized by the simulation of the presence of transverse seismic restraints, represented through the binding of the support shear deformations in the transversal direction. The model with beam grillage deck and the bearings transversely "blocked" will be called from now on Model 2. The comparison between the natural frequencies of the first modes along X, Y and Z between the latter and a model

characterized by shell slab and the same supports leads to the following results in terms of percentage errors:

Direction	Mode Shell	f Shell (Hz)	Mass% Shell	Mode Beam	f Beam (Hz)	Mass% Beam	Err% f
X	1	1.03	39.7	1	0.99	40.3	**3.88**
Y	6	1.63	27.5	7	1.70	27.9	**4.29**
Z	30	5.31	15.9	29	5.38	15.9	**1.32**

Table 23 *: Percentage errors between shell and beam grillage models*

As can be seen from the table above, the percentage error regarding the first mode for which there is a significant effective mass along Z, which is the mode direction in which the slab is more deformed, is acceptable and equal to 1.32%; in the in plane directions, although larger, the errors are still acceptable. In particular, as regards the longitudinal direction, the shell model is more rigid, while in the transverse one, the beam model is characterized by a higher frequency.

The modal shapes of Model 2 for the first modes with significant effective mass in the three directions are presented in the following figure:

Mode 1
f = 0.99 Hz

Mode 7
f = 1.70 Hz

Mode 29
f = 5.38 Hz
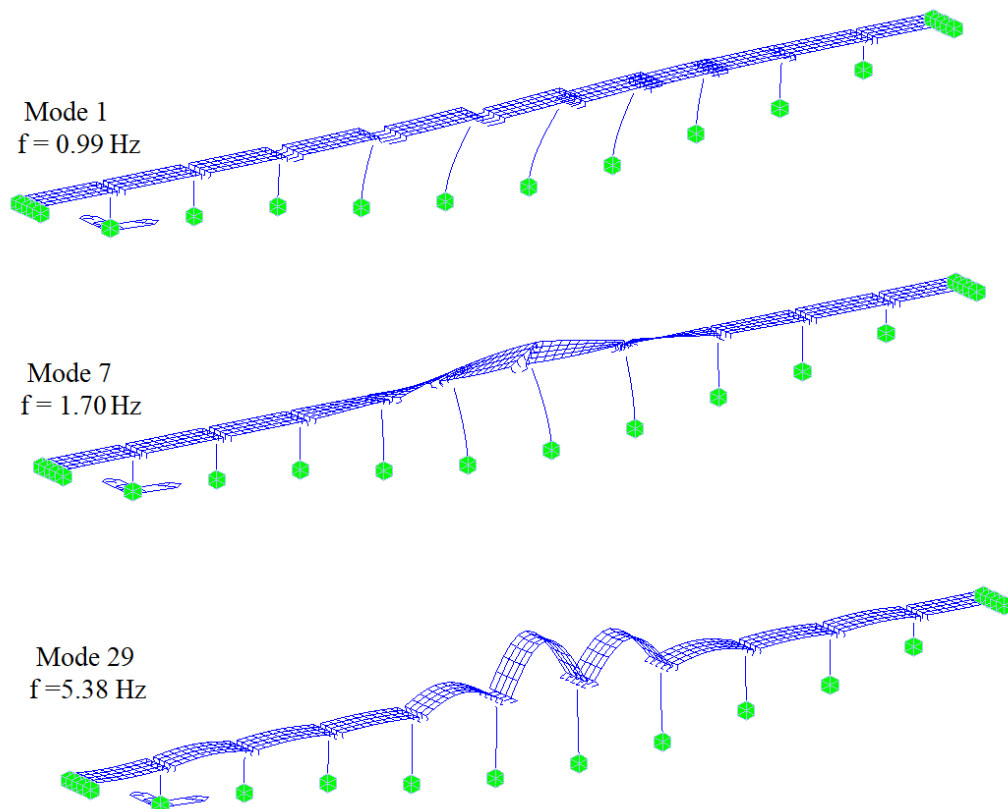
Figure 63 *: Vibration mode shapes for Model 2*

2.5 Dynamic soil-structure interaction modeling

The various types of foundations, such as direct and on piles, represent the typical mean of force transmission from the structure to the ground. In all typologies it is assumed that the seismic motion comes from deep layers with vertical propagation direction, and therefore it is assumed to be characterized by shear waves. The motion u_{gz} at the generic depth z, is called free field motion at the coordinate $z = 0$ in the absence of structure and indicated as u_g.

Considering the effects of the presence of the structure, results in a modification of the free-field motion, with a different motion associated with the interface between the ground and the structure, with the presence of deformations locally induced by the forces of inertia transmitted by the structure, that is what is called inertial interaction. The effect of changing the free-field motion due to inertial interaction is represented by a translation u_f and a ϑ_f rotation of the foundation, represented in the following figure for direct foundations:
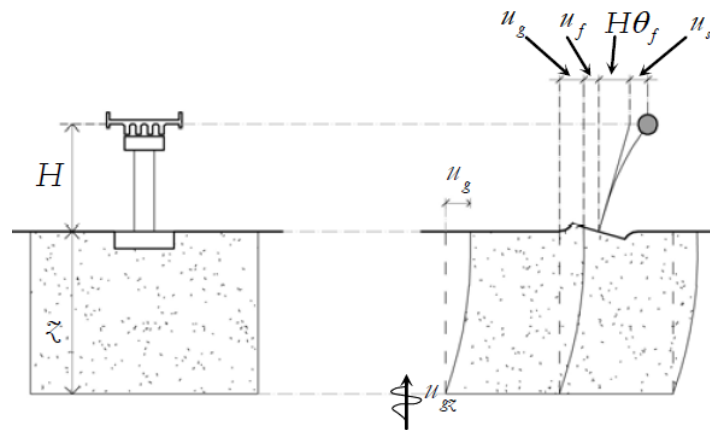
Figure 64 : Dynamic soil-structure interaction in surface footings

The other aspect of the phenomenon is commonly referred to as kinematic interaction, which is normally neglected in the case of direct foundations, if small in size. In the case of foundations on piles, the phenomenon of kinematic interaction is instead clearly evident, as the piles immersed in the ground are involved in its deformation, opposing to it and modifying it locally, depending on the relationship between the stiffness of the pile and of the ground. The actions on the piles will therefore be the

sum of the kinematic effect associated with the deformation of the ground and the inertial effect, associated with the forces transmitted by the structure. As for the structure, its motion will be a consequence of the inertial interaction and of the alteration of the motion due to the modification of the wave field, due to the presence of the piles. The dynamic soil-structure interaction for this type of foundations, in which both the kinematic and dynamic aspects are present, is represented in the following figure:
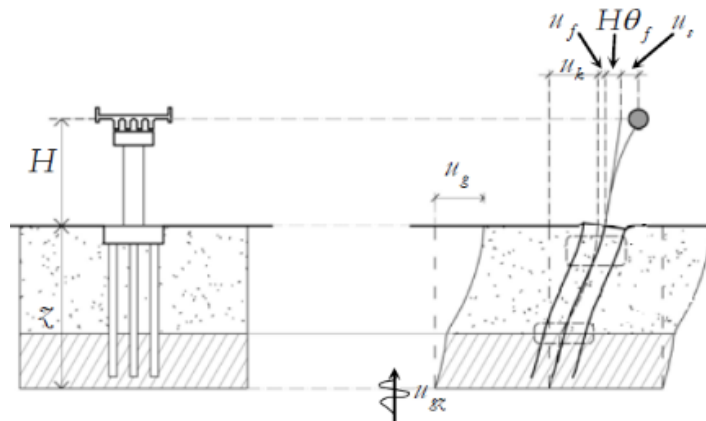
Figure 65 : Dynamic soil-structure interaction in footings with piles

As mentioned in paragraph §2.1, the foundations of the viaduct in question are of the direct type; therefore the modeling of the dynamic interaction will consist exclusively in the modeling of the inertial interaction, through the impedance functions.

2.5.1 Definition of the impedance functions

An introduction to the concept of impedance functions is a prerequisite for understanding the modeling of inertial interaction. Given a system subjected to an harmonic excitation $P(t)$, with a resulting displacement $u(t)$, the impedance function can be defined as the ratio between the load $P(t)$ and the response $u(t)$. It is a complex function, since the two terms of the ratio are not in phase, due to the presence of radiation and material damping in the system for all modes. The expression of the impedance function can be derived starting from a single degree of freedom system characterized by mass m, a spring with stiffness k and damping with coefficient c. Its impedance is expressed as:

$$\overline{K} = \frac{P(t)}{u(t)} = (k - m\omega^2) + i\,c\,\omega \qquad (2.76)$$

Since in the expression (2.76) can be noted the dependence on the frequency, the expression can be rewritten highlighting this dependence [21]:

$$\overline{K}(\omega) = k_1(\omega) + i\,k_2(\omega) \qquad (2.77)$$

Where

- $k_1 = k - m\omega^2$ or $k_1 = k$ if a massless system is considered;
- $k_2 = c\,\omega$.

In both cases of massless SDOF system and SDOF system with mass m, the imaginary part of the impedance function is proportional to the frequency. The real component, named "dynamic stiffness" is instead rendered dependent on the frequency by means of the inertial effect of the mass: its dependence on ω is attributed to the influence that the latter has on inertia, since soil properties are practically independent from frequency. The imaginary component, on the other hand, reflects the radiation and material damping generated in the system, coming from the energy carried by waves spreading away from foundation and energy dissipated in the soil by hysteretic action.

Focusing now on footings having three axis of symmetry, two in the vertical plane and one in the horizontal plane, it was taken a triad of axes, X and Y in the horizontal plane and Z in the vertical plane. The footing considered is characterized by 6 degrees of freedom:

- A vertical displacement along the Z axis u_v;
- Two sliding displacements along the X and Y directions u_{hx} and u_{hy};
- A rotation about the Z axis ϑ_t;
- Two rocking rotations about the X and Y axes ϑ_{ry} and ϑ_{rx}.

where the vertical displacement and torsion are uncoupled, whereas there is a coupling between the horizontal displacements along X and the rocking movements around the Y axis, and between the displacements along Y and the rocking movements around the X axis. For harmonic excitations with circular frequency ω, following the analogy

114

with the expression for a massless single degree of freedom system, the impedance of the reactions at the base of the footing is linked to the displacements by:

$$\{R\} = [\overline{K}]\{u_b\} \tag{2.78}$$

where $[\overline{K}]$ represents the impedance matrix and $\{u_b\}$ is the displacement vector of the geometric center of the footing base [21]. The impedance matrix $[\overline{K}]$ is expressed as:

$$[\overline{K}] = \begin{bmatrix} \overline{K}_v & 0 & 0 & 0 & 0 & 0 \\ 0 & \overline{K}_{hx} & 0 & \overline{K}_{hxry} & 0 & 0 \\ 0 & 0 & \overline{K}_{hy} & 0 & \overline{K}_{hyrx} & 0 \\ 0 & \overline{K}_{hxry} & 0 & \overline{K}_{ry} & 0 & 0 \\ 0 & 0 & \overline{K}_{hyrx} & 0 & \overline{K}_{rx} & 0 \\ 0 & 0 & 0 & 0 & 0 & \overline{K}_v \end{bmatrix} \tag{2.79}$$

Where each of the terms is a complex function as in the single degree of freedom system. The terms out of the main diagonal represents the coupled horizontal displacements-rocking, that turned out to be generally negligible in the superficial footings modeling for the usual values of soil Poisson's ratio. The dynamic soil-structure interaction will be hence modeled in this case through three translational springs, three rotational springs and six dashpots located at the foundation base. In the case of time domain analysis, as in the case at study, the impedance cannot be a frequency dependent parameter and it will be necessary to evaluate it for a precise ω value that is nevertheless significant for the structural response. The procedure adopted for the computation of the frequency used for the calculation of the impedance will be explained in detail below.

Gazetas et al. in [22] give a complete set of algebraic formulas and dimensionless charts to compute the dynamic stiffnesses and damping coefficients of foundations harmonically oscillating on a homogeneous half-space, both for surface and embedded foundations. In the current work was chosen to compute the impedance functions following the procedure given for the first option; indeed the report of the Sordo Viaduct expressly states that the foundations are of the direct type.

Moreover the only information regarding the soil concerns the subsoil category B for the entire development of the viaduct. Therefore, in the current work, the impedance functions have been evaluated in the two extreme values of the range that characterizes this category of subsoil, in order to evaluate the difference in the effects on displacements and stresses due to the soil deformability variation.

2.5.2 Impedance functions computation

The computation of the impedance functions was carried out for the surface footing under examination, characterized by the base geometrical dimensions of 10.5 m along the transversal viaduct direction and 7.5 m along the longitudinal one.

The formulas and dimensionless charts are given in the paper [22] for a generic shape circumscribed rectangle of width 2B and length 2L, with L > B, since the results are not significantly sensitive to the exact circumscribed rectangle; a fortiori they will be valid for a rectangular shape such as that of the case at study. In the computations of the impedances, a new reference frame will be introduced, with origin in the center of gravity of the foundation base, where the x axis coincides with the Y global axis and the y axis is parallel to the X longitudinal axis of the viaduct.
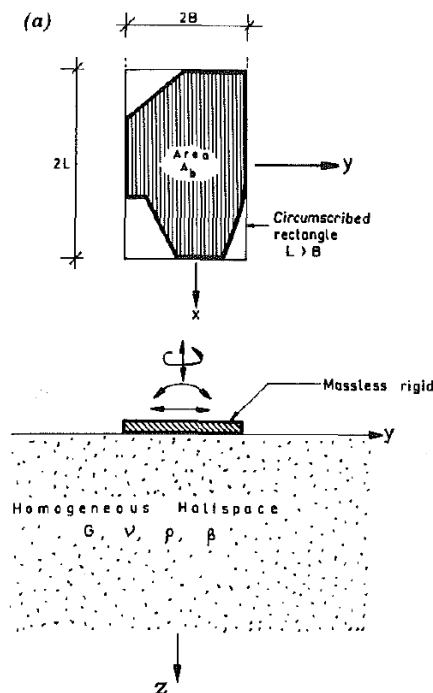
Figure 66 : Surface foundation of arbitrary shape

In order to compute the impedances, in the six modes of vibration, for a rigid, presumably massless foundation, the following values are needed:

- The base area A_b, the half width and half length of the base rectangle B and L and the area moments of inertia about the x, y, and z axes referred to the soil-foundation contact surface I_{bx}, I_{by} and I_{bz}:

B	$3.75\ m$
L	$5.25\ m$
I_{bx}	$369.1\ m^4$
I_{by}	$723.5\ m^4$
I_{bz}	$1092.7\ m^4$
$\chi = A_b/4L^2$	0.71

Table 24 : Foundation geometrical parameters

- G and v, respectively the soil shear modulus and the soil Poisson's ratio;
- V_s and V_{la}, that are respectively the shear wave velocity and the Lysmer's analog wave velocity, which can be defined as the apparent propagation velocity of compression-extension waves under the foundation, expressed in function of V_s and v through the expression:

$$V_{la} = \frac{3.4}{\pi\,(1-v)}\,V_s \tag{2.80}$$

With the intention of evaluating the effects of the dynamic soil-structure interaction for the extremes of the range that characterizes a subsoil category B, the values of the parameters listed in Table 25 were taken. The subscript min refers to the most deformable soil condition within the range, while the subscript max is referred to the most rigid soil in the interval concerning the category B.

The NTC 2018, in paragraph §3.2.2, provides that the soils, as in the case at study, made up of soft rocks and deposits of very thickened coarse-grained soils or very consistent fine-grained soils, are characterized by values of equivalent propagation velocity of shear waves between $360\ m/s$ and $800\ m/s$.

The range for the Poisson's ratio, characteristic of gravel sand soil, was taken as $0.3 \div 0.4$, whereas the soil density, typical of very dense soil, was chosen equal to $1900 \ kg/m^3$.

Furthermore, the soil was considered as an homogeneous, isotropic and linear elastic medium, where the velocity of propagation can be connected to its density ρ and to its shear modulus G through the following expression:

$$V_s = \sqrt{\frac{G}{\rho}} \qquad (2.81)$$

Since the shear modulus G, the modulus of elasticity E and the Poisson's ratio are connected by the following:

$$G = \frac{E}{2\,(1+v)} \qquad (2.82)$$

it is evident that a lower bound value for the shear modulus is associated to the maximum range value of the Poisson's ratio v_{max} and vice versa. Starting from the values selected for V_{smin} and V_{smax}, through the equation (2.81) the lower and upper bounds for G have been computed, associated respectively to the values v_{max} and v_{min} for the Poisson ratio.

The material parameters obtained are presented in the following table:

Upper Bound		Lower Bound	
ρ	$1900 \ kg/m^3$	ρ	$1900 \ kg/m^3$
V_{smin}	$360 \ m/s$	V_{smax}	$800 \ m/s$
G_{min}	$246 \ MPa$	G_{max}	$1216 \ MPa$
v_{max}	0.4	v_{min}	0.3
V_{lamin}	$649.4 \ m/s$	V_{lamax}	$1236.9 \ m/s$

Table 25 : Material parameters for the surface foundation

Once known the parameters reported in Table 25, it is possible to compute the static stiffness for each vibration mode, both for the lower bound V_{smin} and the upper bound V_{smax}, according to the expressions given by Gazetas for surface foundations on homogeneous half space:

Vibration Mode	Static stiffness	Values for V_{smin}	Values for V_{smax}
Vertical z	$K_z = \dfrac{2GL}{(1-v)}(0.73 + 1.54\chi^{0.75})$	$8{,}3\ 10^6\ kN/m$	$35{,}1\ 10^6\ kN/m$
Horizontal y	$K_y = \dfrac{2GL}{(2-v)}(2 + 2.50\chi^{0.85})$	$6{,}3\ 10^6\ kN/m$	$29{,}1\ 10^6\ kN/m$
Horizontal x	$K_x = K_y - \dfrac{0.2GL}{(0.75-v)}\left(1 - \dfrac{B}{L}\right)$	$6{,}1\ 10^6\ kN/m$	$28{,}3\ 10^6\ kN/m$
Rocking rx	$K_{rx} = \dfrac{G}{(1-v)}I_{bx}{}^{0.75}\left(\dfrac{L}{B}\right)^{0.25}\left(2.4 + 0.5\dfrac{B}{L}\right)$	$103{,}7\ 10^6\ kN\ m$	$438{,}8\ 10^6\ kN\ m$
Rocking ry	$K_{ry} = \dfrac{3G}{(1-v)}I_{by}{}^{0.75}\left(\dfrac{L}{B}\right)^{0.15}$	$180{,}7\ 10^6 kN\ m$	$764{,}6\ 10^6\ kN\ m$
Torsion t	$K_t = 3.5GI_{bz}{}^{0.75}\left(\dfrac{B}{L}\right)^{0.4}\left(\dfrac{I_{bz}}{B^4}\right)^{0.4}$	$201{,}5\ 10^6 kN\ m$	$995{,}1\ 10^6\ kN\ m$

Table 26 : *Static stiffness computed for the extremity of the range for sub soil category B*

As can be seen from the Table above, the values concerning the stiffness computed for the upper bound of the soil range, as expected, are higher than that calculated for the lower bound.

The dependence of the real part of the impedance on the frequency is evident in the dynamic stiffness coefficient; it is in fact a function, for the six degrees of freedom, of the parameter a_0, a dimensionless circular frequency expressed as:

$$a_0 = \frac{\omega B}{V_s} \tag{2.83}$$

The dynamic stiffness coefficients for the translational and rotational degrees of freedom, for $0 \leq a_0 \leq 2$ are reported in the Table below:

Vibration Mode	Dynamic stiffness coefficient
Vertical z	$k_z = k_z(a_0, L/B)$ plotted in Fig.67
Horizontal y	$k_y = k_y(a_0, L/B)$ plotted in Fig.67
Horizontal x	$k_y \cong 1$
Rocking rx	$k_{rx} \cong 1 - 0.2a_0$
Rocking ry	$k_{ry} \cong 1 - 0.26\,a_0$
Torsion t	$k_{rz} \cong 1 - 0.14\,a_0$

Table 27 : *Dynamic stiffness coefficients for a surface foundation*

The paper provides the plots of k_z and k_y for different values of the ratio L/B. In order to reproduce the plot of the dynamic stiffness coefficients k_z and k_y for the value of the viaduct foundation $L/B = 1.4$, it was first necessary to digitize the graphs in order to obtain the values to be interpolated. In particular, the curves for the two L/B upper and lower values closest to $L/B = 1.4$ were imported and appropriately scaled in the AutoCAD software, in which was hence carried out the sampling of the values for intervals of a_0 of amplitude 0.05. Once obtained the two curves, the values for $L/B = 1.4$ were computed through interpolation. The resulting plot are represented below:
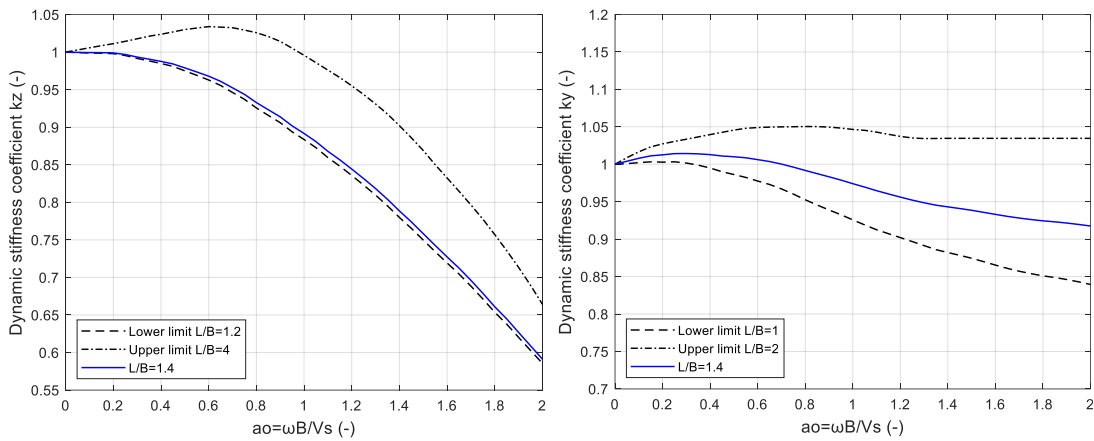
Figure 67 : *Dynamic stiffness coefficients kz and ky*

Once defined the dynamic stiffness coefficient for each vibration mode, the real part of the impedance can be expressed as the product between the static stiffness and the dynamic stiffness coefficient itself $\bar{K}(\omega) = K \, k(\omega)$.

Considering the radiation damping coefficients, they can be expressed as indicated in Table 28.

Vibration Mode	Radiation dashpot coefficient
Vertical z	$C_z = \rho \, V_{la} \, A_b \, c_z(a_0, L/B)$
Horizontal y	$C_y = \rho \, V_s \, A_b \, c_y(a_0, L/B)$
Horizontal x	$C_x = \rho \, V_s \, A_b$
Rocking rx	$C_{rx} = \rho \, V_{la} \, I_{bx} \, c_{rx}(a_0, L/B)$
Rocking ry	$C_{ry} = \rho \, V_{la} \, I_{by} \, c_{ry}(a_0, L/B)$
Torsion t	$C_t = \rho \, V_s \, I_{bz} \, c_t(a_0, L/B)$

Table 28 : *Radiation dashpot coefficients for a surface foundation*

The total damping coefficient can be considered as the sum of the radiation component and of a term including the soil hysteretic damping β, $C_\beta = 2\overline{K}\,\beta/\omega$, which won't be taken into account in the current work, due to the Rayleigh damping contribution acting to the whole system. The plots of $c_{z,y,rx,ry,t}$ were computed following the same procedure explained for k_y and k_z, thus obtaining the following graphs function of a_0:
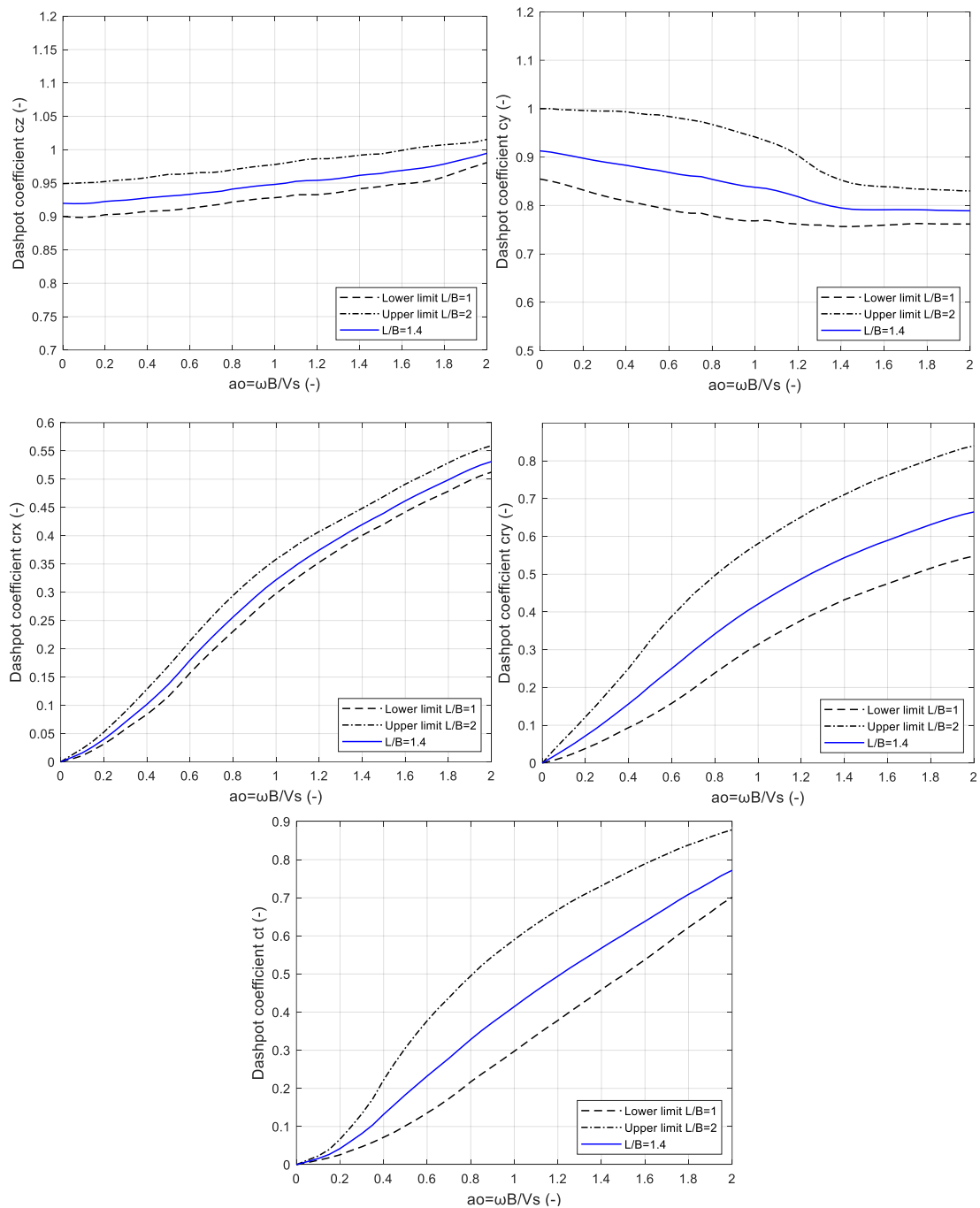
Figure 68 : *Radiation damping coefficients $c_z, c_y, c_{rx}, c_{ry}, c_t$*

The main problem related to the calculation of the impedance consists in the evaluation of the frequency in correspondence to which its real and imaginary part are computed. In fact, carrying out a step-by-step analysis in the time domain, the need to have parameters that don't depend on frequency appears evident.
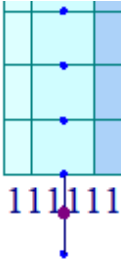
Firstly, in order to appreciate how much the coefficients vary in the range of frequencies of interest, the trends of the real and imaginary part of the impedance $\overline{K}$ and C have been obtained in function of the natural period. In the following figure are shown the trends near the natural period obtained previously for the pier model, equal to 0.95 s. As can be seen in the graph below and in the graphs reported in the Appendix, the coefficients, both for the case V_{smin} and V_{smax}, doesn't vary significantly near the abovementioned natural period.
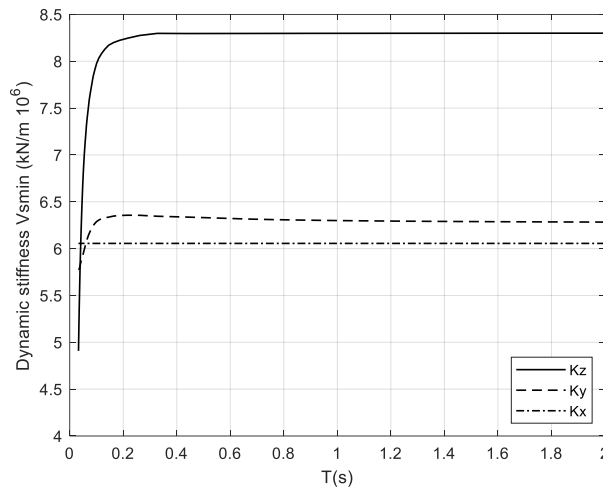
Figure 69 : Translational dynamic stiffness coefficients $\overline{K}$ for Vsmin

The impedance values were introduced into the model through six springs and six dashpots, located at the base of the foundation. In particular, it was chosen to model the foundation as a rigid body. At the operational level, a mass and its rotational inertias were introduced, in the center of gravity of the foundation. A node has been introduced at the Z coordinate which corresponds to the base of the foundation itself. Subsequently, a rigid link was inserted to connect the master node of the center of gravity of the rigid body to the slaves nodes located in the node at the base of the pier shaft and in the node at the base of the foundation. The masses, the rotational inertias and the foundation modeling in the Midas GEN code are represented below, in the reference frame of the foundation:

m	$441.5\ t$
I_{ry}	$4234.5\ t * m^2$
I_{rx}	$2247.7\ t * m^2$
I_{rz}	$6126\ t * m^2$

Figure 70 : *Pier foundation representation in the Model*

Although the real and imaginary parts of the impedance don't vary noticeably around the natural period of 0.95 s, an operating procedure has been introduced to be able to evaluate in the most appropriate way the frequency associated to the impedance. The procedure was carried out for 4 models: two models in which springs and dampers were introduced at the base with the parameters calculated for V_{smin} and V_{smax} starting from Model 1, and two models with the parameters computed for V_{smin} and V_{smax} starting from the Model 2. In particular, in a first phase attention was paid exclusively on the stiffness, introducing in the model those calculated with the initial period of the pier model, equal to 0.95 s, for all 4 models. Therefore in each model:

- The stiffnesses of the springs to be attributed to the base of the foundations were calculated for a period $T_0 = 0.95\ s$;
- Through an eigenvalue analysis, the fundamental period T_1 of the model that reproduces the viaduct in its entirety, with the springs computed for $T_0 = 0.95\ s$, was evaluated;
- After the evaluation of the new natural period, the stiffness at the base of the foundation was calculated starting from T_1;
- The new natural period T_2 of the model was evaluated in a model with the springs calculated for T_1;
- The procedure was repeated until convergence, that is when the difference between two successive natural periods was negligible, i.e. until $T_{i+1} - T_i < \varepsilon$ was obtained.

123

As an example, for Model 1, characterized by an initial period $T_{in} = 0.965\ s$, the introduction of the dynamic soil-structure interaction, for the parameters computed starting from V_{smin}, led to the following results:

- The stiffness values computed from T_0 changed the natural period from $0.95\ s$ to $T_1 = 0.991\ s$, with an associated percentage error of 4%, not considered acceptable;
- The values of the stiffness where then computed through the new value of $a_0(T_1) = 0.066$ and introduced in the model;
- The new natural period value $T_2 = 0.991\ s$ was found, with an associate percentage error of 0% with respect to the previous model, which indicates that convergence to the first natural period of the structure has been achieved.

The same procedure was then applied to all the models, with the following results, with the stiffness expressed in the global reference frame of the viaduct:

	$Model\ 1\ V_{smin}$	$Model\ 1\ V_{smax}$	$Model\ 2\ V_{smin}$	$Model\ 2\ V_{smax}$
T_{in}	0.965 s	0.965 s	1.004 s	1.004 s
T_0	0.95 s	0.95 s	0.95 s	0.95 s
$a_0(T_0)$	0.069	0.031	0.069	0.031
T_1	0.991 s	0.971 s	1.034 s	1.011 s
$err\%_{T1,To}$	4%	2%	8.4%	6.4%
$a_1(T_1)$	0.066	0.030	0.063	0.029
T_2	0.991 s	0.971 s	1.034 s	1.011 s
$err\%_{T2,T1}$	0%	0%	0%	0%
$a_2(T_2)$	0.066	0.030	0.063	0.029
k_x	$6.30\ 10^6$ kN/m	$29.20\ 10^6$ kN/m	$6.30\ 10^6$ kN/m	$29.20\ 10^6$ kN/m
k_y	$6.06\ 10^6$ kN/m	$28.32\ 10^6$ kN/m	$6.06\ 10^6$ kN/m	$28.32\ 10^6$ kN/m
k_z	$8.30\ 10^6$ kN/m	$35.13\ 10^6$ kN/m	$8.30\ 10^6$ kN/m	$35.13\ 10^6$ kN/m
k_{rx}	$177.54\ 10^6$ kN m	$758.62\ 10^6$ kN m	$177.67\ 10^6$ kN m	$758.86\ 10^6$ kN m
k_{ry}	$102.29\ 10^6$ kN m	$436.09\ 10^6$ kN m	$102.34\ 10^6$ kN m	$436.20\ 10^6$ kN m
k_{rz}	$199.65\ 10^6$ kN m	$990.92\ 10^6$ kN m	$199.73\ 10^6$ kN m	$991.08\ 10^6$ kN m

Table 29 : Stiffness foundation parameters for Model 1 and Model 2

As can be seen in this first phase in the table above, the introduction of the soil-structure interaction doesn't produce a significant increasing of the natural period of the structure.

Moreover, it has to be pointed out that, despite the increase in stiffness given by the limitation of the bearings shear deformations in the transverse direction, the first period of the structure in Model 2 is larger than that of Model 1. This is due to the fact that the first mode in both models is translational along the longitudinal direction, so the difference between the periods of the two models is actually due to the different modeling of the deck rather than to the limitation on the transversal supports deformations.

Once the convergence to the first natural period of the structure has been achieved, the most relevant modes for the foundations degrees of freedom were evaluated in the models. For each degree of freedom, the stiffness and the dashpot coefficients have been computed for the frequency value linked to the mode that most mobilized the foundation for the degree of freedom itself.

The eigenvalues and eigenvectors relating to the first 50 modes were therefore found, and only those characterized by a participant mass larger than 5% were considered. It was chosen to consider this number of modes because the 50th is the first one for which there is a relevant effective mass for the translation along Z, while, considering the translations along X and Y, a significant participant mass had already been obtained in the first modes.

For the modes considered, the eigenvectors normalized with respect to the maximum displacement were analyzed, in order to have an estimate of how much the foundations moved in each mode with respect to the other components of the structure. Once the natural period of the mode for which the maximum value of this relative displacement is obtained was identified for each degree of freedom, the dynamic stiffness values and the damping coefficients for the six DOFs were calculated.

The following table shows the components of the eigenvectors ϕ for which the maximum of each displacement or rotation and the corresponding mode have been obtained.

	Model 1 V_{smin}		Model 1 V_{smax}		Model 2 V_{smin}		Model 2 V_{smax}	
	Mode	ϕ_j	Mode	ϕ_j	Mode	ϕ_j	Mode	ϕ_j
u_x	11	0.0098	11	0.0015	1	0.01	5	0.0022
u_y	9	0.0087	9	0.002	18	0.0401	18	0.0101
u_z	49	0.0293	50	0.0065	32	0.0331	31	0.0071
R_x	5	0.003	5	0.0007	27	0.0199	16	0.0024
R_y	50	0.0024	51	0.0004	30	0.0039	30	0.0004
R_z	13	0.0002	10	0.0001	21	0.0003	22	0.0001

Table 30 : Eigenvector components for Model 1 and Model 2

Considering the periods of the modes reported in Table 30, the stiffness in the 4 models was computed. However, a further iteration was necessary: the insertion of new stiffness values, calculated considering the most significant modes for each degree of freedom, led to a new value of the first fundamental period. Therefore, once inserted in the models the values of the stiffness obtained for the modes of the table above, the new values of the periods for the modes of Table 30 were read in the results of the eigenvalue analysis, and through these values the stiffness was calculated again; this was done again until the convergence regarding the first natural period of the structure.

In order to get an insight into the meaning of the computed C_j values ($j = z, y, z, rx, ry, t$), for each mode assumed to be independent with respect to the others, according to Gazetas, an equivalent damping ratio ξ_j and ξ_i respectively for translational and rotational modes was evaluated through the expressions:

$$\xi_j = \frac{C_j}{2\sqrt{\overline{K}_j m}} \qquad (2.84) \qquad\qquad \xi_i = \frac{C_i}{2\sqrt{\overline{K}_i I_p}} \qquad (2.85)$$

Where $j = z, y, x$ $i = rx, ry, rz$ $j = x, y, z$; m is the pier mass and I_p are the pier mass inertia moments about the base X, Y and Z axes, computed for a mean pier height.

The application of the second phase of the set out procedure led to the following values, expressed in the global viaduct reference frame, for the real and imaginary parts of the impedance and to the following damping factors; the translational stiffness

is reported in *kN/m*, the rotational one in *kN m*, whereas the translational and rotational damping coefficients are respectively in *kN s/m* and *kN s m*.

	$T_{initial} = 0.965\ s$			Model 1 V_{smin}			$T_{final} = 0.992\ s$	
Mode	*Dir*	T_j [s]	$a_0(T_j)$	$\bar{K}_j$	C_j	$\xi\%$	$\xi\%_{Mod.}$	*Modified* C_j
11	X	0.63	0.10	6318508	48790	38	20	25351
9	Y	0.66	0.09	6055840	53865	43	20	24819
49	Z	0.19	0.34	8228713	89951	62	20	28931
5	RX	0.73	0.09	1176416884	27600	0.9	0.9	27600
50	RY	0.19	0.34	9657017	37961	0.7	0.7	37961
13	RZ	0.61	0.11	198487105	13149	3.7	3.7	13149
	$T_{initial} = 0.965\ s$			Model 1 V_{smax}			$T_{final} = 0.971\ s$	
Mode	*Dir*	T_j [s]	$a_0(T_j)$	$\bar{K}_j$	C_j	$\xi\%$	$\xi\%_{Mod.}$	*Modified* C_j
9	X	0.65	0.05	29237856	119700	45	20	53667
11	Y	0.62	0.05	28316550	108964	40	20	54534
50	Z	0.19	0.16	35114394	170372	57	20	59763
5	RX	0.71	0.04	756378322	24049	0.4	0.4	24049
51	RY	0.19	0.16	425050145	24795	0.2	0.2	24795
10	RZ	0.63	0.05	988603247	12439	1.6	1.6	12439

	$T_{initial} = 1.004\ s$			Model 2 V_{smin}			$T_{final} = 1.034\ s$	
Mode	*Dir*	T_j [s]	$a_0(T_j)$	$\bar{K}_j$	C_j	$\xi\%$	$\xi\%_{Mod.}$	*Modified* C_j
1	X	1.03	0.06	6298574	48969	39	20	25311
18	Y	0.32	0.20	6055840	53865	43	20	24819
32	Z	0.19	0.35	8225240	89974	62	20	28924
27	RX	0.18	0.33	165075378	112938	3.7	3.7	112938
30	RY	0.19	0.35	96472649	38630	0.7	0.7	38630
21	RZ	0.27	0.25	194605612	44543	12.8	12.8	44543
	$T_{initial} = 1.004\ s$			Model 2 V_{smax}			$T_{final} = 1.011\ s$	
Mode	*Dir*	T_j [s]	$a_0(T_j)$	$\bar{K}_j$	C_j	$\xi\%$	$\xi\%_{Mod.}$	*Modified* C_j
5	X	0.63	0.05	29235825	108969	40	20	54532
18	Y	0.29	0.10	28316550	119700	45	20	53667
31	Z	0.19	0.16	35113664	170394	57	20	59763
16	RX	0.38	0.08	749162284	45373	0.7	0.7	45373
30	RY	0.19	0.16	424858591	25282	0.2	0.2	25282
22	RZ	0.24	0.12	978178517	34324	4	4	34324

***Table 31** : Final dynamic stiffnesses and dashpot coefficients for the 4 Models*

In the table above are indicated the values of the first natural periods in the fixed-base condition and after the introduction of the soil-structure interaction, respectively named $T_{initial}$ and $T_{final.}$

Moreover it can be noted that the effective damping ratio for the rotational modes is quite small, whereas the damping factors $\xi\%$ associated to the translational vibration modes turn out to be very high, especially considering the vertical direction.

The high translational percentages are mainly due to the different levels of radiation damping, consequence of the spreading waves generated at the soil foundation interface. When the structure is characterized by vertical oscillations, the waves are emitted in phase and reach long distances, with a consequence lost of energy in the foundation and with associated high amounts of radiation damping. On the other hand, the waves 180° out of phase sent by two points symmetrically located on the opposite sides of a rocking foundation cancel each other in their meeting at a certain distance along the center line, thus not dissipating a high amount of energy.

However the translational damping factors $\xi\%$ are too high, since they have been anyway obtained by modeling the soil as an homogeneous, isotropic and linear elastic medium.

They have therefore been modified, and rendered equal to 20% for the translational modes; subsequently the damping coefficients to be inserted in the models, named in the table above "modified C_j", were derived from these modified values $\xi\%_{Mod.}$

3

NUMERICAL SEISMIC VULNERABILITY ASSESSMENT OF THE VIADUCT

3.1 Analysis on Model 1

As previously described, Model 1 is characterized by a deck represented by means of both beam and plate elements, and by bearings able to perform large shear deformations both in transversal and longitudinal direction of the viaduct, as no additional "shear keys" are introduced. Consequently, probably not being the bearings able to transmit the inertia forces to the pier base, in Model 1 the non-linearity in the pier itself hasn't been introduced. The current paragraph is aimed at representing the results coming from linear dynamic analysis on the viaduct; more precisely, the effects of the dynamic soil-structure interaction will be analyzed in the structural response, both through a direct integration time history analysis and a response spectrum analysis.

3.1.1 Direct integration: linear time history analysis results

As regards the direct integration time history analysis, it was carried out as explained in paragraph §2.3.1. Firstly, the static loads were defined and the spectrum compatible accelerograms generated by SIMQKE were imported in the model. Due to the non-dissipative nature of the model, they were created from the definition of a response spectrum at the life safety limit state SLV, rather than at the collapse prevention limit state SLC, with the associated parameters listed in Table 32. Also the vertical seismic component was considered, following the prescriptions of the NTC 2018. According to the latter, vertical seismic input must be taken into account:

- if the site where the construction arises is characterized by a ground acceleration, as in the case at study, higher than 0.15g;
- if the structure has the presence of almost horizontal elements with spans larger than 20 m, or of prestressed elements.

a_g/g	0.206
F_0	2.454
T_c^*	0.36 s
$TRISE$	5 s
$TLVL$	10 s
DUR	25 s

Table 32 : *SLV parameters for the accelerograms in SIMQKE*

As provided by the NTC, seven groups of accelerograms have been considered, in order to compute the response through the average of the most unfavourable values.
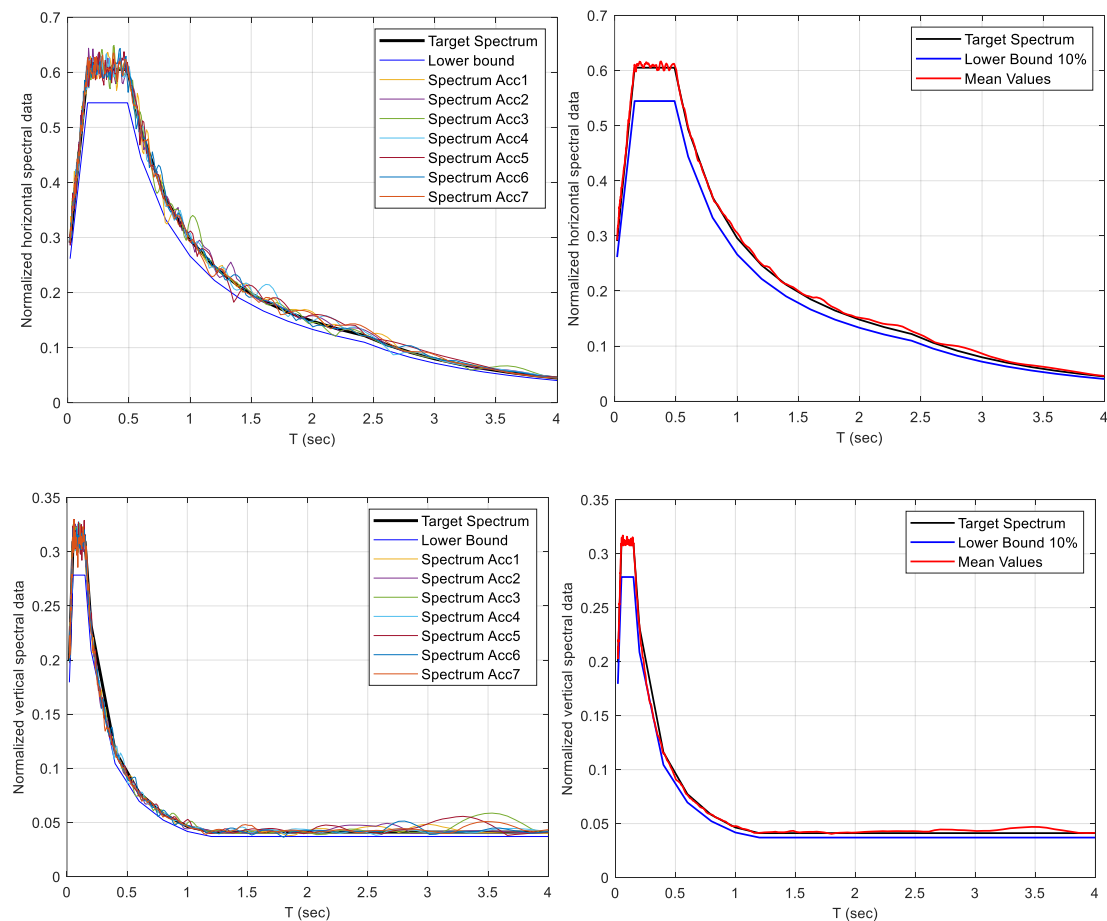
Figure 71 : *SLV Specta associated to the 7 groups of accelerograms selected in SIMQKE*

From the figure above, the spectrum compatibility of the accelerograms generated can be observed: the average of the spectral ordinates associated with them is, for each period value, above the lower limit equal to 10%, both considering the vertical and horizontal components. After importing the accelerograms into Midas GEN, a linear time history analysis was performed in the fixed-base model, and in the models with dynamic soil-structure interaction evaluated for V_{smin} and V_{smax}, named in the following as "Model 1 V_{smin}" and "Model 1 V_{smax}".

In terms of damping, the Rayleigh model was applied to the whole system in the time history load case, whereas the radiation soil damping contribution was introduced by 6 dashpots in the node of each foundation base, through the C_j values computed previously and reported in Table 31. The frequency range of interest for the Rayleigh damping was defined considering 50 modes, since the 50th is the first mode with a significant effective mass for the translation along Z. The range for the frequencies of interest for the three models is therefore represented as follows:

Model 1 Fixed Base		Model 1 V_{smax}		Model 1 V_{smin}	
f_{lower}	f_{upper}	f_{lower}	f_{upper}	f_{lower}	f_{upper}
1.04 Hz	5.32 Hz	1.03 Hz	5.29 Hz	1.01 Hz	5.21 Hz

Table 33 : Frequency range of interest in Model 1

Since they don't vary significantly between the models, it was decided to set a single Rayleigh curve, considering approximately as range of interest the interval from the minimum of the values, equal to 1.01 Hz, to the maximum one, equal to 5.32 Hz. The Rayleigh curve was then evaluated through the choice of the four frequency and damping factor parameters ξ_1, ξ_2, f_1 and f_2 which, inserted in the system (2.68), made the curve as constant as possible in the frequency range of interest. The final values are shown in Table 34.

ξ_1	ξ_2	f_1	f_2	α	β
0.05	0.065	1.1 Hz	7 Hz	0.553	0.003

Table 34 : Parameters of the Rayleigh curve in fixed-base Model 1, Model 1 Vsmin and Model 1 Vsmax

The resulting curve, which represents the Rayleigh damping for Model 1, Model 1 V_{smin} and Model 1 V_{smax}, is characterized by the following shape:
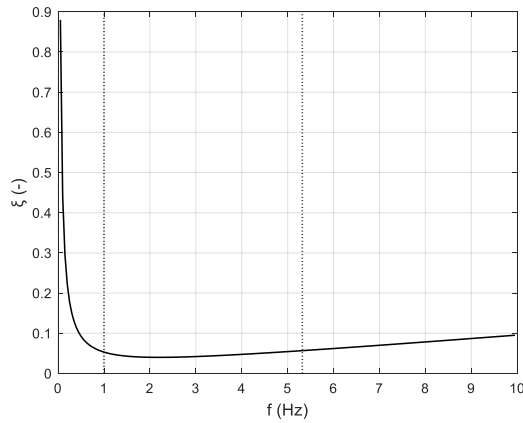
***Figure 72** : Rayleigh damping curve in fixed-base Model 1, Model 1 Vsmin and Model 1 Vsmax*

The results of the eigenvalue analysis had already shown how the natural periods of the structure had increased both in the case of Model 1 V_{smax} and Model 1 V_{smin}, with a larger increase in the case of the latter. This is consistent to the fact that there has been a transition from rigid constraints to translational and rotational springs representing the SSI, which has reduced the stiffness of the whole system. Given the higher deformability of the soil associated to smaller shear wave velocities, it is also expected that the increase in the natural periods is more visible in the case of V_{smin}. The percentage errors of each natural period in both SSI models with respect to its equivalent in the fixed-based structure are shown in Figure 73 for the first 30 modes; the highest percentage error was found in the second mode of Model 1 V_{smin}, equal to 4.7%, whereas for Model 1 V_{smax} the highest value observed is equal to 1.1%, even in this case in mode 2. Furthermore, the natural periods coming from eigenvalue analysis in the three models are shown in the Appendix.
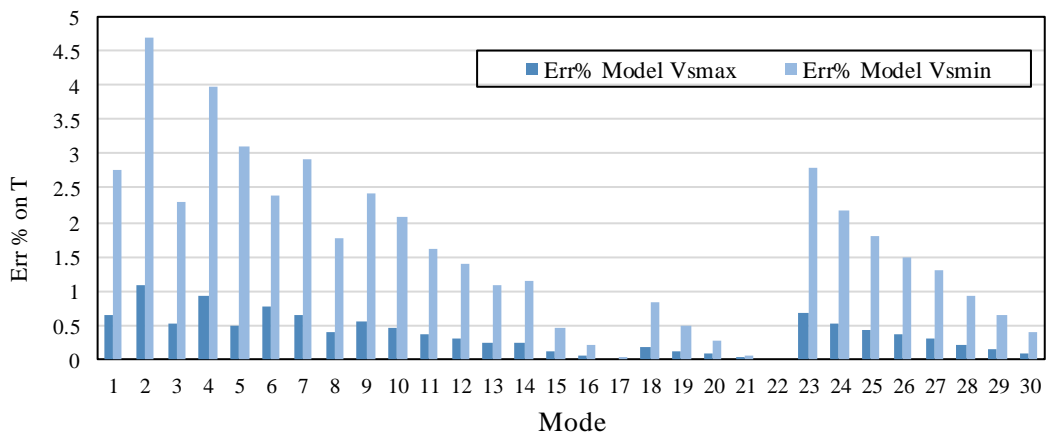
***Figure 73** : Err% of the periods in Model 1 Vsmin and Vsmax with respect to the fixed-base model*

Considering the bearings, the maximum shear in the beam elements representing the supports, in both directions, was found for each group of accelerograms; then the average value of the shear found for each group was calculated for each bearing, and with it, through the equation (2.72) the shear deformations in the transverse and longitudinal directions of the viaduct were evaluated. The bearings have been ordered, starting from Pier 1, following the numbering represented in the figure below:
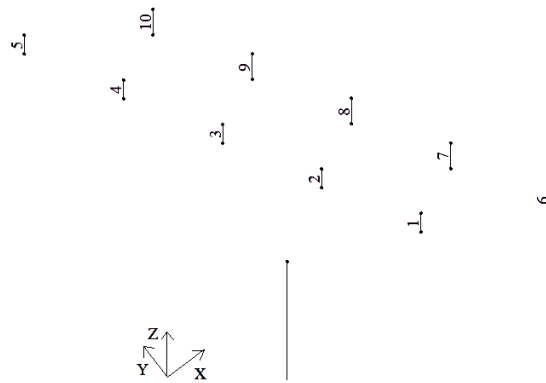
Figure 74 : Numbering order of the supports

The check, carried out in Model 1 V_{smin} and in Model 1 V_{smax} separately for the X and Y directions, lead to shear deformation values in both models, shown in Appendix for each bearing, ranging between a maximum of 110% and a minimum of 43%. It should be pointed out that the support in which the 43% of shear deformation is experienced, is not verified in the orthogonal direction, characterized by a shear strain equal to 90%. The shear strain exceeds the 75% limit for all the bearings, except for five of the supports of the deck of Pier 8.

Considering the check about the friction between the neoprene and the concrete of the deck beam, the same shear values were exploited to compute the tangential stresses $\tau_h = F_{shear}/A_{base}$, and compared to the values of σ_v obtained from the average on the axial forces. The verification $\tau_h \leq \mu\sigma_v$, with μ taken conservatively equal to 0.6, leads to acceptable results, reported in Appendix, in all the bearings except for three supports on Pier 8. The results in Appendix have been listed for Model 1 V_{smin} only, since the percentage errors of the latter with respect to the Model 1 V_{smax}, in terms of supports deformations and tangential stresses, are very small, as they don't exceed the 0.12%.

It is therefore evident that the verifications in terms of friction lead to less conservative results than those obtained in terms of shear deformations.

Considering the analysis of the values in terms of displacements, the following graphs show the displacement values at the top of the piers, both in the model with fixed-base and in the model with SSI computed from V_{smax}.
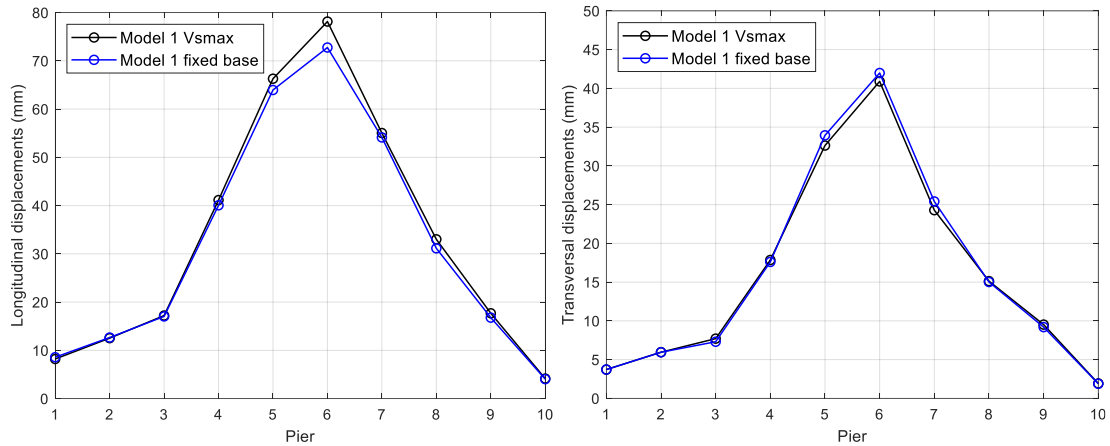
Figure 75 : Comparison of top pier displacements between Model 1 fixed-base and model 1 Vsmax

The top pier displacements regarding the model with V_{smin} weren't shown, since their percentage errors with respect to the case of V_{smax} are extremely small, characterized by a maximum of 0.16% and 0.34% respectively along the longitudinal and transversal direction. It can therefore be stated that the effects of the dynamic soil-structure interaction on the displacements at the top of the piers don't vary much in the range considered for the shear waves velocities V_s.

Furthermore, from the figure above, it can be observed that the top pier displacements are larger in the longitudinal direction than in the transversal one; this is consistent to what was observed in the previous chapter for the model of the single pier, in which turned out to be stiffer in its bending in the transversal direction than in the longitudinal one. Considering the comparison with the fixed-based model, in the models that consider the SSI, an increase in the longitudinal displacements for the tallest piers and a decrease in the transverse ones was found.

With the introduction of the SSI, what is anticipated is a decrease in the actions acting on the structure and therefore in the internal forces, because of the increase in the

natural periods of the structure, as well as an increase in the displacements at the top of the piers, due to the rigid motions of the foundations. Actually, these effects don't always occur, as the radiative damping given by the soil also comes into play. In the case under examination, for example, there are damping ratios for rotational modes even smaller than 1%, which lead to an increase in the forces on the structure, compared to the 5% that was tried to give to the structure, in the range of frequencies of interest, by setting the Rayleigh damping.

Furthermore, the reason why there is no generalized increase in displacements can be attributed to the fact that the contribution of the SSI to the period increment is not very significant, as a category of subsoil B also in the lower bound of its range is associated to a soil that is not noticeably deformable.

The soil-structure dynamic interaction didn't produce noticeable differences even in terms of shear at the base of the piers, as can be seen in the following table:

	Transversal Shear (kN)			Longitudinal Shear (kN)		
Pier	Fixed base	V_{smax}	V_{smin}	Fixed base	V_{smax}	V_{smin}
1	2212.7	2212.4	2212.5	1767.0	1768.1	1767.7
2	2355.5	2355.8	2355.9	1793.7	1794.0	1794.5
3	2015.6	2015.5	2015.5	1579.2	1579.8	1580.3
4	1960.4	1960.3	1960.5	1492.5	1493.0	1493.0
5	2120.2	2120.2	2120.1	1494.8	1494.5	1494.8
6	2592.7	2592.6	2592.5	1659.0	1658.8	1658.7
7	1854.7	1855.1	1855.2	1367.2	1367.4	1367.3
8	2076.4	2076.4	2076.5	1512.4	1512.5	1512.6
9	2161.6	2161.7	2161.7	1377.0	1377.0	1376.6
10	1982.2	1982.0	1982.1	1621.7	1622.3	1620.3

Table 35 : Base shear comparison between Model 1 fixed-base, Model 1 Vsmin, Model 1 Vsmax

An overview of how effectively considering the SSI influences the shear forces at the base of the pier is given by the following graphs, which show the percentage errors in the base shear obtained in the SSI models with V_{smin} and V_{smax}, with respect to the fixed-base model.
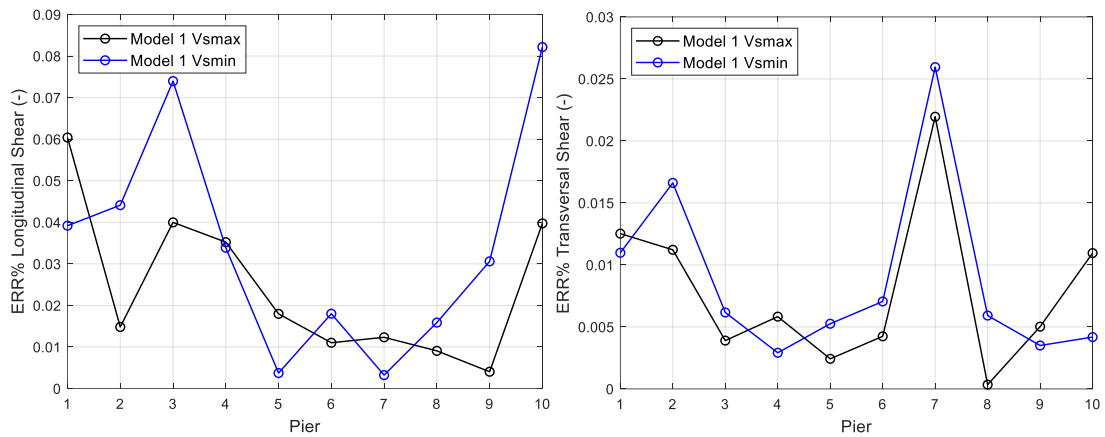
Figure 76 : Error% with respect to the fixed-base model shear

The higher percentage error are observed in the model with a soil-structure interaction computed from V_{smin}, both in the case of longitudinal and transversal directions, equal respectively to 0.026% and 0.082%.

From the results obtained from the direct integration time history analysis, it can therefore be deduced that in Model 1 the effects of the dynamic soil-structure interaction had a negligible influence on the structure, both in terms of internal forces and in terms of displacements. However, the maximum percentage errors regarding the pier base shear and natural periods of the viaduct with respect to the fixed-base model were more evident, as expected, in Model 1 V_{smin}.

3.1.2 Dynamic response spectrum analysis results

The linear dynamic analysis with response spectrum, introduced in paragraph §2.3.2, has been applied to Model 1. In the analysis on the fixed-based model there are no problems in carrying out this type of analysis, while for the models in which the SSI has been considered, it is necessary to introduce some considerations, in order to be able to take into account in the analysis the different nature and extent of energy dissipation in the various components of the system: the soil contributes to the damping of the system with a very high rate in the translational modes, and with a damping factor smaller than 5% for rotational modes.

The inhomogeneity in the distribution of dissipations generally leads, for this type of systems, to the choice of using direct integration methods without passing through the

modal transformation; however, in the current work the response spectrum analysis will be carried out, with the aim of comparing the results with that obtained for time history analysis through direct integration described in paragraph §3.1.1.

The weighted damping method, explained below, allows to identify the equivalent damping factors ξ_j, weighted by means of the strain energies in the modal deformed shape, with which to carry out the modal analysis with response spectrum. They are automatically calculated by the Midas GEN software through the selection, in the definition of the response spectrum load case, of the so called "Strain & energy proportional" method. The damping ratios listed in Table 31 for each vibrational mode were then inserted in the code and associated to the boundary at the base of the foundations. This results in a response spectrum analysis in which the spectrum is modified in each mode by means of the computed weighted ξ_j.

In order to understand the nature of these modal damping factors, however, it is necessary to analyze the way in which they were evaluated; for this purpose, the formulation proposed by Roesset in [23] is analyzed. The case of a non-homogeneous system subject to harmonic excitation in steady state conditions is thus considered. It is assumed that this system consists of n_v elastoviscous components and n_h hysteretic components. Hence at steady state, assuming a single principal mode, in resonance conditions, that is where the natural frequency ω_j is equal to that of the excitation, the oscillations can be written by means of the relation:

$$\boldsymbol{q}(t) = A\boldsymbol{\varphi}_j \sin\left(\omega_j + \theta\right) \tag{3.1}$$

Where A is a parameter that depends on the amplification factor, as well as on the stiffness and on the amplitude of the excitation, and $\boldsymbol{\varphi}_j$ is the eigenvector associated to the mode considered. The ratio between the energy dissipated by the viscous forces and the maximum elastic energy stored in the system during steady state oscillations for the elastoviscous components, characterized by stiffness $k^{(l)}$ and damping coefficient $c^{(l)}$, can be written through the relation:

$$\frac{W_{D,j}^{(V)}}{V_{Emax,j}^{(l)}} = \sum_{l=1}^{n_v} 2\pi\omega_j \frac{c^{(l)}}{k^{(l)}} \tag{3.2}$$

For the hysteretic components characterized by hysteretic damping factor $\mu^{(r)}$ the ratio can be instead written as:

$$\frac{W_{D,j}^{(H)}}{V_{Emax,j}^{(r)}} = \sum_{r=1}^{n_H} 2\pi\mu^{(r)} \tag{3.3}$$

The ratio between the total energy dissipated by the system and the total maximum elastic energy, can therefore be expressed as:

$$\frac{W_{D,j}}{V_{Emax,j}} = \frac{\sum_{r=1}^{n_H} 2\pi\mu^{(r)} V_{Emax,j}^{(r)} + \sum_{l=1}^{n_v} 2\pi\omega_j \frac{c^{(l)}}{k^{(l)}} V_{Emax,j}^{(l)}}{\sum_{r=1}^{n_H} V_{Emax,j}^{(r)} + \sum_{l=1}^{n_v} V_{Emax,j}^{(l)}} \tag{3.4}$$

To calculate the value of the equivalent modal damping factor, therefore, the equality between (3.4) and the ratio between the dissipated energy and that stored by the viscous oscillator with modal properties ω_j and ξ_j is required, equal to $4\pi\xi_j\omega/\omega_j$, which in resonance conditions is equal to $4\pi\xi_j$. The weighted modal damping factor can thus be expressed as:

$$\xi_j = \frac{1}{2} \frac{\sum_{r=1}^{n_H} \mu^{(r)} V_{Emax,j}^{(r)} + \sum_{l=1}^{n_v} \omega_j \frac{c^{(l)}}{k^{(l)}} V_{Emax,j}^{(l)}}{\sum_{r=1}^{n_H} V_{Emax,j}^{(r)} + \sum_{l=1}^{n_v} V_{Emax,j}^{(l)}} \tag{3.5}$$

The method used to evaluate the weighted damping will now be applied to the viaduct in question, weighing the individual contributions by means of the strain energies in the deformed shape of the first mode.

Starting from the model of the pier, its deformed shape in the first mode was considered, that is along the longitudinal direction for the viaduct under examination.
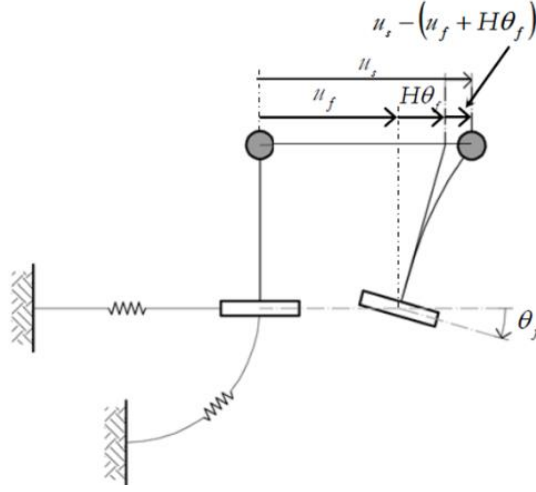
Figure 77 : Flexural pier deformation schematization for the first mode

Considering the quantities $\bar{K}_x$, $\bar{K}_{ry}$ and the modified dashpot coefficients C_x and C_{ry} listed in Table 31 both for the case of V_{smin} and V_{smax}, the deformation energies have been computed. Given the vector of the displacements depicted in Figure 77 $\boldsymbol{u}^T = \{u_f, \theta_f, u_s\}$, with the associated deformed shape $\boldsymbol{\varphi}^T = \{\varphi_1, \varphi_2, \varphi_3\}$, the strain energy stored in the system is equal to the sum of the following contributions:

- The elastic strain energy linked to the translation of the foundations:

$$E_{uf} = \frac{1}{2}\bar{K}_x{\varphi_1}^2 \qquad (3.6)$$

- The elastic strain energy linked to the rocking of the foundations:

$$E_{\theta f} = \frac{1}{2}\bar{K}_{ry}{\varphi_2}^2 \qquad (3.7)$$

- The elastic strain energy linked to the dissipations in the structure. If the eigenvectors are normalized through $\boldsymbol{\varphi}^T \boldsymbol{M} \boldsymbol{\varphi} = 1$, the total elastic energy stored in the system can be simply computed as half of the square of the circular frequency of the mode, since:

$$\omega_1{}^2 = \frac{\boldsymbol{\varphi}^T \boldsymbol{K} \boldsymbol{\varphi}}{\boldsymbol{\varphi}^T \boldsymbol{M} \boldsymbol{\varphi}} \qquad (3.8)$$

Then, by subtracting, from the total elastic energy evaluated, the sum of the E_{uf} and $E_{\theta f}$ of the total number of foundations in the N piers, the energy stored in the structure has been computed as:

$$E_s = \frac{\omega_1{}^2}{2} - \sum_{i=1}^{N} E_{uf} - \sum_{i=1}^{N} E_{\theta f} \qquad (3.9)$$

The corresponding dissipated energies have been evaluated starting from the energy stored as follows:

- The strain energy dissipated in the structure was computed as:

$$E_{ds} = 4\pi \xi_s E_s \qquad (3.10)$$

- The strain energy dissipated through the translation and the rotation of the foundations was instead computed through the following expressions:

$$E_{duf} = \frac{1}{2} C_x \omega_1 \varphi_1{}^2 \qquad (3.11) \qquad E_{d\theta f} = \frac{1}{2} C_{ry} \omega_1 \varphi_2{}^2 \qquad (3.12)$$

In analogy to the (3.5), the equivalent damping was calculated with the expression:

$$\xi_{eq} = \frac{1}{4\pi} \frac{E_{duf} + E_{d\theta f} + E_{ds}}{E_{uf} + E_{\theta f} + E_s} \qquad (3.13)$$

The following values have been obtained for the Model 1 V_{smin} and V_{smax}:

$$\boldsymbol{\xi_{Vsmin}} = 4.6\% \qquad \boldsymbol{\xi_{Vsmax}} = 4.94\%$$

As can be seen from the results, the modal damping decreased compared to that of the structure; this is to be attributed to the damping rate provided by the interaction with the soil regarding the rotational modes, smaller than 5%, which evidently in this mode have a larger influence than the high rate given by the translational vibrational modes.

It may be useful to compare the values of weighted damping evaluated above through the (3.13) and those deriving from a simplified single degree of freedom system, commonly employed in simplified analysis of inertial interaction, shown in Figure 78.

It consists of a single degree of freedom model, with height h, mass m, stiffness k, and viscous damping coefficient c. The base of the structure is characterized by a

translation u_f with respect to the free field motion u_g and by a rotation θ. Since the lateral response of the structure in one direction only was considered, only two impedance terms are necessary: in this case the impedance function are represented, for the rocking and translation modes, respectively by $\bar{K}_{ry}$ and $\bar{K}_x$, whose imaginary components represent the effects of damping.
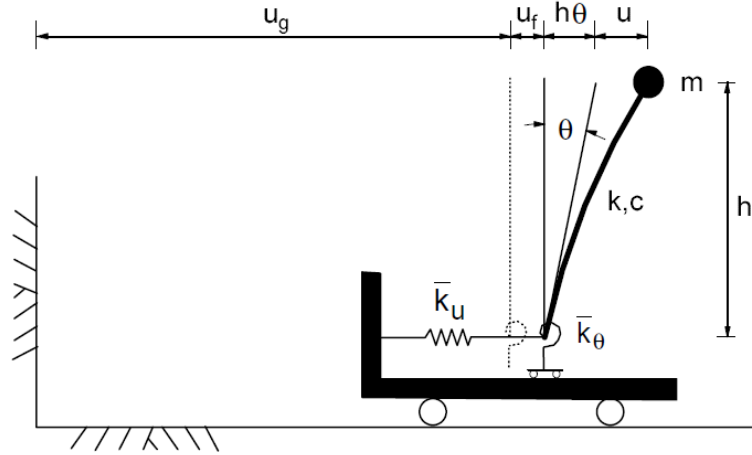
Figure 78 *: Simplified model for the analysis of the inertial interaction*

Veletsos and Meek (1974) found that the maximum seismically induced deformations of the oscillator in Figure 78 could be predicted accurately by an equivalent fixed-based single degree-of-freedom oscillator with period $\bar{T}$ and damping ratio $\bar{\xi}$.

Following this approach, it is therefore possible to calculate the period $\bar{T}$ and the equivalent damping $\bar{\xi}$ of the soil-structure system. $\bar{T}$ can be calculated from the following expression, in function of the period T_0 of the fixed-base oscillator:

$$\bar{T} = T_0 \sqrt{1 + \frac{k}{K_x}\left(1 + \frac{K_x}{K_{ry}}h^2\right)} \qquad (3.14)$$

Where:

- k is the stiffness of the oscillator, taken equal to $3EI_y/h^3$;
- K_x and K_{ry} are the static stiffnesses of the foundation, computed in Table 29;
- h is the height of the pier. In order to compute the equivalent damping for the viaduct using this simplified model, it was decided to calculate the equivalent period with a value of h that is the average height of the piers of the entire

viaduct; in accordance with the model presented in paragraph §2.1, the height of each pier has been considered as the distance between its base and the plane of the supports.

Once evaluated the equivalent period, it is possible to compute the equivalent damping factor through the following expression:

$$\bar{\xi} = \left(\frac{T_0}{\bar{T}}\right)^3 \left[\xi + \frac{(2-v)\pi^4\delta}{2\sigma^3}\left(\frac{c_x\,r^2}{k_x^2\,h^2} + \frac{c_{ry}}{k_{ry}^2}\right)\right] \tag{3.15}$$

Where:

- r is the equivalent radius of the foundation, that is the equivalent radius of a circular foundation with the same area of the rectangular one under examination;

- δ is the ratio between the average density of the structure and that of the foundation soil, equal to:

$$\delta = \frac{m}{\rho\pi r^2 h} \tag{3.16}$$

- σ is the relative stiffness between soil and structure, represented as:

$$\sigma = \frac{T_0 V_s}{h} \tag{3.17}$$

- c_x, c_{ry}, k_x, k_{ry} represent the dynamic impedance coefficients.

As can be noted from the expression (3.15), the radiative damping rate, since part of the energy accumulated by the structure is transmitted to the soil and dispersed, produces an increase of damping with respect to the structural one ξ. However, the sum of the two damping contributions is reduced by the term $(T_0/\bar{T})^3$; this reduction is due to the fact that the rigid motion of the foundation decreases the proper bending displacements in the structure, thus reducing its capacity to dissipate energy [24].

The application of the simplified model given by Veletsos and Meek led to the following results, where it can be noted that, also in this case, the damping factor relative to the first mode is decreased with respect to that of the fixed-base structure.

$$\xi_{Vsmin} = 4.40\% \qquad \xi_{Vsmax} = 4.84\%$$

In order to understand how much the damping factors computed manually through the formulations of Roesset and Veletsos differ from those calculated by the code, the weighted damping factors computed by Midas GEN are shown in the following graphs.

The latter show the damping factors for a number of modes associated with a total participating mass in both the X, Y and Z directions equal to 90%, however neglecting those with an effective mass smaller than 1%. The modes considered were respectively *315* for V_{smax} and *147* for V_{smin}.
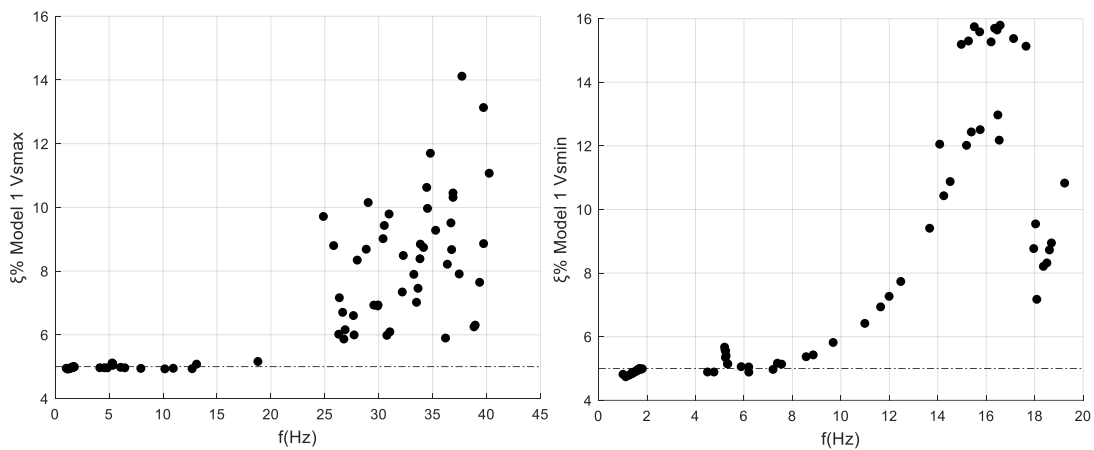
Figure 79 : *Modal damping factors in Model 1 Vsmin and Model 1 Vsmax*

As can be seen in the graphs above, obtaining the equivalent damping factor by weighing by means of the strain energies exclusively with respect to the deformation in the first mode, leads to results compatible only with the lower modes; indeed in the higher ones evidently the damping rates linked to the rigid translation of the foundations, set equal to 20%, play a fundamental role, making the weighted damping much larger than 5%.

It is deduced that the simplified method introduced by Veletsos and Meek doesn't fit the calculation of the weighted damping for the viaduct, as it underestimates the damping for higher frequencies, associated with non-negligible effective mass. Furthermore the weighted damping factor computed by the code for the first mode is equal to 4.8% for V_{smin} and 4.95% for V_{smax}.

The response spectrum modal analysis carried out in Midas GEN, following the passages previously exposed in paragraph §2.3.3, through the damping factors shown

143

in Figure 79, led to the following results in terms of base shear in the transversal and longitudinal directions of the viaduct:
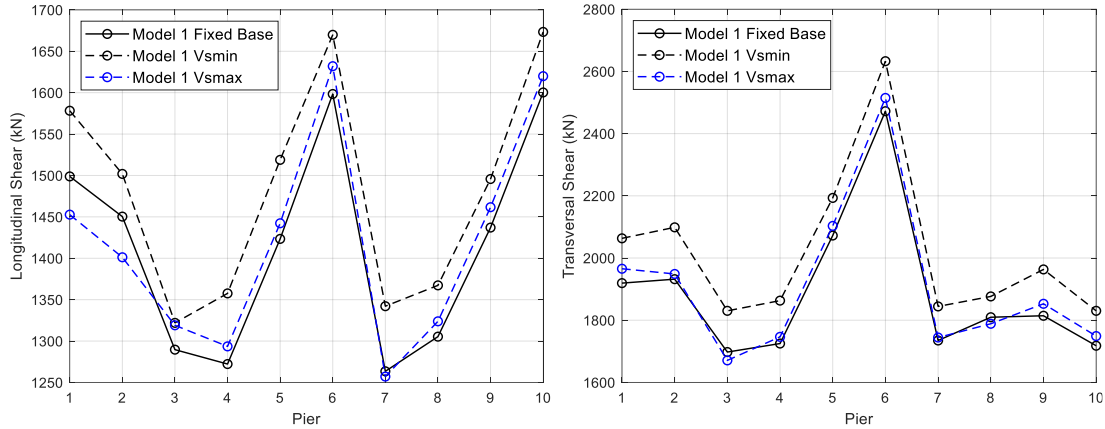
Figure 80 *: Transversal and longitudinal shear in Model 1 according to RS analysis*

From the graphs above, showing the value of the shear of the piers for the three models, can be observed that, for V_{smin}, the shear visibly increases compared to that of the fixed-based model. The same trend can be observed for the case of V_{smax}, where however this increase is less significant.

This behavior is consistent to the evaluated weighted modal damping factors; it can be noted, for example, that in the first mode ξ is smaller than 5% for both models that consider the soil-structure interaction; in particular it is smaller for the V_{smin} model, consequently leading to larger values of stresses. Finally, the following trends indicate that the percentage errors with respect to the fixed-based model decrease as the shear waves velocity increases:
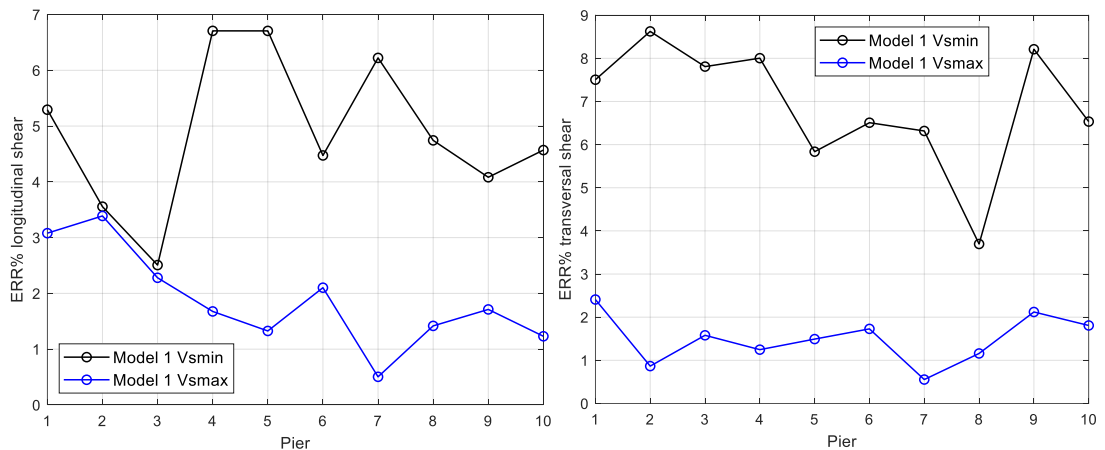
Figure 81 *: ERR% with respect to the fixed-base model of the base shear for RS analysis*

144

The introduction in the model of the dynamic soil-structure interaction produces, according to the results of the RS analysis, a generalized increase in the displacements at the top of the piers for both models, which, as can be seen from the following graphs, is more significant for the model associated with the highest level of soil deformability:
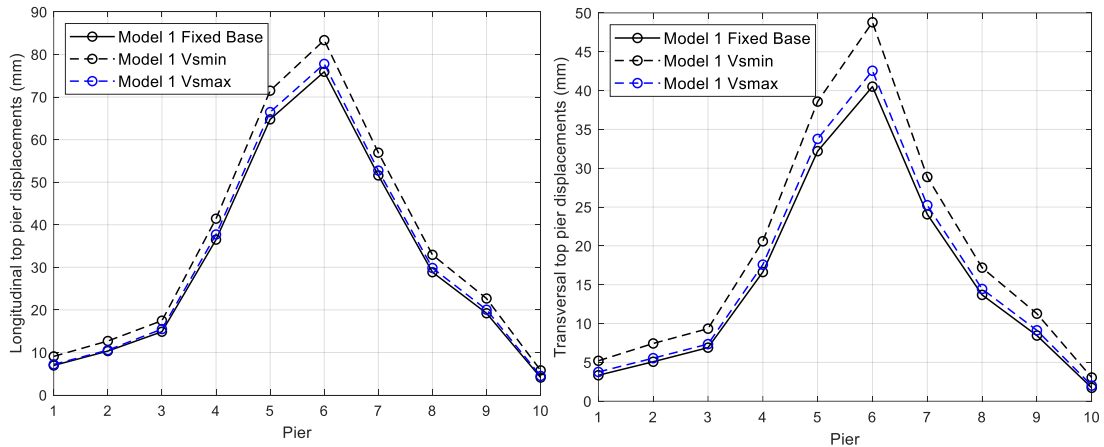
Figure 82 : *Transversal and longitudinal top pier displacements in Model 1 for RS analysis*

This is compatible to the fact that the natural periods have generally increased with the introduction of the soil-structure interaction, more significantly for the model associated to a smaller shear waves velocity, with a consequent increase in the spectral ordinates in terms of displacement. Moreover, the displacements at the top of the pier, as expected, are smaller in the transversal direction, since the pier is stiffer in its bending in the YZ plane. However, as can be observed from the following graphs, the maximum percentage errors with respect to the fixed-base system have been obtained for the longitudinal top displacement of Pier 10.
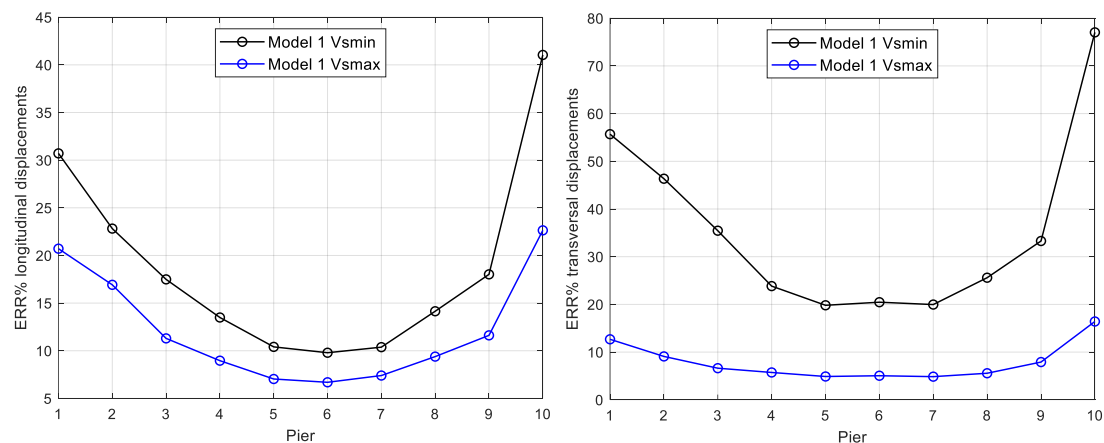
Figure 83 : *ERR% with respect to the fixed-base model of the top pier displacement for RS analysis*

Finally, from the response spectrum analysis results, the checks on the bearings deformation can be derived: the shear deformation values in both models, shown in Appendix for each bearing, range between a maximum of 110% and a minimum of 40%. With regard to the shear deformations of the supports, the analysis with response spectrum appears less conservative than that for direct integration.

Indeed, in the RS analysis, the deformations don't exceed the limit of 75% even for the bearings of Pier 5 in the V_{smin} model and for pier 6 in the V_{smax} model, in addition to those of Pier 8 also verified in the case of direct integration time history analysis. Finally, the checks on the friction between the support and the deck beam are satisfied in the RS analysis results for all supports.

It may be useful to make a comparison between the results obtained in the two types of analysis, both in terms of base shear and top displacement of the piers, in order to understand whether the modal analysis carried out through the weighted damping can actually be a valid alternative to the time history analysis by direct integration, being the latter associated to higher computational costs.

The percentage errors of the shear values obtained through the response spectrum analysis with respect to those coming from the direct integration, are shown in the following trends, for both the SSI models:
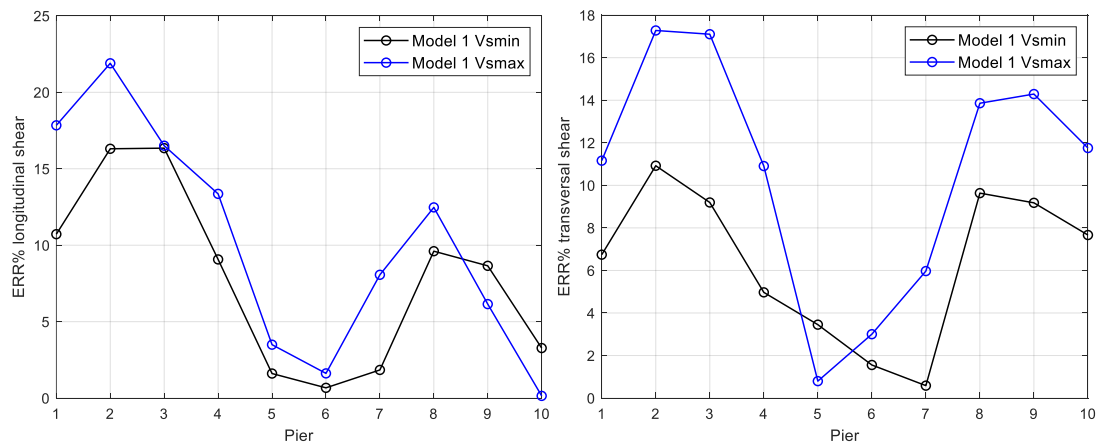
Figure 84 : ERR% of shear in RS analysis with respect to DI results

From the results displayed in the graphs above, it can be noticed that the errors are certainly not negligible for the end piers of the viaduct, as they reach a value even

146

higher than 20%. On the other hand, for the piers of the central spans of the viaduct, the percentage errors are acceptable both considering the transverse and the longitudinal shear. However, the causes of the discrepancy in the results of these types of analysis are not attributable a priori to the way in which the distribution of dissipations in the structure is taken into account in the modal analysis. In fact, the differences could be due to the fact that each accelerogram doesn't precisely follow the trend of the design elastic spectrum, since it is characterized by oscillations around its values. Furthermore, in the direct integration analysis, the Rayleigh damping curve in correspondence of some frequencies in the range of interest is associated with a damping factor smaller than 5%, which for higher frequencies increases noticeably. On the other hand, however, the response spectrum analysis has a degree of accuracy which is significantly influenced by the entity and the number of modes considered.

Taking into account these considerations, it was decided to carry out a comparison, in the fixed-based model, between three types of analysis: the already in-depth time history analysis through direct integration, the modal analysis with response spectrum, and finally a linear modal superposition time history analysis with a 5% damping factor for all the modes considered. It is necessary to point out that, for the analysis, a number of modes such that the sum of the effective mass along X, Y and Z was equal to 90% was considered. Subsequently, for the response spectrum analysis, among the modes, only those with a participant mass larger than 1% were selected.

 The results are shown in terms of percentage errors with respect to the linear modal time history analysis:
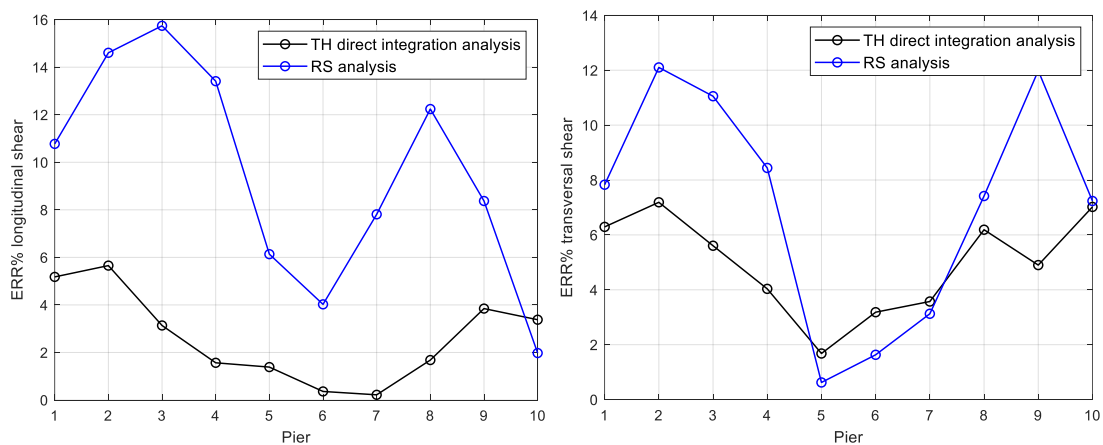
Figure 85 *: ERR% of RS and DI shear base with respect to the modal superposition analysis results*

147

The results of the modal superposition analysis turned out to be closer to those of the direct integration than those coming from the response spectrum one. It can therefore be deduced that the Rayleigh curve constructed for the direct integration analysis appropriately represents the damping coefficient in the frequency range of interest, and that therefore the differences in the results are to be attributed to the modes considered for the response spectrum analysis.

However, it was not considered appropriate to increase the number of modes that come into play in the RS analysis, since, to obtain the results associated to the errors of Figure 85, the *464* modes necessary to obtain 90% effective mass in the three directions had already been considered.

Considering the longitudinal displacements, in the comparison with the analysis by modal superposition, the RS analysis produces larger errors than the TH analysis through direct integration. In the transversal direction, on the other hand, for almost all the piers the latter is instead associated with higher percentage errors, although the maximum value, equal to 9%, is obtained for the response spectrum analysis.
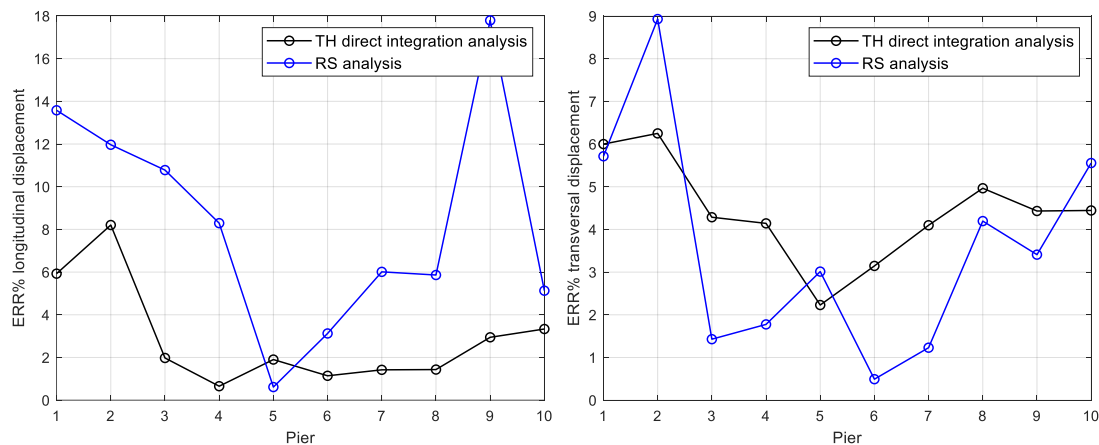
Figure 86 : *ERR% of RS and DI top pier displacements with respect to the modal superposition analysis results*

3.1.3 Shear and bending checks at the pier base

After the evaluation of the forces and displacements in the linear models that consider the dynamic soil-structure interaction, it can be appropriate for completeness to evaluate whether the preliminary design of reinforcement of paragraph §2.1 actually satisfies the checks on the piers in terms of shear and bending.

The verifications were made according to the results of the TH analysis through direct integration; it was arbitrarily chosen to carry out the verification exclusively on the model characterized by shear waves with velocity V_{smax}, since the results shown in the previous paragraph show how the differences in internal forces and displacements for the two models V_{smax} and V_{smax} are negligible.

As regards the bending check on the highest pier, it was decided to consider the maximum values of the moments along X and Y as acting on the pier, although it couldn't be necessarily the worst condition; the choice is due to the fact that, carrying out the verification for each pair of values Mx and My, would have been associated to a too high computational cost.

The axial force was instead set equal to the sum of the axial force coming from the gravitational loads and the worst condition between the average of the maximum dynamic compression forces and the average of the maximum tension ones. For consistency with what was done for the preliminary check of the pier reinforcement, a reduction coefficient of 3.5 was applied to the internal forces due to dynamic loads. The forces acting on Pier 6 are therefore:

M_x	M_y	$N_{compression}$	$N_{tension}$
13732.14 kN m	7898.68 kN m	6058.16 kN	5511 kN

Table 36 : Bending and compression forces on Pier 6

The $M_x, M_y,$ N domain defined, as in paragraph §2.1, from the parabola rectangular law for concrete and from an elastic-perfectly plastic behavior for steel, is shown in the following diagram:
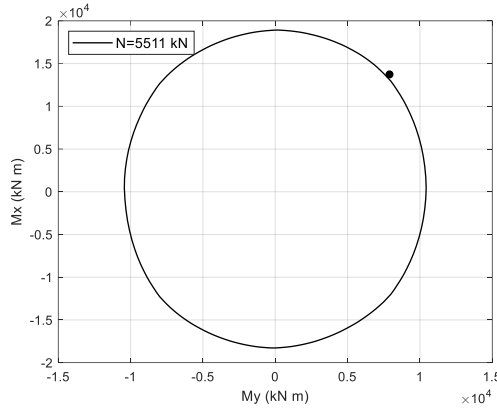
Figure 87 *: My Mx N domain for N=5511 kN in Pier 6*

Figure 87 shows how effectively the forces acting on the piers correspond to a point on the edge of the domain.

The shear verifications were instead carried out starting from the expression of the shear strength provided by the NTC 2018 for elements without the presence of shear resistant reinforcement; this choice was made considering the fact that the transverse reinforcements, although present, are not closed. The shear resistance was thus evaluated as:

$$V_{Rd} = max \left\{ \begin{array}{l} \left[0.18 \, k \, \frac{(100 \, \rho_1 \, f_{ck})^{\frac{1}{3}}}{\gamma_c} + 0.15\sigma_{cp} \right] b_w \, d \\ (\nu_{min} + 0.15\sigma_{cp})b_w d \end{array} \right. \qquad (3.18)$$

Where:

- d is the effective depth of the section;
- $k = 1 + (200/d)^{1/2}$;
- $\nu_{min} = 0.035 \, k^{3/2} f_{ck}^{1/2}$
- ρ_1 is the is the geometric ratio of tension longitudinal reinforcement which extends for more than $(l_{bd} + d)$ beyond the section considered, where l_{bd} is the anchor length;
- σ_{cp} is average compression stress in the section, computed starting from the axial forces listed in Table 37.
- b_w represents the minimum section width;
- γ_c is the concrete safety factor.

Considering the evaluation of the parameter d, since the section has an octagonal rather than a rectangular shape, only the length parallel to the X or the Y axis was conservatively considered.

The checks were carried out for the piers in which the maximum value of the shear in the longitudinal and transverse direction was found, that are respectively Pier 2 and Pier 6. The forces acting on the elements are therefore:

V_x Pier 2	V_y Pier 6	N_{compr} Pier 2	N_{compr} Pier 6
616.11 kN	813.44 kN	4844.1 kN	6058.2 kN

Table 37 : Shear and compression forces on Pier 2 and Pier 6

The equation (3.18) leads to the following values for the shear strength:

V_{Rx} Pier 2	V_{Ry} Pier 6
790.5 kN	1166.9 kN

Table 38 : Shear strength for Pier 2 and Pier 6

As can be seen from Table 38, the piers considered satisfy the shear resistance checks. However, it is necessary to take into account that the results of Model 1 were obtained through linear analysis, where the non-linearities were taken into account through the behavior factor q, computed with the current standards. The option to study the dynamic response of a new model seems therefore appropriate, in which the non-linearities could be included through the material constitutive laws.

3.2 Analysis on Model 2

As described above, Model 2 was realized through a deck modeled with a beam grillage. Moreover, the presence of transverse seismic restraints was simulated through scale factors applied to the bearing section shear stiffness in the transversal direction of the bridge. Finally, the non-linearities at the base of the pier were introduced through a fiber formulation, already introduced and in-depth in paragraph §2.2.

The plastic hinge region, in order to avoid too high computational costs, has been limited to a length from the pier base computed following the prescriptions of the current standards:

$$L_{pl} = 0.1 L_v + 0.17\, h + 0.24 \frac{d_{bl} f_y}{\sqrt{f_c}} \tag{3.19}$$

Where:

- L_v is the distance measured along the pier axis between the base and the section characterized by zero bending moment, taken in this case equal to the whole pier height;
- h is the section height; in the case at study it was taken as the maximum dimension in the octagonal section, in order not to underestimate the length of the plastic hinge region;
- d_{bl} represents the longitudinal bars diameter;
- f_c and f_y are respectively the concrete compressive strength and the yield strength of the longitudinal steel.

As can be seen in the following table, the non-linear behavior has been attributed to the first two finite elements of length L_{EF} in which the pier is discretized starting from its base. In fact, it is the minimum number of finite elements that must be considered so that the total length in which the non-linear behavior is attributed is larger than L_p.

Pier	L_{EF}	L_p	$L_{tot} = 2L_{EF}$
1	1.36	1.70	2.72
2	1.62	1.83	3.24
3	1.62	1.99	3.23
4	1.53	2.40	3.07
5	1.50	2.67	3.00

6	1.54	2.71	3.07
7	1.45	2.61	2.89
8	1.56	2.27	3.13
9	1.47	2.05	2.94
10	1.33	1.55	2.65

Table 39 : Length of the plastic hinge region in the piers

The eigenvalue analysis, whose results in terms of natural period are shown in the Appendix, similarly to what was obtained in Model 1, shows how the introduction in the model of the soil-structure dynamic interaction doesn't lead to a significant increase in periods. This can be noted by the percentage errors of the first natural period in the models calculated from V_{smin} and V_{smax} with respect to that of the fixed-based model, equal respectively to 2.97% and 0.69%. In the previous paragraph, the fact that such percentage errors are not associated with significant effects in terms of base shear and displacement in the structure was observed, especially considering the results of the time history analysis for direct integration. Since the latter will be the type of analysis used for the non-linear dynamic analysis of the current paragraph, it was decided to select the V_{smin} model, in which the maximum percentage errors in terms of natural period were found, to carry out the next analysis.

3.2.1 Direct integration: non-linear time history analysis results

The direct integration non-linear time history analysis was performed as explained in paragraph §2.3.1 for the non-linear case, with the same fiber discretization of the non-linear model of the single pier analyzed in paragraph §2.4.1 and displayed in Figure 47. Moreover, the seven spectrum compatible groups of time histories generated through SIMQKE have been obtained from the values of Table 17.

The frequency domain of interest for the Rayleigh damping was defined considering 32 modes in this Model, since the 32nd is the first mode with a significant effective mass for the translation along Z. The range for the frequency of interest in this model thus includes values from 0.97 Hz to 5.4 Hz, with a Rayleigh curve created from the following values in the system (2.68), shown in Figure 37.

153

ξ_1	ξ_2	f_1	f_2	α	β
0.06	0.065	0.8 Hz	7 Hz	0.556	0.003

Table 40 : Parameters of the Rayleigh curve in fixed-base Model 2

The results of the non-linear time history analysis of the structure subjected to the seismic action of the Sordo Viaduct site are mainly preparatory to those carried out in the following paragraph. Precisely, through its results, the following structural elements have been identified:

- The pier in whose base section the concrete fiber characterized by the maximum compressive deformation was present;
- The pier in whose base section the steel fiber characterized by the maximum tension deformation was present;
- The pier subjected to the maximum base shear;
- The bearings with the maximum longitudinal shear deformation.

The non-linear time history analysis, carried out starting from the time histories generated at the SLC with the parameters of the site in question, can also be useful to have an estimate of how much the ductility at the base of the pier was actually exploited. As expected, given the large cross-sectional dimension of the pier shaft with respect to its small amount of reinforcements, the compressive concrete strains are not very large; in fact, the concrete fibers remain all in the elastic range under the site seismic action, while the steel fibers have all exceeded the yielding limit. The following figure shows the tension steel fiber state in the last step of the analysis, and the stress strain curve of one of the steel fibers, in which the hysteretic cycles of the Menegotto and Pinto constitutive law can be observed:

154
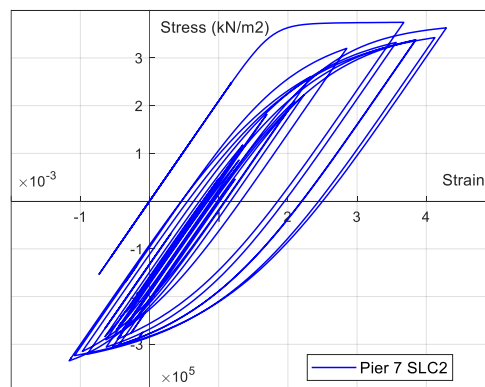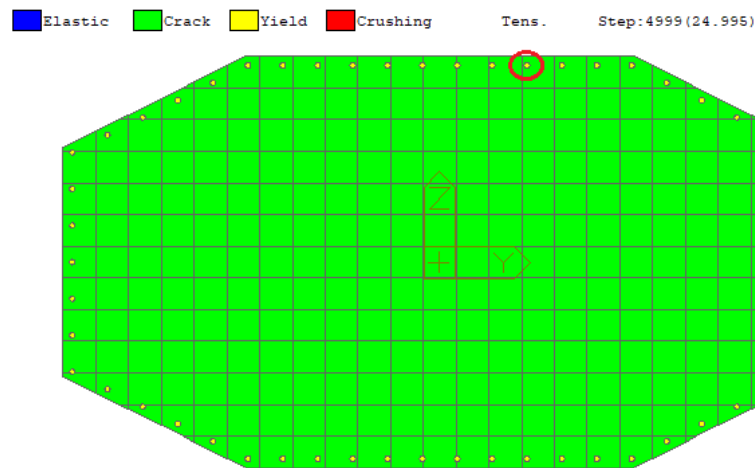
Figure 88 : Steel fiber stress strain law of Pier 7 (Top) and tension fiber state in Pier 7 base section

The Kent and Park constitutive behaviour attributed to the steel fibers produces the concrete cracking from the first step of the time history analysis; considering steel, on the other hand, after a linear branch, the loading and unloading cycles after the yield limit described in paragraph §2.2.2 for the Menegotto and Pinto model can be observed in the graph above.

3.2.2 Incremental Dynamic Analysis (IDA)

The incremental dynamic analysis, is a parametric method recently emerged which aims at evaluating the performance of a structural system subjected to seismic action. It involves subjecting a structural model to one or more ground motion records, each scaled to multiple levels of intensity, thus producing response curves in function of the intensity level. Consequently, it implies several dynamic analysis, where each step is referred to an accelerogram scaled by an appropriate scale factor.

The IDA is a multi-purpose and widely applicable method; among its objectives the deep understanding of the range of response versus the range of the potential ground motion plays an important role, together with the purpose of evaluating the structural implications that could occur due to a severe ground motion level.

Moreover, it allows to investigate the changing in the structural response due to the increase of the ground motion intensity, providing also an estimate of the dynamic capacity of the structural system. A crucial point concerns the choice of an intensity

measure (IM) parameter that could fully describe the importance of the seismic action, and a damage parameter (DP) that could be able to represent the dynamics response of the structure. As regards the former, IMs are typically related to the characteristics of ground shaking and to the dynamic properties of the structure. While the spectral acceleration at the first and dominant mode of vibration is a widely used choice in the case of buildings, in bridge structures, where no single dominant mode typically exists and given the importance of higher modes in the structural response, the use of spectral acceleration corresponding to a single mode of vibration will probably turn out to be inefficient because of a multi-modal structural response [25]. To take into account these considerations, the peak ground acceleration, chosen as intensity parameter in the current thesis, has become a popular IM for the incremental dynamic analysis in bridges.

Instead, more than one DP were selected as damage parameters, in order to have a complete view of the evolution of the structural response with the increase of the seismic intensity measure. In detail, for the pier, the maximum deformations of the steel and concrete fibers were selected, as well as the maximum shear at the base of the piers themselves. It was also chosen to analyze the evolution of the longitudinal shear deformation in the supports, as representative of the structural response of the viaduct.

Before going into the specific aspects concerning the application of the method, it is necessary to provide some definitions to fully define the terminology and the quantities that will be used in the following.

Given the vector $\boldsymbol{\lambda}^k$, which collects the scale factors of the *k-th* accelerogram:

$$\boldsymbol{\lambda}^k = \left(\lambda_1^k, \lambda_2^k, \dots \lambda_n^k\right) \tag{3.20}$$

the Scale Factor (SF) of a scaled accelerogram $\boldsymbol{a}_{\lambda_i}{}^k$ is the non-negative scalar $\lambda_i^k = [0, +\infty)$ that produces $\boldsymbol{a}_{\lambda_i}{}^k$ when multiplicatively applied to the unscaled acceleration time history $\boldsymbol{a}^k$. Consequently, applying a scale factor smaller than 1 to the accelerogram, generates a decrease in the seismic action acting on the structure and vice versa. Although the SF is the simplest way to characterize the scaled images of

156

an accelerogram, it is not compatible with reality from a seismic point of view, since seismogenic phenomena cause earthquakes recordings of different intensities, which qualitatively manifest substantial differences [26].

The non-negative scalar $I_{\lambda_i}^k \in [0; +\infty)$ is instead the value assumed by the seismic intensity parameter IM relating to the k-th accelerogram $\boldsymbol{a}_{\lambda_i}{}^k$ scaled through the relative scale factor λ_i^k:

$$I_{\lambda_i}^k = \lambda_i^k\, I^k \qquad\qquad (3.21)$$

Finally the Damage Measure (DM) or Structural State Variable, is a non-negative scalar $D_{\lambda_i}^k \in [0; +\infty]$ that characterizes the response of the structural model due to a prescribed seismic loading [27]. A DM is therefore an observable quantity that is part of, or can be deduced from, the output of the corresponding non-linear dynamic analysis.

A Single-Record IDA Study is a dynamic analysis study of a given structural model parameterized by the scale factor of one ground motion time history. It involves a series of dynamic non-linear analysis performed under scaled images of an accelerogram, selected in such a way as to cover the whole range from elastic to non-linear, until failure.

The results of the S-R IDA should be a continuous curve showing the trend of the damage parameter in function of the IM variation. However, the results are given as discrete points to be interpolated in the diagram, because of the discrete increments of the scale factor. If the interpolated IDA curve is considered, it can be defined as a representation of the link between the damage parameter and the seismic intensity parameter, that is the cause-effect relationship.

If, on the other hand, the observations refer to a set of accelerograms scaled by appropriate scale factors, the incremental dynamic analysis is named Multi Record Incremental Dynamic Analysis (MR-IDA). The result of this analysis is a set of interpolated curves that report the trend of the damage parameter in function of the seismic intensity measure. In particular, seven groups of time histories will be used in the current thesis, for consistency with what is prescribed by current standards,

according to which the response of the structure can be evaluated as the average of the most unfavorable effects. From the results deriving from the seven groups of accelerograms, the median curve was evaluated, in order to make a comparison with the limit values set for the chosen damage parameters.

It should be pointed out that the IDA is accelerogram specific: when subjected to different ground motions, a model will produce quite different responses which are difficult to be predicted a priori. This behavior can be easily observed from the results given in [27], where a five-storey frame subjected to four different records is shown in the following figure:
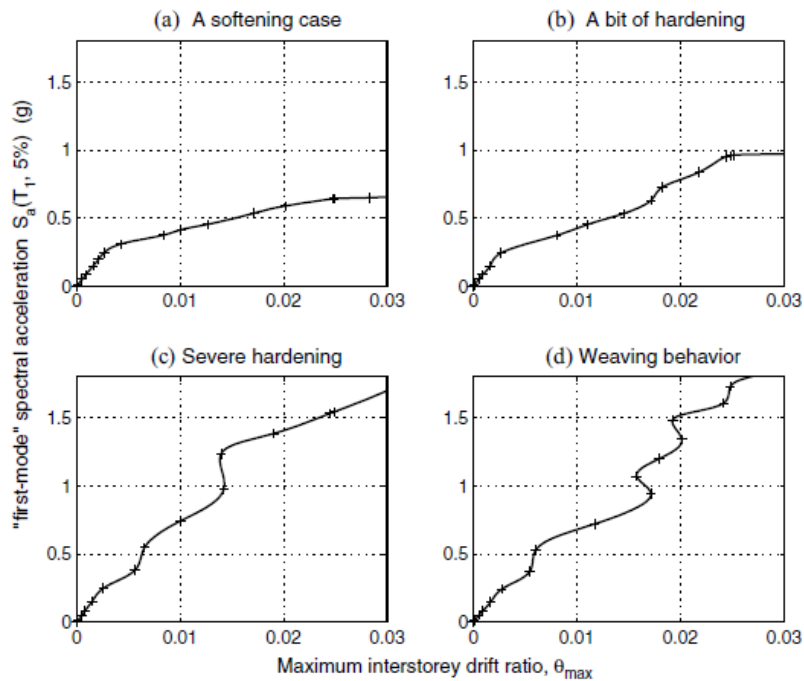
Figure 89 : *IDA results for a five-storey frame subjected to four different records*

All curves represented in Figure 89 exhibit a distinct elastic linear region, which is consistent to the fact that for small stress values a linear elastic behavior is expected in the structure, until any element reaches the elastic limit.

It should also be observed that the curve (a), after the linear elastic phase, is characterized by a softening branch: after reaching a certain value of seismic intensity, the value of the damage parameter rapidly increases, accelerating towards large drifts and eventual collapse. This behavior is due to the loss of stiffness associated to a given value of the seismic intensity. Curve (b) is instead characterized by a hardening phase

between the linear branch and the softening one, whereas curves (c) and (d) seem to weave around the elastic slope; in their hardening branches small increases in the damage parameter are associated to significant increment in the seismic intensity parameter. The twisting patterns which characterize the curves (c) and (d) displays that the structures experienced both acceleration and deceleration in the DM accumulation. The latter could be of such significance as to stop the DM accumulation or reverse it, consequently making it a non-monotonic function with respect to the intensity measure, as in case (d).

The incremental dynamic analysis was carried out for the following scale factors, with an associated PGA ranging from 0.08 g to 0.96 g:

$$\lambda^{SLC} = (0.25, 0.5, 0.75, 1, 1.25, 1.5, 1.75, 2, 2.3, 2.6, 3)$$

The damage parameters chosen regard the structural elements for which the maximum values in terms of internal forces and deformations have been obtained in the model with the SF equal to 1.

Once performed the analysis for the seven groups of accelerograms, the discrete points were interpolated separately for each accelerogram, thus obtaining continuous curves showing the relationship between the intensity measure, represented by the PGA, and each of the damage parameters selected for a given ground motion. Finally, the median curve was evaluated and compared to the stress and strain limits selected.

Given the results obtained for the non-linear time history analysis with a scale factor equal to 1, illustrated in the previous paragraph, it is expected that the failure at the base of the pier occurs when the ultimate deformation of steel rather than the ultimate compressive concrete strain is reached; therefore, it was decided to take the tensile steel deformation as first damage parameter to be analyzed. In the following curve each interpolated point represents the maximum tensile strain among those of the steel fibers of the base section of Pier 6, when the structure is subjected to the k-th SLC_k accelerogram scaled through a component of the λ^{SLC} vector. It should be pointed out that, since the limit for the tensile steel strain doesn't appear explicitly in the constitutive law, its ultimate deformation has been conventionally set equal to 1%.
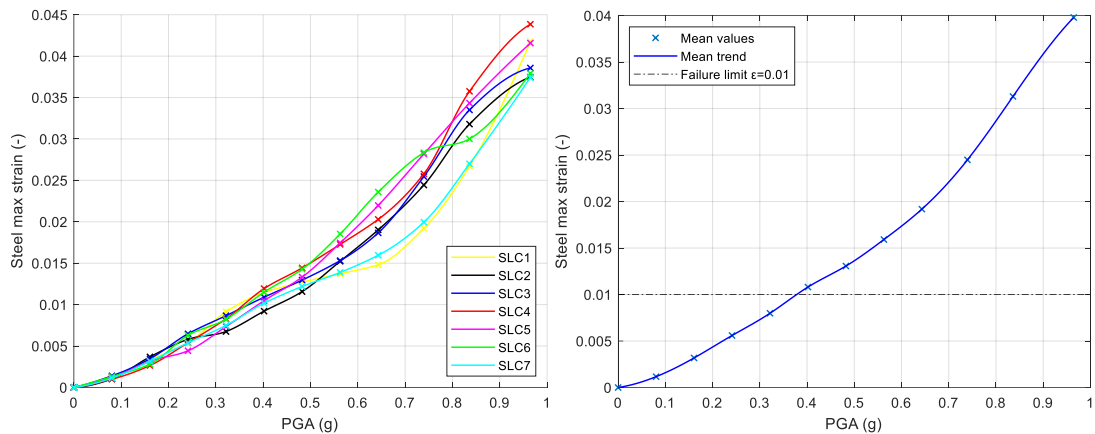
Figure 90 : *IDA for the fiber maximum tensile steel strain in the base of Pier 6*

In the graphs above, similarly to that displayed in Figure 89, it can be noticed that different ground motions produce significantly different responses, after a first branch associated with small values of the seismic intensity parameter, in which they are characterized by a similar trend. The weaving around the initial slope is particularly evident for the time history SLC6, while the ground motions SLC7 and SLC1 present a large branch in which the increase of the intensity parameter produces a small increase in the damage one, represented by the steel deformation. Finally, the values of the median curve show that the site PGA, equal to 0.32 g, doesn't correspond to the selected deformation limit, which is reached instead for a PGA equal to about 0.4 g. The second damage parameter considered for the incremental dynamic analysis is the maximum compressive deformation experienced by the concrete fibers in which the section at the base of Pier 6 is discretized.
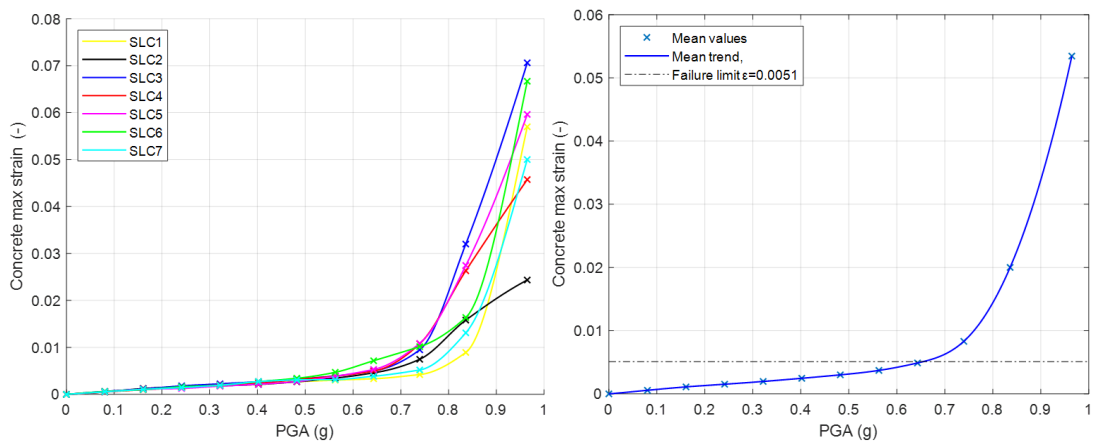
Figure 91 : *IDA for the fiber maximum compressive concrete strain in the base of Pier 6*

160

The trend of the curves about the concrete deformation, unlike those of steel, follows the behavior similar to that of curve (a): after reaching a certain value for the seismic intensity parameter, an acceleration in the damage accumulation is experienced; consequently, small increases in the IM correspond to large increments in the damage parameter. Furthermore, for PGA up to about 0.5 g there is an almost linear behavior between cause and effect, until the 0.0051 ultimate deformation is reached in correspondence to an intensity parameter of about 0.7 g. From the comparison between the results about the concrete and steel fibers, it can be noticed that the latter reach their ultimate limit for smaller values of seismic input. The analysis of the stress-strain curve of the considered steel and concrete fibers for the PGA closest to that associated with their ultimate deformation can be interesting; The following graphs show the curves for a scale factor for steel and concrete respectively equal to 1.25 and 2:
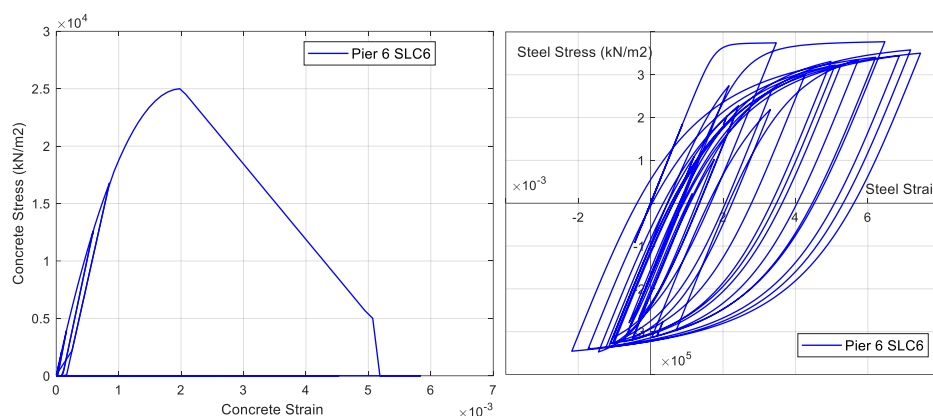
Figure 92 : Stress-strain curve for a Steel fiber (SF=1.25) and a Concrete fiber (SF=2) in Pier 6

As in the stress-strain curve of the steel fiber, the characteristics of the hysteresis cycles of the Menegotto and Pinto model can be easily identified, while in the concrete fiber the non-linear branch followed by the decreasing linear one typical of the Kent and Park constitutive model is identifiable; after a few cycles of loading and unloading, the concrete fiber reaches its ultimate deformation, equal to the value 0.0051 set in the constitutive non-linear material properties.

The shear checks on the section at the base of the pier were carried out in post-processing, through an IDA curve that allowed the comparison between the maximum shear forces acting at the base of the pier along the X and Y direction and the shear strength calculated in accordance with the expression (3.18), in which the evaluation

of the compressive axial forces acting at the pier base was also necessary. Firstly, the shear along the transversal and longitudinal direction was considered in function of the PGA; then the DP was represented by the ratio between the average shear values obtained for each scale factor and the shear strength; the checks will be on Pier 2 and Pier 10 respectively for the shear along the transversal and longitudinal directions.
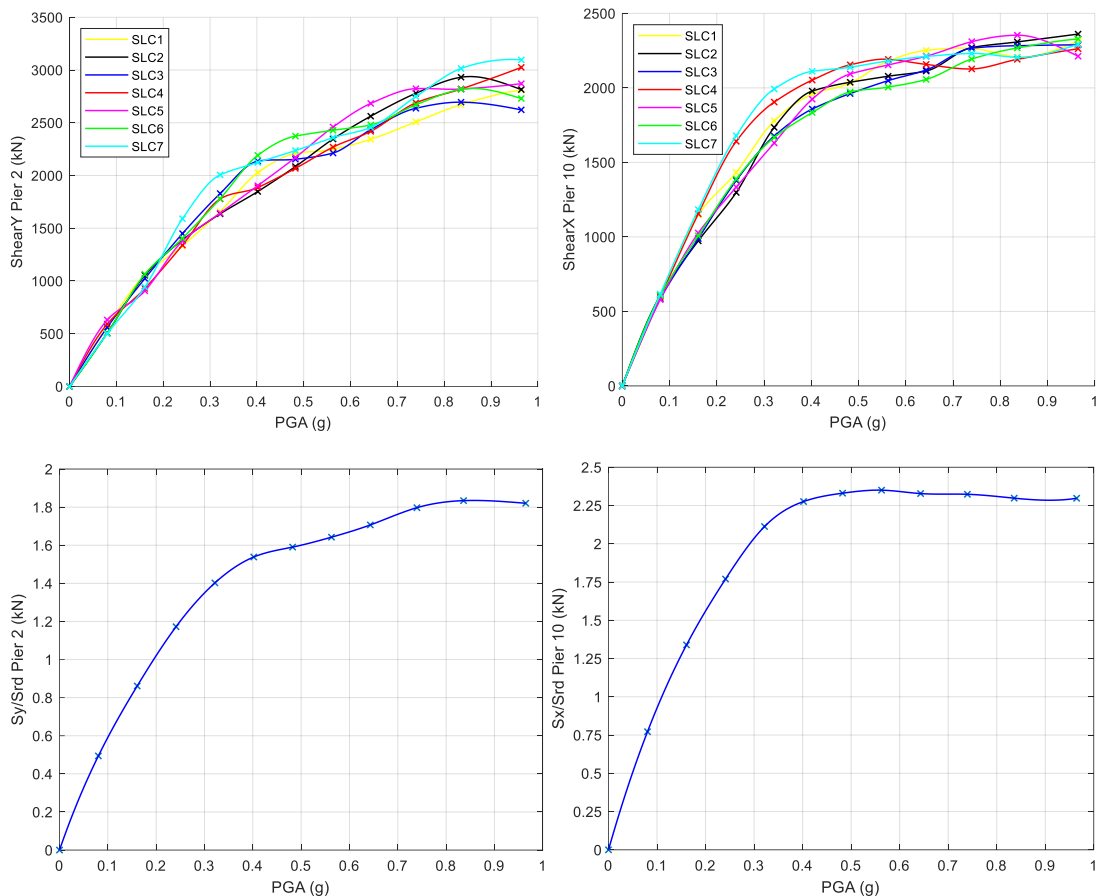
Figure 93 : IDA for the shear base in Pier 2 and Pier 10

The graphs representing the ratio, in the median curve, between the acting and the resistant shear show that the shear strength of the pier is reached for a PGA equal to 0.2 g for the transversal shear and for 0.1 g for the longitudinal one. This indicates that the verification for the Pier 2 and Pier 10 is not satisfied, as the strength limit has already been exceeded for the intensity measure characteristic of the site, equal to about 0.3 g.

As already mentioned in the previous paragraphs, the excessive shear deformation of the neoprene supports is an important parameter for the response of the entire viaduct.

162

Therefore, the longitudinal shear deformation of the bearings was taken as the last damage parameter to be analyzed; the following curves show the results for the support in which the maximum value of the longitudinal shear was found for a scale factor equal to 1:
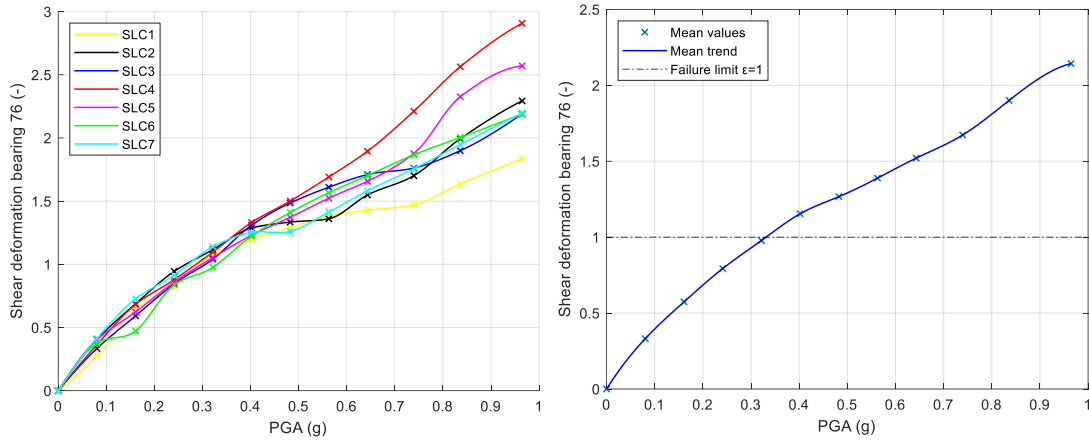
Figure 94 : IDA on the neoprene support 76 on Pier 9

Unfortunately, as can be seen from the graphs above, the supports do not verify the checks, as the deformation limit has been reached even for a scale factor equal to 1. Furthermore, the curves generated for each time history have the same characteristics of oscillation around to the initial slope for almost all accelerograms. Furthermore, the neoprene support has been modeled without considering the state of its state of degradation, since no reduction coefficient has been applied to the ultimate shear deformation; therefore, this consideration leads to the conclusion that the replacement of neoprene bearings is necessary, or alternatively, the retrofit by actual isolation devices can be carried out.

4

1:5 SCALE PHYSICAL MODEL OF A SPAN OF THE VIADUCT

4.1 Introduction to the shaking table

The RAFAEL project includes experimental tests on a physical model concerning the 1:5 scale reproduction of a span of the Sordo Viaduct. The tests that will be carried out on the viaduct concern both static and dynamic tests. The latter involve the use of an experimental tool, the shaking table. Although in the current work the results of these experimental tests will not be analyzed, it is useful, to have a vision of the purpose of the realization of the physical model, a description of the instrument on which the tests will be performed.

Dynamic tests on shaking tables are generally associated with small-scaled models, as in the case at study, as they are of limited size in plan, unable to include the entire length of the span. This typology of experimental test requires high accuracy both for the equipment used to apply the loads (usually servo-hydraulic actuators) and for the control system.

The shaking tables are earthquake simulators able to reproduce, on large prototypes, any real event recorded up to now: therefore, they represent the main test tool for evaluating the dynamic and seismic behavior of structures. The first tables were made between the end of the 60s and the early 70s, and were often used for testing scale models with linear elastic behavior, thanks to the development of electro-hydraulic servo-equipment, the improvement of hardware and tools for control and data acquisition [28]. From the late 90s, the tables became a subject of intense study and research for the development of a new test tools generation, with the following features:

- High accuracy in the reproduction of displacements;

- Dimensions such as to dynamically test many types of structures, on reduced scale, to evaluate the post-elastic behavior of the tested systems;

- Ability to accurately reproduce seismic inputs, characterized by large maximum ground displacements.

The seismic engineering laboratory of the ENEA research center in Casaccia (RM) has two shaking tables with 6 degrees of freedom among the largest in Europe. They allow to carry out triaxial seismic tests for the seismic qualification of systems and equipment for nuclear plants, in addition to the qualification of components and systems for industrial applications, rail transport, the aerospace industry, civil engineering and the protection of artistic heritage. It also allows to perform dynamic characterization and experimental verification of the effectiveness of innovative seismic protection technologies for delicate equipment and control systems for strategic post-seismic infrastructures [28].

The shaking table of the R.C. ENEA which will be used to perform the dynamic tests on the physical model is characterized by:

- a 4.00 m x 4.00 m platform;

- a maximum test load of 10 tons;

- a maximum peak acceleration equal to 3 g, in an unloaded board condition;

- a peak speed equal to 0.5 m / s;

- a maximum allowable displacement of ± 125 mm;

Figure 95 *: Shaking table, 4m x 4m, of the Research center ENEA Casaccia (Rome).*

4.2 Description of the physical model

The physical model consists of a 1:5 scale reproduction of a viaduct span, with limitations primarily due to the size of the shaking table, characterized by a 4 m x 4 m base, and secondly linked to the realization of structural elements with dimensions significantly reduced compared to those of the usual commercial production. The materials, dimensions and shapes of the cross sections of the elements follow those of the real viaduct, however with the introduction of some changes that represent the right compromise between the desire to make a good representation of the real viaduct and the actual production of the structural elements.

A representation of the physical model deck is given by the following figure:
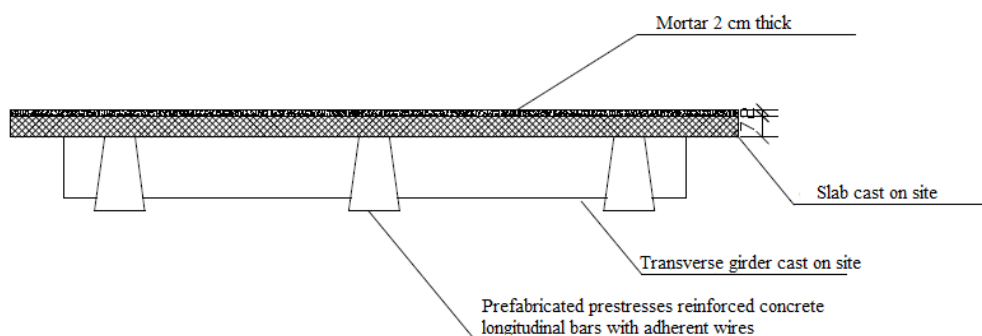
Figure 96 : *Transversal view of the deck*

As can be easily seen, in the scaled model, a configuration with three deck beams was chosen, increasing the width of the cross-section and modifying the position of the beams without significantly changing the structural response of the deck compared to a pattern with five longitudinal beams. Even the slab doesn't fully respect the scale factor in its thickness: instead of 4.4 cm corresponding to the 1:5 scale, a 7 cm thickness was considered, then balancing this increase with the choice of a material characterized by a small specific gravity, a lightweight concrete. Cross girders at the end and in the middle of the deck were cast on site, made with a class of concrete lower than that of the real viaduct, in order to balance their size, larger than that would be obtained by precisely respecting the scale factor, equal to 1/5. The following materials were used for the elements that constitute the model:

166

- The prefabricated beams are made with concrete class C40/50, with a maximum aggregate size of 12 mm; the prestressing reinforcement was realized with 3x3 strand with $fptk = 1860\ MPa$ and initial tension equal to *1300 MPa*;
- The cross beams, cast on site, are characterized by a class of concrete C25/30;
- The slab is made with structural concrete cast on site LC30/33;
- The ordinary pier and deck reinforcement is of type B450A;
- The pier, the cap beam and the foundation beam are made with a concrete class C25/30 class.

The piers, which rest on a foundation curb, were designed of different heights, equal to 3.2 m and 2.2 m, although the inclination of the deck around the transverse direction of the bridge was not represented in the model. The difference in height between of the piers was created through the introduction of a rectangular basement under the 2.2 m high pier, in order to increase the stiffness.

The cap beam top view and the side view of the scale model are shown below:
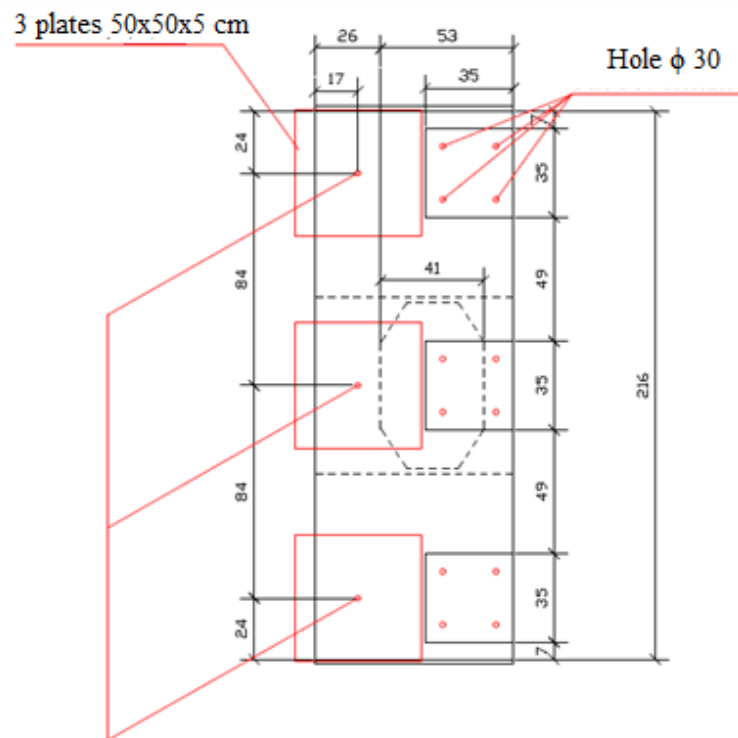
Figure 97 : *Top view of the cap beam*
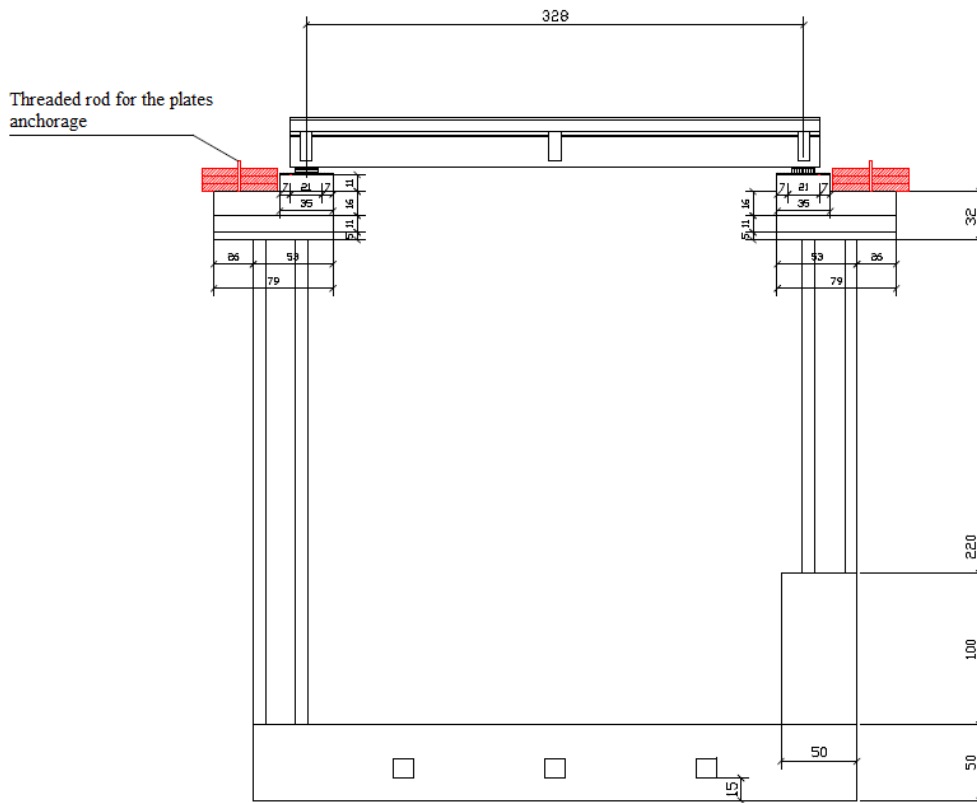
Figure 98 : Lateral view of the scaled model

As can be seen from the figures above, steel plates were introduced in both piers, anchored to the cap beam through a threaded bar, with the aim of simulating the presence of the adjacent deck. The number of plates for each threaded bar is equal to three, in order to avoid a too high total thickness, which could lead to unwanted collisions with the deck when the latter experiences displacements in the longitudinal direction after the placement of the seismic devices; this aspect was also taken into consideration through an increase in the height of the support rods, characterized by a size of 0.35 m x 0.35 m in plan. Given the presence of nine plates, a total mass of 900 kg weighing on each pier was simulated. Furthermore, given the insufficient size of the cap beam in the longitudinal direction, its dimension was increased, reaching a size of 79 cm. This operation has a double action, as it also allows to increase the weight on the pier. Plates were anchored to the supports with holes, characterized by a diameter ϕ 30 and a depth of 6 cm, on which the various types of isolation devices and non-reinforced neoprene supports will be placed to carry out the experimental tests on the scaled model. The plan view of the deck shows the presence of holes with

dimensions 5x10cm, in such a way as to allow the passage of the ropes for the deck lifting.
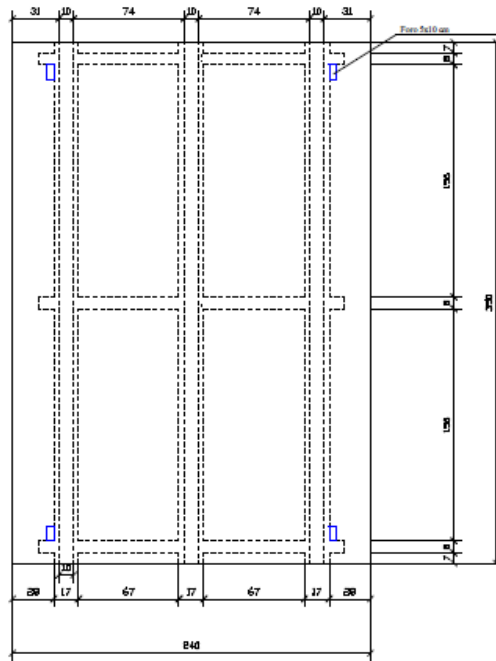
Figure 99 : Top view of the deck

Also in the foundation beam holes for lifting are present, in correspondence to which a diagonal reinforcement has been placed. The reinforcement pattern of the structural elements in the scaled model was designed with allowable stress method, as to reproduce faithfully the reinforcement of the Sordo Viaduct. Further drawings and pictures of the model are represented in the Appendix.
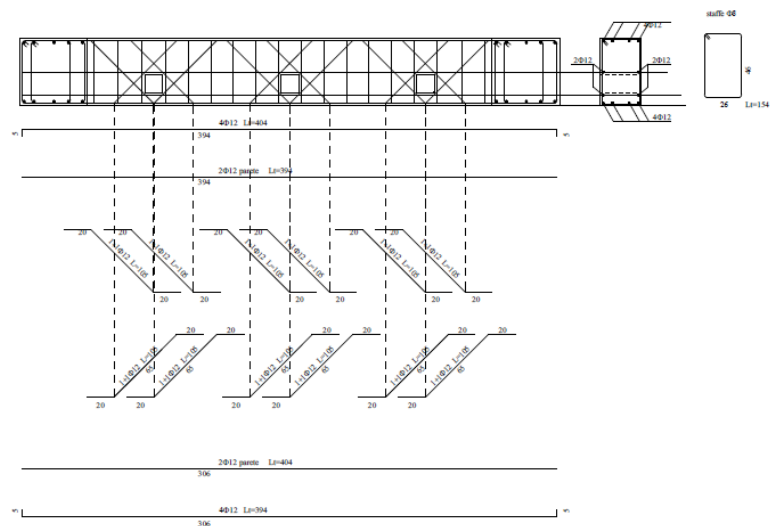
Figure 100 : Foundation beam reinforcement pattern

4.3 Preliminary design of the isolation devices

In Chapter 3 the modeling results, both in the linear and non-linear fields, led to the awareness of the need to replace the existing neoprene supports of the structure. The physical model, with the aim of studying the effects of the substitution of the supports on the response of the viaduct, was created in such a way as to be able to place several typologies of support between the substructure and the superstructure. The tests will initially be carried out separately, as well as with the pre-existing neoprene supports, for two types of modern isolation devices.

The current paragraph has the purpose of carrying out the preliminary design of these two device typologies; very interesting in a common design practice such as the pre-sizing, in the case at study, are the aspects that must be taken into consideration related to the scaled realization of the specimen. In fact, in this case, the resistance characteristics of the material weren't scaled, as the scaling was carried out exclusively on the length parameter.

In order to understand all aspects related to the preliminary design of the devices, the introduction of the general concept of seismic isolation in bridges is necessary.

A seismic isolation system consists of a set of isolation devices, placed between the substructure, which remains anchored to the ground and includes foundations, piers and abutments, and the superstructure, normally consisting of the deck, which remains seismically isolated. The set of devices constitutes the isolation interface.

The isolation system includes the connection elements and any additional constraints arranged to limit horizontal displacements due to non-seismic forces. Moreover, as for buildings, also for bridges the superstructure and substructure must remain in a substantially elastic range also for the ULS verification. Larger reliability is required of the isolation system, due to its critical role [29]. Among the specific design indications for bridges with seismic isolation, the following should be highlighted:

- The effects of the accidental eccentricity of the masses can be neglected;

- The separation joints between the different portions of the deck and between the deck and the substructure must be sized in such a way as to allow the proper functioning of the isolation system.

The isolation devices have in the first place the function of supporting vertical loads, with a consequent need of a large stiffness in the vertical direction; they must also be characterized by a small stiffness in the horizontal direction, in order to allow horizontal displacements, as well as by dissipative and lateral restraint capacity with adequate stiffness under non-seismic horizontal loads. The types of isolation devices widely used and dealt with in depth in NTC, which will also the two types chosen in the case at study, are:

- The reinforced elastomeric isolators, consisting of alternating layers of rubber and steel, whose dissipative capacity can be increased by inserting a lead tube;
- Sliding isolators with curved surfaces, with dissipative and re-centering capacity linked respectively to the friction between the surfaces and to their shape [30].

4.3.1 Preliminary design of a reinforced elastomeric isolator

The former typology of isolators consists of layers of rubber with diameter D_e, thickness t_i, which usually assumes values that differ by a maximum of 1-2 mm from the quantity $D_e/100$, and steel plates with diameter $D = D_e - 20 \; mm$, and thickness t_s usually larger than 2 mm. Furthermore, two steel plates with a thickness t_{ss} larger than 20 mm delimit the device at the top and bottom extremities. In the center of the device a hole of diameter D can be realized, usually useful in the production phases.

Subsequently, the two steel plates are connected by bolting to further steel plates characterized by a square section, with a side larger than D_e, from which the metal anchors start, in such a way as to guarantee the shear connection between the superstructure and the substructure [30]. The steel layers give a large stiffness in the vertical direction, limiting the phenomenon of lateral buckle that characterizes the rubber layers.
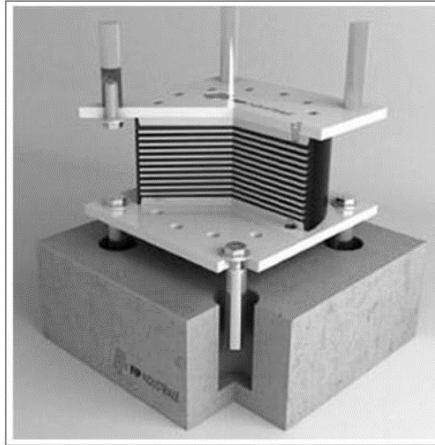
Figure 101 : Reinforced elastomeric isolator

In the case at study, it was decided to create *HDRB* high damping devices, i.e. high damping rubber bearing, characterized by a viscous damping value between 10% and 15%, as choosing the option of low damping isolators would have led to the need for the use of further devices that contribute to the damping itself.

In order to carry out the verifications, the introduction of the definition of the following parameters is necessary:

- the steel plates area A';
- *L,* that is the free lateral surface area of the single elastomer layer, equal to $\pi\, Dt_i$ in the absence of internal holes;
- $t_e = n_g t_i$, i.e. the total rubber thickness;
- the effective reduced area under an imposed relative displacement d_e between the two isolator faces, equal to $A_r = (\varphi - sen(\varphi))\pi D^2/4$, where φ is computed as $\varphi = 2\arccos(d_e/D)$;
- the primary shape factor $S_1 = A'/L$;
- the secondary shape factor $S_2 = D/t_e$

Finally, the dynamic shear modulus of the device G_{din}, is the shear modulus associated to the horizontal stiffness:

$$K_e = \frac{G_{din}A'}{t_e} \tag{4.1}$$

The shear modulus is usually, for commercial materials, in a range from a minimum of 0.4 MPa to a maximum of 1.4 MPa, corresponding respectively to soft and hard rubber.

Once the necessary parameters for the sizing have been defined, the preliminary design of a system consisting of four *HDRB* high-damping elastomeric isolators associated to the viaduct deck in scale 1:5 was carried out, with a deck mass equal to $2.4 kN/g$.

The first design step consists in the choice of the period T_{is} to be given to the isolated system through the realization of the devices; in fact, the insertion of the isolators is aimed at increasing the structural natural period, with smaller accelerations in terms of spectral ordinates, with a consequent decoupling of the motion of the superstructure with respect to that of the substructure. With this purpose, a fundamental period for the structure was imposed, corresponding to an acceleration value on the response spectrum that is smaller than that of the same structure without devices, with an increase in the associated displacement spectral ordinate.

A crucial aspect in defining T_{is} is the definition of the design spectrum related to the physical scaled model: the goal is to impose an equality between the accelerations of the real structure and those of the scaled model.

The design spectrum must be indeed scaled appropriately, considering the relationship between the periods and between the accelerations. Indicating with the subscript R the quantities relating to the real structure and with M those relating to the model, for the accelerations the following equation must be satisfied:

$$a_M = a_R \qquad (4.2)$$

The proper periods to be obtained through the isolation system of the real viaduct and that of the scaled physical model are shown in the following table, in which the ratio between them has been assumed to be equal to the square root of the scale factor ($\sqrt{5}$):

Mode	Direction	T_{is} for the scaled model	T_{is} for the real viaduct
1	X	0.22 s	0.49 s

Table 41 *: Natural periods for the real Viaduct and for the scaled model*

After choosing the ordinate value in the SLC spectrum of the scaled model, associated to the value of the damping factor ξ_{is} that will be given to the isolation system, the period T_{is} was selected.
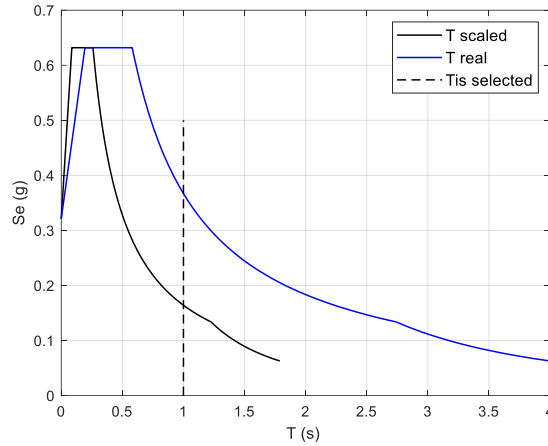
Figure 102 : SLC Site spectrum scaled spectrum for the HDRB system with ξis=10%

As regards the choice of the T_{is} value in the scaled structure, it can be assumed as the vibration period of the isolated structure only if it guarantees the necessary decoupling, that is, if it is larger than three times the period of the non-isolated structure. In the case under examination:

- It was decided to give the isolation system a damping factor ξ_{is} equal to 10%;
- The period was chosen equal to **1s** for the scaled structure, to which a period of **2.24 s** is associated for the real structure.

This choice meets the criteria for Tis, as it is included in the interval:

$$(3 * 0.22)s \leq T_{is} \leq 3s$$

The next step consists in calculating the equivalent horizontal stiffness associated with the period T_{is}. For the purpose of a preliminary design of the isolators, the theoretical total K_{esi} stiffness of the isolation system in the horizontal direction was therefore defined, starting from a model consisting of the superstructure, considered rigid and constrained with a rotational elastic element around the vertical axis Z, of stiffness K_z, and with two linear elastic elements in the horizontal directions X and Y. The latter are characterized by the horizontal stiffness $K_{esix} = K_{esiy} = K_{esi}$.

174

With regard to the purely translational motions of the structure in the two horizontal directions, the following relation holds:

$$T_{is} = 2\pi \sqrt{\frac{M}{K_{esi}}} \qquad (4.3)$$

By setting the period T_{is} previously chosen and known the mass M of the deck, equal to $2.4 \, kN/g$, the total stiffness of the isolation system can be obtained as:

$$K_{esi} = \left(\frac{2\pi}{T_{is}}\right)^2 M = 0.097 \, kN/mm \qquad (4.4)$$

For the selected pattern, containing four identical elastomeric isolators, the stiffness K_e of the single elastomeric isolator was obtained:

$$K_e = \frac{K_{esi}}{4} = 0.024 \, kN/mm \qquad (4.5)$$

In order to design the isolation system, an estimate of the displacements spectral ordinate is necessary. The latter is evaluated from the acceleration spectral ordinate at the SLC, for the damping factor ξ_{is}, through the relation:

$$S_{De} = S_e \left(\frac{2\pi}{T_{is}}\right)^2 = 41 \, mm \qquad (4.6)$$

It should be emphasized that the effects of the horizontal action acting in the orthogonal direction must be added to the effects of the seismic action in the direction considered. Therefore, the maximum design displacement was obtained as:

$$d_e = d_{ex} + 0.3d_{ey} = Sde(T_{is}) + 0.3\, Sde(T_{is}) = 55 \, mm \qquad (4.7)$$

Known the horizontal stiffness of the isolation device, the maximum displacement and the vertical load V, the device can be designed for the assumed 10% damping factor. In the case under examination:

K_e	V	d_e
$0.024 \, kN/mm$	$(M*g)/6 = 4 \, kN$	$55 \, mm$

The preliminary design was carried out with the following criteria, in such a way as to design a device as proportionate as possible:

- Steel plates diameter equal to twice the design displacement: $D = 2\,d_e$;
- Shear modulus equal to the smaller value in the commercial range $G = 0.4MPa$;
- Thickness of the horizontal rubber layer t_i approximately equal to $D_e/100$;
- Total thickness of the rubber t_e approximately equal to $D/4$.

From the available data, it is impossible to create a configuration of four devices relating to the deck system that can satisfy all the requirements listed above, suitable for creating a well-proportioned device. A preliminary design that can satisfy the largest number of requirements and that is characterized by a horizontal stiffness associated with a period of 1s is the following:

Total rubber thickness	t_e	**158**	mm
Steel plates diameter	D	110	mm
Shear modulus	G	0.4	N/mm2
Horizontal stiffness of the i-th device	K_e	0.024	kN/mm
Total horizontal stiffness	K_{etot}	0.097	kN/mm
Period of the scaled model	T_{is}	1.0	s
Thickness of the i-th rubber layer	t_i	2	mm
Thickness of the i-th steel plate	t_s	2	mm
Primary shape factor	S_1	13.8	-
Secondary shape factor	S_2	0.7	-

Table 42 : Parameters for the preliminary design of the isolator system

However, to create isolation devices with a horizontal stiffness associated with a period of 1s for the analyzed scaled structure, the only solution that satisfies the requirements on the diameter and that is achievable with a shear modulus G in the commercially available range, is characterized by non proportionate total thicknesses of the rubber:

$$K_e = \frac{GA}{t_e} = \frac{G\pi D^2}{4t_e} \qquad (4.8)$$

Considering the critical load V_{cr}, the following expression is satisfied, evaluated starting from the dynamic shear modulus G and from the effective reduced area A_r under an imposed a relative displacement between the two faces of the isolator:

$$V_{cr} = G_{din} A_r S_1 \frac{D}{t_e} \tag{4.9}$$

Where:

- $G_{din} = 0.4 \ MPa$
- $A_r = \left(\varphi - sen(\varphi)\right)\frac{D^2}{4} = 3716 \ mm^2$, with $\varphi = 2arccos(d_e/D)$
- $S_1 = A'/L = 13.8$ is the primary shape factor.

In the case under examination, the check on the following ratio is satisfied:

$$\frac{V_{cr}}{V} = \frac{14.3}{4} = 3.6 \geq 2 \tag{4.10}$$

The NTC 2018 also impose a limit on the angular deformation due to shear and on the total one γ_t; in fact, they require the following checks to be satisfied:

$$\gamma_s = \frac{d_e}{t_e} = 0.349 \ \leq 2 \tag{4.11}$$

$$\gamma_t = \gamma_s + \gamma_c + \gamma_a = 0.65 \ \leq 5 \tag{4.12}$$

Where:

- γ_s represents the angular deformation due exclusively to shear;
- γ_c is the shear deformation of the elastomer produced by compression, for which the technical standards report the following expression:

$$\gamma_c = 1.5 \frac{V}{S_1 A_r G_{din}} = 0.294 \tag{4.13}$$

- γ_a represents the shear deformation of the elastomer produced by bending, evaluated through the following relationship in the case of a circular isolator; it is a function of the angle of rotation α of the horizontal layers of rubber between the steel plates:

$$\gamma_a = \frac{3}{8} \frac{\alpha \ D^2}{t_e t_i} = 0.008 \tag{4.14}$$

An alternative preliminary design based on the reduction of the shear modulus G to 0.2 MPa is proposed, which would allow to obtain the horizontal stiffness value previously calculated for the device with a significantly smaller value of the total thickness of the rubber.

Total rubber thickness	t_e	80	mm
Steel plates diameter	D	110	mm
Period of the scaled model	T_{is}	1	s
Thickness of the i-th rubber layer	t_i	2	mm
Thickness of the i-th steel plate	t_s	2	mm
Primary shape factor	S_1	13.8	-
Secondary shape factor	S_2	1.4	-
Critical load	V_{cr}	14.3	kN
V_{cr}/V		3.6	-

Table 43 : Parameters for the 1st alternative of preliminary design of the isolator system

A second option, associated with a smaller critical load, provides for the realization of an isolator with a central hole having a diameter equal to $D/2$, in such a way as to act on the stiffness without reducing the shear modulus G.

Total rubber thickness	t_e	120	mm
Steel plates diameter	D	110	mm
Period of the scaled model	T_{is}	1	s
Thickness of the i-th rubber layer	t_i	1.5	mm
Thickness of the i-th steel plate	t_s	2	mm
Primary shape factor	S_1	9.2	-
Secondary shape factor	S_2	0.92	-
Critical load	V_{cr}	8.9	kN
V_{cr}/V		2.2	-

Table 44 : Parameters for the 2nd alternative of preliminary design of the isolation system

Although the first option leads to a more proportionate isolator, the second alternative is more easily achievable, as a material characterized by a shear modulus lower than 0.4 MPa is hardly available in the commercial field.

4.3.2 Preliminary design of a friction pendulum isolator

The sliding isolator with curved surfaces (CSS), incorporates without the aid of other elements:

- The re-centering function, given by the curved surface which allows the device to return to its position when the external horizontal action stops;
- The dissipative function, since the surfaces are not lubricated and, therefore the friction is not reduced.
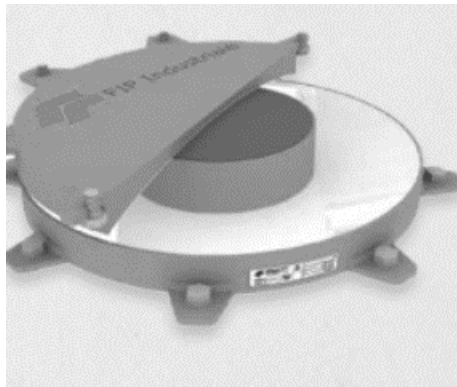
Figure 103 : Friction pendulum isolator

To understand the advantages of sliding isolators with curved surfaces, a simple pendulum of length R and mass m in free oscillation can be considered. For small oscillations, the equilibrium equations in the generic configuration, identified by θ, between the inertia force and the recall force due to the weight mg, is expressed as:

$$mR\ddot{\theta} + mg\theta = 0 \qquad (4.15)$$

Comparing it with that of the simple oscillator, the period of oscillation is obtained, independent of the mass:

$$T = 2\pi\sqrt{R/g} \qquad (4.16)$$

The relationship above shows a fundamental characteristic for the preliminary design of an isolation system with sliding isolators characterized by curved surfaces, i.e. the period is not influenced by the mass of the superstructure, and can be consequently chosen by fixing only the radius of curvature of the devices [30].

Furthermore, the stiffness of a CSS is a function of the vertical load V acting on the device, as this ensures that the center of gravity of the stiffnesses coincides with the projection on the isolation plane of that of the masses of the superstructure.

The preliminary design can be performed by setting the radius R and the coefficient of friction μ. An iterative procedure thus started by assigning a first attempt displacement d_1 and calculating the corresponding period and damping:

$$T_{is,1} = 2\pi \sqrt{\frac{1}{\left(\frac{1}{R} + \frac{\mu}{d_1}\right) g}} \qquad (4.17) \qquad \xi_{is,1} = \frac{2}{\pi \left(\frac{d_1}{\mu R} + 1\right)} \qquad (4.18)$$

On the displacement spectrum relative to the damping value $\xi_{is,1}$, in correspondence with the period $T_{is,1}$, a new displacement value d_2 is read for the following iteration. The procedure ended when $d_i - d_{i-1}$ was smaller than a certain tolerance, consequently obtaining the values of the period and of the damping.

In the case at study, the values for the radius R and the friction coefficient μ were set, respectively equal to 500 mm and 0.04. The values of the period and of the damping of the isolator system were then evaluated with the iterative procedure explained above. The values of the period and of the damping of the isolation system were initially calculated, given the radius and the coefficient of friction chosen, for a first attempt value for the design displacement equal to 100 mm:

$$T_{is,1} = 2\pi \sqrt{\frac{1}{\left(\frac{1}{R} + \frac{\mu}{d_1}\right) g}} = 1.29 \qquad (4.19) \qquad \xi_{is,1} = \frac{2}{\pi \left(\frac{d_1}{\mu R} + 1\right)} = 11\% \qquad (4.20)$$

The value of the displacement d_2 for the following iteration was identified, equal to the value of the displacement spectrum plotted for $\xi_{is} = 11\%$ for the period $T_{is} = 1.29\ s$. Known the displacement d_2, the values of the period and of the damping were calculated again, until the convergence on the displacement value was reached. The parameters obtained regard the third iteration, and are equal to the following values:

$$\begin{aligned} d &= 125\ mm & \mu &= 0.04 \\ V &= 24\ kN & Tis &= 1.32\ s \\ R &= 500\ mm & \xi is &= 9\% \end{aligned}$$

5

CONCLUSIONS AND FUTURE DEVELOPMENTS

In the current thesis, the main objective was to assess the seismic vulnerability of the Sordo Viaduct. It was pursued through steps with a progressively higher computational cost.

In fact, starting from an approximate analysis for the evaluation of the M-N interaction domain at the base of the pier, a more refined model of the pier itself was assessed, which took into account the non-linearities at its base. Subsequently, the contributions of the other structural elements, such as supports and deck, were also introduced in the numerical evaluation of the seismic response of the viaduct in question.

A model of the bridge in its entirety was in fact created, starting from eigenvalue analysis to evaluate the modal shapes of the viaduct itself, according to two main models that took into consideration the different modeling of the deck and that of the supports.

Progress was made towards the introduction in the models of the phenomenon regarding the dynamic interaction of the structure with the soil deformability, and its influence on the response of the structure has been studied. In particular, through the representation of the seismic action by means of artificial ground time histories generated with the SIMQKE software and by means of a response spectrum, it was possible to make a comparison between the results from the two different typologies of analysis, in order to evaluate whether, in a numerical model inhomogeneous from the dissipative point of view, the linear modal dynamic analysis could be a valid alternative to the direct integration one, being the latter associated to higher computational costs. Actually, from the comparison, emerged that in the response spectrum linear dynamic analysis the influence of the dynamic soil-structure interaction phenomenon was much more marked than in a time history analysis

through direct integration, in which it produced small variations in terms of displacement at the top of the pier and in terms of base shear.

A further step towards the evaluation of the seismic vulnerability of the Sordo Viaduct, was carrying out analysis that were focused on the evolution of the damage parameters in terms of deformations and internal forces in the various structural components of the viaduct with respect to the increase in the seismic intensity level, with the dual purpose of assessing the state of internal forces and deformations in the viaduct subjected to the site seismic intensity, and to predict for which level of intensity measure the limit states set for its elements would be reached.

The results showed that, the deformation limits at the base of the pier in terms of maximum fiber compression strain and steel fiber tension deformation haven't been exceeded in the two materials under the seismic action of the site in question. However, considering the shear forces at the pier base, the shear strength was reached for scale factors even smaller than 1; this is mainly due to the fact that the pier is characterized by non-closed shear reinforcement, which doesn't perform their function in the shear strength increase.

Furthermore, the main problem seems to be associated with the neoprene bearings: even the intervention carried out constraining their transversal shear deformations, through transversal seismic restraints, the problem related to their excessive deformation is not eliminated. Indeed, even in this model, the longitudinal shear strains are closed to their limit value, selected equal to 100%, for the scale factor that represents the seismic intensity of the site, not even considering a coefficient that indicates the deterioration of the neoprene support.

As far as future developments are concerned, both the experimental and the numerical levels can be deepened. As regards the numerical modeling and the post-processing of the data obtained, incremental dynamic analysis could be carried out for a larger number of time histories, in order to make the results more suitable from the probabilistic point of view, with a subsequent evaluation of the viaduct fragility curve. Numerous factors could be introduced in the model, such as a non-linear behavior for the neoprene supports; as a further interesting future development, the neoprene

bearings could be replaced in the software by the model of real isolators in Midas Gen code, obviously with linear analysis for all structural elements for this case.

Possible future developments may also regard the experimental analysis, carrying out a post-processing of the results coming from static tests and dynamic tests on the shaking table, carried out on the built physical scaled model.

6
APPENDIX

6.1 Photographic survey of the Sordo Viaduct
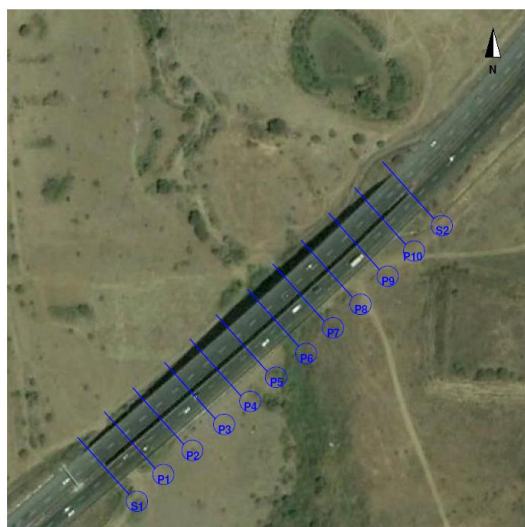
Figure 104 : Top view of the Sordo Viaduct

Figure 105 : Global side view of the two Sordo Viaduct roadways

Figure 106 : *Global side view of a roadway*

Figure 107 : *Bottom view of the two viaduct roadway*

Figure 108 : Pier view

Figure 109 : Roadway view

6.2 Graphs and analysis results
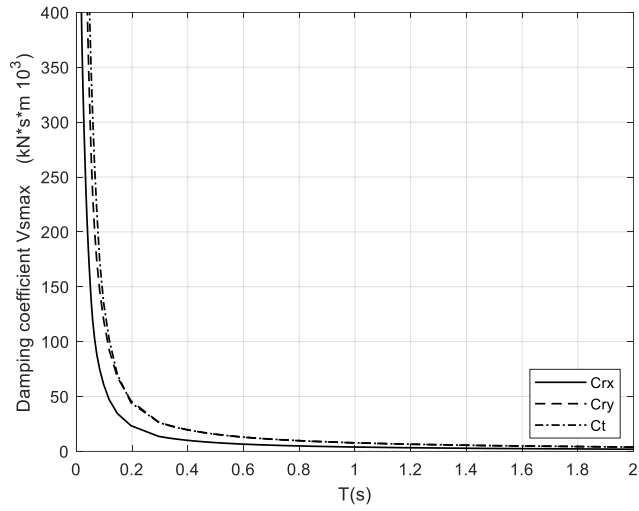
Figure 110 *: Rotational damping coefficients for Vsmax*
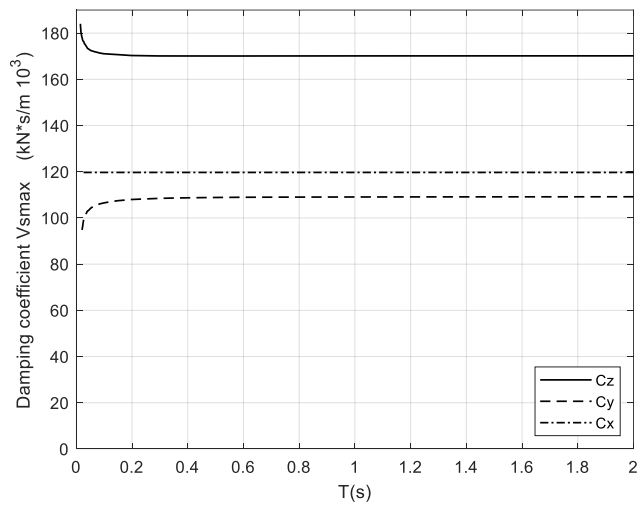
Figure 111 *: Translational damping coefficients for Vsmax*
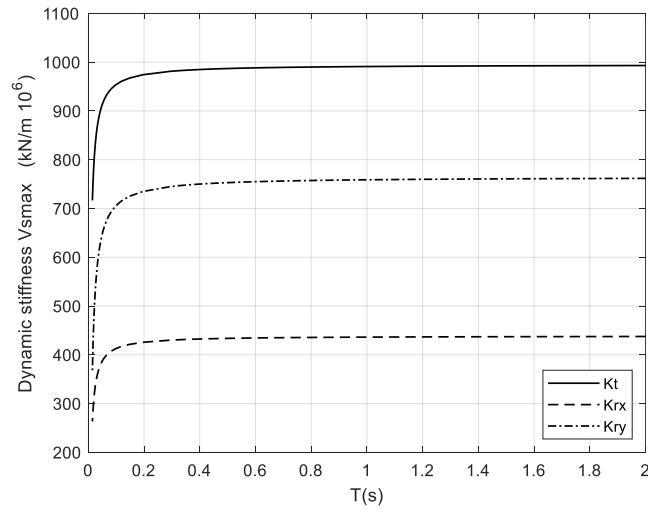
Figure 112 *: Rotational stiffness coefficients for Vsmax*
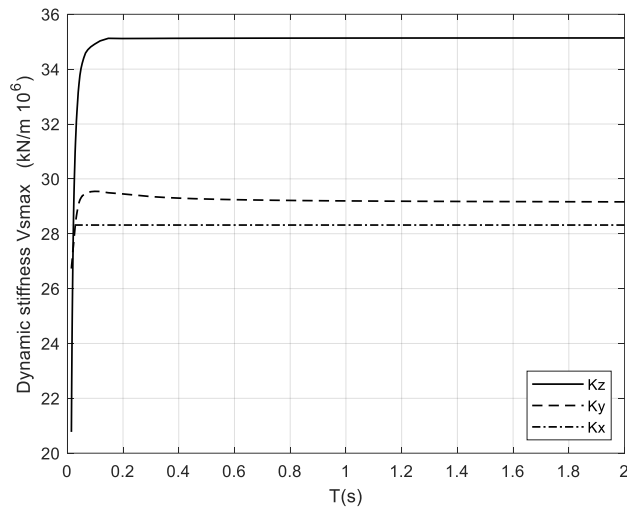
Figure 113 *: Translational stiffness coefficients for Vsmax*
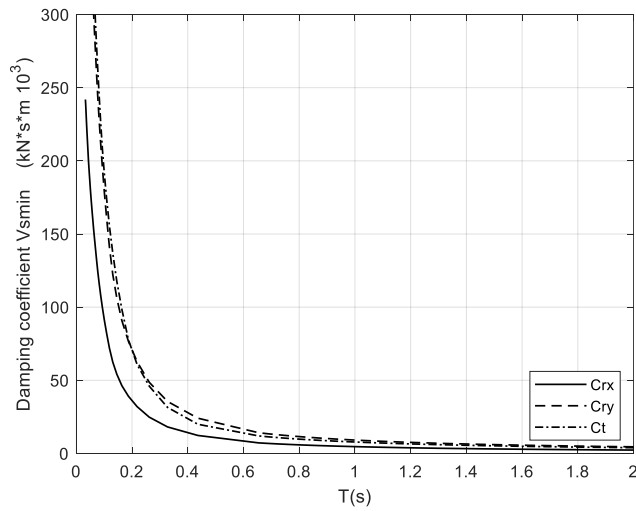
Figure 114 *: Rotational damping coefficients for Vsmin*
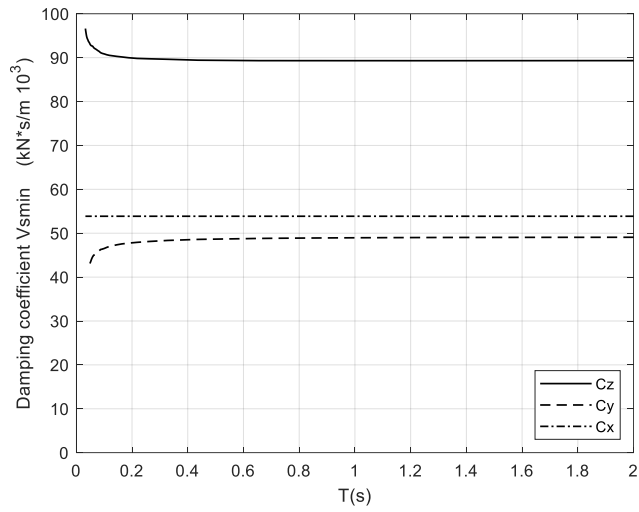
Figure 115 *: Translational damping coefficients for Vsmin*
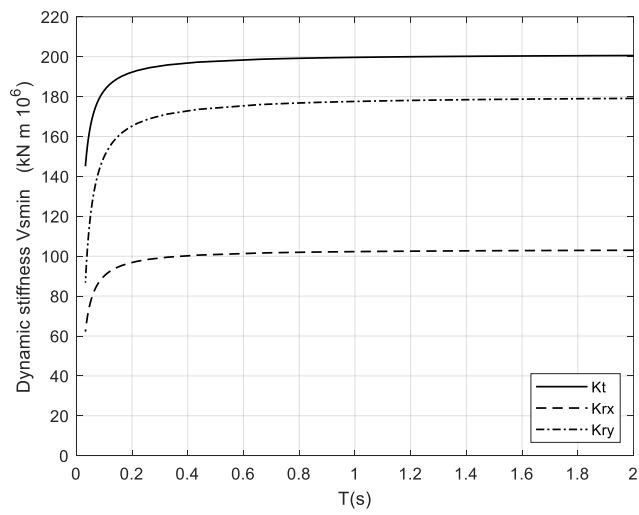
Figure 116 *: Rotational stiffness coefficients for Vsmin*

189

Mode	T [s] Model 1 Fixed Base	T [s] Model 1 V_{Smax}	T [s] Model 1 V_{Smin}
1	0.965	0.971	0.992
2	0.851	0.860	0.891
3	0.796	0.800	0.814
4	0.766	0.773	0.797
5	0.705	0.708	0.727
6	0.703	0.708	0.719
7	0.669	0.674	0.689
8	0.653	0.656	0.665
9	0.642	0.645	0.658
10	0.625	0.628	0.638
11	0.618	0.620	0.628
12	0.611	0.613	0.619
13	0.603	0.605	0.610
14	0.593	0.595	0.600
15	0.592	0.593	0.595
16	0.590	0.590	0.591
17	0.587	0.587	0.587
18	0.576	0.577	0.580
19	0.562	0.562	0.565
20	0.553	0.553	0.554
21	0.548	0.549	0.549
22	0.544	0.544	0.544
23	0.486	0.489	0.499
24	0.440	0.443	0.450
25	0.415	0.417	0.422
26	0.401	0.402	0.407
27	0.391	0.393	0.397
28	0.385	0.386	0.388
29	0.380	0.380	0.382
30	0.376	0.376	0.377
31	0.373	0.373	0.374
32	0.372	0.372	0.372
33	0.371	0.371	0.371
34	0.275	0.276	0.281
35	0.263	0.265	0.269
36	0.257	0.258	0.262
37	0.241	0.242	0.245
38	0.237	0.239	0.244
39	0.229	0.230	0.233
40	0.222	0.224	0.230
41	0.218	0.219	0.222
42	0.210	0.211	0.214

Mode	T [s] Model 1 Fixed Base	T [s] Model 1 V_Smax	T [s] Model 1 V_Smin
43	0.205	0.206	0.210
44	0.200	0.201	0.203
45	0.196	0.197	0.203
46	0.193	0.194	0.197
47	0.193	0.193	0.196
48	0.190	0.191	0.193
49	0.189	0.189	0.192
50	0.188	0.189	0.192

Table 45 *: Natural periods from Eigenvalue analysis in Model 1 for the first 50 modes*

Mode	T [s] Model 2 Fixed Base	T [s] Model 2 V_{Smax}	T [s] Model 2 V_{Smin}
1	1.004	1.011	1.034
2	0.824	0.829	0.844
3	0.722	0.725	0.737
4	0.665	0.667	0.677
5	0.630	0.632	0.640
6	0.604	0.605	0.633
7	0.586	0.598	0.611
8	0.584	0.585	0.589
9	0.570	0.571	0.573
10	0.561	0.561	0.562
11	0.556	0.556	0.560
12	0.553	0.553	0.556
13	0.518	0.528	0.553
14	0.464	0.473	0.501
15	0.405	0.414	0.442
16	0.369	0.378	0.407
17	0.290	0.298	0.325
18	0.284	0.292	0.320
19	0.275	0.276	0.281
20	0.263	0.265	0.269
21	0.257	0.258	0.267
22	0.237	0.242	0.262
23	0.235	0.239	0.244
24	0.222	0.224	0.230
25	0.195	0.200	0.222
26	0.195	0.196	0.202
27	0.191	0.192	0.197
28	0.186	0.187	0.196
29	0.186	0.187	0.190
30	0.185	0.186	0.189
31	0.185	0.186	0.189

32	0.185		0.186		0.188	
33	0.185		0.185		0.187	
34	0.184		0.185		0.186	
35	0.184		0.184		0.186	
36	0.184		0.184		0.185	
37	0.180		0.182		0.185	
38	0.178		0.179		0.182	
39	0.173		0.175		0.180	
40	0.168		0.169		0.171	
41	0.166		0.166		0.168	
42	0.164		0.164		0.165	
43	0.163		0.163		0.164	
44	0.163		0.163		0.163	
45	0.162		0.162		0.163	
46	0.160		0.161		0.162	
47	0.160		0.160		0.162	
48	0.155		0.156		0.161	
49	0.148		0.151		0.160	
50	0.147		0.150		0.156	

Table 46 : *Natural periods from Eigenvalue analysis in Model 2 for the first 50 modes*

Bearings	εy	εx	Check ε	τhy	τhx	$\mu * \sigma v$	Check τ
1	0.89	0.90	NO	0.80	0.81	1.34	OK
2	0.89	0.89	NO	0.80	0.80	0.97	OK
3	0.89	0.89	NO	0.80	0.80	0.95	OK
4	0.89	0.89	NO	0.80	0.80	0.98	OK
5	0.89	0.89	NO	0.80	0.80	1.29	OK
6	0.93	0.70	NO	0.84	0.63	1.33	OK
7	0.93	0.70	NO	0.84	0.63	0.98	OK
8	0.93	0.70	NO	0.84	0.63	0.97	OK
9	0.93	0.70	NO	0.84	0.63	0.99	OK
10	0.93	0.70	NO	0.84	0.63	1.28	OK
11	0.95	0.86	NO	0.85	0.77	1.34	OK
12	0.95	0.86	NO	0.85	0.77	0.97	OK
13	0.95	0.86	NO	0.85	0.77	0.96	OK
14	0.95	0.86	NO	0.85	0.77	0.98	OK
15	0.95	0.86	NO	0.85	0.77	1.34	OK
16	0.96	0.79	NO	0.87	0.71	1.34	OK
17	0.97	0.79	NO	0.87	0.71	0.97	OK
18	0.97	0.79	NO	0.87	0.71	0.96	OK
19	0.97	0.79	NO	0.87	0.71	0.98	OK

20	0.96	0.79	NO	0.87	0.71	1.33	OK
21	0.88	0.73	NO	0.79	0.66	1.32	OK
22	0.88	0.73	NO	0.79	0.66	0.96	OK
23	0.88	0.73	NO	0.79	0.66	0.96	OK
24	0.88	0.73	NO	0.79	0.66	0.98	OK
25	0.88	0.73	NO	0.79	0.66	1.33	OK
26	0.89	0.71	NO	0.80	0.64	1.33	OK
27	0.89	0.71	NO	0.80	0.64	0.97	OK
28	0.89	0.71	NO	0.80	0.64	0.97	OK
29	0.89	0.71	NO	0.80	0.64	0.98	OK
30	0.89	0.71	NO	0.80	0.64	1.33	OK
31	0.75	0.84	NO	0.67	0.76	1.36	OK
32	0.75	0.84	NO	0.68	0.76	0.98	OK
33	0.75	0.84	NO	0.68	0.76	0.97	OK
34	0.75	0.85	NO	0.68	0.76	0.99	OK
35	0.75	0.85	NO	0.67	0.76	1.35	OK
36	0.81	0.55	NO	0.73	0.50	1.31	OK
37	0.81	0.54	NO	0.73	0.49	0.98	OK
38	0.81	0.54	NO	0.73	0.48	0.98	OK
39	0.81	0.54	NO	0.73	0.48	0.99	OK
40	0.81	0.54	NO	0.73	0.49	1.35	OK
41	0.77	0.93	NO	0.69	0.84	1.37	OK
42	0.77	0.92	NO	0.69	0.83	0.98	OK
43	0.77	0.91	NO	0.69	0.82	0.97	OK
44	0.77	0.92	NO	0.69	0.82	0.98	OK
45	0.77	0.93	NO	0.69	0.83	1.39	OK
46	0.78	0.59	NO	0.70	0.53	1.34	OK
47	0.78	0.57	NO	0.71	0.52	0.97	OK
48	0.78	0.57	NO	0.71	0.51	0.97	OK
49	0.78	0.58	NO	0.71	0.52	0.99	OK
50	0.78	0.61	NO	0.70	0.55	1.37	OK
51	1.03	1.02	NO	0.93	0.92	1.49	OK
52	1.03	1.01	NO	0.93	0.91	1.00	OK
53	1.03	1.01	NO	0.93	0.91	0.98	OK
54	1.03	1.01	NO	0.93	0.91	0.99	OK
55	1.03	1.01	NO	0.93	0.91	1.53	OK
56	1.10	0.71	NO	0.99	0.64	1.46	OK
57	1.10	0.69	NO	0.99	0.62	0.97	NO
58	1.10	0.67	NO	0.99	0.61	0.97	NO
59	1.10	0.67	NO	0.99	0.60	0.99	NO
60	1.10	0.68	NO	0.99	0.61	1.49	OK
61	0.90	0.50	NO	0.81	0.45	1.38	OK

62	0.90	0.45	NO	0.81	0.40	0.98	OK
63	0.90	0.43	NO	0.81	0.39	0.97	OK
64	0.90	0.45	NO	0.81	0.41	0.98	OK
65	0.90	0.51	NO	0.81	0.46	1.40	OK
66	0.84	1.02	NO	0.76	0.92	1.44	OK
67	0.84	1.02	NO	0.76	0.92	0.97	OK
68	0.83	1.02	NO	0.75	0.92	0.97	OK
69	0.84	1.06	NO	0.76	0.95	0.99	OK
70	0.84	1.09	NO	0.76	0.98	1.48	OK
71	0.74	0.63	OK	0.67	0.57	1.34	OK
72	0.74	0.63	OK	0.67	0.56	0.97	OK
73	0.74	0.63	OK	0.67	0.56	0.96	OK
74	0.74	0.63	OK	0.67	0.57	0.98	OK
75	0.74	0.64	OK	0.67	0.58	1.35	OK
76	0.78	0.83	NO	0.70	0.75	1.35	OK
77	0.78	0.82	NO	0.70	0.74	0.97	OK
78	0.78	0.82	NO	0.70	0.73	0.96	OK
79	0.78	0.81	NO	0.70	0.73	0.97	OK
80	0.78	0.81	NO	0.70	0.73	1.37	OK
81	0.91	0.58	NO	0.82	0.52	1.36	OK
82	0.91	0.58	NO	0.82	0.52	0.97	OK
83	0.91	0.59	NO	0.82	0.53	0.97	OK
84	0.91	0.60	NO	0.82	0.54	0.98	OK
85	0.91	0.61	NO	0.82	0.55	1.36	OK
86	0.88	0.83	NO	0.79	0.75	1.36	OK
87	0.88	0.83	NO	0.79	0.75	0.98	OK
88	0.88	0.83	NO	0.79	0.75	0.97	OK
89	0.88	0.84	NO	0.79	0.75	0.98	OK
90	0.88	0.85	NO	0.79	0.76	1.38	OK
91	0.83	0.53	NO	0.75	0.48	1.31	OK
92	0.83	0.53	NO	0.75	0.47	0.98	OK
93	0.83	0.53	NO	0.75	0.48	0.97	OK
94	0.83	0.53	NO	0.75	0.48	0.97	OK
95	0.83	0.54	NO	0.75	0.49	1.30	OK
96	0.78	0.74	NO	0.71	0.67	1.34	OK
97	0.79	0.74	NO	0.71	0.67	0.98	OK
98	0.79	0.75	NO	0.71	0.67	0.98	OK
99	0.79	0.75	NO	0.71	0.67	0.99	OK
100	0.79	0.75	NO	0.71	0.68	1.32	OK
101	0.95	0.78	NO	0.86	0.71	1.32	OK
102	0.95	0.78	NO	0.86	0.71	0.97	OK
103	0.95	0.78	NO	0.86	0.71	0.95	OK

104	0.95	0.79	NO	0.86	0.71	0.98	OK
105	0.95	0.79	NO	0.86	0.71	1.27	OK
106	0.93	0.90	NO	0.84	0.81	1.34	OK
107	0.94	0.89	NO	0.84	0.80	0.98	OK
108	0.94	0.89	NO	0.84	0.80	0.96	OK
109	0.94	0.89	NO	0.84	0.80	0.99	OK
110	0.93	0.89	NO	0.84	0.81	1.29	OK

Table 47 : Direct integration Time history linear analysis - Bearings checks on Model 1 Vsmin

Bearings	V_{smin}			V_{smax}		
	εy	εx	$Check\ \varepsilon$	εy	εx	$Check\ \varepsilon$
1	0.75	0.80	NO	0.76	0.78	NO
2	0.75	0.79	NO	0.76	0.77	NO
3	0.75	0.78	NO	0.76	0.77	NO
4	0.75	0.79	NO	0.76	0.77	NO
5	0.75	0.80	NO	0.76	0.78	NO
6	0.81	0.61	NO	0.81	0.62	NO
7	0.81	0.60	NO	0.81	0.61	NO
8	0.81	0.60	NO	0.81	0.60	NO
9	0.81	0.60	NO	0.81	0.61	NO
10	0.81	0.61	NO	0.81	0.62	NO
11	0.92	0.77	NO	0.89	0.76	NO
12	0.92	0.77	NO	0.89	0.75	NO
13	0.92	0.76	NO	0.89	0.75	NO
14	0.92	0.77	NO	0.89	0.75	NO
15	0.92	0.77	NO	0.89	0.76	NO
16	0.93	0.71	NO	0.91	0.69	NO
17	0.93	0.70	NO	0.91	0.69	NO
18	0.93	0.70	NO	0.91	0.68	NO
19	0.93	0.70	NO	0.91	0.69	NO
20	0.93	0.71	NO	0.91	0.69	NO
21	0.80	0.65	NO	0.78	0.64	NO
22	0.80	0.64	NO	0.78	0.63	NO
23	0.80	0.64	NO	0.78	0.63	NO
24	0.80	0.64	NO	0.78	0.63	NO
25	0.80	0.65	NO	0.78	0.64	NO
26	0.80	0.59	NO	0.78	0.58	NO
27	0.80	0.58	NO	0.78	0.58	NO
28	0.80	0.58	NO	0.78	0.57	NO
29	0.80	0.58	NO	0.78	0.58	NO

30	0.80	0.59	NO	0.78	0.58	NO
31	0.72	0.86	NO	0.71	0.82	NO
32	0.72	0.84	NO	0.71	0.81	NO
33	0.72	0.82	NO	0.71	0.79	NO
34	0.72	0.84	NO	0.71	0.81	NO
35	0.72	0.86	NO	0.71	0.82	NO
36	0.75	0.52	OK	0.74	0.51	NO
37	0.75	0.51	OK	0.74	0.50	NO
38	0.75	0.49	OK	0.74	0.49	NO
39	0.75	0.51	OK	0.74	0.50	NO
40	0.75	0.52	OK	0.74	0.51	NO
41	0.74	0.98	NO	0.72	0.95	NO
42	0.74	0.94	NO	0.72	0.92	NO
43	0.74	0.91	NO	0.72	0.89	NO
44	0.74	0.94	NO	0.72	0.92	NO
45	0.74	0.98	NO	0.72	0.95	NO
46	0.75	0.64	NO	0.74	0.61	OK
47	0.75	0.61	NO	0.74	0.59	OK
48	0.75	0.59	NO	0.74	0.56	OK
49	0.75	0.61	NO	0.74	0.59	OK
50	0.75	0.64	NO	0.74	0.61	OK
51	1.01	1.00	NO	0.98	0.98	NO
52	1.01	0.99	NO	0.99	0.96	NO
53	1.01	0.97	NO	0.98	0.95	NO
54	1.01	0.99	NO	0.99	0.96	NO
55	1.01	1.00	NO	0.98	0.98	NO
56	1.06	0.68	NO	1.03	0.67	NO
57	1.06	0.66	NO	1.03	0.65	NO
58	1.06	0.64	NO	1.03	0.63	NO
59	1.06	0.66	NO	1.03	0.65	NO
60	1.06	0.68	NO	1.03	0.67	NO
61	0.87	0.48	NO	0.85	0.47	NO
62	0.87	0.44	NO	0.85	0.43	NO
63	0.87	0.40	NO	0.85	0.40	NO
64	0.87	0.44	NO	0.85	0.43	NO
65	0.87	0.48	NO	0.85	0.47	NO
66	0.81	1.11	NO	0.80	1.08	NO
67	0.81	1.08	NO	0.80	1.05	NO
68	0.80	1.03	NO	0.79	1.00	NO
69	0.81	1.08	NO	0.80	1.05	NO
70	0.81	1.11	NO	0.80	1.08	NO
71	0.68	0.65	OK	0.67	0.62	OK

72	0.68	0.63	OK	0.67	0.60	OK
73	0.68	0.61	OK	0.67	0.58	OK
74	0.68	0.63	OK	0.67	0.60	OK
75	0.68	0.65	OK	0.67	0.62	OK
76	0.72	0.82	NO	0.70	0.79	NO
77	0.72	0.80	NO	0.70	0.77	NO
78	0.72	0.78	NO	0.70	0.75	NO
79	0.72	0.80	NO	0.71	0.77	NO
80	0.72	0.82	NO	0.70	0.79	NO
81	0.83	0.73	NO	0.82	0.70	NO
82	0.83	0.71	NO	0.82	0.69	NO
83	0.83	0.70	NO	0.82	0.68	NO
84	0.83	0.71	NO	0.82	0.69	NO
85	0.83	0.73	NO	0.82	0.70	NO
86	0.81	0.85	NO	0.80	0.83	NO
87	0.82	0.84	NO	0.80	0.82	NO
88	0.82	0.83	NO	0.80	0.81	NO
89	0.82	0.84	NO	0.80	0.82	NO
90	0.81	0.85	NO	0.80	0.83	NO
91	0.83	0.60	NO	0.82	0.60	NO
92	0.83	0.59	NO	0.82	0.59	NO
93	0.83	0.57	NO	0.82	0.58	NO
94	0.83	0.59	NO	0.82	0.59	NO
95	0.83	0.60	NO	0.82	0.60	NO
96	0.78	0.91	NO	0.78	0.89	NO
97	0.78	0.90	NO	0.78	0.88	NO
98	0.78	0.89	NO	0.78	0.87	NO
99	0.78	0.90	NO	0.78	0.88	NO
100	0.78	0.91	NO	0.78	0.89	NO
101	0.81	0.68	NO	0.80	0.70	NO
102	0.81	0.68	NO	0.80	0.70	NO
103	0.81	0.67	NO	0.80	0.69	NO
104	0.81	0.68	NO	0.80	0.70	NO
105	0.81	0.68	NO	0.80	0.70	NO
106	0.78	0.79	NO	0.78	0.79	NO
107	0.78	0.78	NO	0.78	0.79	NO
108	0.78	0.78	NO	0.78	0.78	NO
109	0.78	0.78	NO	0.78	0.79	NO
110	0.78	0.79	NO	0.78	0.79	NO

Table 48 : *Response spectrum analysis - Bearings checks on Model 2 Vsmin and Vsmax*

6.3 Geometry of the 1:5 physical model
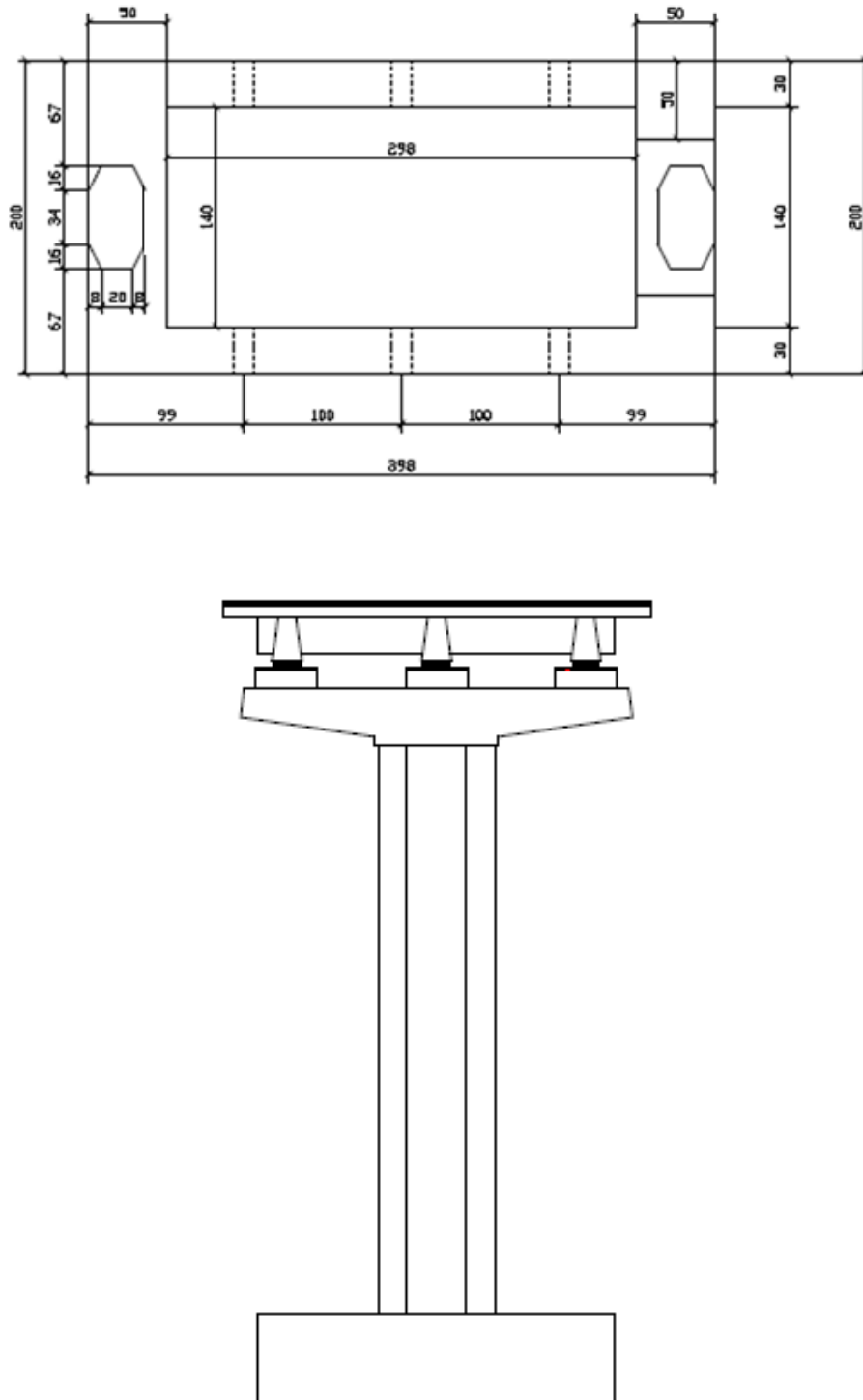
Figure 117 : *Top and front view of the 1:5 physical model*

6.4 Pictures of the 1:5 physical model

Figure 118 : Foundation beam and pier basement

Figure 119 : Pier shaft reinforcement pattern

Figure 120 : Substructure of the Physical model

Figure 121 : *Prefabricated prestressed deck beams*

Figure 122 : *Concrete casting of the slab*

References

[1]   R. Pefano (2020), "Gestione dei ponti esistenti Il quadro normativo Italiano e il confronto con alcune normative internazionali", *Ingenio: informazione tecnica e progettuale.*

[2]   Reluis (2009), "Linee guida e manauale applicativo per la valutazione della sicurezza sismica e il consolidamento dei ponti esistenti in c.a." *Progetto Reluis 2005-2008 Valutazione e riduzione del rischio Sismico di ponti esistenti.*

[3]   M. J. N. Priestley, F. Seible, and G. M. Calvi (1996) "Seismic Design and Retrofit of Bridges", *John Wiley & Sons, Inc.*

[4]   T. Paulay, M. J. N. Priestley (1992), "Seismic design of reinforced concrete and masonry buildings", *John Wiley & Sons, Inc.*

[5]   Ministero delle Infrastrutture e dei Trasporti (2019), "Istruzioni per l'applicazione dell'«Aggiornamento delle Norme tecniche per le costruzioni»" *Suppl. Ordin. alla Gazzetta Uff. n. 35 del 11 febbraio 2019.*

[6]   P. Tortolini, M. Petrangeli, A. Lupoi (2011), "Criteri per la verifica e la sostituzione degli appoggi in neoprene di viadotti esistenti in zona sismica", *Italian Conference ANIDIS 2011.*

[7]   Ministero delle Infrastrutture e dei Trasporti Consiglio Superiore dei Lavori Pubblici (2020), "Linee guida per la classificazione e gestione del rischio ed il monitoraggio dei ponti esistenti".

[8]   A. K. Chopra (2019) "Dynamics of structures: theory and applications to earthquake engineering" *Prentice-hall international series in civil engineering mechanics William J. Hall.*

[9]   J. J. Bommer and A. B. Acevedo (2004),"The use of real earthquake accelerograms as input to dynamic analysis", *Journal of Earthquake Engineering vol.8.*

[10]   M. Esposito (2008) "Accelerogrammi spettrocompatibili per la progettazione delle strutture:Valutazione comparativa della risposta sismica", *M.Sc. Thesis, Università degli studi di Napoli Federico II.*

[11]   I. Iervolino, C. Galasso, E. Cosenza (2009), "REXEL: computer aided record selection for code-based seismic structural analysis", *Bull Earthquake Engineering, 339–362.*

[12]   Vanderplaats Research & Development (2008), "Midas GEN Analysis Manual".

[13]   G. Monti and N. Nisticò (2002), "Simple Probability-Based Assessment of Bridges Under Scenario Earthquakes", *Journal of Bridge Engineering, Vol. 7, Issue 2.*

[14]   F. Viesi (2007) "Confronto tra modellazioni a plasticità diffusa e concentrata per strutture in c.a.: la scuola di Bisignano", *M.Sc. Thesis, Università degli studi di Bologna.*

[15]   B. D. Scott., R. Park, M. J. N. Priestley (1982) "Stress-Strain Behavior of Concrete Confined by Overlapping Hoops at Low and High Strain Rates", *ACI Journal.*

[16] H. Wang, S. F. Qin, and W. J. Xu (2011),"Seismic analysis of prestressed bridge pier based on fiber section", *Procedia Eng.*, vol. 21

[17] S. Coccia (2007) "Nuova modellazione del comportamento delle cerniere plastiche nel c.a.", *PhD Thesis, Università degli studi di Roma Tor Vergata.*

[18] F. C. Filippou, E. P. Popov, and V. V. Bertero (1983), "Effects of bond deterioration on hysteretic behavior of reinforced concrete joints", *Earthquake Engineering Research Center, Univ. California, Berkeley.*

[19] M. Bosco, E. Ferrara, A. Ghersi, E. M. Marino, and P. Rossi (2016), "Improvement of the model proposed by Menegotto and Pinto for steel", *Engineering Structures*, vol. 124.

[20] F. Perotti (2019), "Handouts of Dynamics of structures", Politecnico di Milano.

[21] J. G. Sieffert, F. Cevaer (1992), "Handbook of impedance functions: Surface foundations", *Editions Ouest-France.*

[22] G. Gazetas (1991), "Formulas and Charts for impedances of surfaces and embedded foundations", *Journal of Geotechnical Engineering, Vol. 117, Issue 9*

[23] J. M. Roesset, R. V. Whitman, R. Dobry (1972), "Modal analysis for structures with foundation interaction", *ASCE National Structural Engineering Meeting, Cleveland.*

[24] F. De Silva, F. Ceroni, M. Pecce, S. Sica (2014), "L'interazione terreno-struttura sotto azione sismica: il caso di studio del Campanile del Carmine a Napoli", *Convegno Nazionale di Geotecnica, Baveno.*

[25] G. J. O'Reilly, R. Monteiro (2019), "On the efficient risk assessment of bridge structures", *7th International Conference on Computational Methods in Structural Dynamics and Earthquake Engineering.*

[26] L. Alota (2018), "Effetto delle incertezze sulla valutazione probabilistica della vulnerabilità sismica di strutture esistenti", *M.Sc. Thesis, Politecnico di Milano.*

[27] D. Vamvatsikos, C. A. Cornell (2002), "Incremental dynamic analysis", *Earthquake Engineering and Structural Dynamics*, *vol. 31.*

[28] D. Paolini (2015), "Elaborazione e analisi dati di spostamento acquisiti tramite sistema motion capture 3D di edifici in muratura sottoposti a prove sismiche su tavola vibrante", *M.Sc. Thesis, Università degli studi di Roma Tre.*

[29] P. Clemente (2017), "L'isolamento sismico dei ponti: criteri di progetto e applicazioni", *Ingenio: informazione tecnica e progettuale.*

[30] P. Clemente, F. Saitta, G. Buffarini, G. Bongiovanni (2019), "L'isolamento sismico edifici esistenti: criteri di progetto e applicazioni", *Grafill.*

[31] Ministero delle Infrastrutture e dei Trasporti (2018), "Norme tecniche per le costruzioni", *DM 17/01/2018.*

Ringraziamenti

Un sentito grazie a tutte le persone che mi hanno permesso di arrivare fin qui e di portare a termine questo lavoro di tesi.

Desidero ringraziare il Prof. Federico Perotti, relatore della tesi, che con la sua disponibilità e competenza mi ha dato supporto in questi mesi e ha reso il corrente lavoro un'esperienza di cui fare tesoro.

Ringrazio tutto il team con cui sono entrata in contatto presso il C.R. Enea Casaccia, in particolar modo i miei correlatori, l'Ing. Fernando Saitta e l'Ing. Ivan Roselli, e l'Ing. Paolo Clemente, i quali mi hanno supportato e affiancato con professionalità durante il tirocinio.

Grazie ai miei genitori, che hanno sempre accettato le mie scelte e mi hanno permesso di seguire i sogni, credendo in me.

Ringrazio Ilaria e Federica e Federico, che con la loro simpatia hanno allietato le mie giornate, grazie per volermi bene così come sono.

Grazie Luca, che mi ha aiutato ad andare avanti e ad affrontare le mie difficoltà, sostenendomi sempre e comunque, grazie per l'amore che mi trasmetti ogni giorno.

Desidero ringraziare i miei zii, in particolare zio Maurizio, che mi ha supportato e guidato verso le scelte più giuste.

Ringrazio i miei amici dell'Università, che hanno reso il mio percorso di studi molto più ricco a livello umano.

Desidero ringraziare Michela e Andrea, che hanno reso l'ultimo anno molto più facile da superare con la loro simpatia e amicizia sincera.

Un grazie a Rocco e Roberta, che mi hanno accompagnato nelle risate e nelle difficoltà di ogni giornata di studio.

Grazie a chi mi ha permesso realmente di raggiungere questo traguardo, te ne sei andata durante il mio percorso, ma lo so che sei sempre con me e che mi sostieni da lassù. Grazie nonnina.

October 07, 2021

Chiara Mariani